Dissertation
submitted to the
Combined Faculties for the Natural Sciences and for Mathematics
of the Ruperto-Carola University of Heidelberg, Germany
for the degree of
Doctor of Natural Sciences

Put forward by

Diplomingenieur für Technische Physik: JAN MEINEN
Born in: BREMEN

Oral examination: 20. July 2010

T R A P S

THE KEY TO ATMOSPHERIC NANO-SCIENCE

Referees: Prof. Dr. Thomas Leisner

Prof. Dr. Ulrich Platt

TRAPS – Schlüsseltechnologie zur Untersuchung nanoskaliger Materie in der Atmosphäre

Die Bedeutung von Nanopartikeln für Prozesse in der Atmosphäre rückt zunehmend in das Interesse von Forschern. In vielen natürlichen Kondensationsprozessen sind die Kondensationskeime kleiner als $10\,nm$ im Durchmesser. Die ist genau der Übergangsbereich vom Cluster zum Festkörper, in dem physikalische und chemische Eigenschaften größenabhängig sind und stark von Obenflächenkontaminationen und Kontakt zu anderen Oberflächen abhängen. Bisher gab es keine Möglichkeit die fundamentalen Eigenschaften von freien, massenselektierten Nanopartikeln mit definiertem Ladungszustand und Durchmessern von 3 bis 30 nm in Laborexperimenten zu untersuchen.

Diese Arbeit zeigt die Notwendigkeit auf Laborexperimente zu entwickeln, die freie Nanopartikeln ohne vorherige Abscheidung auf Substraten oder Filtern zu untersuchen. Als Anwendungsbeispiel in der Atmosphärenforschung werden Eiswolken diskutiert, die sich an Nanopartikeln meteorischen Ursprunges in der Mesosphäre bilden.

Mit der TRAPS Apparatur ist es nun möglich verschiedene spektroskopische Methoden an freien Nanopartikelstrahlen oder gefangenen Nanopartikelwolken anzuwenden. Massenspekrometrie, optische Extinktionsspektroskopie und Innerschalen-Photoionisationsspektroskopie werden als Anwendungsbeispiele gezeigt. Als wissenschaftliches Novum werden Experimente zur Untersuchung von Eisnukleation an Nanopartikeln und die Bestimmung von Eiswachstumsgeschwindigkeiten unter mesosphärischen Bedingungen sowie XPS Messungen an sub-10 nm SiO_2 Partikeln gezeigt.

TRAPS – The key to atmospheric nano-science

The relevance of nanoparticles in atmospheric processes is a new topic of atmospheric research. In many condensation processes, the condensation nuclei are in the sub $10\ nm$ diameter range. Properties of particles with size in the transition region from cluster to bulk are size dependent and highly sensitive to surface contamination and contact to other surfaces. No investigation of the fundamental properties of free, mass selected nanoparticles with defined charge state and diameters from 3 to $30\ nm$ has been feasible in laboratory experiments so far.

This works illustrates the requirement of laboratory experimental methods for the investigation of free nanoparticles without the need for accumulation on substrates or filters. Ice clouds forming on meteoric smoke particle are given as example for the atmospheric relevance of this work.

The TRAPS apparatus provides a free nanoparticle beam or a trapped nanoparticle cloud to different spectroscopic methods. Experiments like mass spectrometry, extinction spectroscopy and photoelectron spectroscopy are demonstrated as investigation methods, applicable to nanoparticles of this size range. A method for the investigation of ice nucleation on nanoparticles and determination of growth rates under mesospheric conditions and a method for XPS studies sub-$10\ nm$ SiO_2 particles are shown as novel scientific results.

Contents

List of publications

Broadband Cavity Enhanced Differential Optical Absorption Spectroscopy (CE-DOAS) – applicability and corrections.
Platt. U; Meinen, J.; Pöhler, D.; Leisner, T.
Atmos. Meas. Tech., 2, 713-723, 2009

The TRAPS apparatus: Enhancing target density of nanoparticle beams in vacuum for X-ray and optical spectroscopy.
Meinen, J.; Khasminskaya, S.; Baumann, W.; Rühl, E. and Leisner, T.
Aerosol Science and Technology, 44, 316-328, 2010

Technical Note: Using a high finesse optical resonator to provide a long light path for differential optical absorption spectroscopy: CE-DOAS.
Meinen, J.; Thieser, J.; Platt, U.; Leisner, T.
Atmos. Chem. Phys., 10, 3901-3914, 2010

Core level photoionization on free sub-10 nm nanoparticles using synchrotron radiation.
Meinen, J.; Khasminskaya, S.; Eritt, M.; Leisner, T.
Antonsson, E.; Langer, B.; Rühl, E.
Rev. Sci. Instr., in review

Patents

Durchstimmbare Radiofrequenz-Hochspannungsversorgung für Multipol-Ionenspeicher als Nanopartikelführung und –speicher
Leisner, T.; Meinen, J.; Österreicher, B.
Patent Pending at German Patent Office. Reference Number 10 2009 023 700.3.

Drehscheibenverdichter zum agglomerationsfreien Überführen von partikelgeladenen Gasvolumina, Verfahren zum Betreiben desselben und Verwendung
Meinen, J.; Saathoff, H.
Patent Pending at German Patent Office. Reference Number 10 2009 032 752.5.

CHAPTER 1

Introduction

TRAPS stands for **T**rapped **R**eactive **A**tmospheric **P**article **S**pectrometer. The TRAPS apparatus is an experimental setup for the investigation of free nanoparticles in the size regime from 3 to 15 nm in diameter by various spectroscopy techniques, which have the need for more or less high vacuum in common. It is particularly a valuable tool for the investigation of aerosol involving atmospheric processes in altitudes of the mesopause region, since those conditions can be simulated and carefully controlled in this device. As it is shown later in great detail, the key requirements of the various techniques for the characterization of nanoparticles are high number densities of free nanoparticles in the atmosphere of interest. It is essential to investigate the particles without prior deposition on substrates or filters since this would alter surface controlled effects. The methodology should comprise careful control of particle size and diameter distribution. The experimental techniques should be able to determine the stoichiometric composition, the crystal and electronic structure of the particles, optical properties and reaction kinetics at the particle's surface.

Nanoparticles in the diameter range from 3 to 30 nm have found widespread application in science and technology ranging from atmospheric science over quantum computing application to pharmaceutical formulations [Shaw and Liu, 2008]. The TRAPS apparatus provides a tool for the application of advanced

techniques of spectroscopy on free, levitated nanoparticles. For the first time, XPS spectra of Si atoms in free, mass selected sub-10 nm diameter nanoparticles were recorded. This was accomplished by using an intense nanoparticle beam in combination with a third generation synchrotron radiation source and efficient collection of the produced photoelectrons. The approach appears to be promising for a broad range of studies of fundamental and applied research including environmental studies. Contrary to former approaches, the experiment does not require the use of free electron lasers, where access is presently limited to prototype experiments.

In many natural processes, condensation proceeds via critical nuclei, which are in the sub $10\,nm$ diameter range. Such nanoparticles have become subject of considerable interest in atmospheric science, recently. More specifically, nanoparticles formed by the condensation of evaporating meteoric material are thought to be the nuclei for the formation of ice particles giving rise to the phenomena of noctilucent clouds and polar mesopause summer echoes [Gadsen, 1982; Rapp and Lübken, 2004]. The lack of laboratory experimental techniques for the investigation of free nanoparticles with atmospheric relevance was the motivation for the development of the TRAPS apparatus. A representative of atmospheric interest is the investigation of reaction kinetics on airborne particles. It will be shown for the first time that heterogeneous nucleation rates of ice on free, mass selected sub-10 nm particles and ice particle growth rates can be determined by cavity assisted extinction spectroscopy and compared to classic nucleation theory models. By this experiment, fundamental questions of mesopause ice cloud research can be investigated by laboratory experiments instead of rocket missions, which are hampered by technical difficulties and high costs.

It was the scope of this thesis to perform the fundamental design, construction and proof-of-principle testing of an appropriate device – *the TRAPS apparatus* – beginning in June 2007.

This thesis is organized as follows: The mesopause region is identified as one exemplary experimental field for the advanced spectroscopy techniques of the TRAPS apparatus in chapter 2. First the physics of noctilucent clouds and polar mesopause summer echoes are discussed. Then open scientific questions are identified which can be investigated by methods provided by the TRAPS apparatus. In chapter 3 all modules of the TRAPS apparatus are described from the technical point of view. So the reader gains an overview of the device and its properties. In section 4 the key technology, the high density nanoparticle beam inlet, is described in great detail since design and characterization of this module was the main challenge in the past three years. In this chapter great effort is put into the explanation of all theoretical details needed to be known for simulation, design and application of the novel elements. Finally, detailed characterization experiments are described in this chapter. In chapter 5, the first proof-of-principle application of the novel technology is described. It is shown for the first time that cavity enhanced optical extinction spectroscopy can be used to determine the extinction cross section of nanoparticles and can be facilitated to monitor ice nucleation on nanoparticles. In chapter 6, the second proof-of-principle experiment using the novel free nanoparticle beam inlet is given. For the first time ever, x-ray photoionization spectra from the Si $L_{3,2}$-edge are recorded from sub $100\,nm$ nanoparticles in a free particle beam setup. Chapter 7 summarizes the technical and methodical advances gained in the past three years, and gives an outlook to atmospheric relevant experiments, which are performable with the status quo of the TRAPS apparatus.

CHAPTER 2

Experimental fields of TRAPS

Nanometer-sized particles play an important role in many areas of science and technology. For instance, chemical reactions on the surface of these particles play a key role in astrochemistry, plasma reactors and industrial combustion processes, where nano-sized particles are the building blocks of soot generation. In atmospheric chemistry, heterogeneous chemistry on ice particles of polar stratospheric clouds is known to be responsible for the repartioning of chlorine reservoir species into photochemically active species capable to catalytically destroying ozone. At higher altitudes nanoparticles give rise to the phenomena of NoctiLucent Clouds (NLC) and Polar Mesospheric Summer Echoes (PMSE). Primary particles from ablating meteors interact with the enclosing plasma in the mesopause region causing structures in the free electron density observable as strong radar echoes. These particles also act as condensation nuclei for water vapor to form ice particles of visible size. To date much of the knowledge of surface chemistry on nanoparticles is derived from traditional surface science methods of bulk materials, probing the entire volume of the particle. The surface to volume ratio as well as the morphology and structure of the surface of a nanoparticle may be significantly different from agglomerated particle samples or even bulk material. In this chapter meteoric smoke particles, which cause the phenomena of NLC and PMSE, are discussed as example for the properties of nano-sized particles.

2.1 Aerosols in the Mesosphere

Noctilucent clouds were first mentioned in the science journal, Nature, in 1885 by Leslie. He described 'a sea of luminous silvery-white clouds' which he observed during twilight in the month of July [Leslie, 1885]. These early observers very quickly realized that the luminous cirrus-like clouds must be illuminated by the sun and therefore must exist at extreme altitude [Backhouse, 1886]. From several thousand photographs taken in the subsequent years O. Jesse calculated an average height of the NLC to be $(82.08 \pm 0.1)\,km$ [reference in Gadsden and Schröder, 1989]. This is in good agreement with modern measurement using lidar, satellites and rocket-borne instruments. With the advent of the Mesosphere-Stratosphere-Troposphere (MST) radar 100 years later, it was then found that also a large number of ice particles of subvisible size exist. These particles lead to strong radar echoes which are nowadays known as polar mesosphere summer echoes [Ecklung and Balsley, 1981].

In the following sections the available understanding of NLCs and PMSEs is summarized. The discussion will point to the open questions which may be solved by experimental techniques gained by the TRAPS apparatus.

2.1.1 The earth's atmosphere

Many of the planets and satellites in the solar system have a spherical envelope of gas, named atmosphere. The atmosphere of most planets consists mainly of hydrogen and helium, while the atmospheres of the three inner planets (Venus, Mars and the Earth) also contain oxygen or oxidized species (e.g. CO_2). The Earth is unique in being the only planet in our solar system that possesses an oxidizing atmosphere, produced by biological activity [Wayne, 2000].

The Earth's atmosphere is usually divided into a number of spheres according to its vertical temperature profile, each region with its individual but interrelated chemistry and physics (Figure 2.1a). The pressure p of the Earth's atmosphere decreases roughly exponentially with altitude. For an atmosphere of uniform temperature, T, it would be

Eq. 2.1 $$p = p_0 \, exp\left[-\frac{m\,g\,z}{k\,T}\right]$$

where p_0 is the pressure at the Earth's surface, m is the average molecular mass of the gases, g is the acceleration due to gravity, z is the altitude and k is Boltzmann's constant. The scale height $(k\,T/m\,g\,z)$ is the altitude over which p drops by a factor of $1/e$. It is clear from Figure 2.1a that the scale height in the real atmosphere is not constant with altitude.

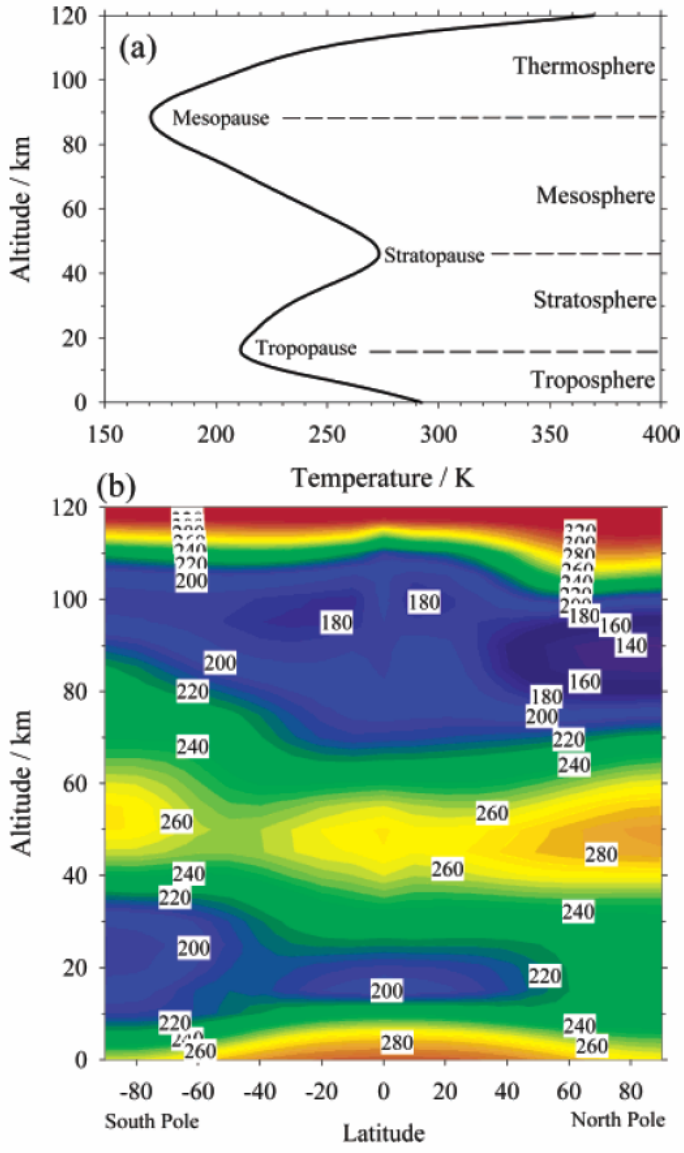

Figure 2.1. (a) Temperature profile between 0 and 120 km for July, 40°N, identifying the regions of the atmosphere. (b) Plot of temperatures (K) as a function of altitude and latitude during July. (reproduced from Plane [2003]).

A full radiative transfer model for the description of the atmosphere temperature profile has to take into account the absorption and emission of radiation to and from space, including the effect of IR active species and the effect of aerosols and clouds as well as the effect of photochemistry [Wayne, 2000]. The temperature decreases from the Earth's surface with increasing altitude through the troposphere ($10-18\,km$). A heated air parcel begins to expand and rise. While expansion is adiabatic, it cools at a rate defined as the adiabatic lapse rate, $\Gamma = -dT/dz$. Convection only occurs when the lapse rate of the atmosphere exceeds the adiabatic lapse rate of the air parcel. In the tropopause the atmospheric lapse rate becomes negative. The stratospheric lapse rate is negative since heating via the adsorption of UV radiation above $200\,nm$ by ozone becomes increasingly important with altitude. Convective mixing of air between the troposphere and the stratosphere is limited. The ozone mixing ratio peaks sharply in the stratosphere at about $25-30\,km$, and decreases with pressure above. It reaches sufficiently small levels for the photochemical heating to become inefficient and thus, above the stratopause ($\sim 50\,km$), the atmospheric lapse rate becomes positive again. The temperature falls until the point is reached where the radiative loss of heat due to IR active molecules becomes inefficient. Above the mesopause ($85-95\,km$) the mean free path length of the air molecules is so large ($\sim 1\,m$), that the translational temperature of the molecules and atoms is larger than the rotational and vibrational temperatures. The heat loss by collisional energy transfer and subsequent emission of IR active species is inefficient in this altitude. The thermosphere has a negative lapse rate since absorption of UV and X-ray radiation at wavelength below $180\,nm$, mostly by O_2, leads to rapid warming with altitude.

The region exceeding from about 75 to 110 km is often referred to as the Mesosphere/Lower Thermosphere (MLT) region. The MLT is of particular interest because it forms the boundary between the atmosphere and space. The thermal energy put into this region comes from the solar radiation and solar wind, and a nearly equivalent amount of energy from below in the form of gravity waves, tides and planetary waves [Wayne, 2000].

Figure 2.1b is a height-versus-latitude plot of temperature during mid-summer of the northern and southern hemisphere. It can be seen in the figure, that unlike in the

lower atmosphere, which is warmer in summer, the coldest part of the atmosphere is the polar summer mesopause around $85\ km$ altitude. Temperatures fall below $130\ K$ and even below $100\ K$ at extreme occasion [Rapp and Lübken, 2004]. The low temperatures are caused by limited local heating, since most solar extreme UV radiation (EUV, $1-50\ nm$) is removed in the thermosphere and ozone concentrations are too low for efficient UV heating, as described above. As a further consequence of the low pressure, CO_2 acts as efficient IR radiator. The reason for the low temperature in the summer mesopause are upwelling gravity waves, which originates from the troposphere from a variety of sources, including orographic forcing, cumulo-nimbus storms, and cyclonic fronts [Plane, 2004]. Parts of their energy pass the stratosphere and become unstable and break in the mesosphere, since the wave amplitude increases with falling pressure. These breaking gravity waves deposit energy and momentum in the MLT. The resulting drag on the zonal wind results in a southward meridional flow causing an ascending air flow in the high northern latitudes. This upwelling air is cooled by adiabatic expansion, leading to the very low temperatures in the summer polar mesosphere.

The volume mixing ratio of water vapor is in the region of some ppm [Rapp and Lübken, 2004]. Water molecules are transported to the MLT from the stratosphere where the water vapor produced by the oxidation of methane is roughly equal to the small flux of water vapor across the tropopause [Wayne, 2000]. During the summer, transport of water to the MLT is largest because of the strong upwelling air. The lifetime of water becomes rather short with increasing altitude (month to days) since Lyman-α radiation (hydrogen $n = 2 \rightarrow 1$ transition, $121.6\ nm$) is on the main water photolysis line [Gumbel and Megner, 2009]. In spite of the resulting low water mixing ratios, the atmosphere in the mesopause region can become supersaturated when temperature falls below $150\ K$ leading to the formation of ice particles which give rise to the phenomena of NLCs and PMSEs.

2.1.2 Meteoric smoke particles

Sources of meteoroids in the Earth's atmosphere are sublimating comets orbiting the sun, fragments from the asteroid belt beyond Mars, and dust particles from long decayed cometary trails [Plane, 2003]. The average daily mass input into the

atmosphere is a quite uncertain quantity. Estimates by different techniques span over the range of $20 - 240\ t\ d^{-1}$, the mean diameter range is $60 - 200\ \mu m$ and the mean entry velocity was reported to be in the range of $11 - 72\ km\ s^{-1}$ [Plane, 2003].

The penetrating meteoroids undergo rapid frictional heating caused by their high entry velocity. Particles with diameter smaller than $500\ \mu m$ can be treated as isothermally heated because the heat permeates the particle fast enough. The constituent minerals of the particles consecutively vaporize when the particle's temperature approaches $2000\ K$. The physics of this process has been treated in detail by several investigators [Love, 1991; Kalashnikova et al., 2000; Hunten et al. 1980]. From simple ablation models it can be estimated that the peak of the ablation occurs close to $90 - 100\ km$ altitude [Hunten et al., 1980]. Nucleation models assume that the relative metallic abundances in the ablated vapor are given by their meteoric abundances (by weight): Mg 12.5 %, Fe 11.5 %, Al 1.7 %, Ni 1.5 %, Ca 1.0 %, and Na 0.6 % [Plane, 2003]. The gas-phase chemistry of the metal-atom layers is widely understood and recently reviewed by Plane [2003]: For instance, the Fe^+ ion has a half-filled outer s orbital and reacts with O_3 and O_2 to form FeO^+ and FeO_2^+, respectively. The rate of neutralization of the ions is governed by a competition between O and electrons. Although $Fe(OH)_2$ is thermodynamically the most stable form of iron, it is formed slowly because of the low water mixing ratio in the upper mesosphere. FeOH is the resulting major iron reservoir below the peak of the Fe layer. It is possible that FeOH is oxidized by O_3 to form FeOOH. This oxy-hydroxide is the stable building block of the mineral goethite (α-FeO(OH)), which has been detected in stratospheric particles of meteoric origin [Rietmeijer, 2001].

Actually, the exact composition of meteoric smoke has so far not been directly determined from observations. Hematite (Fe_2O_3) and silicon oxide (SiO) are dealt as good choice for laboratory model studies [Rapp, 2009]. Plane [2003] argued that meteoric smoke particles are presumably composed of metallic compounds which polymerize together with silicon oxides. Boren and Olivero [1984] reported the direct observation of hematite-particles from mesospheric altitudes.

2.1.3 Charging of mesospheric aerosol particles

Ions and electrons are most abundant at altitudes greater than 60 km (i.e. within the mesosphere and above). The mechanisms, the ionized atmosphere is generated by, vary with altitude. In low altitudes ($60 - 85\ km$) the most important mechanism is Lyman-α photolysis of NO producing NO^+. Above $85\ km$ the main ionization mechanism is photolysis by EUV and X-ray radiation, which predominantly generates O_2^+ and N_2^+, respectively [Wayne, 2000].

Mesospheric aerosol is embedded in this plasma, so that it should become charged itself. This is proved by numerous in situ measurements of charged mesospheric aerosol using electrostatic detectors (for a recent review see Rapp et al. [2007]). Capture processes of thermal electrons balancing with photoemission are the accepted processes for the charging of particles in this altitude [Rapp, 2009]. Usually the work function of pure ice is too large to allow photoemission to compete with electron capture, thus the predominant aerosol charge should be negative. However, there is high experimental evidence for the co-existence of negatively and positively charged particles under the conditions of the polar summer mesopause [Rapp, 2007]. Ion mobility experiments yielded the insight that particles with sizes in the lower nanometer range are positively charged, whereas larger particles are charged negatively [Brattli, 2009]. Rapp [2009] presented a possible physical explanation for this co-existence. This takes into account the photodetachment of electrons from charged particles of different material (water ice, hematite, and silicon oxide). They calculate the photoionization time constants τ_p according to

Eq. 2.2 $$\tau_p = \left(\int_0^{\lambda^*} F(\lambda)\, \sigma\left(d_p, n, \lambda\right)\, Y(\lambda)\, d\lambda \right)^{-1}$$

where $F(\lambda)$ is the flux of solar photons at wavelength λ, $Y(\lambda)$ is the quantum yield, and $\sigma\left(d_p, n, \lambda\right)$ is the absorption cross section of the particle, depending on particle diameter d_p, complex refractive index $n = m + i\,k$, and wavelength. $\lambda^* = h\,c/E^*$ is the critical wavelength to which the integration is carried out, where h is Planck's constant, c is the speed of light, and E^* is the threshold energy for photodetachment/photoemission as a single photon process. The values of τ_p are

compared to time constants for electron attachment τ_e, which is calculated according to

Eq. 2.3 $$\tau_e = \frac{1}{\alpha_e N_e}$$

with

Eq. 2.4 $$\alpha_e = \frac{\pi}{4} {d_p}^2 \, v_t \left(1 + \sqrt{\frac{e^2}{8 \, \varepsilon_0 \, k \, T \, d_p}}\right)$$

α_e is the electron capture rate, where v_t is the mean thermal velocity of the electrons, e is the electron charge, ε_0 is the permittivity of space, k is Boltzmann's constant, T is the temperature, which is taken equal for all charged and neutral constituents, and N_e is the free electron density. Note that Eq. 2.4 becomes invalid for small particle diameter ($d_p < 4\,nm$) [Megner and Gumbel, 2009] and Eq. 2.1 assumes that the complex refractive index of the bulk is the same as for nanoparticles.

Photodetachment and photoionization is a highly material-specific problem. It can be seen from complex refractive index data for the different materials that water ice basically does not absorb radiation at wavelength of the solar spectrum in this altitude, and iron oxide and silicon oxide species show strong absorption from the UV throughout the visible wavelength range. Due to the large work function of water ice (8.7 eV) the photodetachement is only governed by Lyman-α radiation [Rapp, 2009]. Thus photodetachment time constants of the metal oxides are about 6 orders of magnitude smaller than those of water ice. For Fe_2O_3, photodetachment is more than 4 orders of magnitude faster than electron attachment to the neutral particle. Photoemission is found to be faster for all diameters larger than $3\,nm$ as electron attachment to a singly positively charged particle (electron density $\sim 1000\,cm^{-3}$). Rapp [2009] arguments, that there is no means by which the particle could become negative under solar radiation. For water ice it is just the opposite, since photodetachment and ionization are so slow that even for small electron densities, particles will become negatively charged.

2.1.4 Mesospheric ice microphysics

A recent review of microphysics of mesospheric ice clouds can be found in Rapp and Thomas [2006]. In this section a brief discussion of heterogeneous ice nucleation on meteoric smoke particles leading to PMSEs and NLCs is discussed.

Homogeneous nucleation of water ice particles is not possible under mesospheric conditions since this process exhibits a Gibbs free energy barrier that cannot be overcome under typical conditions [Witt, 1969]. Heterogeneous nucleation on nuclei with a diameter larger than $4\,nm$ is commonly accepted as a predominant process. Rapp and Thomas [2006] reexamined the possible pre-existing nuclei: Large proton hydrate ion clusters, soot (elemental carbon) particles, sulfuric acid aerosol particles, sodium bicarbonate, sodium hydroxide, and meteoric smoke particles. No hydrate ion clusters of sufficient size to act as condensation nuclei have been found so far and there is no reliable thermodynamical explanation of ice nucleation via amorphous hydrate ion clusters [Zasetsky et al., 2008]. Ionic nucleation is only feasible under certain extreme atmospheric conditions, which is believed to play a minor role in the nucleation of mesospheric ice particles [Gumbel et al., 2003]. There is no experimental evidence for the existence of soot particles, sulfuric acid aerosol particles, sodium bicarbonate, and sodium hydroxide in the mesopause region. Hence, meteoric smoke particles are considered as the most likely candidate for nuclei of mesospheric ice particles. Their existence was confirmed by in situ measurements of their charged fraction with diameters larger than $4\,nm$ [Schulte and Arnold, 1992; Gelinas et al., 1998; Lynch et al., 2005; Rapp et al., 2005].

Nucleation of water ice particles on meteoric smoke nuclei is illustrated in Figure 2.2. The most important processes can be summarized as follows [Rapp and Thomas, 2006]: Ice nucleation takes place at the altitudes with largest saturation ratio $S = p_{H_2O}/p_{Sat}$ (where p_{H_2O} is the water vapor partial pressure and p_{Sat} is the equilibrium vapor pressure of water over ice). These are the altitudes where the temperature is lower than the water vapor frost point temperature. Small meteoric smoke particles settle down from higher altitudes or nucleate in this region. With a maximum rate at the temperature minimum, they act as condensation nuclei for the water vapor to form ice particles [Gadsen and Schröder, 1989]. But the saturation of water vapor in the

altitude of the temperature minimum ($86-90\,km$) is close to $S = 100$ [Lübken, 1999], so homogeneous nucleation is negligible. Once the ice particles have formed, they grow by the direct deposition of water on their surface. They settle due to gravity and consume the available water vapor on their way through the atmosphere until they leave the altitudes where the temperature is lower than the frost point temperature. Mean winds (vertical and horizontal), and small scale motions (i.e. waves and turbulence) extend the residence time in the ice existing region.

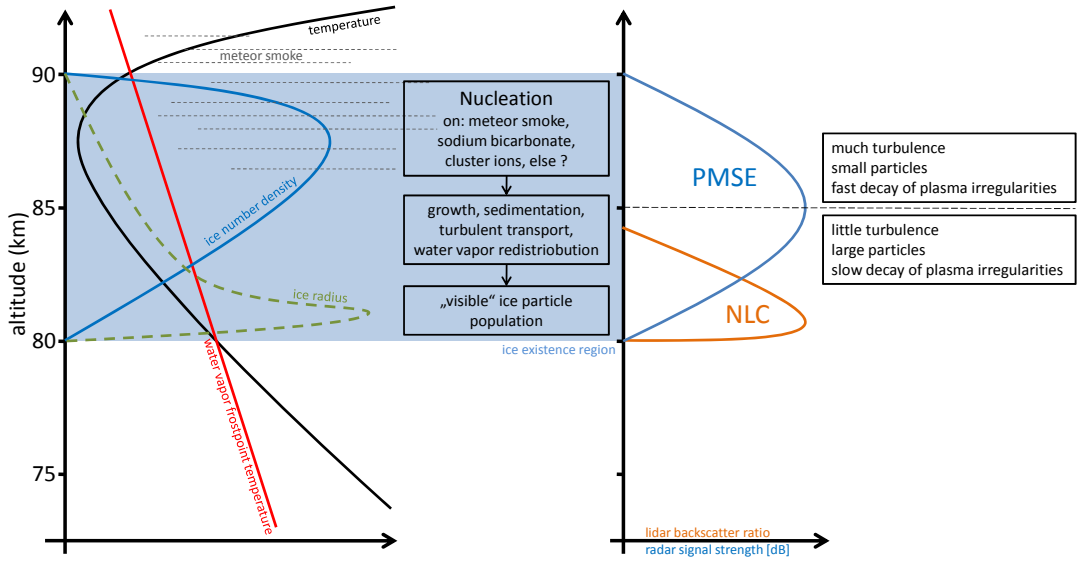

Figure 2.2. Schematic summation of the current understanding of mesospheric ice clouds and the most important contributions and processes during its evolution (adapted from Rapp and Lübken [2004]). The right part of Figure 2 indicates that only the largest ice particles at the bottom of the ice particle layer become visible as NLC, whereas the whole layer modifies the ambient plasma of the D-region and hence gives rise to intense radar echoes called PMSE.

Once the particles have reached diameters larger than $60\,nm$, they scatter light sufficiently so that they can be observed by ground-based or space-born instruments as NLC. This happens typically in the lower ice existing region ($80-84\,km$). Particles become charged by Lyman-α radiation and interact with the ambient plasma of the D-region (ionosphere at $70-90\,km$ altitude; electron density maximum caused by Lyman-α photoionization of NO; not existing at night). In addition, the $80-90\,km$ altitude range is the region in the atmosphere where gravity waves propagating from below grow unstable and produce turbulences. The charged ice particles are transported by the turbulent velocity field leading to small scale

structures in the spatial distribution of the charged particles. Since there must be charge neutrality, this leads to small scale structures in the spatial distribution of the free electron number density [Cho and Röttger, 1997]. The radio refractive index is determined by the electron number density at these altitudes. The transport of charged ice particles by the turbulent velocity field causes irregularities in the electron number density and correspondingly in the radio refractive index. Those structures are observable by suitable radars as strong backscatter. These effects are called PMSE (see Rapp and Lübken [2004] for a recent review). The radius of the particles determine the lifetime of the irregularities, because of their size dependent diffusion. Typical values for the lifetime are reported from just a few minutes for small radii at altitudes above 85 km, and several minutes to hours for the larger radii in lower altitudes [Rapp and Lübken, 2004].

PMSE exists over the whole altitude of the ice existing region. Ice particles which settle out of the cold mesopause region and start to evaporate, become invisible for radars and lidars. One of the most compelling observations supporting this physical picture, is frequent coincidence of lower edges of PMSE and NLC [Lübken et al., 2004]. An example of such a measurement is shown in Figure 2.3.

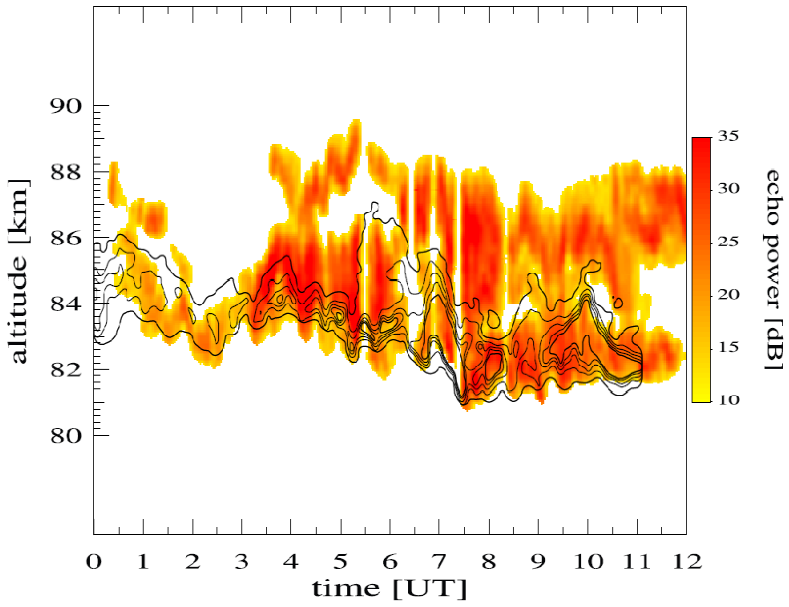

Figure 2.3. Common volume measurement of PMSE and NLC on 5/6 August 2001 at Spitzbergen (reproduced from Lübken et al. [2004]). The radar echo power above noise is shown in dB (color contour). The backscatter ratios measured by lidar are shown in the (unlabeled) black contour lines.

Though there is a general consensus regarding this picture of relevant microphysical processes described above, several details of these microphysics are unknown and put a considerable uncertainty to the capability of quantitatively describing the physics of mesospheric ice clouds [Rapp and Thomas, 2006].

Number densities of nanometer-sized particles and ice particles are found by in situ measurements in the order of thousands per cubic centimeter in the mesosphere [Brattli et al., 2009]. Recent model studies, which include the residual circulation from the summer to the winter pole, however, suggest much lower densities of neutral meteoric smoke particles in the summer mesopause [Megner, 2008; Megner and Gumbel, 2009; Rapp, 2009]: As few as 10 particles per cubic centimeter with diameter larger than 4 nm are left as active ice nuclei in the summer mesopause. The high number of ice particles is contrasting to the low number of potential ice nuclei and implies that nucleation on neutral meteoric smoke particles cannot account for the total observed ice population. Megner et al. [2008] suggested that negatively charged meteoric smoke particles may solve this dilemma. For charged particles the potential barrier of the Gibbs free energy disappears for temperature below 130 K [Gumbel and Megner, 2009], so that the critical radius no longer exist and even particles with diameters smaller than 4 nm may act as condensation nuclei.

Usually, mesospheric ice nucleation is treated in the framework of the classical liquid drop theory [Rapp and Thomas, 2006]. The underlying assumptions are that molecular clusters and small nanoparticles can be characterized reasonably well by using bulk properties of the condensed matter, possibly with some modifications to account for microphysical effects, and that the surface of the nucleus is perfectly wettable. On this basis the Gibbs free energy depending on temperature and particle size can be determined as depicted in Figure 2.4. The Gibbs free energy has a term describing the energetic preference for condensation when the saturation ratio is $S > 1$, and a second term describing the Kelvin effect, i.e. the energy needed to increase the curved particle surface. Figure 2.4 illustrates the energy barrier for ice nucleation of the Gibbs free energy of surface formation. At this maximum of the Gibbs free energy, the amount of surface energy needed to add a water molecule to the droplet just corresponds to the bulk energy released upon this addition.

Energetics of ice nucleation at a charged particle is different. There is an additional attractive interaction between the central charge and the dipole of the water molecule. This is described by the addition of a Coulomb term to the Gibbs free energy, resulting in the Thomson equation [Castlemann et al., 1978]. The resulting size dependence of the Gibbs free energy is shown as dashed lines in Figure 2.4. For moderately low temperatures a stable energetic minimum exists and the energy barrier is significantly lower than for neutral particles. At lower temperatures, the energy barrier disappears completely.

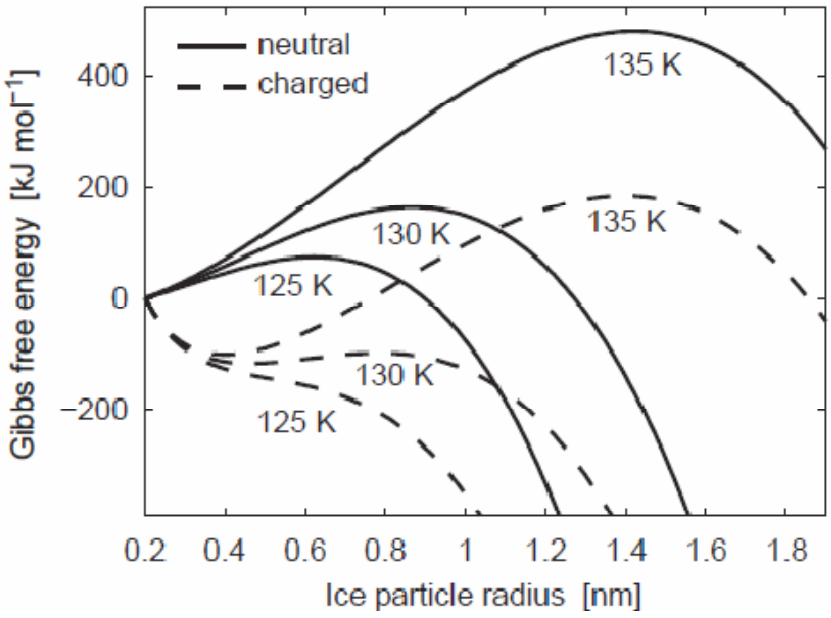

Figure 2.4. The Gibbs free energy of ice particle formation at various temperatures (reproduced from Gumbel and Megner [2009]). Solid lines denote growth on a neutral nucleus, dashed lines denote growth on a singly charged nucleus. Atmospheric conditions are an air density of $2\ 10^{14}\ cm^{-3}$ and a water vapor concentration of $2\ ppm$.

The applicability of the classical drop theory is highly questionable since mass density, surface energy, electrical characteristics, crystalline structure, surface stoichiometric composition, intermolecular interactions, and wettability may be significantly different from the materials' bulk properties. A rigorous microphysical description is usually not available as quantum mechanical properties and multibody wave functions are not sufficiently well known [Gumbel and Megner, 2009]. A

deeper discussion of these ideas has recently been given by Zasetsky et al. [2009]. They also discussed a formation scenario by homogeneous nucleation for mesospheric ice particles starting with small amorphous water clusters that consist nearly exclusively of surface molecules. The amorphous-to-crystal transition to cubic ice is the next step. Since cubic ice is metastable, there must be a subsequent transition to hexagonal ice that is the most stable ice polymorph at mesospheric conditions.

2.2 Scientific questions to address with TRAPS

Aerosol particles play an important role in heterogeneous chemistry, cloud formation, and ice nucleation in the atmosphere. These processes are the largest uncertainly in the description of the Earth climate system [IPCC, 2007]. Heterogeneous chemistry of nano-sized particles is predominantly determined by their surface properties, i.e. the chemical composition and specification of the constituents at the aerosol surface. For investigation of the surface properties, the particles are ideally investigated in the presence of the gas atmosphere of interest and even more important, without prior collection of the aerosols on a substrate or filter which may alter their physical and chemical properties.

For the case of meteoric smoke particles and ice particles forming NLCs and PMSEs, many open questions could be answered by a method enabling the investigation of the physical and chemical properties of free nanoparticles in atmospheric conditions of the mesopause region. It was noted by many researchers that the microphysics of the mesospheric ice particles is the most important remaining open question about the actual origin of the ice particles to be answered. Rapp and Lübken [2004] stated, that *'the nature of these particles and their influence to both the local chemistry (heterogeneous reactions) but also the radiative transfer and hence the energy budget of the middle atmosphere have to be investigated'*. Gumble and Megner [2009] made a statement on the application of the classic liquid drop theory to nanoparticles *'more laboratory measurements representative for mesospheric conditions will be needed to quantify the validity and limitations of the classical approach'*. Even fundamental physical effects like charging of particles by photodetachment is expected to be size dependent within the size range of particle found in the mesosphere. Rapp [2009] noted in his basic theory on photodetachment and electron attachment that *'quantitative information from laboratory measurements of the photoemission properties of meteoric smoke particles is not available'* and thus *'laboratory measurements of processes like electron capture and photoemission in the transition size region from molecular clusters to nanoparticles are badly needed'*.

It is the scope of the TRAPS apparatus to investigate and answer some of the questions in chemistry and physics of atmospherically relevant nanoparticles, namely:

1. What are the stoichiometry and the crystalline structure of iron-oxide and silicon-oxide nanoparticles? Is it different at the surface?

2. Are surface energy and electrical characteristics of the nanoparticle's surface equal to the bulk material? Are they dependent on particle size and material?

3. Is the complex refractive index of the material dependent on particle size?

4. What is the fundamental initial process of water deposition on a particle's surface? Are there active sites at the particle surface? What is the crystalline structure of ice nucleated on nanoparticles? Is it amorphous, cubic or hexagonal? Is the ice nucleation rate dependent on particle type, size and charge?

5. Is the classical nucleation theory applicable to saturation ratios, nuclei dimensions, and nuclei-types under mesopause conditions? What effect does a charge on nuclei have?

CHAPTER 3

Modules of the TRAPS apparatus

The investigation of the physical and chemical properties of nanoparticles with atmospheric relevance requires some experimental prerequisites. Particles must be synthesized in a well defined manner. Particle size should be controllable and the particle diameter distribution has to be small. The stoichiometric composition of the particles should be regulated by the synthesis. The nanoparticles should be transferred to the experiment efficiently without contacting a surface or agglomeration. The experimental characterization of the particles should be performable in the atmosphere of interest but without the need of accumulating the nanoparticles on substrates or filters. Therefore the particles have to be investigated by means of a free particle beam or a cloud of electrically charged particles in an electrodynamic ion-trap. Investigation methods separately probing the particle's surface and the core are advantageous. Time resolved size determination of the particles can give insights to ice nucleation processes at the nanoparticle surface.

The TRAPS apparatus is a unique experimental platform for the investigation of nanoparticles with atmospheric relevance. For the best of my knowledge, there is no comparable apparatus available to the world-wide scientific community obtaining comparable performance in the investigation of particles in the size region from molecular clusters to nanoparticles.

In the following section the modules of the TRAPS apparatus are described.

3.1 Overview of the TRAPS apparatus

The TRAPS apparatus is engineered as a modular and mobile laboratory for experiments with nanoparticles in vacuum. A wide range of airborne nanoparticles can be produced in-situ by different methods. The particles are sampled into the high vacuum chamber by a highly efficient inlet system in order to supply a high density nanoparticle beam for experiments and characterization methods requiring low background pressure. Levitated, charged nanoparticles can be accumulated and stored in ion-traps for a prolonged time prior to extraction from the trap in a high density particle pulse. Detectors for different purposes can be mounted at the apparatus.

The setup of the TRAPS apparatus as used in the KIT laboratory in Karlsruhe is depicted in Figure 3.1. Airborne nanoparticles are produced at ambient pressure from spraying solvent containing salt or dispersed particles by an atomizer or an electrospray ionization source (particle sources are not shown in Figure 3.1). A microwave plasma particle source operating at $20 - 150\,mbar$ can be used to provide airborne nanoparticles with high number density. Basic principles of the nanoparticle sources used, the characterization experiments and the consideration of choice are discussed in section 3.2 and 3.3. The particle inlet system (I in Figure 3.1) consists of an aerodynamic lens (a), a differential pumping stage (b) and an electrodynamic ion-guide (c). A short introduction to aerodynamic lenses is given in section 3.4. Section 3.5 discusses fundamentals of electrodynamic ion-guides and traps. Since the high density nanoparticle inlet system is the experimental key for investigations of nanoparticles in the TRAPS apparatus, development and characterization of this module is described in great detail in chapter 4. The experiment section is arranged perpendicular to the inlet system (II in Figure 3.1). This allows a photon beam to interact with the particle beam or the nanoparticle cloud stored in the linear electrodynamic cage (f). This section can be cooled to low temperatures by a cryostat (g). All ion-guiding and trapping elements are described in section 3.5. In the KIT laboratory setup of the TRAPS apparatus, optical extinction spectroscopy of the nanoparticle ions in the ion-cage (f) can be measured. The extinction cell is described in section 3.6 and detailed descriptions of the experimental method and proof of principle measurements are given in chapter 5. A detection unit

(III in Figure 3.1) can be mounted perpendicular to the experiment section (II). For the use of a single particle detector (i) a differential pumping stage is needed (h). Particle detectors are described in section 3.7.

3.1.1 Adaptability

Ultra short laser pulses, synchrotron radiation and photons from free electron lasers are suitable for the spectroscopic investigation of nanoparticles. Mass spectrometers and TEM analysis of deposited particles determine mass, size and structure of the particles. All techniques have the demand of vacuum; therefore the vacuum chamber of the TRAPS apparatus is completely realized with standard DN150-CF vacuum flanges to fit to supplementary instrumentation. The particle beam propagates along the rotational axes of the vacuum parts. All three sections of the TRAPS apparatus can be mounted to standard vacuum devices in any orientation. Supply of power, cooling water and process gases can be provided in every standard vacuum laboratory.

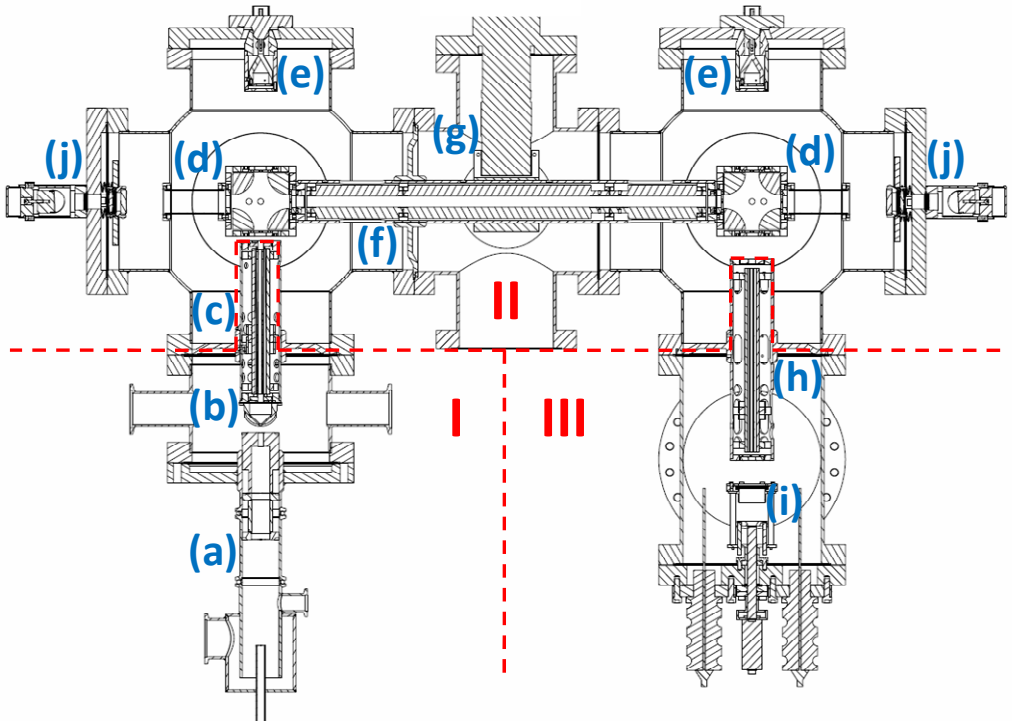

Figure 3.1. Schematic diagram of the TRAPS apparatus. (a) Aerodynamic Lens, (b) Differential pumping stage with skimmer, (c) Inlet octopole ion-guide, (d) Quadrupole deflector, (e) Faraday cup electrometer, (f) Quadrupole ion-trap, (g) Cryostat, (h) Octopole ion-guide, (i) CEM single particle detector, (j) optical cavity mirror mounts.

3.2 Ambient pressure nanoparticle sources

Particles were generated from solution by two ambient pressure sources: An atomizer with attached silica dryer [Liu and Lee, 1975] was used to create $20 - 50\ nm$ particles of NaCl and $NaHCO_3$ from solution. A commercial electrospray unit (TSI Model 3480) is used to create $10 - 30\ nm$ particles of $Mg(NO_3)_2$ and NaCl from solution. Both methods provide a particle density of about $10^6\ cm^{-3}$ at ambient pressure [Aerosol Electrospray, TSI User's Manuel Model 3480, 2008]. The fraction of singly charged particles is usually below $10\ \%$ [Fuchs, 1963]. Particles generated by these two methods were transferred into the first ion-trap of the TRAPS apparatus and $\sim 10^6$ ions were accumulated in this trap routinely. For many experiments the particle number density achievable with these two sources is not sufficient. Though it is principally possible to accumulate tore $\sim 10^8$ ions from these sources in an ion-trap with very low loss rate, the load time will become inconvenient.

The particle sources have to be operated with helium as carrier gas in order to provide good functionality of the aerodynamic lens inlet (see chapter 4). Since no electrospray source operated with helium as carrier gas was published in the literature before, the method is briefly described here.

3.2.1 Electrospray particle source with helium as carrier gas

A commercial electrospray unit (ES) was used to transfer ions or insoluble solid particles from solution to gas phase. This aerosol generator has a well controlled particle size distribution and stable particle output concentration. It can – in principle - produce particles in the size range 2 to $100\ nm$ and concentrations up to $10^7\ cm^{-3}$ [Chen et al., 1998]. The principle of work can be found in numerous publications [Cole, 1997; Chen et al., 1995]. However, particle concentrations of about $10^6\ cm^{-3}$ were achieved when helium is used as carrier gas.

The need for using helium as carrier gas of the particles introduces problems with the operation of the ES particle source. Helium is ionized at lower electric fields than nitrogen. This facilitates corona discharge between the capillary and the anode of the electrospray unit. Consequently, it is not possible to apply sufficient voltage at the electrospray capillary in order to start spraying an aqueous solution. CO_2 can be used

for quenching the corona discharge. Since CO_2 has high density, the mixture of helium and CO_2 has changed gas properties related to pure helium. The amount of CO_2 needed for quenching of the corona discharge is so high ($\sim 50\,\%$), that the aerodynamic lens of the TRAPS apparatus does not focus the particle beam into the skimmer efficiently any more. This problem can be reduced by decreasing the surface tension and increasing the electrical conductivity of the solution sprayed so that a lower electric field is required for the spray. Methanol or acetonitrile was mixed to the water since these liquids have higher electrical conductivity and lower surface tension as pure water.

For measurement of $Mg(NO_3)_2$ nanoparticle size distributions, solutions of typical concentrations of $10^3\ mol\ l^{-1}$ are prepared in $80\,\%$ acetonitrile and $20\,\%$ water. The conductivity of the mixture was $60\ \mu S\ m^{-1}$ which is insufficient for ES. By adding an amount of about $10^3\ mol\ l^{-1}$ NaCl to the solution, the connectivity is increased to $1894\ \mu S\ m^{-1}$ at pH 6. This solution was sprayed using nitrogen or helium as carrier gas. In both cases a small amount of CO_2 was used to inhibit corona discharge between the electrospray capillary and anode. For nitrogen $12\,\%$ and for helium $12.5\,\%$ CO_2 was added which results in a mean molecular weight of $29.5\ amu$ and $8.3\ amu$, respectively. The latter mixture is feasible to be used with the ADL.

Figure 3.2 shows the size distributions of $Mg(NO_3)_2$ particles sprayed with nitrogen and helium as carrier gas measured by a SMPS system (differential mobility analyzer TSI Model 3080 and condensation particle counter TSI 3025). The size distribution is similar in both cases and peaks at about $14\ nm$. Whereas the size distribution of the particles produced with helium shows a more pronounced side peak at about $23\ nm$. The particle number concentration decreases by a factor of four with use of helium in comparison to nitrogen. But the reduction of the solution's surface potential and the enhancement of the conductivity enables the spaying of solutions in helium dominated atmosphere. This procedure allows the use the ES as particle source for sub $30\ nm$ diameter nanoparticles which are subsequently focused by an aerodynamic lens.

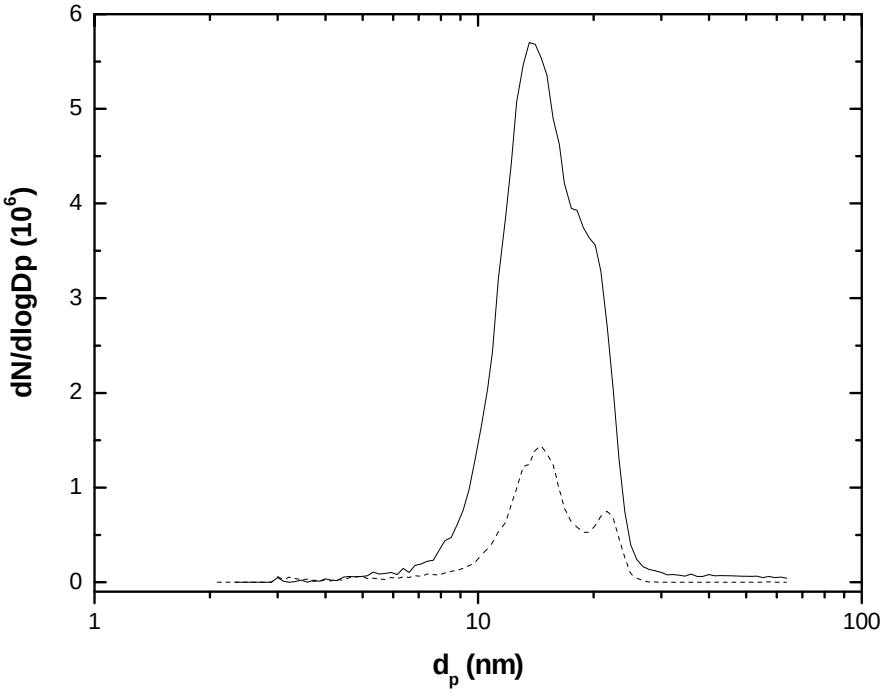

Figure 3.2. SMPS size determination of $Mg(NO_3)_2$ particles produced by electrospray ionization from solution with nitrogen (drawn line) or helium (dotted line) as a carrier gas. The peak of the size distribution are $14.0\,nm$ and $14.5\,nm$ for nitrogen and helium, respectively.

3.3 Microwave plasma particle source (MPPS)

Plasma processes are very efficient in terms of nanoparticle production in the gas phase. They have comparatively low energy consumption in combination with superior particle number density, and in case of proper selection of operating conditions a narrow particle size distribution. Narrow size distributions are obtained, because particle formation in plasma synthesis is, in contrast to conventional gas phase or wet chemistry synthesis, not necessarily a diffusion driven process; rather, it may be controlled by particle charging. Gas phase nucleation of particles has the additional advantage of avoiding particle coatings from buffer or stabilizer contained in the sprayed solution.

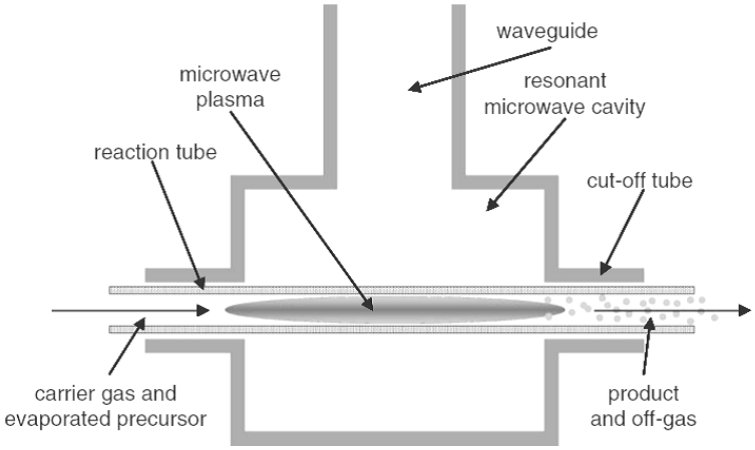

Figure 3.3. Microwave plasma system working at reduced pressure. (reproduced from Vollath 2008)

There are a number of reviews on plasma synthesis [Szekely, 1984; Boulos, 1984; Heberlein, 1989; Taylor and Vidal, 1999; Manolache and Denes, 2000; Kaneko et al., 2002; Vissokov et al., 2003]. Thus, fundamental theory of plasmas and particle production processes in plasmas is not repeated here. The microwave plasma system chosen for the TRAPS apparatus is a low pressure system with a resonant microwave cavity [Vollath, 2007; Vollath, 2008]. These systems are simple in design and universal in application. Figure 3.3 shows the plasma zone which is located in a quartz-glass tube inside the resonant microwave cavity. The waveguide feeds the system with microwave energy. During the synthesis evaporated precursor, transported by carrier and reaction gases, is flowing through the reaction tube and particle formation occurs inside the plasma.

3.3.1 The MPPS device

The microwave plasma reactor built for the TRAPS apparatus produces $3-15\ nm$ diameter SiO_2 and Fe_2O_3 particles at high concentrations ($10^9-10^{12}\ cm^{-3}$ in a $10-150\ mbar$ helium atmosphere). The design follows [Szabo et al., 1997; Szabo and Vollath, 1999; Baumann et al., 2005, Mätzing et al., 2003]. The source of the microwave radiation is a system consisting of a microwave power supply (MT1250D-112HC), a magnetron head (MH1250S-212BA), an isolator and tuner (Muegge Electronic GmbH, Germany) and an in-house-designed microwave resonator which focuses the microwave energy on its rotational axis. The maximum HF-output of the power supply is $1250\ W$ at a frequency of $2.45\ GHz$.

Figure 3.4 shows the setup used for the production of SiO_2 nanoparticles. The microwave reactor consists of a quartz tube $26\ mm$ in diameter. The flow rates of precursors and carrier gas, which are fed into this tube, are controlled by mass flow controllers. In order to produce SiO_2 nanoparticles a gas flow ($4500\ sccm$) of 0.02 % SiH_4 and 4 % O_2 in helium is feed into the microwave plasma zone. The reactor tube is fixed in the center of the microwave resonator. The microwave plasma is ignited in a pure helium buffer gas flow. Particles are produced as soon as the precursor is added. The precursors are mixed directly upstream the plasma zone.

For the production of Fe_2O_3 nanoparticles from liquid $Fe(CO)_5$ an appropriate evaporation and mixing is needed. Figure 3.5 shows the scheme of the mixing unit which is located upstream from the plasma zone. $Fe(CO)_5$ vapor is highly oxidizing and condenses easily at surfaces. Thus it cannot be leveled by a mass flow controller. The evaporation and mixing unit shown in Figure 3.5 has a cooled reservoir of liquid $Fe(CO)_5$ (30 to $-30\ °C$) at moderate pressure (~$200\ mbar$). Pure helium is dosed with $100\ sccm$ into inlet (a). Liquid $Fe(CO)_5$ is poured with a needle penetrating a membrane sealing inlet (b) into the subjacent cooled basin. $Fe(CO)_5$ vaporizes according to its temperature dependent vapor pressure. A capillary of $240\ mm$ length and $300\ \mu m$ diameter limits the flow of the gas mixture into the plasma zone. Directly upstream from the plasma zone the $Fe(CO)_5$-helium gas mixture is diluted by a flow of $500\ sccm$ O_2 in $3900\ sccm$ helium which enters the reactor by inlet (c).

During particle production, mass flow rates, pressure and microwave frequency and energy are monitored and controlled fully automated in order to provide stable conditions for a constant diameter distribution of the produced nanoparticles.

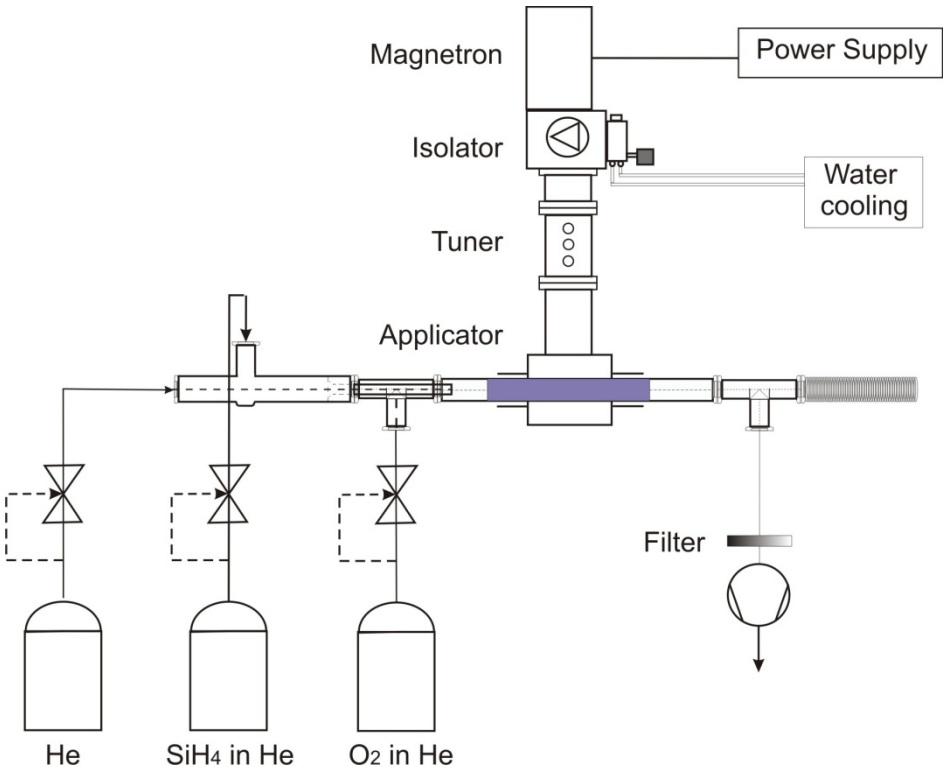

Figure 3.4. Scheme of the microwave plasma particle source (MPPS) for the production of SiO_2 nanoparticles.

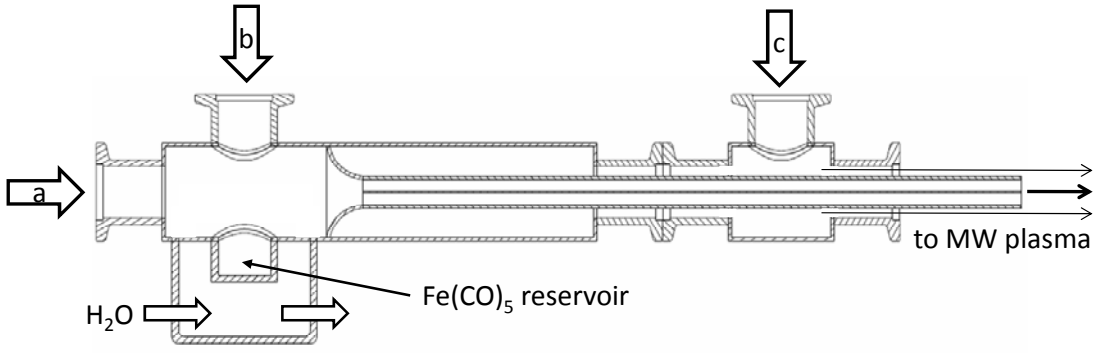

Figure 3.5. Evaporation and mixing unit for $Fe(CO)_5$. He inlet (a); membrane sealing inlet for liquid $Fe(CO)_5$ (b); He/O_2 inlet (c).

3.3.2 Characterization of the MPPS

Nanoparticles produced in the plasma reactor have been characterized by Szabo et al. [1997] and Baumann et al. [2005] by using transmission electron microscopy, particle mass spectrometry and quartz crystal microbalance measurements. On line characterization of the nanoparticles is achieved by an electrostatic deflection particle mass spectrometer (PMS, [Paur et al., 2005], also see section 3.8). Figure 3.6 shows a PMS measurement of the size distribution of SiO_2 particles from the MPPS. Singly and doubly charged particles are produced with both polarities in similar fractions. The mean diameter of the particles is 5.7 nm and the FWHM is 1.1 nm.

The most sensitive parameter for the particle formation inside the plasma is the gas pressure since it controls the mobility of the ions in the plasma. The Particle diameter can be sensitively controlled by varying the pressure as shown in Figure 3.7. At fixed gas flows, evaporation temperature, and microwave energy, the pressure inside the reactor is varied from 20 to 160 $mbar$. This is the pressure region in which the plasma burns stable. SiO_2 and Fe_2O_3 particles with diameter from 3 to 15 nm were produced with this MPPS.

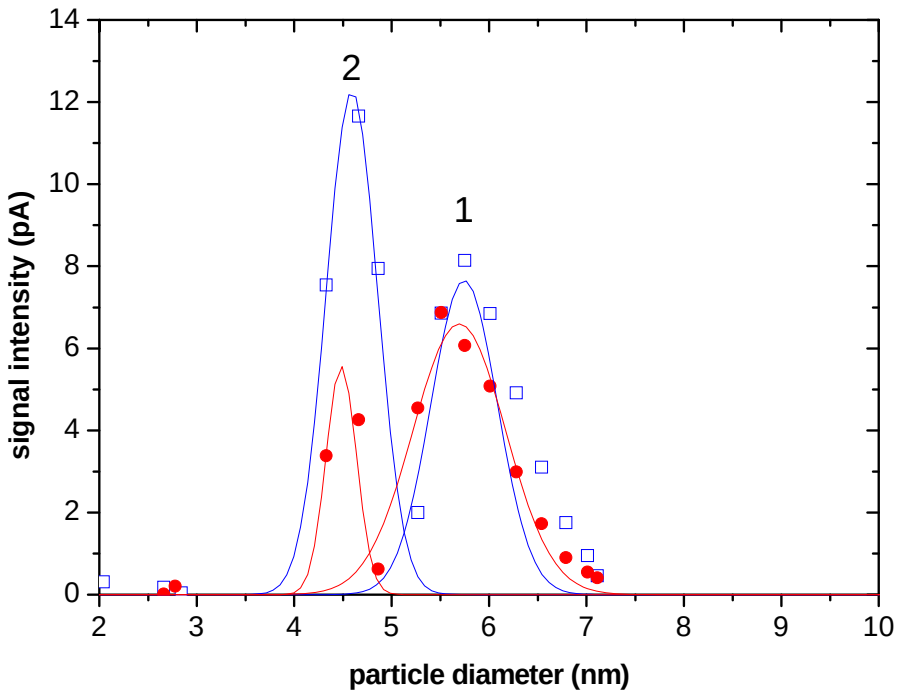

Figure 3.6. Size distribution of both polarities of SiO_2 nanoparticles from the MPPS measured by the PMS. Dots: Positively charged particles. Squares: Negatively charged particles.

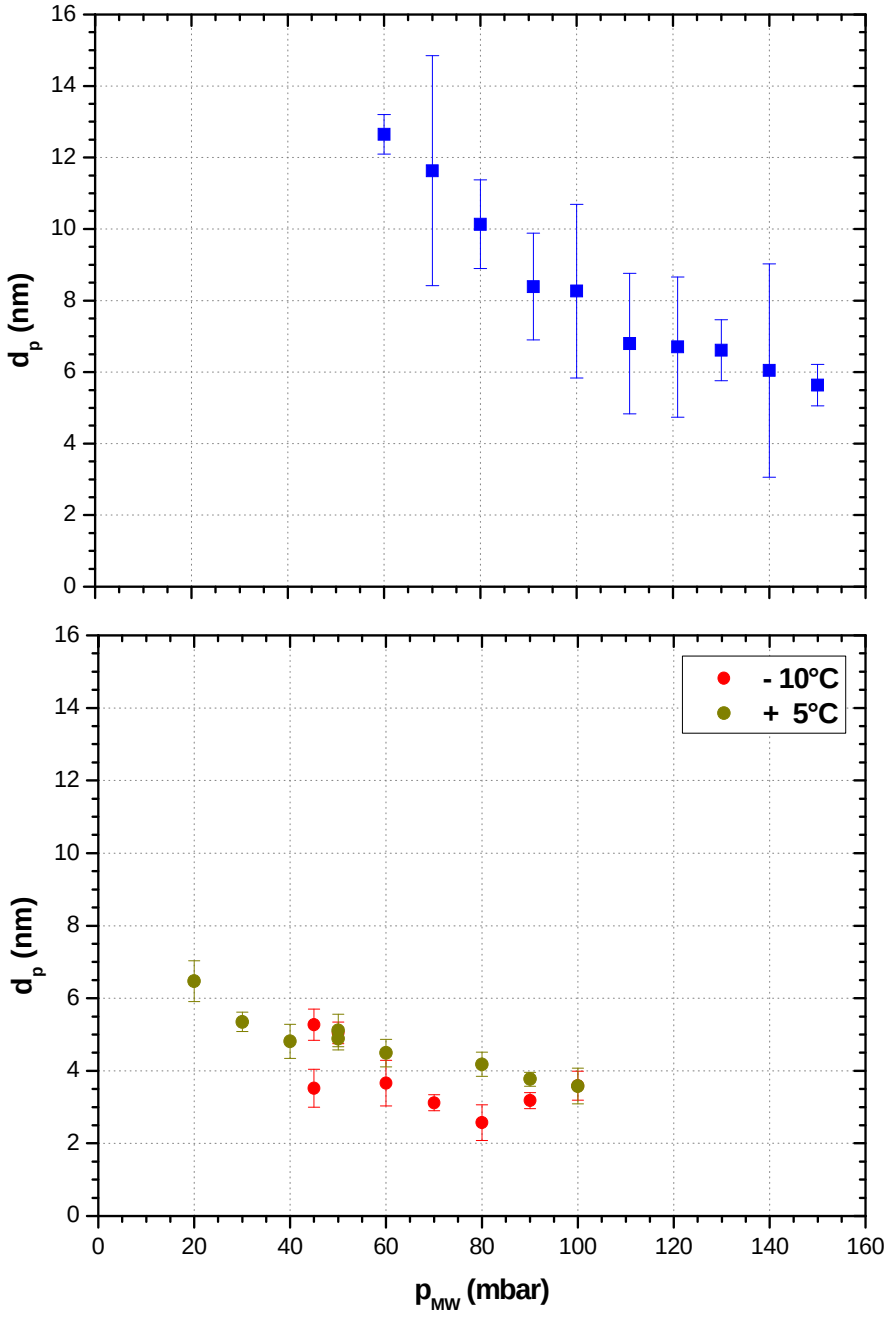

Figure 3.7. Tuneability of particle diameter by reactor pressure. Upper panel: SiO_2, lower panel: Fe_2O_3 (two evaporation temperatures). Particle diameter is measured by the TRAPS-TOF (see below).

3.4 Aerodynamic lens

The Aerodynamic Lens (ADL, [Liu et al., 1955a]) with subsequent differential pumping is used to transfer nanoparticles from ambient or a high pressure regime into the vacuum device with concurrent separation from the carrier gas. An ADL consists of a flow limiting orifice and a subsequent tube with a set of orifices. The gas flow through the tube traverses a series of contraction and expansions at the orifices. Very small particles can follow the streamlines of the gas propagating through an orifice. Large particles will not be able to follow the streamlines because of their inertia. A small mass range will not follow the streamlines but slip to the center rotational axis of the tube (and do not cross it) which leads to a focusing of particle at the center axis. Since the center streamline does not bend at downstream orifices, particle following this streamline stay at the center axis. Each orifice can focus one particle size only. For focusing of a wide range of particle masses a set of orifices is used. A detailed description can be found in chapter 4.2.

The ADL used in the TRAPS apparatus is optimized to focus particles in the size range $3 - 15\ nm$. Since aerodynamics of particles in this size range is dominated by Brownian diffusion, no perfect lens design is available. The lens optimized with computational fluid dynamic simulations is tunable and thus becomes suitable for particle with different density. Basic theory of ADLs, design considerations, computer simulations and validation experiments are described in great detail in chapter 4.

In the TRAPS apparatus the ADL focuses the particles as a tight beam on a skimmer at a differential wall. In comparison to a classic molecular beam inlet, only a small fraction of the particles does not pass the skimmer and is lost in the pumps (see Figure 3.8). It can be shown experimentally that the particle loss of the TRAPS inlet system is lowered by a factor of 100 (see section 4.7.1) by using the ADL instead of a classic molecular beam inlet.

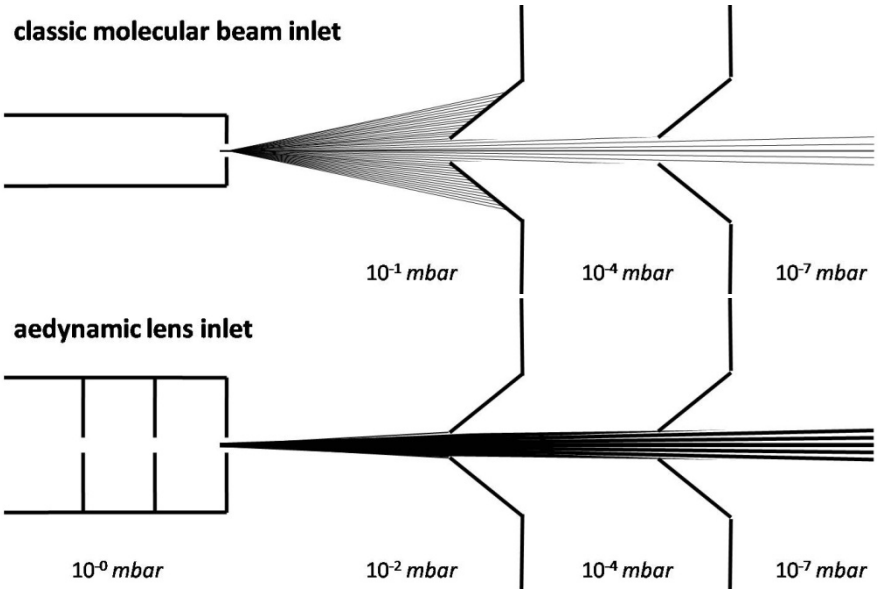

Figure 3.8. Particle inlets for vacuum systems.

3.5 Ion-guides and -traps

Linear ion-guides are standard radio frequency mass spectrometric devices. They are routinely used to guide, moderate, and cool ion beams [Gerlich, 2003]. Details and typical applications are given in a recent review [Douglas et al., 2005].

In multipole ion-guides and ion-traps, charged particles are confined in inhomogeneous, oscillating electric fields which alter fast enough in time to act as a quasi static potential on the particles. Applying an inert background gas, frictional forces are added to the electrodynamic forces. These forces allow deceleration and to continuously storage of the ions within the multipole potential. In the case of a light background gas, such as helium, moderating the much heavier nanoparticles, the action of the background gas can be regarded purely as friction applying the Cunningham correction to Stokes law. A brief discussion of multipole theory is given in section 4.8.

In the TRAPS apparatus, linear multipoles with a RF frequency of $20 - 150\ kHz$ are used to radially confine the particle movement and axially guide the particles within the device. Applying static electric barriers at the inlet and the outlet of the ion-guide, charged particles can be accumulated inside such an ion-guide. A model of an octopole ion-guide used at the inlet of the TRAPS apparatus is shown in Figure 3.9.

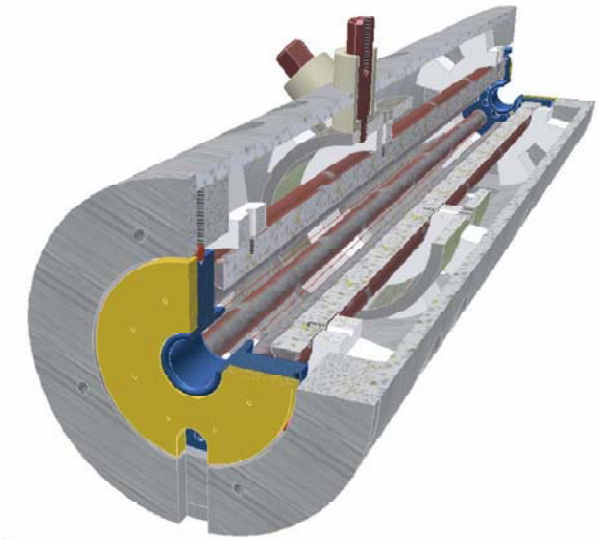

Figure 3.9. Three-dimensional model of an octopole ion-guide used as inlet ion-guide of the TRAPS apparatus.

3.5.1 Ion-guides of the TRAPS apparatus

Three ion-guides (electrodynamic cage: EDC) are comprised by the TRAPS apparatus (Figure 3.10). The particle beam, entering the apparatus via the ADL, passes the skimmer (SKM) and propagates into the first ion-guide (EDC 1, custom made). EDC 1 is a $160\,mm$ long octopole ion-guide with $9.52\,mm$ inner diameter and $3.18\,mm$ rod diameter. The helium background pressure inside can be leveled from 10^{-3} to $10^{-1}\,mbar$ in order to collisionally cool the ions. Two ring electrodes (L_{in}, L_{out}) with $9.52\,mm$ aperture located at the entrance and exit of the ion-guide can be used to apply electric potentials for trapping of ions (see section 4.8.2 for operating modes). Downstream EDC 1 the particle beam passes a quadrupole deflector ($r = 43\,mm$, No. 811989, EXTREL CMS, Pittsburgh, USA) which either focuses the ion beam on the Faraday Cup electrometer (FC 1) or into the second electrodynamic cage (EDC 2).

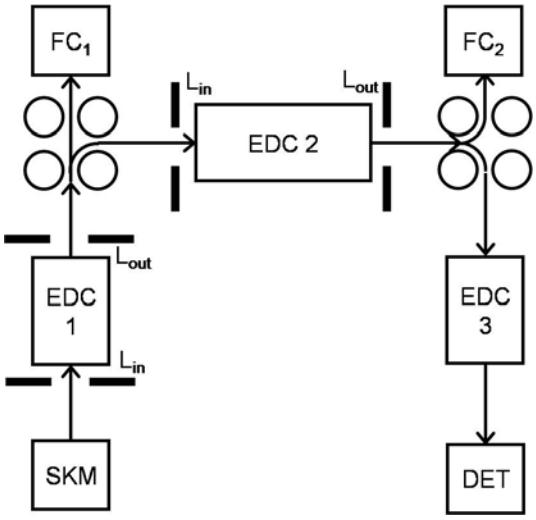

Figure 3.10. Ion-guides in the TRAPS apparatus. EDC 1 and EDC 3 are octopole ion-guides and EDC 2 is a quadrupole ion-guide.

EDC 2 is a $435\,mm$ long quadrupole ion-guide with $12.0\,mm$ inner diameter and $6\,mm$ rod diameter (in house design). The helium background pressure inside can be leveled from 10^{-4} to $10^{-1}\,mbar$. Two ring electrodes with $12.0\,mm$ aperture located at the entrance and exit of the ion-guide (L_{in}, L_{out}). EDC 2 is used to trap high numbers of particles for prolonged time in order to perform spectroscopy experiments on the ion-cloud trapped. The end electrode dc potential field does not penetrate far enough into the quadrupole field. Ions are not ejected quickly on application of a dc

potential between the end electrodes. Therefore, the ion-trap is equipped with an axial electric field gradient inside the quadrupolar electric potential for enhanced ejection of the ions. The axial electric field is generated by the insertion of conical oriented electrode wires between the parallel rods. The design follows Loboda et al. [2000] and Wilcox et al. [2002].

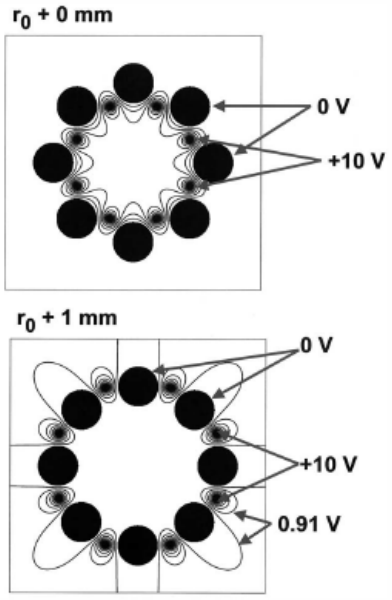

Figure 3.11. Transverse section of an octopole ion-guide with enhanced ejection electrodes located between the parallel rods. Upper panel: Inlet of the ion-guide. Lower panel: Exit of the ion-guide. The isopotential lines change noticeably in the ejection mode for positive ions. (reproduced from Wilcox et al. [2002]).

The subsequent quadrupole deflector is equal to the first quadrupole deflector. It either focuses the ion beam on the Faraday Cup electrometer (FC 2) or into the third ion-guide (EDC 3). EDC 3 is a $200\,mm$ long octopole ion-guide with $9.52\,mm$ inner diameter and $3.18\,mm$ rod diameter (No. 815491, EXTREL CMS, Pittsburgh, USA). Two ring electrodes with $7.62\,mm$ aperture are located at the entrance and exit of the ion-guide. It transfers the ions across a differential pumping stage to the single particle detector (DET).

3.5.2 RF-Generation and electric wiring

In order to adapt an ion-guide for the storage of singly charged nanoparticles, the RF-frequency has to be adjusted to accommodate the high mass-to-charge ratio of the particles. For nanoparticles in the $5-10\,nm$ diameter regime, the RF-frequency

should range between $100\,kHz$ and $30\,kHz$ respectively. Tunable RF generators operating at such low frequencies are not commercially available. Some groups have developed ion-traps which employ a digitally switched square wave pulse chain to drive nanoparticle ion-traps (e.g. Ding et al. [2001] and Ding et al. [2004]). Theoretically, any periodic waveform can provide stable conditions for ion-trapping. The drawbacks of this approach are intensified higher harmonics, which decrease the maximum trapping capacity of such traps. Rapid switching high voltages also increases noise problems to other sensitive equipment around. Therefore, a RF generator based on a ferrite core high voltage transformer driven by a push-pull feedback circuit was designed. It delivers sinusoidal RF voltages up to an amplitude of $2\,kV$ at a tunable frequency between $20\,kHz$ and $150\,kHz$ and was used successfully for the present experiments [Meinen et al., 2009]. A further advantage of this approach is that a DC offset voltage can be superimposed easily to the sinusoidal output voltage in order to define the potential on the axis of the ion-guide.

Ring electrodes at the exit of the ion-guides can be switched from the repelling potential to ground (or another potential) within $500\,ns$ by a fast MOSFET-Push-Pull switch (HTS 61-03-GSM, BEHLKE Electronic GmbH, Germany). All DC potentials are supplied by computer controlled NHQ 213M (iseq Spezailelektronik GmbH, Radeberg, Germany) high voltage modules.

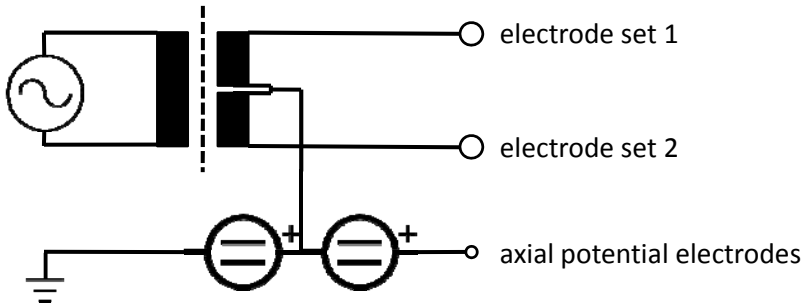

Figure 3.12. Electric wiring diagram of the custom build RF generator for the TRAPS ion-guides.

3.5.3 Reactions under controlled atmospheric conditions

Reactions of the nanoparticles under controlled atmospheric conditions can be performed in the central quadrupole ion-trap (EDC 2). Studies of ice nucleation on nanoparticles require careful control of temperature, pressure and humidity. For the

investigation of ice particles forming noctilucent clouds, a low temperature and low water vapor atmosphere has to be generated inside the ion-trap. Minimum temperatures of $\sim 130\,K$ are reached at the mesopause [Lübken, 1999]. The Water mixing ratio is only some ppm (e.g. Seele 1999) at a pressure in the $10^{-2}\,mbar$ range.

The housing of the quadrupolar ion-trap is mounted to a cold finger cooled by a closed cycle helium cryostat (DE-104B-T and ARS-4HW, Advanced Research Systems Inc., Macungie, USA) as shown in Figure 3.13. The electrode rods and the quadrupole deflectors are mounted to the housing with thermal contact. Without gas load, this assembly can be cooled to $< 40\,K$. If the housing is filled by a buffer gas in the $10^{-2}\,mbar$ range, the minimum achievable temperature is $< 130\,K$. Up to $2\ 10^8$ particles can routinely be stored at every temperature. The background pressure inside the central quadrupole ion-trap can be leveled from 10^{-4} to $10^{-1}\,mbar$ by a leak valve attached directly to the housing of the ion-guide. The pressure inside the housing is monitored by a capacitive pressure gauge (CTR-91, Oerlikon Leybold Vacuum GmbH, Köln, Germany). The gas leaking into the ion-guide housing can either be dry or humidified. For humidification the gas passes a water bubbler and a subsequent cooling unit which can be cooled to $-40\,°C$. With this setup low water vapor concentrations can be created by freezing out the water vapor.

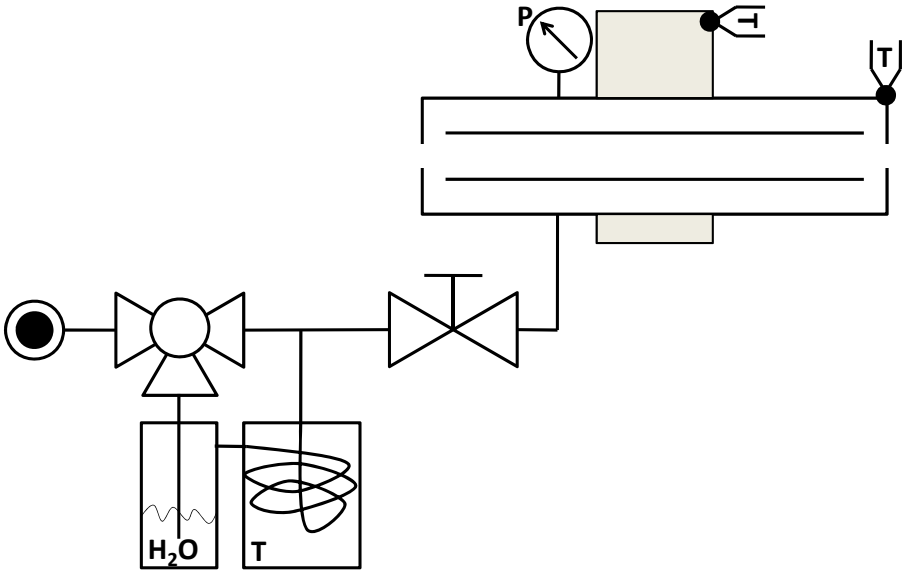

Figure 3.13. Central quadrupolar ion-trap with temperature, pressure and humidity control elements.

3.6 Optical extinction cell

Experimental studies of optical properties of nanoparticles are not trivial, as the relatively low absorption cross sections of small particles prevent the use of regular spectroscopic methods to obtain optical information. Cavity ring-down spectroscopy (CRDS) has been proven to be very sensitive and it has been applied successfully in the gas phase for the detection of trace gases (e.g. Meinen et al. [2010] and many other). CRDS is based on an optical cavity built of two (or more) highly reflective mirrors, in which a short light pulse of a given wavelength is introduced. By measuring the lifetime of the light pulse inside the cavity (named ring-down time), one is able to determine the intrinsic loss of the cavity due to transmission through the mirrors and the extinction of the material inside the cavity. The losses as a function of wavelength arising from nanoparticles inside the cavity correspond directly to the extinction spectrum of the particles.

Cavity ring-down extinction spectroscopy of free ions in a linear ion-trap was reported first by Terasaki et al. [2007] and Majima et al. [2008]. About 10^8 Mn^+ ions were trapped in a $40\ cm$ long octopole ion-trap. The ion-trap was placed in a high-finesse optical cavity with a total optical path-length of $8\ km$. The cavity was pumped by the frequency-doubled output of an optical parametric oscillator (MOPO). Later experiments of this group on Ag_9^+ cluster also facilitate the MOPO laser as light source. It was recently shown (e.g. Meinen et al. [2010]), that incoherent light sources for cavity assisted spectroscopy are superior in terms of mechanical stability of the optical setup and overall experimental simplicity. Therefore a light emitting diode (LED) with center wavelength at $405\ nm$ (H2A1-H405, Roithner Lasertechnik, Austria) is used as incoherent light source for pumping of the optical cavity. The FWHM of the LED emission spectrum was not specified experimentally, but it is usually in the range of $10 - 15\ nm$ (see datasheets at www.roithner-laser.com).

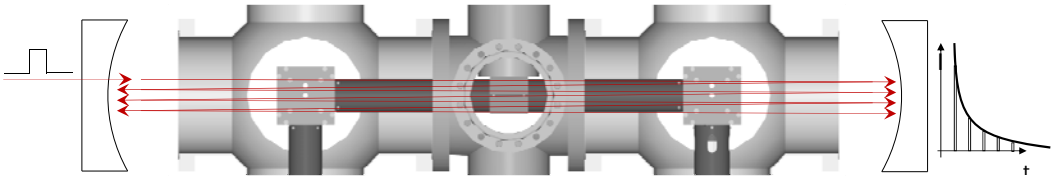

Figure 3.14. Central quadrupole ion-trap placed in a high-finesse optical cavity.

In the TRAPS apparatus the “folded” light path of the optical cavity traverses the central quadrupole ion-trap (Figure 3.14). The mirrors are fixed on a custom build kinematic mirror mount attached at the center of an ISO-CF150 vacuum flange (Figure 3.15). The mirror is adjustable by micrometer screws accessible from outside the vacuum chamber. A quartz-glass window centered at the vacuum flange enables coupling of light into the vacuum chamber. A $110\,mm$ plan-concave quartz-glass lens is fixed at the mirror mount next to the mirror. With this assembly it is possible to place an optical fiber as light source outside the vacuum chamber. A $(400 \pm 40)\,nm$ laser-line filter (FB400-40, ThorLabs, U.S.A.) is placed in front of the vacuum window for reduction of stray light. The exit mirror flange holds a photon multiplier tube (PMT, 9124B+QL30F, ET Enterprises Ltd, U.K.) and a light tight housing. The mirror reflectivity is $R = 99.995\,\%$ at the center wavelength, $415\,nm$, and the bandwidth is $\pm 15\,nm$ (Model 901-0010-0415, Los Gatos Research Inc., U.S.A.). The distance between the mirrors is $810\,mm$ and the path-length of one traverse through the ion-cloud is $450\,mm$. A typical attenuation time of a ring-down decay is $20\,ms$. Thus a typical total path-length achieved with this setup is $6\,km$. This corresponds to an effective path-length inside the ion-cloud of $3.3\,km$. If assumed that 5 % change in attenuation time can be detected, the spectrometer is sensitive for an absorption coefficient of $\alpha \approx 2\,10^{-10}\,cm^{-1}$ (theory of cavity enhanced spectrometers is discussed in section 5).

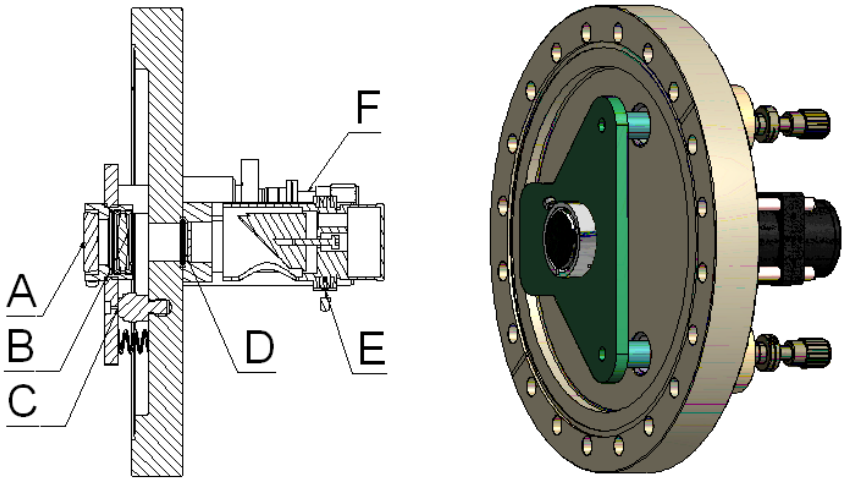

Figure 3.15. Cross section and scheme of the custom build mirror mount. A: mirror, B: plan-concave lens, C: gimbal mount, D: vacuum window, E: support for LINOS “Mikrobank” optical elements, F: micrometer screw.

For the detection of mono-exponential ring-down decay, light pumping the cavity has to be turned off rapidly. It turned out during development of the instrument's electronics as a good rule of thumb, that the decay of the light source has to be about ten times faster than the change in decay that has to be detected for proper instrument sensitivity. In this case the decay of the light source has to be faster than $200\,ns$. No commercial electronics are suitable for this task. A custom build LED power supply based on a half bridge driver (IR2104) with two downstream HEXFETs (IRF 710) is able to turn off the LED with a decay time of $< 180\,ns$. The LED light is coupled into a quartz-fiber (diameter $200\,\mu m$, $NA = 0.5$) by a condenser optic ($f_1 = 25\,mm$, $f_2 = 60\,mm$, all plan-concave quartz-glass lenses).

The PMT at the exit of the cavity is supplied by a high voltage typically in the range of $-780\,V$ to $-810\,V$ (PMT Driver C3830, Hamamatsu Photonics, Germany). The current of the PMT is amplified by $10^4\,V/A$ and $80\,MHz$ bandwidth (DHPCA-100, FEMTO Messtechnik GmbH, Germany). The signal is sampled by a fast digitizer (NI PCI-5152, National Instruments, U.S.A.). Data acquisition and processing is programmed in LabView (LabView 8.6, National Instruments, U.S.A.).

3.7 Particle detectors

Particle detectors are used to monitor the particle beam density, the number of particles in a pulse exiting an ion-trap, or single particles from a charge reversal experiment. For the number of application two different kinds of detectors are employed: A Faraday cup electrometer (FC), and a channel electron multiplier based single particle counter (CEM).

The scheme of the FC is shown in Figure 3.16. The electrometer is used to monitor the charge carried by the particle beam. It consists of a conical electrode in a shielded housing. The front aperture of the housing is covert by a thin mesh with 95% open face in order to improve the electric shielding. Different aperture sizes from $8\ mm$ to $20\ mm$ diameter are used. Particles impinging on the electrode transfer their charge to it. A floating shield BNC vacuum feedthrough enables the amplification of the current by using a current to voltage amplifier (DLPCA-200, FEMTO Messtechnik GmbH, Germany). For monitoring the continuous particle beam, the high gain and low speed mode of the amplifier is used ($10^{11}\ V/A, 1\ kHz$). Particle pulses have high intensity so they can be resolved in time with higher accuracy ($10^{9} - 10^{10}\ V/A, 50 - 7\ kHz$). The lowest particle hitting rate distinguishable from background noise was $0.1\ pA$ which corresponds to $1.6\ 10^{6}\ s^{-1}$.

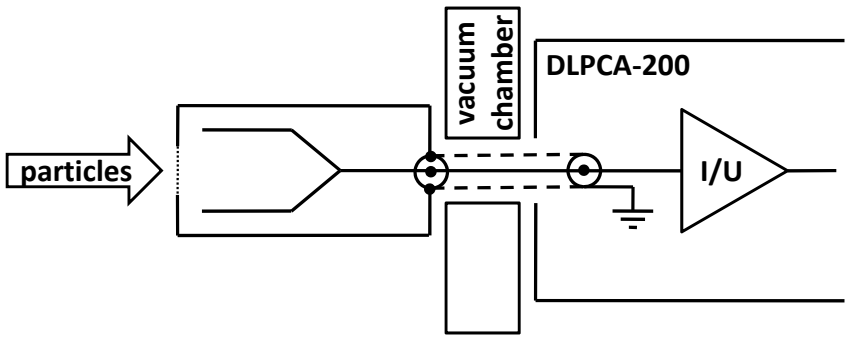

Figure 3.16. Scheme of the Faraday cup electrometer.

The CEM single particle counter is used to detect ions extracted from the ion-cloud in an ion-trap by charge reversal spectroscopy. In this technique an ion-trapp is filled with singly charged negative ions. By photoionization with a subsequent Auger process, particles turn from negative to positive charge. The axial electrostatic barrier of the ion-trap becomes attractive for the positive ion and the ion escapes from the

trap. Since absorption cross sections of the particles are small and the probability of a subsequent Auger process is < 1 the beam of positive ion exiting the ion-trap will be far below the detection limit of a FC. A detector with a detection limit $< 10^3\ s^{-1}$ is needed – a "single particle detector".

For molecular ions and very small clusters such single particle detectors are based on Daly type detectors [Daly, 1960], Microchannel plates (MCPs, [Wizas, 1979]) or channel electron multipliers (CEMs, [Goodrich and Wiley, 1962]). Modern CEMs are superior in terms of experimental simplicity since they can be stored and handled in an ambient atmosphere, their surface can easily be cleaned if coated with particles and they come up with relatively high mechanical stability.

3.7.1 Feasibility study of a CEM based single particle detector

CEMs have a high surface resistance of the electrode where electrons or charged particles impinge. When a potential is applied between the input and output end of the CEM, the resistive surface forms a continuous dynode. A dynode has the property of emitting secondary electrons when primary particles impinge upon it. This process is called secondary electron emission. Through this process, a CEM is capable of detecting a particle or electron that has entered its funnel-shaped input aperture. These primary particles generate secondary electrons that are accelerated down the channel by a positive bias. Upon striking the interior surface of the channel walls, these electrons then generate further secondary electrons. The resulting avalanche process produces an easily detectable output pulse of charge containing up to 10^8 electrons with pulse duration of about $8\ ns$.

The detection efficiency of CEM, MCP or other detectors based on secondary electron emission depends on ion energy, mass and composition [Gilmore and Seah, 2000; Fraser, 2002; Rietmann et al. 2006]. For single atomic ions or small clusters the efficiency of secondary electron emission upon impinge at the dynode (= detection efficiency) is near 1 independent of ion composition [Gilmore and Seah, 2000]. With increasing atomic mass unit (amu) of the ion, the detection efficiency decreases since much of the kinetic energy is directly transferred into deformation, fragmentation and thermal energy. For large particles, secondary electrons are exited into vacuum from

direct transfer of the ion's kinetic energy [Fraser, 2002]. Gilmore and Seah [2000] and Rietmann et al. [2006] give an analytical relationship of the secondary electron yield γ as a function of particle velocity v:

Eq. 3.1 $$\gamma(v) = A\, v\left(1 - \left(\frac{1}{1+(v/v_0)^n}\right)^{1/n}\right)$$

Where A is a scaling term experimentally determined to be $A = 10^{-4}$, v_0 is a threshold velocity and $n = 4.5$. At high velocities, this function reduces to a linear function of velocity. The emitted secondary electrons are amplified inside the CEM as described by a Poisson distribution:

Eq. 3.2 $$W = 1 - \sum_{i=0}^{\infty}(1-a)^i\ P_i$$

Eq. 3.3 $$P_i = \frac{\gamma^i}{i!}e^{-\gamma}$$

In this relationship a is the detection efficiency of the dynode for electrons. The detected signal intensity correlates with the detection efficiency $W(v)$ which is a function of particle velocity. In a constant electric acceleration field, particle velocity decreases with particle diameter. Figure 3.17 shows the detection probability of an ion as a function of particle diameter. More than 20 % of 3 nm diameter are detected for particles with 10 keV kinetic energy. If the kinetic energy is increased to 30 keV more than 40 % of the particles are detected. This quite sufficient detection efficiency rapidly decreases for higher mass ions. Particles with 15 nm diameter have a detection efficiency of about 2 % at 30 keV kinetic energy.

The model derived by Gilmore and Seah [2000] and Rietmann et al. [2006] is extrapolated from experiments with molecular ions. As the ion mass increases, a significant fraction (between 25 and 50 % [Fraser, 2002]) of the ion energy is lost on impact with the dynode as a result of bond breaking, deformation and the ejection of small fragments. This fraction is dependent on ion type. Furthermore the secondary ion yield will be modified by coating of the dynode with ions and ion fragments. Thus the real detection efficiency is expected to be lower than predicted by Eq. 3.2 and Figure 3.17.

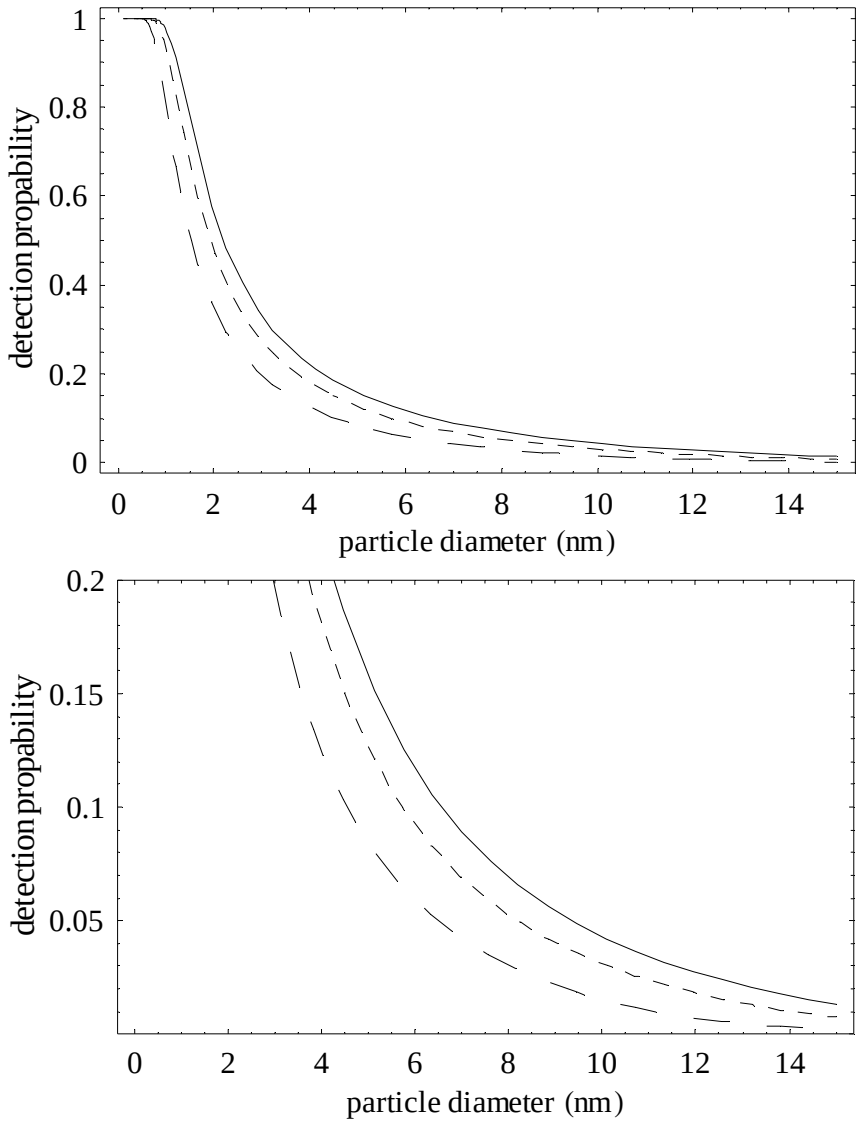

Figure 3.17. Calculated detection probabilities as a function of particle diameter for different particle acceleration voltages. (long dashed line: $E_{kin} = 10\ keV$, short dashed line: $E_{kin} = 20\ keV$, solid line: $E_{kin} = 30\ keV$).

The CEM-based single particle detector consists of an ion acceleration field, a CEM, a scintillator, a photon guiding quartz rod, a photomultiplier and a data acquisition system (see Figure 3.18). The particles exit the ion-guide with $< 500eV$ kinetic energy. They are accelerated by the potential V_1. In the funnel of the CEM (KBL-15RS, Dr. Sjuts Optotechnik GmbH, Göttingen, Germany) the impacting ion releases an electron which is amplified to an electron bunch in the subsequent tube where the potential V_2 is applied. This electron bunch is accelerated onto a szintillator were each electron excites a light flash. After this second amplification step the light is coupled out of the vacuum by a quartz-glass rod with $10\ mm$ diameter. The exiting

light is detected and converted in an electron avalanche by a PMT (H7155, Hamamatsu Photonics Deutschland GmbH, Herrsching am Ammersee, Germany), which is the third amplification. The resulting current signal is turned into TTL pulses by an appropriate single photon counting unit inside the PMT.

Figure 3.19 shows the darkcount rate of the setup for varying acceleration potentials V_1 recorded with zero potential V_2 at the CEM. Ions can be accelerated up to $25\,keV$ at $\sim 10^{-6}\,mbar$ without increasing the darkcount rate by photons from corona discharge at the high voltage electric feedthrough of the vacuum chamber. The scheme of the experimental setup used for characterization of the CEM-based single particle detector is shown in Figure 3.10. Negative ions are separated from the particle beam by the first quadrupole deflector prior to entering EDC 2. Particle number in a pulses is regulated by filling EDC 2 with different time before turning the exit potential to ground. The second quadrupole deflector is used to guide particle pulses either on FC_2 or the single particle detector unit. EDC 3 is used to guide the ions through another differential pumping step which lowers the pressure to $< 10^{-6}\,mbar$.

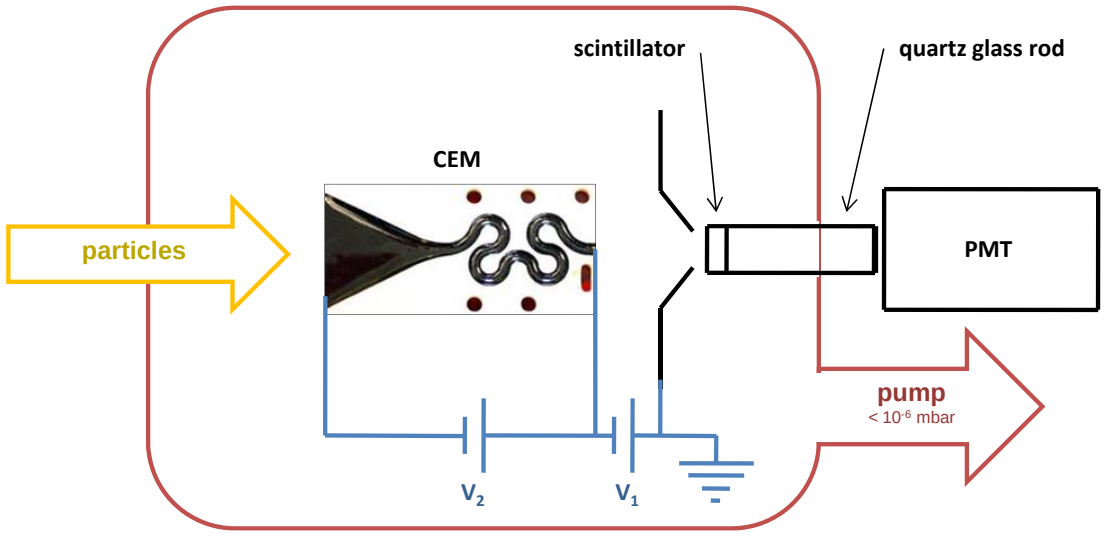

Figure 3.18. Scheme of the CEM-based single particle detector.

The loss of particle in EDC 3 is characterized by substituting the CEM by FC_3. Figure 3.20, upper panel, shows that no particle loss can be measured within the experimental certainty. Count rates in Figure 3.20 represent the maximum current generated by the particle pulse impacting on the detector. For a FC this current is a

direct measure of the particle number impinging at the electrode. Since the CEM-based single particle detector has three amplification steps, the count rate is a multiple of the particle rate impinging at the funnel-shaped dynode of the CEM. Thus Figure 3.20, lower panel, demonstrates that there is a linear relationship between particle hitting rate and count rate of the detector assembly. Note, that Figure 3.20 does not give any information about the detection efficiency of the CEM-based single particle detector.

SiO_2 nanoparticles with $d_p = (11.1 \pm 1.7)\, nm$ were used for this study. The pressure in EDC 2 was 1.9 $10^{-2}\, mbar$ and in the CEM chamber 8.9 $10^{-7}\, mbar$. The acceleration potential was $V_2 = 10\, kV$ and the dynode potential was $V_2 = 500\, V$. The darkcount rate of the CEM-based detector was $150\, cts/s$.

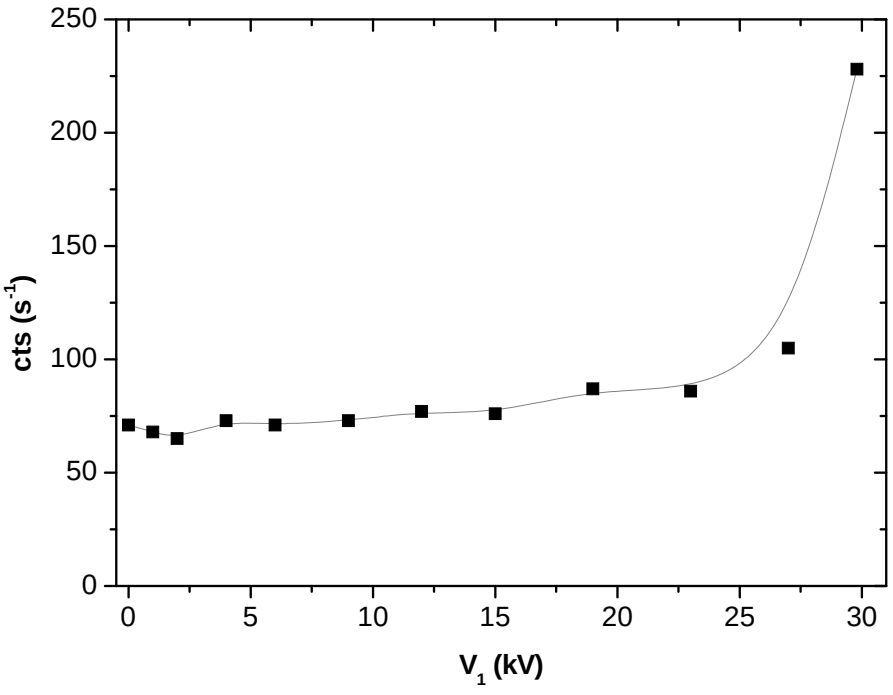

Figure 3.19. Darkcount rate at different acceleration potentials.

This feasibility study shows, that the CEM-based detector assembly comes up with a linear dependence of particle hitting rate to count rate. If an absolute measure of the particle hitting rate is required, the detector has to be carefully calibrated. From Figure 3.19 and Figure 3.20 lower panel, it can be roughly estimated, that particle hitting rates ~ 250 particles s^{-1} can be resolved from background. If the darkcount

rate can be suppressed by a pulse height analyzer, even a smaller hitting rate can be resolved from background. This will be the scope of future work.

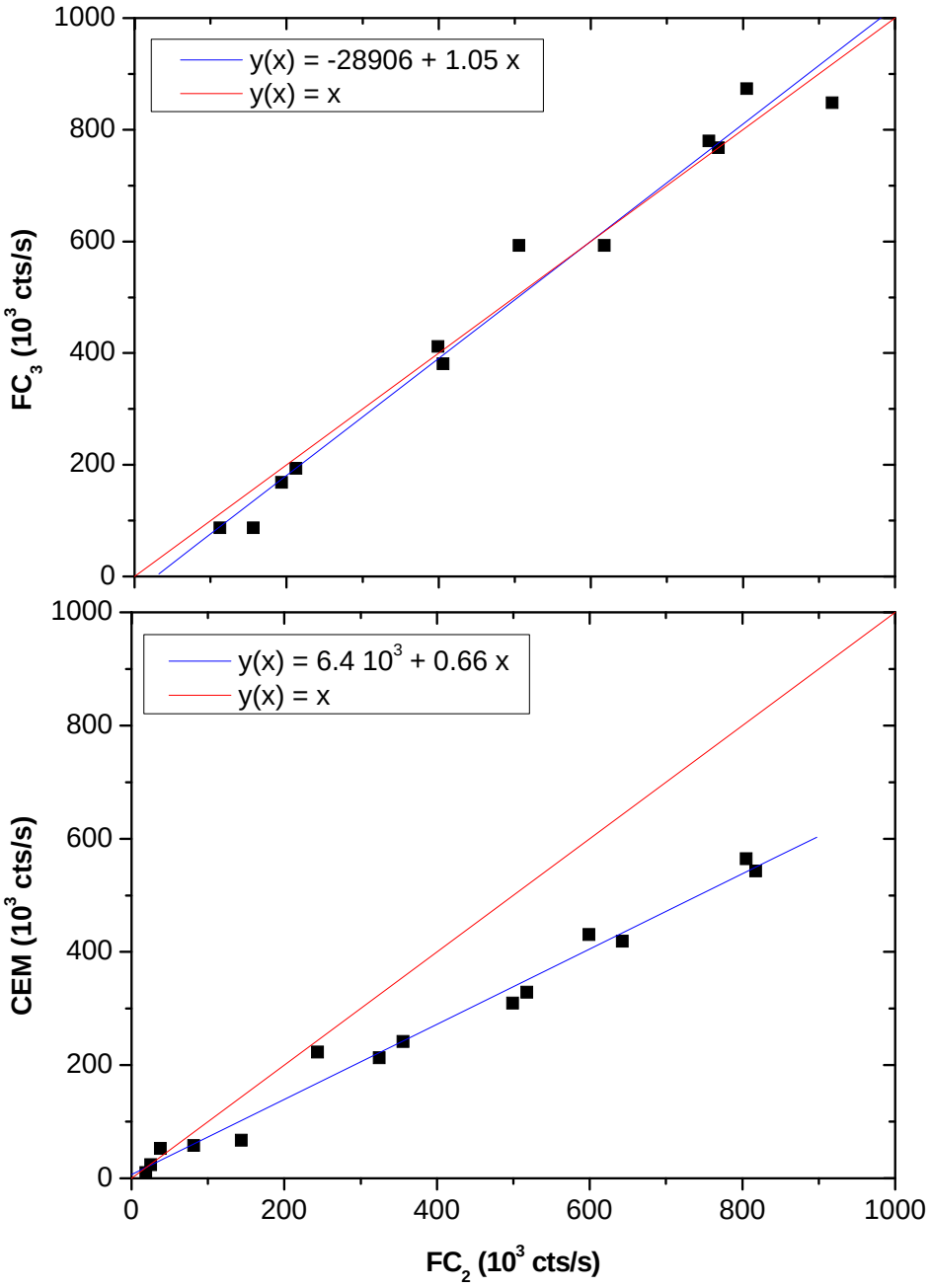

Figure 3.20. Count rate of Faraday cup electrometer compared with CEM-based single particle detector. The setup for this experiment is shown in Figure 3.10. Upper panel: The detector downstream EDC 3 is a FC. Lower panel: The detector downstream EDC 3 is the CEM.

3.8 Particle Mass Spectrometer

Particle Mass Spectrometers have been developed in the late nineties by several groups (e.g. Ziemann et al. [1995], Gard et al. [1997] and Jayne et al. [2000]). These devices, which are commercially available meanwhile, can sample particles from ambient in the diameter range from $50\,nm$ to several micrometers. They are able to detect particles from relatively low number concentrations up to $10^5\ cm^{-3}$. These two parameters limit their use for primary particles in flames or plasmas of industrial relevance. The particle mass spectrometer (PMS) developed by Mülhopt et al. [2002] is able to measure nanoparticles in the diameter range $0.3 - 30\,nm$ with number concentrations up to $10^{13}\ cm^{-3}$ [Mülhopt et al., 2002; Mätzing et al, 2003; Paur et al., 2005].

Gas borne nanoparticles are probed from the aerosol source by a two stage molecular beam sampling system. In the first stage $(10^{-3}\ mbar)$, super-sonic expansion of the sample volume into the free-molecular regime leads to freezing of any gas-particle interaction. By this, agglomeration of the particles is quenched. From the center of the free jet, a molecular beam is extracted by means of a skimmer and further expand into the high vacuum chamber. Figure 3.21 shows the skimmer and the high vacuum chamber with time-of-flight instrumentation. The vacuum system requires a conventional rotary pump and two turbomolecular pumps with a total capacity of $750\ l\ s^{-1}$.

In the detection chamber, the particle beam passes a deflection capacitor which separates the charged particles according to their polarity and deflects them according to their kinetic energy-to-charge ratio $(0.5\ e\ v^2\ m\ z^{-1})$. By varying the deflection voltage, particles of different energy-to-charge ratios reach the Faraday cups, which are located symmetrically at fixed off-axis positions at the end of the detection chamber. The current signal generated at the FCs is proportional to the incoming number of particles multiplied by their average charge. Depending on the aerosol system, the current signal is in the range of $10 - 10000\ fA$. The measurement of such low currents is accomplished by means of ultra sensitive preamplifiers ($5\ 10^9\ V\ A^{-1}$, LCA-1K-5G, FEMTO Messtechnik GmbH, Berlin, Germany).

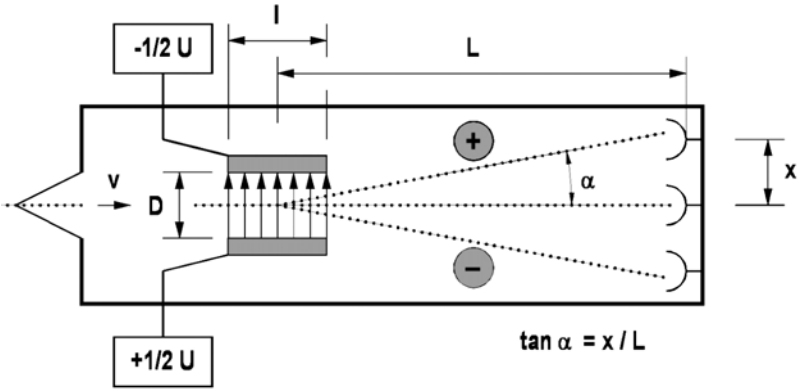

Figure 3.21. Particle Mass Spectrometer (PMS) without particle inlet.

To convert the recorded spectra into a particle diameter distribution, the average number of charges z, the particle speed v and the material density ρ must be known. The investigations of Paur et al. [2005] show comparable results obtained from PMS and Transmission Electron Microscopy (TEM) measurements [Baumann et al., 2005; Mätzing et al., 2003]. The approximate diameter of the material sampled from the molecular beam was determined by TEM. However, the sampling and micrograph analysis of these particles by TEM appear to be difficult which is due to the poor contrast of the particles and overlapping of particles. A typical mass spectrum of Fe_2O_3 nanoparticles from the microwave particle plasma synthesis (MPPS) achieved by the PMS is shown in Figure 3.22 in comparison to the analysis of TEM micrographs.

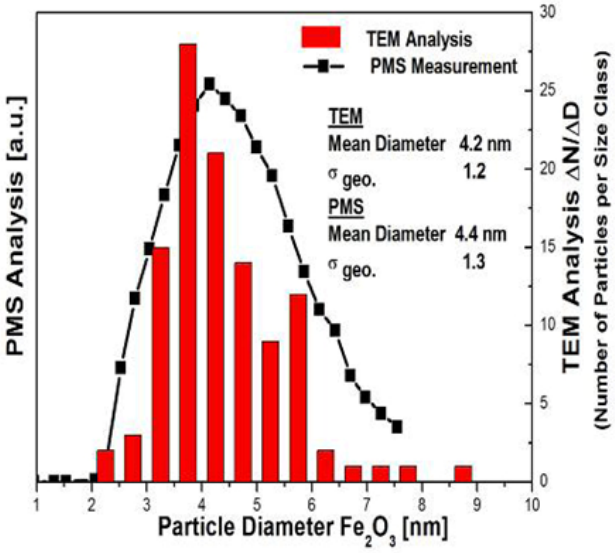

Figure 3.22. Size distribution of iron oxide nanoparticles by TEM and by PMS measurements (reproduced from Baumann et al. [2005]).

CHAPTER 4

High Density Nanoparticle Beam Inlet

4.1 The particle inlet section of the traps device

4.1.1 Overview

An overview of the particle inlet section of the TRAPS apparatus is given in Figure 4.1. The upper graph shows all relevant elements which are passed by the nanoparticles on their way into the experimental zone of the vacuum device. The corresponding levels of pressure are depicted in the lower graph. Nanoparticles are produced in the Microwave Plasma Particle Source (MPPS); downstream the quartz glass reactor they pass a $6\ mm$ diameter metal tube of $20\ cm$ length. Then they pass a $6\ mm$ diameter conducting rubber hose of $80\ cm$ length before they enter the TRAPS device through a Flow Limiting Orifice (FLO). The size of the FLO can be adapted to the particle source pressure in order to level the helium gas flow to approximately $1100\ Pa\ l\ s^{-1}$ by a choked nozzle expansion. In case of using the MPPS, the diameter of the FLO is $1000\ \mu m$. For a particle source providing particles suspended in helium at atmospheric pressure a FLO with $150\ \mu m$ diameter has to be used. The pressure downstream the FLO can be leveled using a vacuum pump with a valve in order to adjust the inlet pressure of the AeroDynamic Lens (ADL) to the type of particles to be focused. A typical inlet pressure level for sub $10\ nm$ silica particles is $900\ Pa$.

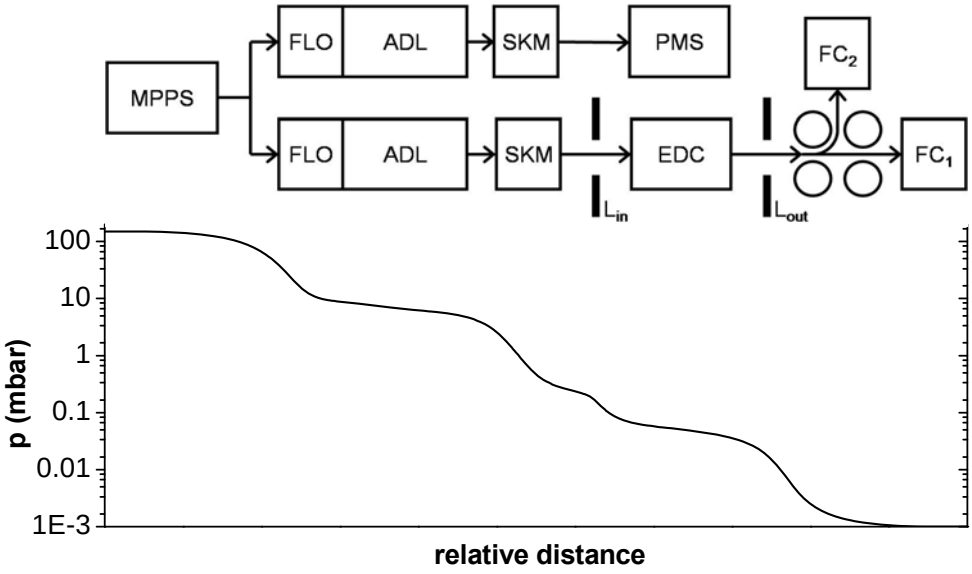

Figure 4.1. Schematic diagram of the particle inlet section of the TRAPS apparatus. As a particle source the Microwave Plasma Particle Source (MPPS) is depicted. Further elements are Flow Limiting Orifices (FLO) SKiMmers (SKM), AeroDynamic Lens (ADL), Particle Mass Spectrometer (PMS), ElectroDynamic Cage (EDC) with entrance and exit lens (L_{in}, L_{out}), and Faraday Cups (FC_n). The corresponding levels of pressure are depicted in the lower graph.

The particles pass the ADL, where the particle beam is focused into a SKiMmer (SKM) with $3\,mm$ opening diameter. A roots vacuum pump is used to remove the separated gas from the particles between ADL and SKM. A typical outlet pressure of the ADL is $10\,Pa$. Depending on the device used, the particles now enter either a Particle Mass Spectrometer (PMS) or an ElectroDynamic Cage (EDC) of the TRAPS device, where they can be trapped by electric potentials at the inlet lens (L_{in}) and the exit lens (L_{out}). The pressure level inside the EDC is about $1\,Pa$, sufficient to collisionally cool the particles entering the EDC. When the exit lens is switched to ground, the particle beam enters the experiment zone of the vacuum device. In this example a quadrupole bender is used to direct the particle beam onto one of the Faraday Cup electrometers (FC_n). The pressure level in the experiment zone of this setup is below $0.1\,Pa$. In the complete TRAPS apparatus the quadrupole bender is used to direct one polarity of the particle beam into a second EDC where the experiments are performed (see Figure 3.1).

In the following sections theory, design and characterization of the ADL and the EDC is described in detail.

4.2 Aerodynamics of particle focusing

Transferring small, airborne particles into vacuum by an aerodynamic lens (ADL) is well understood for most demands. Liu et al. have provided the basis for focusing fine particles onto a single streamline [Liu et al., 1995a; Liu et al., 1995b]. An ADL system typically consists of three parts: A flow limiting orifice, focusing lenses, and an acceleration nozzle. The choked inlet orifice determines the mass flow through the system and reduces the pressure from ambient to working pressure of the focusing lenses. The focusing lenses are a series of orifices contained in a tube that creates converging and diverging flow accelerations and decelerations. By this series of contractions and expansions of the gas flow the particles are separated from the carrier gas due to their inertia and focused into a tight particle beam. The acceleration nozzle controls the operating pressure within the lens assembly and accelerates particles to downstream destinations. Lenses for many particle types and different vacuum systems have been designed. Huffman et al. [2005] give a comprehensive review of the characteristics and performance of most previous ADL systems. These systems achieve optimal particle beam focusing in a diameter range between $100\ nm$ and $1\ \mu m$ [Lee et al., 2008].

Few groups have reported ADLs for smaller nanoparticles: To our knowledge the first work concentrating on particles $< 30\ nm$ was Wang et al. [2005a]. They present geometries for a set of so called inverted ADLs for small nanoparticles with various densities [Wang et al., 2006] which are frequently in use nowadays. It seems however, that the focusing performance reported for these lenses is comparatively poor for particles $< 20\ nm$ [Wang et al., 2006; Passig et al., 2006]. For example, Passig et al. have only been able to enhance the particle transmission efficiency through a skimmer system by a factor of two for $10\ nm$ particles by using an ADL designed to the guidelines of Wang et al. [2005] (see Figure 4.3 in [Passig et al., 2006]).

There are basically two reasons for the difficulty of focusing small nanoparticles: (1) The minimum achievable divergence of the beam is dominated by Brownian motion for small nanoparticles. A high axial speed of the particles reduces this effect [Wang et al., 2006]. (2) ADLs make use of the particle inertia by accelerating them

towards the lens axis. This leads to a slip motion of the particles when the gas streamlines bend strongly downstream from an orifice. This effect decreases with the third power of the particle diameter. Small nanoparticles tend to follow closely the gas streamlines. This effect could be compensated by higher gas flux at lower pressure, but maximum gas flow is limited by the pumping capacity of the vacuum system. A higher gas flux increases the radial ratio of the acceleration of the particles towards the center axis and the mean axial velocity of the particles in the reattachment zone.

As it has been shown by Wang et al. [2006], focusing of small nanoparticles is achievable by combining multiple orifices with sub-optimal Stokes Number. The drawback is not only a high gas flux but also an increased sensitivity on the gas type, the pressure as well as the density and diameter of the particles. This makes it difficult to design a lens capable of focussing particles smaller than $30\ nm$ in diameter which have various densities and a broad size range, as it can be done for larger particles (e.g. for a particle diameter range from $30\ nm$ to $1000\ nm$ [Zhang et al., 2004; Liu et al., 2007]. For the TRAPS apparatus, a tuneable ADL rather than an ADL with wide acceptance for different particle diameters was developed.

4.3 Theory of aerodynamic focusing

In this section basic formalisms are described which are useful for the understanding of the physical processes in a particle laden gas flow propagating through an orifice.

Figure 4.2 shows the schematic of a single lens system with an orifice at position $x = 25\ mm$. In the graph a plot of a gas streamline and a trajectory of a particle are depicted. Far upstream from the orifice, the selected particle follows the gas towards the orifice at a radial distance of R_{pi}. As the gas approaches the orifice, it is accelerated inward in a steadily increasing manner, such that the particle closely follows the streamline. The particle gains a radial velocity component in inward direction. Downstream the orifice, the streamline bends outward rapidly, such that the particle cannot follow the streamline because of its inertia. One can see that the particle overshoots the gas streamline towards the axis. Downstream of the lens, the particle moves outward slightly and then settles onto a streamline with a smaller radial coordinate R_{po}. The flow of the gas and the concurrent particle movement is characterized by the Reynolds Number, the Mach number and the Stokes Number as described below.

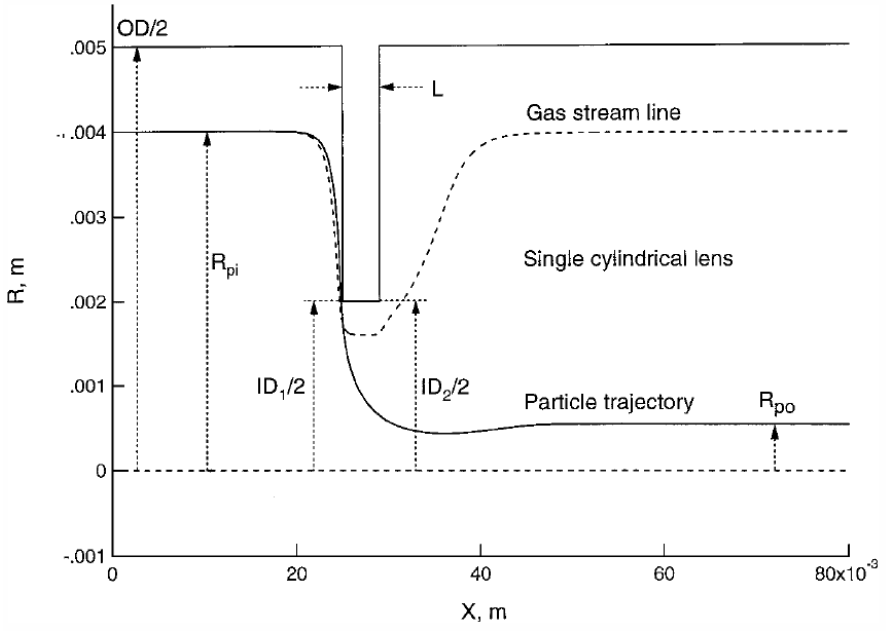

Figure 4.2. Schematic of a single thin cylindrical lens showing a gas streamline and the trajectory of a particle (adapted from Zhang et al. [2002]).

4.3.1 Laminar gas flow through an orifice

The volumetric flow rate Q of a laminar flow in a tube with radius R and the open face $A = \pi R$ is given by the mean velocity of the fluid $\bar{v}$.

Eq. 4.1 $$Q = A\,\bar{v}$$

The mass flow $\dot{m}$ can be defined by using the density ρ of the fluid.

Eq. 4.2 $$\dot{m} = \rho\,Q = \rho\,A\,\bar{v}$$

Bernoulli's law predicts that the mass flow is equal at every location in a tube.

Eq. 4.3 $$\bar{v}_1\,A_1\,\rho = \bar{v}_2\,A_2\,\rho$$

In a stationary tube flow, four forces are acting on the fluid. There might be gravitational force F_g which can be neglected for a horizontal flow direction. The fluid will be forced to move by the pressure difference Δp at the inlet and the outlet of the tube. The corresponding force is $F_p = \Delta p\,A = \pi\,R^2\,\Delta p$. For the laminar case there will be Newtonian force of friction between the fluid and the wall and the infinitesimal small fluid layers $F_f = -\eta\,2\,\pi\,R\,l\,\frac{\Delta v}{\Delta r}$ with the length of the tube l and the dynamic viscosity η. If the flow is stationary the forces must be in equilibrium.

Eq. 4.4 $$\frac{\Delta v}{\Delta r} = -\frac{\Delta p\,R}{2\,\eta\,l}$$

The solution of this equation, if transferred into a differential equation and boundary condition $v(r = R) = 0$ is used, is the Hagen-Poiseuille's law.

Eq. 4.5 $$v(r) = \frac{\Delta p}{4\,\eta\,l}(R^2 - r^2)$$

The volumetric flow rate and the mean velocity are

Eq. 4.6 $$Q = \frac{\pi\,R^4}{8\,\eta\,l}\Delta p$$

Eq. 4.7 $$\bar{v} = \frac{R^2}{8\,\eta\,l}\Delta p$$

Bernoulli's law can be used for the description of a gas flow through an orifice. Using index 1 for the tube and index 2 for the orifice, it can be written as

Eq. 4.8 $$p_1 + \frac{1}{2}\rho\, v_1^2 + \rho\, g\, h = p_2 + \frac{1}{2}\rho\, v_2^2 + \rho\, g\, h = \text{const.}$$

Using Eq. 4.2, Eq. 4.3 and Eq. 4.8 one obtains for the mass flow through an orifice

Eq. 4.9 $$\dot{m} = \frac{A_2}{\sqrt{1-\left(\frac{A_2}{A_1}\right)^4}}\sqrt{\frac{2(p_1-p_2)}{\rho}}$$

Following Wang et al. [2005a] Eq. 4.9 can be written with the discharge coefficient C_d, the expansion factor Y, the contraction factor $\beta = A_2/A_1$, the Reynolds Number Re (see Eq. 4.14) and the specific heat ratio of the gas γ_g.

Eq. 4.10 $$\dot{m} = A_2 \frac{C_d\, Y}{\sqrt{1-\beta^4}}\, p_1 \sqrt{\frac{2M}{R\,T}\frac{\Delta p}{p_1}}$$

$$C_d = \begin{cases} 0.1373\ \mathrm{Re}^{0.5} & (\mathrm{Re} < 12) \\ 1.118 - 0.8873\ \mathrm{Ln}[\mathrm{Re}] + 0.393\ \mathrm{Ln}[\mathrm{Re}]^2 & (12 < \mathrm{Re} < 5000) \\ 0.59 & (\mathrm{Re} \geq 5000) \end{cases}$$

$$Y = 1 - (0.410 + 0.350\beta^4)x/\gamma_g$$

$$x = \frac{p_1-p_2}{p_1}$$

This equation is valid as long as the flow at the vena contracta is subsonic [Ward-Schmith, 1979]. If the pressure difference exceeds a ratio of about two, we obtain a critical flow with supersonic velocity at the vena contracta and the critical mass flow rate $\dot{m}_c$ through an orifice becomes

Eq. 4.11 $$\dot{m} = A_2 \frac{C_d\, Y_c}{\sqrt{1-\beta^4}}\, p_1 \sqrt{\frac{2M}{R\,T}\mathrm{x_c}}\,,$$

where Y_c is the critical contraction factor defined by Eq. 4.10, with

Eq. 4.12 $$x = x_c = \frac{\Delta p_c}{p_1} \approx \left(\frac{2}{\gamma_g+1}\right)^{\frac{\gamma_g}{\gamma_g-1}}$$

The Mach number of the critical flow Ma_c, which is the ratio of gas velocity v and speed of sound $\mathrm{c_g}$, can then be written as

Eq. 4.13 $$\mathrm{Ma}_c = \frac{\mathrm{v}}{\mathrm{c_g}} = Y_c\, C_d \sqrt{\frac{2\, x_c}{\gamma_g}}$$

The Reynolds Number Re is a dimensionless coefficient that gives a measure of the ratio of inertial forces to viscous forces and, consequently, it quantifies the relative importance of these two types of forces for given flow conditions. Here the Reynolds Number for an orifice $\mathrm{Re_f}$ is defined using the orifice diameter d_f as

Eq. 4.14 $$\mathrm{Re_f} = \frac{\rho\, \bar{v}\, d_f}{\eta} = \frac{4\, \dot{m}}{\pi\, \eta\, d_f}$$

4.3.2 Drag forces acting on a particle in a laminar gas flow

The mean free path length of a gas is defined as the mean distance a molecule travels before it interacts with another molecule. The mean free path length λ can be written as the fraction of the mean velocity of the molecule $\bar{c}$ and its collision rate $n_k = \sqrt{2}\, N\, \pi\, d_m^2\, \bar{c}$ using the ideal gas law and the molecular collision cross section d_m [Hinds, 1999].

Eq. 4.15 $$\lambda = \frac{\bar{c}}{n_k} = \frac{1}{\sqrt{2}\, N\, \pi\, d_m^2} = \frac{\eta}{\rho} \sqrt{\frac{\pi\, m}{2\, k_B\, T}} \cong \frac{3\, \eta}{\rho\, \bar{c}}$$

The Knudsen Number Kn is a dimensionless coefficient defined as the ratio of the molecular mean free path length λ to a representative physical length scale L. The representative length scale is $d_f/2$ for an orifice or $d_p/2$ for a particle. The Knudsen Number also can be expressed as a function of Mach number and Reynolds Number when the specific heat ratio of the gas γ_g is known.

Eq. 4.16 $$\mathrm{Kn} = \frac{\lambda}{L} = \frac{\mathrm{Ma}}{\mathrm{Re}} \sqrt{\frac{\gamma_g\, \pi}{2}}$$

Within the particle relaxation length s_p the particle velocity adapts to the flow. It can be calculated using the drag force acting on the particles surface. Assuming a laminar flow around the particle, the gas velocity at the surface of the particle is zero. Thus, Stokes law can be used to calculate the drag force F_D. As soon as the particle

diameter d_p becomes comparable to the mean free path length λ of the gas molecules (Kn ≈ 1), we leave the realm of continuum fluid dynamics. If d_p falls below λ, aerodynamic forces become less efficient and the particle decouples progressively from the flow field. The Cunningham-Slip-Correction factor C of the friction force F_D accounts for this effect [Allen and Raabe, 1985].

Eq. 4.17 $$F_D = \frac{3\pi\,\eta\,\Delta v\,d_p}{C}$$

The corrected drag force F_D is given by the dynamic viscosity η, the velocity difference Δv of particle and gas, the particle diameter d_p and the Cunningham-Slip-Correction factor C. The Cunningham-Slip-Correction can be written as a function of the Knudsen Number $\mathrm{Kn} = 2\lambda/d_p$

Eq. 4.18 $$C(\mathrm{Kn}) = 1 + \mathrm{Kn}\left[\alpha + \beta\,\mathrm{Exp}\left(-\frac{\gamma}{\mathrm{Kn}}\right)\right]$$

Where α, β and γ are parameters known from experiment [Allen and Raabe, 1985]. Combining Eq. 4.17 and Eq. 4.18 with $\mathrm{Kn} = 2\lambda/d_p$ gives a relationship for $F_D(d_p)$. The Cunningham correction factor increases for decreasing particle diameter and pressure (cf. Figure 4.3), thus the limit of the particle drag force $F_D(d_p)$ goes towards zero for decreasing particle diameter d_p. For this reason, it is difficult to aerodynamically focus small nanoparticles with ADLs. Setting the particle drag force F_D to be equal to the inertia force $F_i = m\ dv(t)/dt$, yields a differential equation that has to be integrated two times. Computing the limit as time goes to infinity yields the particle relaxation length s_p.

Eq. 4.19 $$s_p = \frac{\rho_p\,d_p^2\,C}{18\,\eta}\,v_{p0}$$

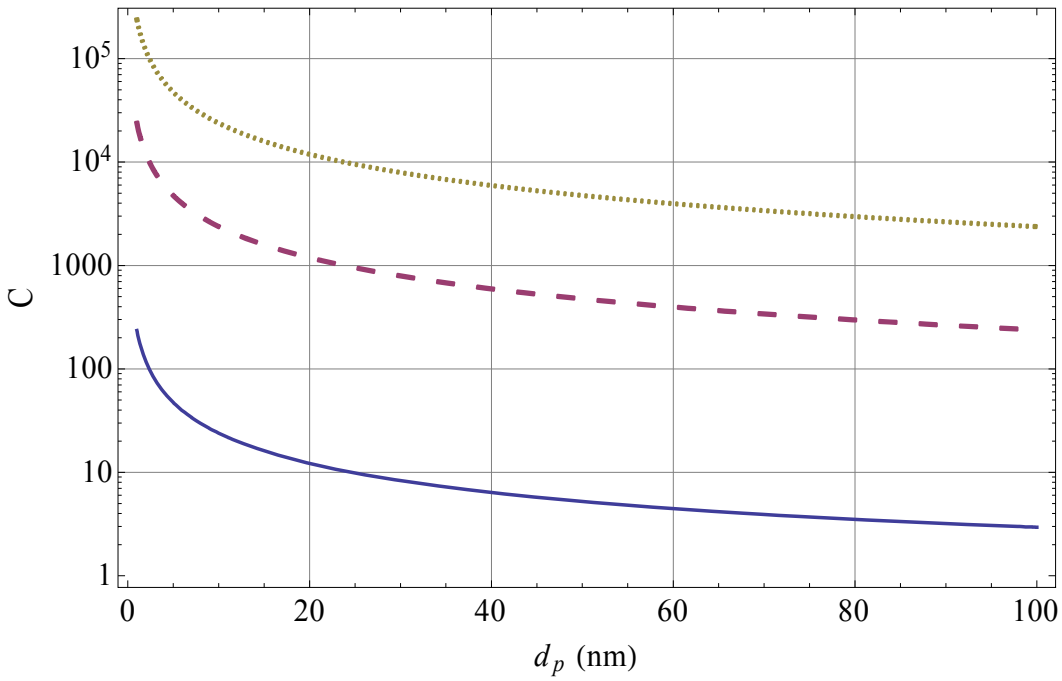

Figure 4.3. Cunningham correction factor C with respect to varying particle diameter d_p. Blue drawn line: $p = 101325\,Pa$ (ambient pressure), red dashed line: $p = 1000\,Pa$ and yellow dotted line: $p = 100\,Pa$.

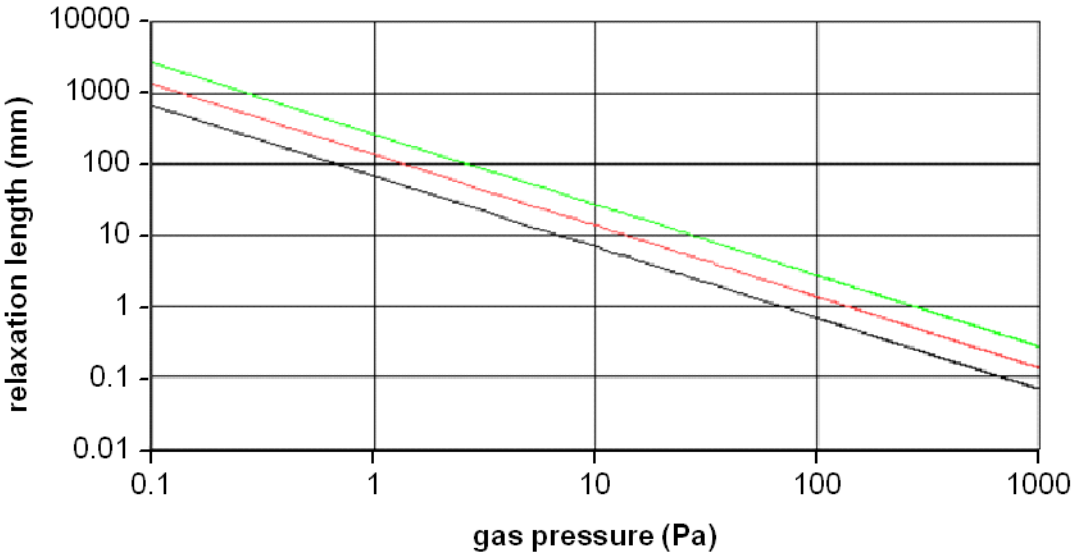

Figure 4.4. Particle relaxation length in helium at varying gas pressures. The SiO_2 particles have diameters of 5 nm (green, top), 10 nm (red, middle) and 20 nm (black, bottom) and a start velocity of 450 $m\,s^{-1}$.

Figure 4.4 shows particle relaxation length for particles typically used in this work. A starting velocity of $450\,m\,s^{-1}$ is used since this is a typical value for particles exiting the aerodynamic lens of the TRAPS apparatus. The particle relaxation length s_p can be written as particle relaxation time τ_p as well. Following Fuchs [1964] the effect of the particle Reynolds Number has to be corrected by the factor $f_d = 1 + 0.15\ \mathrm{Re}_p^{0.687}$.

Eq. 4.20 $$\tau_p = \frac{\rho_p\, d_p^2\, C}{18\,\eta\, f_d}$$

The effect of aerodynamic particle focusing is usually accomplished by an alternating compression and expansion of the carrier gas (see Figure 4.2). Due to inertia effects, particles follow the gas streamlines dependent on the local stream acceleration. This behavior is characterized by the particle Stokes Number S_p.

Eq. 4.21 $$S_p = \frac{\tau_p\, v_g}{d_f}$$

The particle Stokes Number is the ratio of the distance over which the particle velocity differs from the gas stream to a specific length of the device geometry, which is the orifice diameter d_f in this application. The distance over which the particle velocity differs from the gas stream is given by the particle relaxation time τ_p and the stream velocity of the gas v_g in the exit plane of the orifice. S_p depends on particle properties as size d_p and material density ρ_p, and on thermodynamic conditions in the vicinity of the aerodynamic lens. In order to quantify the particle Stokes Number in terms of directly measureable variables, Liu et al. [1996] showed an alternative derivation. The Einstein–Smoluchowski relation links the diffusion constant of a particle in a gas D_p and the mobility of the particle μ_p: $D_p = \mu_p\, k_B\, T$. At the limit of low Reynolds Number, the mobility of the particle is the inverse of the particle drag force coefficient given by Stokes' law for spherical particles. Thus the Einstein–Smoluchowski relation becomes

Eq. 4.22 $$D_p = \frac{k_B\, T\, C}{3\,\pi\,\eta\, d_p} = \frac{k_B\, T}{f_p}$$

The friction coefficient f_p can be calculated for the free molecular regime by the gas kinetic theory [Epstein, 1924] using a empirical coefficient $\alpha \approx 0.9$ and the mass of the gas m_g.

Eq. 4.23 $$f_p = \frac{3\,\pi\,\eta\,d_p}{C} = \frac{2}{3}\,d_p^2\,\rho_g\sqrt{\frac{2\pi\,k_B\,T}{m_g}}\left(1+\frac{\pi\,\alpha}{8}\right)$$

Substituting Eq. 4.13, Eq. 4.14, Eq. 4.20, Eq. 4.23 and the velocity of sound $c = \sqrt{\kappa\,k_B\,T/m_g}$ into Eq. 4.21 one obtains an expression for the particle Stokes Number.

Eq. 4.24 $$S_p = \kappa\frac{m_p}{m_g}\frac{D_p}{\eta}\frac{\mathrm{Ma}^2}{\mathrm{Re}_g}$$

Where $\kappa = c_p/c_v$ is the ratio of heat capacities (adiabatic exponent). In the free molecular regime the ratio of transport coefficients D_p/η is independent of thermodynamic conditions. In this case it can be substituted by the particle aerodynamic diameter d_p. In order to substitute $\mathrm{Ma}^2/\mathrm{Re}_g$ by quantities which can be experimentally determined, the stream velocity of the gas v_g in the exit plane of the orifice is written as a mass flow rate through the geometric area of the orifice.

Eq. 4.25 $$\dot{m} = \frac{\pi}{4}\rho_g\,v_g\,\mathrm{d_f^2}$$

If the ideal gas equation for an incompressible flow at a negligible pressure drop is assumed to be valid, the gas density can be expressed as $\rho_g = \kappa\,p/c^2$. Obviously the Mach and the Reynolds Number can be written analogously.

Eq. 4.26 $$\mathrm{Re}_g = \frac{4\,\dot{m}}{\pi\,\eta\,d_f} \qquad \mathrm{Ma} = \frac{4\,\dot{m}\,c}{\kappa\,\pi\,d_f p}$$

Substituting Eq. 4.23 and Eq. 4.26 in Eq. 4.24, an expression for S_p fully written in quantities which are experimentally accessible can be obtained.

Eq. 4.27 $$S_p = \frac{1}{(1+\pi\,\alpha/8)\sqrt{2\pi\,\kappa^3}}\frac{\dot{m}\,\rho_p\,d_p\,c^3}{p^2\,d_f^3}$$

Various researchers have proposed corrections to this model when particles are a few nanometers in diameter [Tammet, 1995; Loscertales, 2000; de la Mora et al.,

2003; Li and Wang, 2003a; Li and Wang, 2003b]. Considering these corrections, the Stokes Number of a neutral particle can be expressed as

Eq. 4.28 $$S_p = \frac{1}{\left(1+\frac{\pi\,\alpha(dp)}{8}\right)\sqrt{2\pi\,\kappa^3}} \frac{\dot{m}\,\rho_p\,d_p\,c^3}{p^2\,d_f^3} \left(\frac{d_p}{d_p+d_g}\right)^2 \sqrt{1+\frac{m_g}{m_p}}$$

There are three differences between Eq. 4.27 and Eq. 4.28. First α is a function of particle diameter $\alpha(d_p)$ instead of being a constant. Its value changes from 0 for elastic collision (gas/molecule) to ~0.9 for inelastic collision (gas/particle). Second, the term $\left(d_p/(d_p+d_g)\right)^2$ is a correction that accounts for the difference between particle mobility diameter and mass diameter, where $d = d_g + 2h$ and d_g is the gas molecule diameter inferred from gas viscosity, and $2h$ is an "extra distance" estimated to be $0.23\,nm$ [Tammet, 1995]. Finally, the term $\left(1+(m_g/m_p)\right)^{1/2}$ is a correction for the reduced mass of gas molecule and particle. For reasons that will be explained below, I neglect the three corrections mentioned above following the argumentation of Wang et al. [2005a].

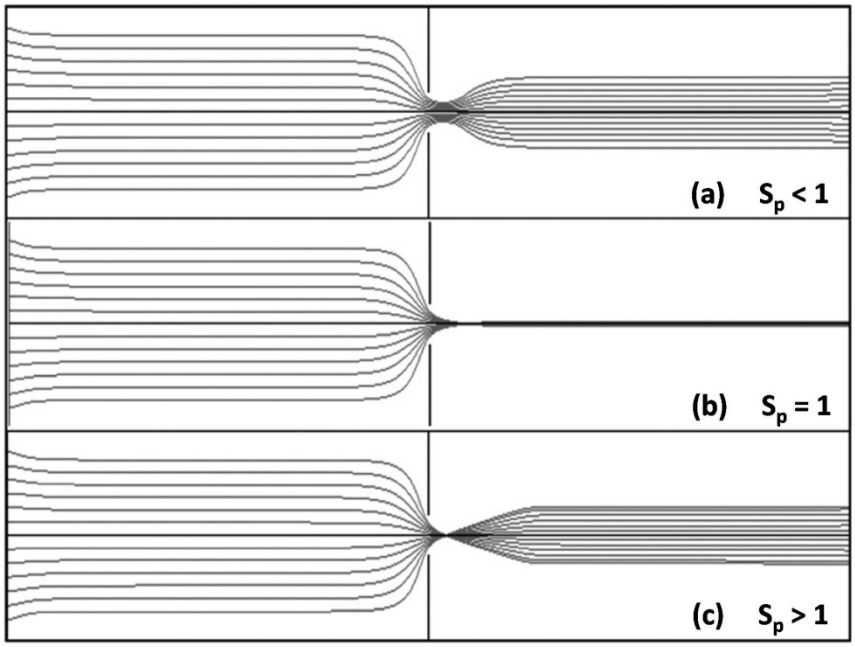

Figure 4.5. Particle focusing of a single lens as calculated by computational fluid dynamic simulations. (a) $S_p < 1$, insufficient focusing, (b) $S_p = 1$, optimal focusing, (c) $S_p > 1$, overfocusing.

The focusing performance of an aerodynamic lens, governed by the particle Stokes Number S_p, is demonstrated in Figure 4.5. For $S_p = 1$ a particle will be focused at the centre line of the lens, independent on its initial off-axis radial distance (b). For $S_p > 1$ particles will pass the centre line and diverge (c) and for $S_p < 1$ the particles will follow the streamlines of the gas (a). For $S_p \gg 1$ the aerodynamic lens act as a size dependent particle filter since the particles will be deposited on its inner surface. Note that for a given flow the Stokes Number depends only on properties of the carrier gas. Typically, lighter carrier gases (smaller m_g) allow focusing of smaller particles. Minimum focusing sizes d_{p1} of particles with a density of $1\ g/cm^3$ in several carrier gases are given in Table 1. If the three corrections of Eq. 4.28 are included, the minimal particle size d_{p2} differs not significantly from d_{p1}. Furthermore, the empirical relations of $\alpha(d_p)$ and d in Eq. 4.28 are fitted from limited experimental data in air, only [Tammet, 1995]. These values might not be valid for other carrier gases. For this reason Eq. 4.27 is used in the following.

For very small particles, optimal Stokes Number cannot be achieved even in light carrier gases. For a fixed geometry and given carrier gas, the mass flow of the gas has to be increased for decreasing particle diameter. This is limited by the maximum pressure drop through one orifice since subsonic flow has to be assured. For very small particles sub-optimal Stokes Numbers have to be accepted. Since the focusing effect of a single orifice with sub-optimal Stokes Number is insufficient, a set of sub-optimal orifices can be used to gradually focus the particle beam until the designated beam diameter is achieved.

Gas	$\boldsymbol{M}$ $(\boldsymbol{g/mol})$	$\boldsymbol{\kappa}$	$\boldsymbol{d_{p1}}$ $(\boldsymbol{nm})$	$\boldsymbol{d_2}$ $(\boldsymbol{nm})$
H_2	2.016	1.4	1.6	2.2
He	4.003	1.63	4.5	5.2
Air	28.966	1.4	12.4	13.2
Ar	39.948	1.668	15.9	16.7
CO_2	44.010	1.310	12.9	13.9

Table 1. Gas properties and minimum focusing particle diameter for five different carrier gases at $296.15\ K$. (reproduced from Wang et al. [2005a]).

The orifice diameter d_f required to focus particles of diameter d_p can be determined by rearranging Eq. 4.27.

Eq. 4.29 $$d_f = \sqrt[3]{\frac{1}{(1+\pi\,\alpha/8)\sqrt{2\pi\,\kappa^3}}\frac{\dot{m}\,\rho_p\,d_p\,c^3}{p^2\,S_p}}$$

This equation is very sensitive to the upstream pressure p in the aerodynamic lens design. Therefore the pressure drop across the orifice needs to be estimated accurately when designing a system with multiple lenses. Since ADLs usually operate at low Reynolds Numbers, viscous effects have to be included in the flow model. Eq. 4.10 accounts for viscous flow and can be used to compute the mass flow through an orifice. When designing a system of multiple lenses with given mass flow and pressure upstream from the first orifice, Eq. 4.29 has to be used to calculate the lens diameter first. Then Eq. 4.10 is used iteratively to calculate the pressure drop across the lens. A software package is available to design aerodynamic lenses by iteratively solving these equations. This procedure will be described in section 4.4.

Non spherical nanoparticles cannot be described by simply Stokes drag force. Caused by their complex surface morphology, their behavior in a gas stream cannot be computed exactly. The dynamic form factor χ relates the drag force of a non spherical particle to a spherical particle. Based on Stokes law the dynamic form factor is $\chi = F_D/(3\pi\,\eta\,v\Delta\,d_e)$. d_e is the particle diameter of a sphere with equivalent volume to the non spherical particle volume. This diameter can be obtained experimentally by investigating the settling velocity of a particle in a gaseous atmosphere. At constant settling velocity there must be an equilibrium of gravitational and drag force and thus

Eq. 4.30 $$3\pi\,\eta\,v\Delta\,d_e = \frac{\pi}{6}\left(\rho_p - \rho_g\right)d_e^3\,g$$

Assuming $\rho_p \gg \rho_g$ and substituting χ in Eq. 4.30, the settling velocity is

Eq. 4.31 $$\Delta v = \frac{\rho_p\,d_e^3\,g}{18\,\eta\,\chi} = \frac{\rho_0\,d_A^3\,g}{18\,\eta} = \frac{\rho_p\,d_S^3\,g}{18\,\eta}$$

In aerosol science, different forms of the settling velocity are used. By using unit desity ($\rho_0 = 1000\ \mathrm{kg/m^3}$) in Eq. 4.31, the relation yields the aerodynamic diameter

d_A. Another diameter typically used is the Stokes diameter d_S. Using the different versions of Eq. 4.31 the aerodynamic diameter can be written as

Eq. 4.32 $$d_A = d_e \sqrt{\frac{\rho_e}{\rho_0 \chi}}$$

The aerodynamic diameter d_A is a useful measure if the characteristics of particles made of different materials have to be compared. d_A is defined as the diameter of a sphere with unit density ($\rho_0 = 1000\ \mathrm{kg/m^3}$) which has the same features as the non spherical particle with unknown density.

4.3.3 Other forces acting on a particle in a laminar gas flow

Additionally to the drag force, there are two more forces acting on a particle moving in a gas stream: A force facilitating diffusion caused by Brownian motion and a lift force acting on non-spherical particles.

According to Liu et al. [1995a] the minimal divergence of a nanoparticle beam exiting an ADL is determined by the Brownian motion, which adds a radial velocity component to the particle beam exiting the nozzle. Assumed that upstream from the nozzle particles are in perfect thermal equilibrium with the surrounding gas, the velocity distribution of the particle thermal agitation can be described by the Maxwell-Boltzmann distribution. During the nozzle expansion, rapid decrease of gas pressure and temperature results in a rapid decrease in the gas-particle thermal collision rate, which will cause the particle thermal random movement to reach the frozen state very quickly. It can be assumed that during this rapid freezing process the shape of the velocity distribution function does not deform significantly, so that the frozen radial velocity v_{pr} can still be approximated by the Maxwell-Boltzmann distribution.

Eq. 4.33 $$f(v_{pr})dv_{pr} = \frac{m_p}{2\pi\, k_B\, T_{pF}} Exp\left[-\frac{m_p\, {v_{pr}}^2}{2\, k_B\, T_{pF}}\right] 2\pi\, v_{pr}\, dv_{pr}$$

The mass of the particle is m_p, k_B is Boltzmann's constant and T_{pF} is the particle frozen temperature. The particles are assumed to initially moving along the axis during the nozzle expansion. Since the particles are in thermal equilibrium while moving into the nozzle, they have reached their terminal thermal velocity at the end of

the nozzle. Obviously, it can be assumed that they also reached the Brownian motion frozen state at that point. Since the point of interest is the particle beam shape at distances much longer as the nozzle diameter, the particle beam spread due to Brownian diffusion before reaching the frozen state is neglected. Therefore, after travelling a distance L in the vacuum chamber the particle radial position r is approximately

Eq. 4.34 $$r = \frac{v_{pr}}{U_{p\infty}} L,$$

where $U_{p\infty}$ is the particle mean speed in the vacuum. Certainly there must be a frozen axial velocity, too. But this velocity is assumed to be significantly smaller than $U_{p\infty}$ and thus is neglected in the following. From Eq. 4.33 and Eq. 4.34 the radial distribution of the particle beam can be obtained.

Eq. 4.35 $$f(r)dr = \frac{1}{\pi\, {a_B}^2} Exp\left[-\frac{r^2}{{a_B}^2}\right] 2\pi\, r\, dr,$$

where

Eq. 4.36 $${a_B}^2 = \sqrt{\frac{2\, k_B\, T_{pF}}{m_p}} \frac{L}{U_{p\infty}}.$$

The beam width is defined as the area in which 90% of the total particle number flux is enclosed. From this definition a beam diameter caused by Brownian broadening $d_{B\,Brown}$ can be defined

Eq. 4.37 $$\int_0^{\frac{d_{B\,Brown}}{2}} f(r)dr = 90\%$$

Substituting Eq. 4.36 one obtains

Eq. 4.38 $$1 - Exp\left[-\frac{{d_{B\,Brown}}^2}{4\, {a_B}^2}\right] = 0.9$$

Eq. 4.39 $$d_{B\,Brown} = 3.04\, a_B$$

Using Eq. 4.39 the Brownian limit of a particle beam can be evaluated at every location L if the particle frozen temperature T_{pF} is known. Since the freezing process occurs rapidly, a temperature close to the upstream gas temperature T_0 can be

assumed. The work of different groups suggests that this is a reasonable assumption [Liu et al., 1995a; Liu et al., 2007; Zhang et al., 2004].

Eq. 4.40 $$d_{B\,Brown}(L) = 3.04\sqrt{\frac{12\,k_B\,T_0}{\pi\,{d_p}^3\,\rho_p}}\frac{L}{U_{p\infty}}$$

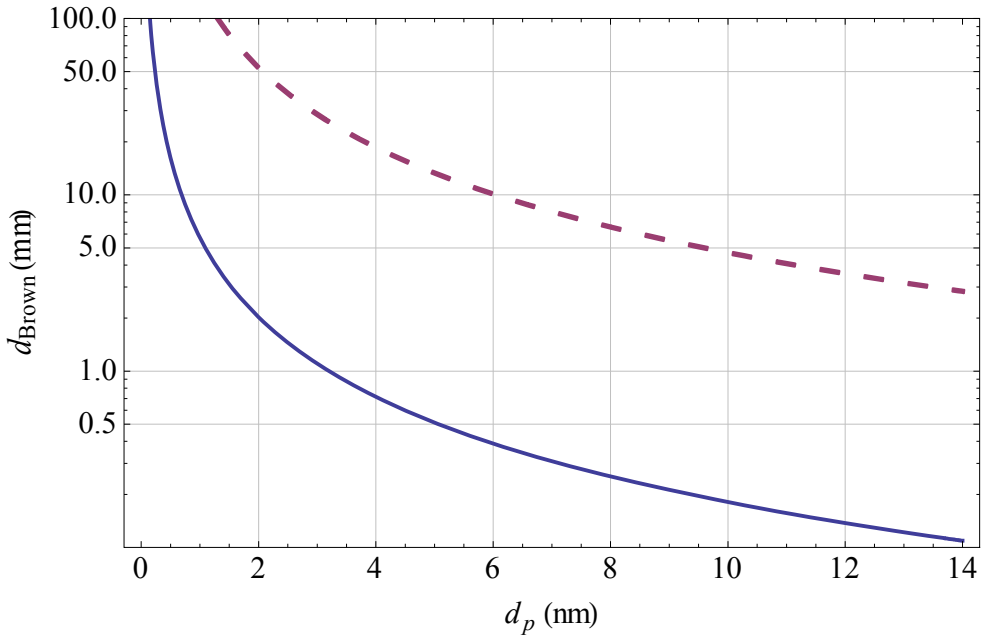

Figure 4.6. Brownian limit of particle beam diameter calculated for 6 nm SiO_2 particles with typical gas flow parameters of the TRAPS-ADL using Eq. 4.40. The drawn blue line corresponds to the location of the skimmer 15 mm downstream from the acceleration nozzle. The dashed red line corresponds to the entrance plane of the faraday cup 390 mm downstream from the acceleration nozzle.

Using typical thermodynamic values of the aerodynamic lens, installed as particle inlet for the TRAPS device (6 nm SiO_2 particles, 860 Pa ADL inlet pressure), the particle beam diameter caused by Brownian motion at the location of the skimmer entrance plane $L = 15\,mm$ is $d_{B,Brown} = 0.4\,mm$ (Figure 4.6). Neglecting any influences by the skimmer and the flow field inside the octopole ion-guide, the particle beam diameter caused by Brownian motion at the location of the entrance plane of the faraday cup $L = 390$ mm is $d_{B,Brown} = 10\,mm$. This estimation of the beam diameter inside the high vacuum region of the device shows that the beam can be focused tightly enough to fulfill the demands of the TRAPS device, since the orifice diameters are $d_f = 3\,mm$ and $d_f = 17\,mm$ for the skimmer and the faraday cup, respectively.

As in the case of Brownian broadening, lift forces on non-spherical particles during nozzle acceleration will produce a particle beam with a nonzero divergence angle even if particles are confined exactly on the axis upstream from the nozzle. In Liu et al. [1995a] a derivation of the lower limit of particle beam width set by this effect is given for some basic geometry. The drag force F_D and the lift force F_L are defined as the components of total force parallel and perpendicular of the direction of the gas flow U_{pg}, respectively. Orientation of the particle relative to the direction of motion is an important parameter that determines these forces. For cylinders of the length L_{cl} and the radius R_{cl} Liu et al. give the expression

Eq. 4.41 $$F_{L\,cl} = -\frac{\pi\,\eta\,R_{cl}^2\,U_{pg}}{\lambda}\left(4-\frac{6-\pi}{2}f\right)\left(1-\frac{L_{cl}^2}{2\,R_{cl}^2}\right)\sin\theta\,\cos\theta,$$

Where again η is the dynamic viscosity, λ is the gas mean free path U_{pg} is the particle velocity relative to the surrounding gas, f is the momentum accommodation coefficient. For a disc of radius R_{ds} and negligible thickness, the drag force is given as

Eq. 4.42 $$F_{L\,ds} = -\frac{\pi\,\eta\,R_{ds}^2\,U_{pg}}{\lambda}\left(4-\frac{6-\pi}{2}f\right)\sin\theta\,\cos\theta$$

The drag force of a spheroid with half length a and radius b is a very complex expression. For the case $a \approx b$, which is a slightly deformed sphere, δ is a factor describing the deviation from a sphere $\delta = (b-a)/a$. Under the condition $\delta \ll 1$, the drag force of a spheroid is just the drag force of a sphere. Thus the lift force can be written as

Eq. 4.43 $$F_{L\,sp} = -\frac{\pi\,\eta\,\mathrm{a}^2\,U_{pg}}{\lambda}\frac{2}{15}[11+(4\pi-3)f]\,\delta\sin\theta\,\cos\theta$$

Finally cuboid particles with sides s_1, s_2 and s_3 the lift force is in the special case $s_3 = s_2 = s$ and $s_1 = s + \Delta s$

Eq. 4.44 $$F_{L\,cb} = -\frac{\eta\,\mathrm{s}^2\,U_{pg}}{\lambda}\left(\frac{\Delta s}{s}\right)\left(4-\frac{6-\pi}{2}f\right)\sin\theta\,\cos\theta$$

G is a factor depending on shape and orientation of the particle only giving a relationship between the drag force F_D and the lift force F_L: $F_L = G\,F_D$. If the axial

force on a particle is primarily drag and the radial force is primarily lift, then the final axial velocity $U_{p\infty}$ and the radial velocity $V_{p\infty}$ can be expressed as

Eq. 4.45 $$U_{p\infty} = \int_0^\infty \frac{F_D}{m_p} dt \quad \text{and} \quad V_{p\infty} = \int_0^\infty \frac{F_L}{m_p} dt = \int_0^\infty \frac{G\, F_D}{m_p} dt$$

The factor G can be assumed as constant and can be taken out of the integral, if the particle does not change orientation during acceleration. Obviously, this assumption is questionable, but it simplifies the problem greatly since then the tangent of the divergence angle is simply G. Since G varies as the particle orientation changes, the particle beam diameter $d_{B\,lift}$ at the downstream distance L is determined by the maximum value G_{max} which can be derived by Eq. 4.41 to Eq. 4.44.

Eq. 4.46 $$d_{B\,lift} = 2\, G_{max}\, L$$

For example G_{max} for a cuboid particle with two equal sides is $G_{max} = 0.251\,\delta$ and thus $d_{B\,lift} = 0.501\,\delta\, L$ with $\delta = \Delta s/s \ll 1$. Similarly, for a slightly deformed sphere, it is $G_{max} = 0.362\,\delta$ and $d_{B\,lift} = 0.724\,\delta\, L$.

It is interesting to compare the particle beam width limited by Brownian motion and lift force. Taking the particle frozen temperature T_{pF} and the axial velocity $U_{p\infty}$ from the CFD simulations one can obtain from Eq. 4.36 and Eq. 4.39

Eq. 4.47 $$d_{B\,Brown} \sim \sqrt{\frac{m}{m_p}} L\ ,$$

where m is the gas molecular mass. For particles larger than $10\,nm$ in diameter, $d_{B\,Brown}$ is less than a few percent of L. For the lift force the limit is of the order

Eq. 4.48 $$d_{B\,lift} \sim \delta\, L\ ,$$

where δ is the factor describing the derivation of the particle shape from a sphere or a cube. For highly irregular particles the lift force can exceed a few percent and thus is a far more severe problem especially for bigger particles. In this work particles are assumed to be perfect spheres since the particles produced by the MPPS were found to be mostly spherical [Szabo and Vollath, 1999; Baumann et al., 2006].

4.4 Designing aerodynamic lenses without CFD simulations

In 2006, Wang and McMurry provided the Aerodynamic Lens Calculator (referred to as ALC herein [Wang and McMurry, 2006]) a valuable design tool programmed in Excel, that enables to design an ADL for any particle diameter range and vacuum system without extended knowledge of aerodynamic simulations. It uses the relations explained in section 4.3 and additional parameterizations from numerical simulations of flow and particle transport through aerodynamic lenses. As shown previously, particle focusing by means of an aerodynamic lens made of a thin plate orifice, is mainly determined by the Stokes Number S_p. The basic concept is to describe the particle terminal axial velocity in the vacuum chamber downstream from the nozzle as a function of the Stokes Number. This allows making an estimate of the particle beam width at arbitrary location. Both, aerodynamic focusing and diffusion broadening are taken into account in this tool by using parameterizations. Particle loss is considered by inertia impaction on the orifice plates, impaction on the spacer walls due to defocusing and losses due to diffusion.

A flow chart for designing aerodynamic lenses is shown in Figure 4.7. First, define the particle density and size range, the carrier gas and the mass flow rate. Second, calculate the operating pressure and dimensions of the lens system for smallest particle size range. In some cases, a value for the maximum operating pressure does not exist since the flow through a lens needs to be subsonic and laminar. Then a lighter carrier gas or multiple lenses operating a sub-optimal Stokes Numbers should be used. Finally, the program estimates the three major performance parameters: size dependent particle terminal axial velocity, beam width, and transmission efficiency.

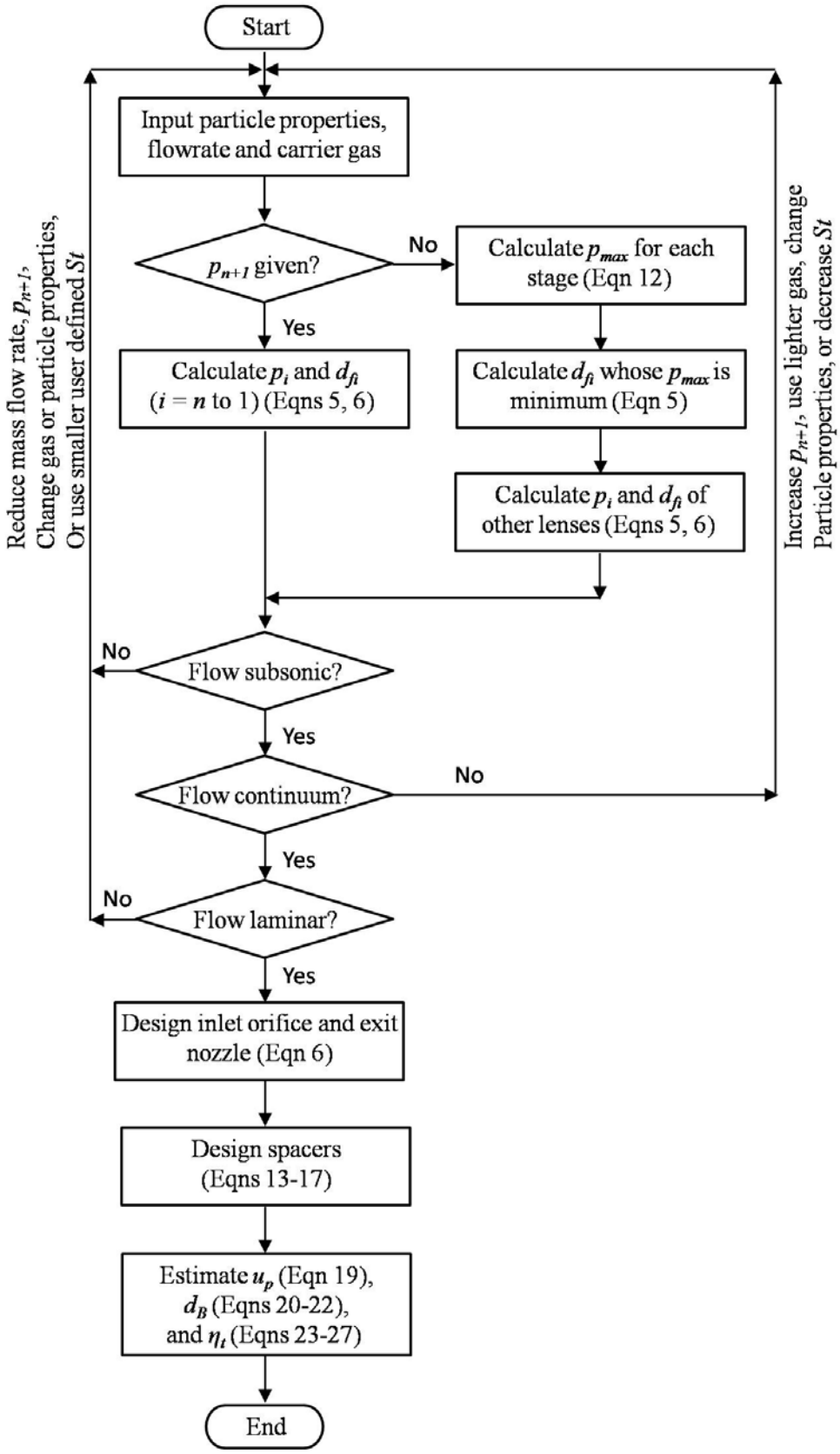

Figure 4.7. Flow chart for the aerodynamic lens design module (reproduced from Wang and McMurry [2006]; equation numbers refer to original paper).

Even though the aerodynamic lens calculator described above is a great design tool that enables to give an optimal design for most purposes, in the low particle mass region it gives much different predictions in comparison to the experiment. This is due to the assumptions and approximations the tool is based on Lee et al. [2008]. One of the most critical points is the lack of knowledge of a functional relationship between the optimal Stokes Number and other parameters. This relationship is usually represented by the overall contraction ratio η_c of the particle beam and the transmission efficiency η_t of particles. In the lens calculator η_c and η_t are characterized as a total of five dimensionless parameters. Too many design parameters must be independently changed in order to find out an optimal Stokes Number for a set of orifices. Thus it is impossible to determine the optimal orifice diameters in a multi-lens system. Consequently assumptions, like constant Mach and Reynolds Numbers at different orifice diameters, are made by the lens calculator. By rearrangement of the equations described in section 4.3.2, Lee et al. [2008] provided a functional relationship to interrelate the Reynolds Number, the Mach number and the upstream pressure in lens geometries. η_c and η_t now can be written as a function of three parameters. But still, they are interrelated and affected by the lens geometry and thermodynamic parameters of the gas flow. Thus they cannot be treated independent at the different orifices as done before by the lens calculator. For instance, the upstream pressure of an orifice should be matched with the downstream pressure of the preceding orifice. This is why full numerical calculation should be made for the entire ADL system so as to predict correct values of the parameters.

4.5 CFD simulations on aerodynamic lenses with ANSYS CFX

Focusing of small nanoparticles is achievable by combining multiple orifices with sub-optimal Stokes Number. As described above, the optimal lens design is given by a large number of parameters which have to be optimized. For the work presented here, we have chosen to use the ALC to obtain a starting point for a lens design calculation which then was optimized by Computational Fluid Dynamic (CFD) simulations. In the case of small nanoparticles, it is advisable to include the whole inlet system into the simulation as demonstrated by Liu et al. [2007] for the first time.

ANSYS CFX (ANSYS Workbench™ 11.0, ANSYS Europe Ltd.) is a commercial computational fluid dynamics package similar to ANSYS FLUENT (ANSYS Europe Ltd.). Both packages are based on the numerical solution of the Navier-Stokes equations discretized on a user defined mesh. CFX is capable to calculate gas flow in the continuum regime of fluid dynamics as long as the Knudsen Number is near or smaller than one. At a typical pressure of helium in an ADL of $100\ Pa$, the mean free path length is $\lambda \sim 250\ \mu m$. A characteristic length of the lens is given by the orifice diameter of $d_o > 1\ mm$. Thus the Knudsen Number for the gas flow inside the ADL is smaller than one (cf. Eq. 4.16) and solving the Navier-Stokes equation without any correction is valid. With respect to the particles in the gas flow, the Knudsen Number is greater than one. In ANSYS CFX, the Cunningham-Correction [Allen and Raabe, 1985] can be applied for the particle drag force via a user supplied routine.

4.5.1 Computational Fluid Dynamics

CFD is a computer-based tool for the simulation of the behavior of systems involving fluid flow, heat transfer, and other related physical processes. It works by solving the equations of fluid flow over a region of interest with specific conditions on the boundary of that region. The set of equations describing the processes of momentum, heat and mass transfer for fluid flows are known as the Navier-Stokes equations. These partial differential equations have no known general analytical solution but they can be discretized and solved numerically. Other processes, such as turbulence, can also be solved in conjunction with the Navier-Stokes equations if an approximating model is used to derive these additional equations.

The numerical approach used in ANSYS CFX is the finite volume technique. In this technique, the region of interest is divided into small sub-regions, called control volumes. The Navier-Stokes equations are discretized and solved iteratively for each control volume. As a result, an approximation of the value of each variable at specific points throughout the domain can be obtained. In this way, one derives a full picture of the behavior of the flow.

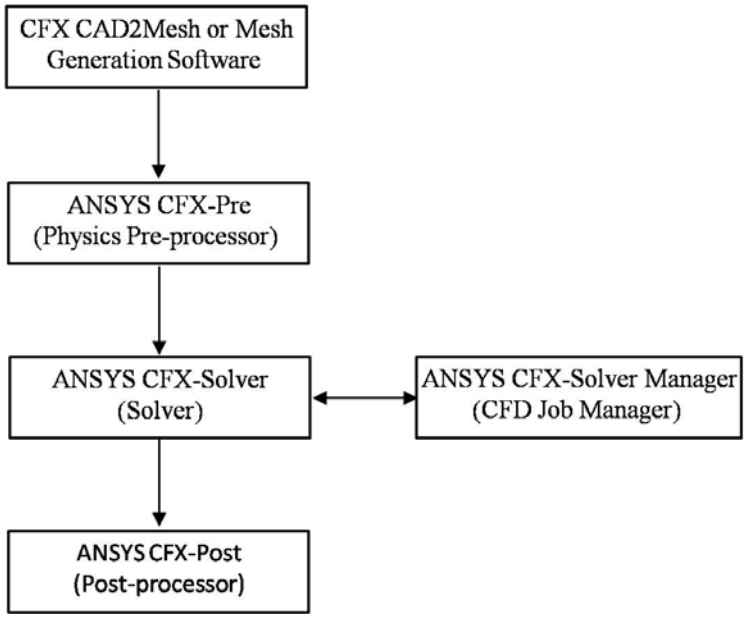

Figure 4.8. Schematic diagram of the work flow with ANSYS-CFX (adapted from ANSYS [2005]).

ANSYS CFX consists of five software modules which are linked by the flow of information required to perform a CFD analysis (Figure 4.8). After identification of the region of interest for the problem to be analyzed, geometry for mesh generation has to be generated. If the geometry already exists in CAD format, it can be imported directly. The mesh is then created in the mesh generation software. Flow physics, boundary conditions, initial values and solver parameters are specified in the pre-processor. User defined functions can also be used to define extra boundary conditions of additional physics on the flow. The CFX-solver optimizes all the solution variables for the simulation of the problem specification generated in the pre-processor. While the CFX-solver computes the solutions of the task at given time-steps, the quality of the solution achieved can be monitored by the solver-manager. The CFX-solver manager can also be used to set up the CFX-solver for parallel

computing. The post-processor graphic tool can be used to analyze and present the simulation results.

4.5.2 Creating a high quality CFD mesh

Creating a well defined, high quality mesh is of fundamental importance in order to achieve a realistic flow from the simulation. Mesh size and finite volume shape have to be adapted to the expected flow characteristics. In principle it is favorable to minimize the size of the finite volumes used for the discretization. Obviously, this approach is limited by the computing power. Each node of a tetrahedral mesh requires approximately $2\ kB$ of working memory (RAM). This limits the maximum size of a mesh to approximately one million nodes on a $32\ bit$ Windows machine providing a maximum of $4\ GB$ of working memory (usually the operating system requires some working memory, too). If a hexahedral mesh can be used, the number of maximum node is doubled. In practice the number of nodes is reduced by adapting the size of the finite volumes to the flow characteristics. The size of a finite volume has to resolve the physics of the flow. For example, if an eddy should be reproduced by the simulation the curls have to be resolved by a high number of finite volumes. If the details of an eddy are not of interest, the thermodynamic properties of the eddy can be parameterized. In this case the finite volume might have the size of the whole curl.

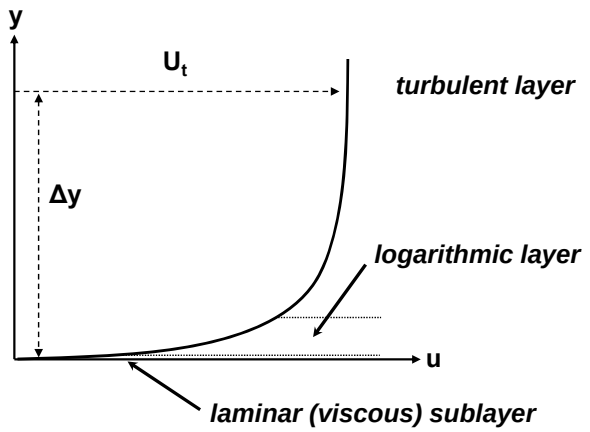

Figure 4.9. Near boundary layers of a fluid flow (adapted from ANSYS [2006]).

In the case of simulating an aerodynamic lens, the flow velocity varies over two orders of magnitudes in the series of contractions and expansions. Since the exact velocity profile in the area of the orifices is crucial for the drag force acting on the particles, a high quality result for the flow field has to be obtained from the

simulation. The velocity profile depends on the shear stress in-between the infinitesimal fluid layers, and the fluid layer with the wall. Near a no-slip wall, there are strong gradients in the dependent variables (Figure 4.9). In addition, viscous effects on the transport processes are large. The near-wall region can be subdivided into two layers. In the viscous sub-layer the flow is almost laminar-like. The viscosity plays a dominant role in momentum and heat transfer in this layer. Further away from the wall turbulence can dominate the mixing process. Finally there is a region between the viscous sublayer and the turbulent layer (if existing), where the effects of molecular viscosity and turbulence are of equal importance. Assuming that the logarithmic profile reasonably approximates the velocity distribution near the wall, it provides an approach to numerically compute the fluid shear stress as a function of the velocity at a given distance from the wall. This means, that in this approximation the wall conditions are connected to the dependent variables at the near-wall mesh node which is presumed to lie in the fully turbulent region of the boundary layer. The logarithmic relation for the near-wall velocity is given by [ANSYS, 2006]:

Eq. 4.49 $$u^+ = \frac{U_t}{u_\tau} = \frac{1}{\kappa}\ln[y^+] + C$$

where:

Eq. 4.50 $$y^+ = \frac{\rho\,\Delta y\,u_\tau}{\eta}$$

Eq. 4.51 $$u_\tau = \sqrt{\frac{\tau_\omega}{\rho}}$$

u^+ is the near-wall velocity, u_τ is the friction velocity, U_t is the known velocity tangent to the wall at a distance of Δy from the wall, y^+ is the dimensionless distance from the wall, τ_ω is the wall shear stress, κ is the Karman constant, ρ is the fluid density, η is the dynamic viscosity and C is a log-layer constant depending on wall roughness. The y^+ value is a measure for the near-wall mesh spacing. It has to be estimated prior mesh generation based on the flow characteristics expected in this region. This is why it is very useful to have an idea of a lens design and associated flow characteristics from the ALC prior starting CFD optimization. A typical result from the mesh optimization in the region of the nozzle is shown in Figure 4.10.

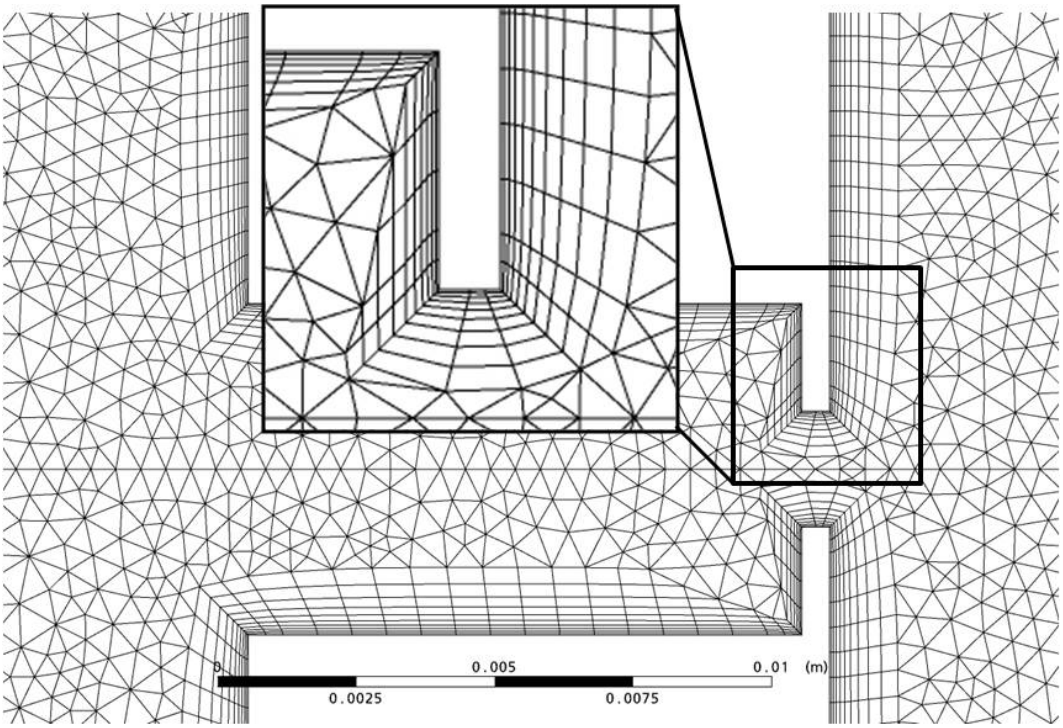

Figure 4.10. Typical mesh used for CFD calculations. The cutout depicts the region of the acceleration nozzle.

4.5.3 Governing equations for CFD calculations

The set of equations to be solved in a CFD calculation are the unsteady Navier-Stokes equations in their conservation form. The transport equations are the instantaneous equations of mass, momentum and energy conservation [ANSYS, 2006]. They can be written as follows:

The continuity equation

Eq. 4.52 $$\frac{\partial \rho}{\partial t} + \boldsymbol{\nabla} \odot (\rho \, \boldsymbol{U}) = 0$$

The momentum equation

Eq. 4.53 $$\frac{\partial \rho \, \boldsymbol{U}}{\partial t} + \boldsymbol{\nabla} \odot (\rho \, \boldsymbol{U} \otimes \boldsymbol{U}) = \boldsymbol{\nabla} \odot \left(-p \, \delta + \mu(\boldsymbol{\nabla} \, \boldsymbol{U} + (\boldsymbol{\nabla} \, \boldsymbol{U})^T)\right) + \boldsymbol{S}_M$$

The energy equation

Eq. 4.54 $$\frac{\partial \rho \, h_{tot}}{\partial t} - \frac{\partial p}{\partial t} + \boldsymbol{\nabla} \odot (\rho \, \boldsymbol{U} \, h_{tot}) = \boldsymbol{\nabla} \odot (\lambda \, \boldsymbol{\nabla} \, T) + \boldsymbol{\nabla} \odot \left(\mu \, \boldsymbol{\nabla} \, \boldsymbol{U} + \boldsymbol{\nabla} \, \boldsymbol{U}^T - \frac{2}{3} \boldsymbol{\nabla} \odot \boldsymbol{U} \, \delta \, \boldsymbol{U}\right) + \boldsymbol{S}_E$$

h_{tot} is defined as the specific total enthalpy, which is of variable properties for the case of compressible gas. $\boldsymbol{U}$ is the velocity vector of the gas, comprising the velocity components in x, y and z direction u, v and w, respectively. The set of seven unknowns (u, v, w, p, T, ρ, h) in the above equations can be closed by adding two algebraic thermodynamic equations: the equation of state, which relates density to pressure and temperature; and the constitutive equation, which relates enthalpy to temperature and pressure. These equations have to be replaced by algebraic approximations which can be solved by numerical methods. Thereby the governing equations are integrated over each finite control volume, so that the relevant quantity (mass, momentum, energy, etc.) is conserved for each control volume. The discretized forms of Eq. 4.52 to

Eq. 4.54 are:

Eq. 4.55 $$V\left(\frac{\rho-\rho^0}{\Delta t}\right)+\sum_{ip}\left(\rho\, U_j\, \Delta n_j\right)_{ip}=0$$

Eq. 4.56 $$V\left(\frac{\rho\, U_i-\rho^0\, U_i{}^0}{\Delta t}\right)+\sum_{ip}\dot{m}_{ip}(U_i)_{ip} = \sum_{ip}(P\, \Delta n_i)_{ip}+\sum_{ip}\left(\mu_{eff}\left(\frac{\partial U_i}{\partial x_j}+\frac{\partial U_j}{\partial x_i}\right)\Delta n_j\right)_{ip}+\overline{S_{U_i}}\, V$$

Eq. 4.57 $$V\left(\frac{\rho\,\phi-\rho^0\,\phi^0}{\Delta t}\right)+\sum_{ip}\dot{m}_{ip}\,\phi_{ip}=\sum_{ip}\left(\Gamma_{eff}\,\frac{\partial\phi}{\partial x_j}\,\Delta n_j\right)_{ip}+\overline{S_\phi}\, V$$

Where V is the control volume, Δn_j is the discrete outward surface vector, the subscript ip denotes evaluation at an integration point, and summations are over all the integration points of the control volume. The superscript 0 refers to the old time level. Δt is the (virtual) time step which has to be chosen from the time a characteristic length is traversed by the fluid with a characteristic flow velocity.

4.5.4 Computation of particle trajectories with CFD

For the numerical calculations, a dilute suspension of particles in an ideal gas is assumed. Particle-particle interactions are neglected, and it is assumed that the presence of the particles does not influence the gas flow. Under these conditions, the flow field can be calculated independent from the particle load. Particles are introduced into the flow field afterwards and their velocities and trajectories are calculated by simple time step integration.

The Lagrangian equation of particle motion in Cartesian coordinates as used by the CFX solver [ANSYS, 2006] is given as:

Eq. 4.58 $$\frac{\partial \boldsymbol{U}_p}{\partial t} = \boldsymbol{F}_D + \boldsymbol{F}_B + \boldsymbol{g}$$

$\boldsymbol{F}_D$ is the drag force per unit mass on a particle, $\boldsymbol{F}_B$ is the Brownian force per unit mass and $\boldsymbol{g}$ is the acceleration of gravity. This simple approach can be used only, when the flow is in the laminar regime and the particles are assumed to be spherical. The expression for the modified Stokes drag force per unit mass including the Cunningham correction is given by:

Eq. 4.59 $$\boldsymbol{F}_D = \frac{3\,\eta\, C_D\, \mathrm{Re}_p}{4\,\rho_p\, d_p^2\, C}\left(\boldsymbol{U} - \boldsymbol{U}_p\right)$$

Where $\boldsymbol{U}$ is the fluid velocity vector and C_D is the drag coefficient, which accounts for the Reynolds Number correction to the Stokes drag as given by [Hinds, 1999].

Eq. 4.60 $$C_D = \frac{24}{\mathrm{Re}_p}\left(1 + 0.15\ \mathrm{Re}_p{}^{0.687}\right)$$

Note, that this correction is significant for larger particles with appreciable slip velocity. For small particles with small slip velocity Re_p is very small and the second term in Eq. 4.60 is negligible. In region of the orifices the gas-particle slip velocity is large and thus the correction gains importance. For small particles in low pressure the Cunningham correction is significant. Substituting Eq. 4.16 in Eq. 4.18 gives the Cunningham correction as a function of mean free path length of the gas. There is a significant change in the gas mean free path length along the particle trajectories.

Therefore, the Cunningham correction factor must be calculated at each node of the mesh from the local gas flow parameters, the particle diameter and the mean free path of the gas using Eq. 4.15.

In ANSYS CFX particle trajectories are computed using the Schiller Naumann drag model by default. This model incorporates the Reynolds Number correction (Eq. 4.60) but it does not correct for the slip of small particles using the Cunningham correction. The user can replace the internal particle drag model by a FORTRAN 77 code. The code used for the present CFD simulations can be found in Appendix A. Figure 4.11 demonstrates the need of using the Cunningham correction on the particle drag force in an ADL simulation.

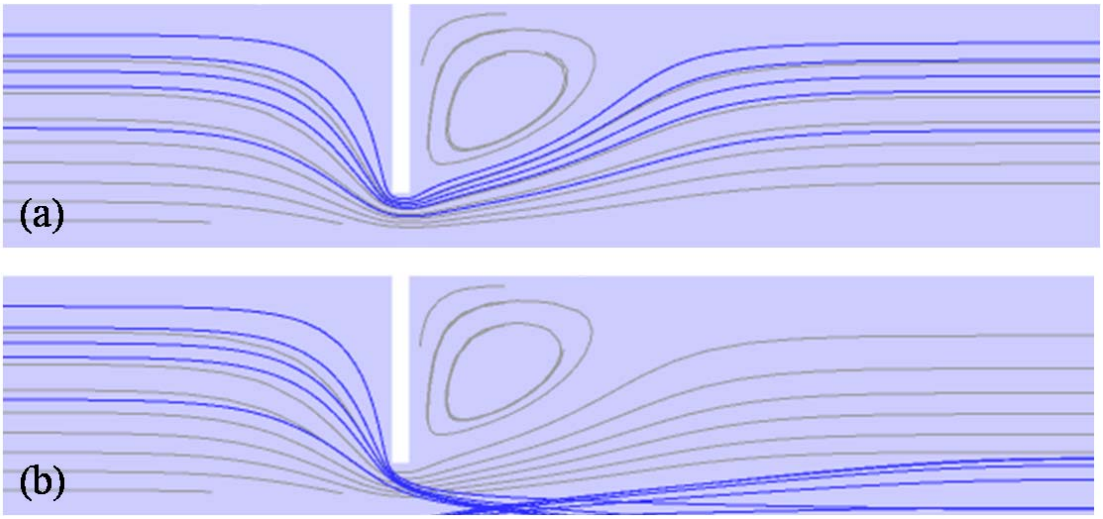

Figure 4.11. Trajectories of $5\,nm$ diameter silica particles (blue) in Helium (streamlines grey) calculated with CFX. (a) Particle drag force is calculated using the Schiller Naumann drag model. (b) Particle drag force is calculated using the user FORTRAN routine incorporating Cunningham correction.

A critical region of the setup is the mach zone downstream from the exit of the lens. CFX can simulate supersonic flows when compressible fluid models are used. However, the calculation of the particle drag force will fail in this region. To our knowledge, this problem remains unsolved independent from the CFD code used. A correction factor, comparable to subsonic flows with small Knudsen Numbers, is not available. Prior publications have followed the concept of Liu et al. [1995b] who argument that the expected particle trajectories are close to the axis after they have passed the ADL, and that inside the Mach zone (zone of silence) the pressure is as

low as $1 - 10^{-2}\ Pa$. They conclude that the radial particle momentum will not be significantly affected by the transit through the zone of silence and the Mach shock wave. This hypothesis might not be completely accurate. During transit of the mach shock disk the particles will be decelerated and heated by the compressed gas inside the shock disk. But since the particle trajectories close to the axis will be perpendicular to the shock disk, only the axial momentum of the particles will be changed. Since beam broadening is allocated to the radial momentum of the particles, Liu et al. came up with the argument that the radial momentum will not be significantly affected. This hypothesis has been validated experimentally by several groups [Liu et al., 1995b; Wang et al., 2005; Liu et al., 2007; Lee et al., 2008].

Brownian motion becomes important for small particles, as shown by Eq. 4.40. Brownian motion is caused by the imbalanced random impacts of the gas molecules that cause the particle to move on an erratic path. The particle diffusion coefficient D_p resulting from Brownian motion is given in Eq. 4.22. For a particle diameter of 5 nm, the average value $D_p = 5\ 10^{-5}\ m^2\ s^{-1}$, and the residence time in the acceleration nozzle is about $t = 4\ 10^{-5}\ s$. Thus, the RMS particle displacement due to Brownian motion is approximately $s = \sqrt{D_p\ t} = 45\ \mu m$. It can be estimated from Figure 4.14 that the particle beam diameter at the exit of the acceleration nozzle is about 55 μm. Beam width and particle displacement are in the same order of magnitude. Thus, the effect of Brownian motion can significantly affect the particle trajectories downstream from the ADL.

The Brownian force per unit mass is described through the fluctuation-dissipation theorem by a Gaussian distribution with mean and mean-square values given by:

Eq. 4.61 $$\langle \boldsymbol{F}_B(t) \rangle = 0$$

Eq. 4.62 $$\langle \boldsymbol{F}_B(t) \odot \boldsymbol{F}_B(t') \rangle = \frac{3\ k_B\ T\ f_p\ \delta(t'-t)}{m_p^2}$$

Where the angular brackets denote averages, and $\delta(t' - t)$ the Dirac delta function. The Dirac delta function has to be replaced by a numerical representation for a computer simulation. Then, the Brownian force per unit mass in direction i at each time step can be written as [Liu et al., 2007]:

Eq. 4.63 $$F_{Bi} = G_i \sqrt{\frac{\pi S_0}{\Delta t}}$$

Eq. 4.64 $$S_0 = \frac{216\,\nu\,k_B\,T}{\pi^2\,d_p^5\,C}\frac{\rho_g}{\rho_p^2}$$

Where G_i are zero-mean, unit-variance, independent Gaussian random numbers, Δt is the time step used in the simulation and ν is the kinematic viscosity. Note, that the time step in the simulation needs to be small enough such that the drag force is almost constant during Δt. From Figure 4.14 and Figure 4.15 it can be estimated, that this would require a time step of $\Delta t < 0.2\ \mu s$. The CFD calculations presented herein, a time step of $0.1\ s$ was sufficient in order to represent all significant features of the gas flow and particle trajectories. With this time step the solver converges in less than 50 iterations. Modeling Brownian diffusion would require time steps reduced by a factor of 500 000. This would approximately provoke the number of iterations to increase by a factor of 700 [ANSYS, 2005]. For the aim of this work, which is optimization of an aerodynamic lens for small nanoparticles, this costly approach is not required. Since it is not the scope of this work to perform fundamental research on aerodynamics of small nanoparticles, Brownian motion can be ignored in the CFD calculations. The additional broadening of the particle beam is subsequently estimated by Eq. 4.40.

4.5.5 Modeling turbulence

The design of an ADL should carefully avoid the occurrence of turbulence. An easy way to check the occurrence of turbulence is to compare a simulation result calculated with and without a turbulent flow model (k-ε-model of CFX) and comparing flow parameters like velocity, pressure and temperature. A high turbulent kinetic energy has to be introduced at the inlet boundary, since the flow downstream from a critical orifice is known to be highly turbulent. The ratio of eddy viscosity and dynamic viscosity is a measure for the turbulence. This value has to be small in comparison to the highly turbulent inlet all over the ADL. In our case, the flow was laminar in all simulations. No internal source of turbulence was found, even when a high turbulent kinetic energy was introduced at the inlet.

4.6 Simulation results

4.6.1 Validation of the simulation methodology

For validation of the simulation methodology, lens "C" of Wang et al. [2005b] with spherical particles of density $1000\ kg\ m^{-3}$ was modeled. Figure 4.12 shows the simulation result of the static pressure and axial flow of the gas and the axial particle velocity at the rotational axis of the lens in comparison to the data given in Figure 4.2 of Wang et al. [2005b]. Figure 4.13 shows the correlation of the simulation results from Wang et al. [2005b] and the CFD calculations presented here. The correlation is 0.999 for the pressure, 0.991 for the gas velocity and 1.004 for the velocity of $10\ nm$ diameter particles. The negligible deviation is mainly due to the inaccuracy in the reading from the Figure in Wang et al. [2005b]. This proves, that the CFD code and mesh generation used is suitable for ADL calculations.

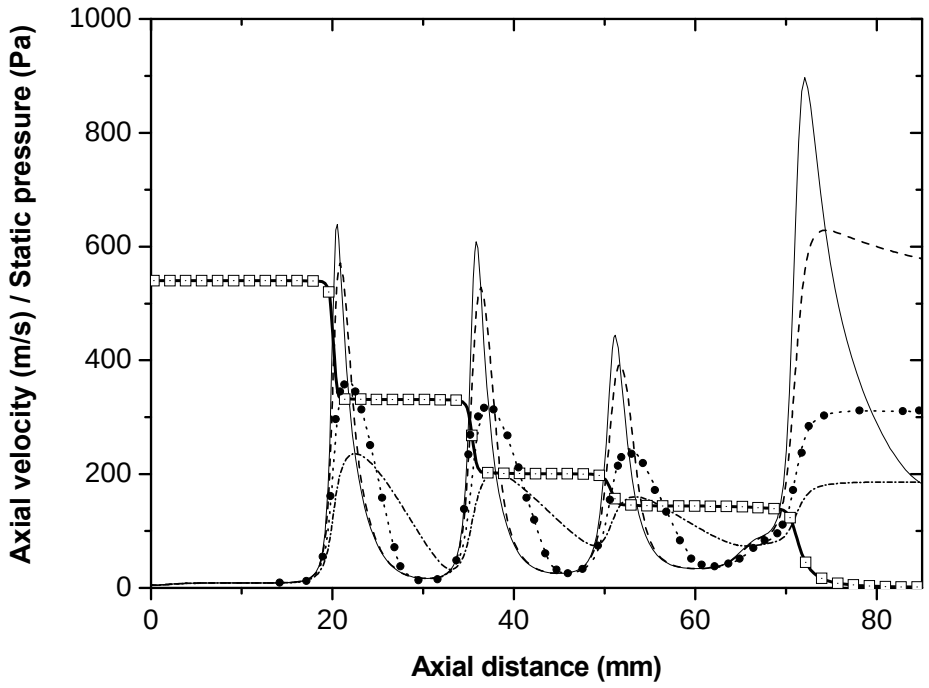

Figure 4.12. Static pressure (bold line), axial gas velocity (slim line) and particle axial velocity (particle diameter $1\ nm$: dashed, $10\ nm$: dotted, $40\ nm$: dot-dashed) along the axis of the nanoparticle lens system "C" from Wang et al. [2005b]. The simulation results from CFX are depicted as lines; results from Wang et al. are given as symbols. For the sake of clarity exemplary data from Wang et al. is shown only.

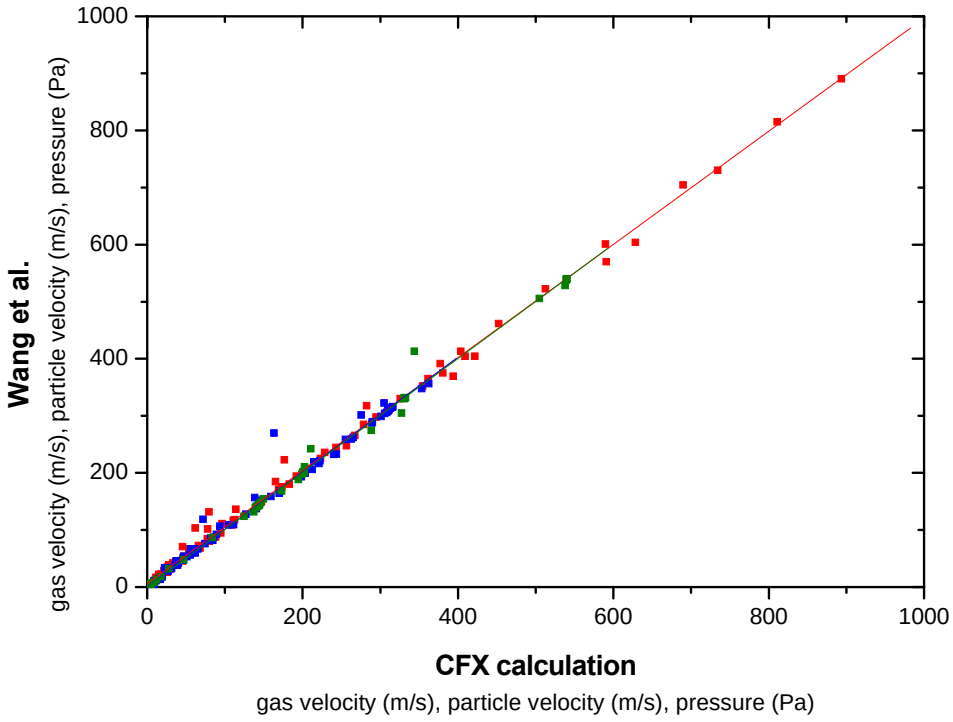

Figure 4.13. Correlation analysis of the simulation parameters gas velocity (red), particle velocity (blue) and gas pressure (green) achieved by Wang et al. [2005b] and the CFD calculations presented here.

4.6.2 Design of a new ADL by CFD calculations

The CFD simulations consider a laminar flow upon entering the first focusing orifice. As recommended by Liu et al. [2007], nozzle and skimmer were included in the calculation. Boundary conditions for the design of the ADL are particle diameter, shape and density, carrier gas, inlet pressure upstream from the critical orifice, outlet pressure downstream from the accelerating nozzle, maximum pumping capacity downstream from the ADL and target size and distance from the ADL outlet. These are far too many boundary conditions to optimize from an initial guess. Therefore the following strategy to design and improve a suitable lens was adopted. First, the ALC was used to make a guess for an appropriate lens design. Using the boundary conditions obtained from this calculation, a high quality mesh for CFD simulation was generated using CFX-Mesh. Than the geometry and the flow parameters given by the ALC are used for a simulation with ANSYS CFX. If the CFD simulation of the first guess revealed that the focusing performance was not sufficient, the inlet pressure of the lens was varied. Changing the inlet pressure affects the gas flow

through the orifices and thus the drag force on the particles. If thereby a sufficient focusing could not be achieved, the diameter of the orifices was varied. Large particles should be focused by the first orifice; smaller particles can be focused by one of the orifices downstream. Finally, the aspect ratio of the nozzle and the size and distance of the skimmer downstream from the ADL was optimized.

Applying this method, several lenses for different purposes were designed. One of these lenses is designed as inlet for $1-15\,nm$ SiO_2 particles into the TRAPS apparatus and will be described in greater detail below. Requirements for this lens were a high particle flux ($10^6-10^8\,particles\,s^{-1}$) at moderate exit pressure ($\sim 1\,Pa$). Therefore, a high pumping capacity and a large skimmer ($d = 3.0\,mm$) was used. An initial guess was made with the ALC restricted only by the maximum pumping capacity. For SiO_2, the smallest particle diameter that can be focused according to the ALC is $8\,nm$. The particle axial velocity downstream from the lens however is rather small which results in excessive beam broadening due to Brownian motion. CFD calculations of that design showed a rather poor focusing performance. By applying the strategy detailed above, ADL parameters were found that perform considerably better. The improved lens is able to focus $1–15\,nm$ SiO_2 particles dispersed in helium. The diameter of the tube between the focusing orifices is $20\,mm$. The thickness of the orifices is $0.5\,mm$. A comparison between the ALC result and the CFX redesign is presented in Table 1.

The performance of the redesigned lens can be compared to the result from the ALC by simulating both geometries with CFX. The divergence angle is a measure for the focusing performance and can be calculated from the radial and the axial velocity component of the particle trajectory. For $1\,nm$ particles it is $1.53°$ and $2.21°$ for the optimized ADL design and the initial design from the ALC, respectively. For $8\,nm$ particles the divergence is $0.32°$ and $0.47°$ and for $15\,nm$ particles the simulations yield $1.26°$ and $4.30°$. This demonstrates that for particles in the diameter range of $1-15\,nm$ the beam divergence is smaller in the redesigned ADL (cf. Figure 4.14). Additionally, the higher particle velocity downstream from the lens (refer to Table 2 and Figure 4.15) reduces Brownian broadening.

It should be mentioned that the calculations were performed for an ideal geometry. Non-spherical particles will significantly vary the beam width (cf. Eq. 4.46). Non symmetric flow fields induce swirl effects at an orifice [Baker, 2000]. Roughness at the edges of the orifices can cause non-stationary effects like fluctuating eddies downstream from the orifice, resulting in turbulence and pulsation [Sigloch, 2008].

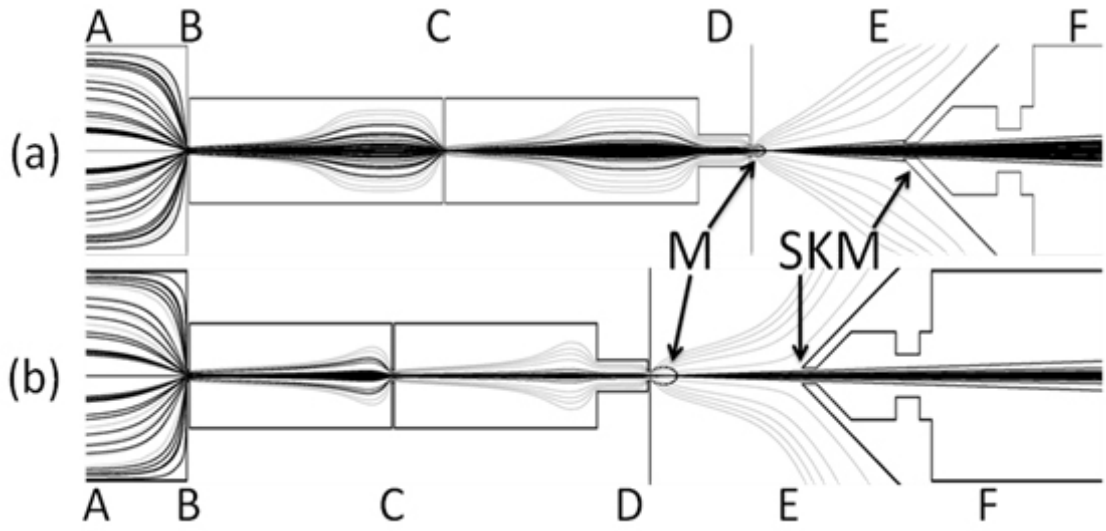

Figure 4.14. Two alternative designs for an ADL focusing spherical SiO_2 particles in Helium. (a) Result from ALC (b) as optimized by CFD calculations, see text. A: ADL inlet with particles homogeneously dispersed in the carrier gas ($900\,Pa$). B: first orifice. C: second orifice. D: acceleration nozzle. E: opening to pump ($25\,Pa$). F: ion-guide ($5\,Pa$). M: Mach zone. SKM: skimmer. Grey lines are the streamlines of the gas. Black lines are the trajectories of the particles with a diameter from $1-15\,nm$. Particles $>8\,nm$ are focused at the first orifice, smaller particles are focused at the second orifice.

The CFD simulation of this ADL shows a focusing of particles $>8\,nm$ at the first orifice (cf. Figure 4.14b). Smaller particles are focused at the second orifice. The distance between the orifices and the tube diameter is chosen not to permit the flow to fully reattach to the walls of the tube. This minimizes beam broadening by diffusion at low flow speed. The second nozzle is chosen to accelerate the particles as strong as possible under the given flow parameters. The pressure drops from 605 to $25\,Pa$ across this nozzle, thus a Mach zone develops downstream. It was found to be preferable, not to place the skimmer in the zone of silence of the Mach zone. Since the particles are well focused while they pass the Mach zone, they will not be defocused

significantly. After passing the skimmer and entering the octopole ion-guide they have a sufficiently small radial momentum to be trapped by the pseudo potential of the octopole.

Figure 4.15 shows the static pressure, axial flow and particle axial velocity along the axis to be compared to the nanoparticle lens system "C" introduced in Wang et al. [2005b]. Obviously, the main difference is the higher axial particle speed in the new design which results in less Brownian broadening downstream from the lens.

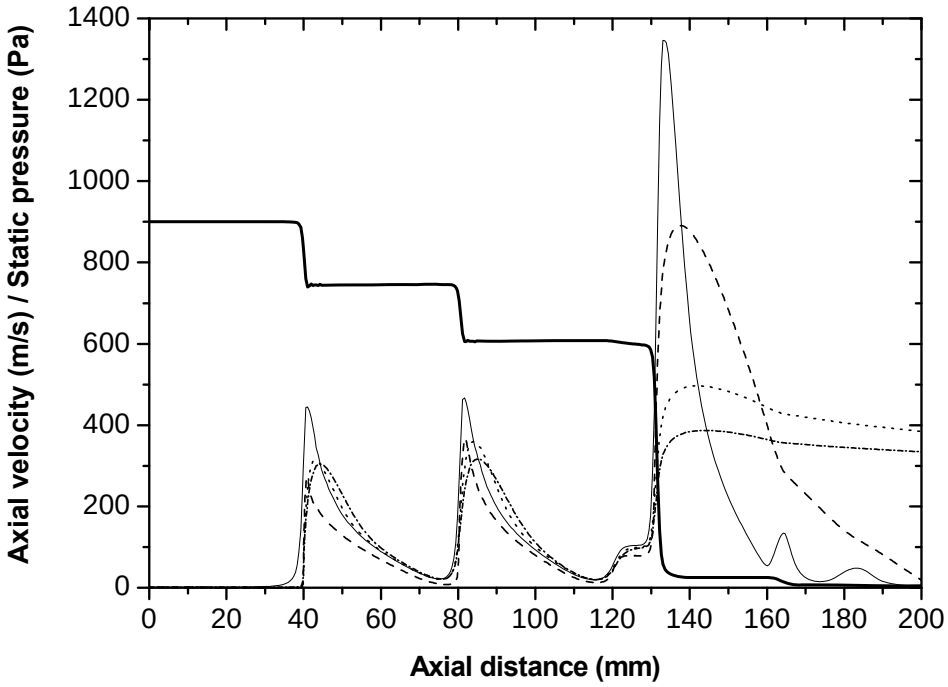

Figure 4.15. Static pressure (bold line), axial gas velocity (slim line) and particle axial velocity (particle diameter 1 nm: dashed, 10 nm: dotted, 40 nm: dot-dashed) along the axis of the nanoparticle lens system for the TRAPS apparatus. This Figure can be compared to Figure 2 in Wang et al. [2005b].

4.6.3 Tuneability of the novel ADL

From the present CFD simulation it can be inferred, that the inlet pressure is a very sensitive parameter of an ADL. If the pressure changes within 10 %, the focusing of a distinct size can be entirely lost. On the other hand, this sensitivity can be advantageously used to tune the lens to a specific particle diameter of interest. The focusing performance of an ADL is governed by the particle Stokes Number S_p (cf. Eq. 4.27). For $S_p = 1$ a particle will be focused at the centre line of the lens. For $S_p > 1$ particles will pass the centre line and diverge. For $S_p < 1$ the particles tend to follow the streamlines of the gas.

If pressure and mass flow are changed, the optimum Stokes Number for a distinct particle diameter will shift to different size. Thereby the lens becomes tunable. Figure 4.16 shows the particle Stokes Number for the TRAPS ADL at two different inlet pressures. The red lines show S_p, calculated at the first (solid squares) and second (open circle) orifice for designated the inlet pressure. Optimum focusing can be expected for $4 - 5\,nm$ particles. The green lines show S_p calculated for a lower inlet pressure. The optimum focusing range has shifted to $10 - 11\,nm$. The shift of the nozzle (crosses) is different from the shift of the orifices. For the designated inlet pressure, S_p of the nozzle fits to the number of the orifices. Once the inlet pressure is changed, S_p of the nozzle changes faster than S_p of the orifices. Since the particles are focused well when they pass the nozzle, they will not be defocused badly, but the useful tuning range of the ADL will be limited by this effect.

This tuning effect is useful for variable composition gas mixtures, as well. For instance, aerosols created by the MPPS are immersed in a carrier gas containing a variable amount of oxygen in helium depending on the amount of precursor used for the reaction. Since oxygen and helium have significantly different viscosity, the particle trajectories are sensitively changed. This can be compensated – at least to some extend – by varying the inlet pressure of the ADL.

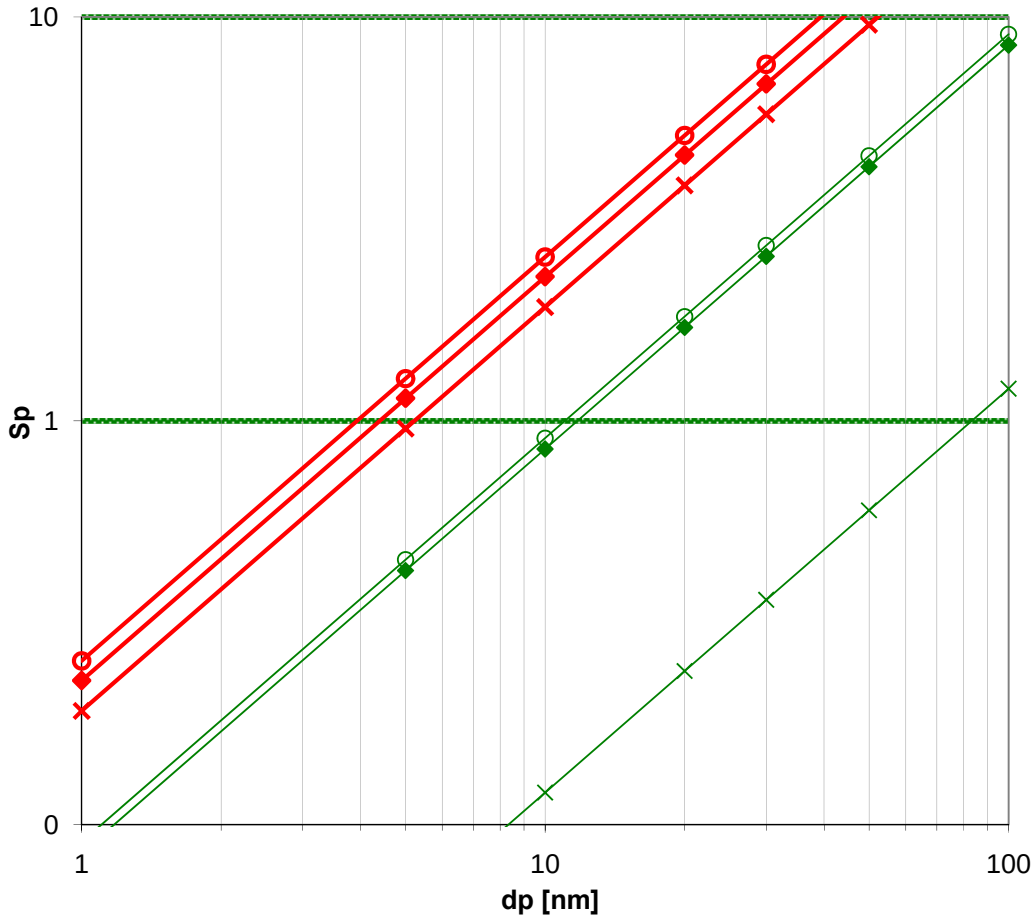

Figure 4.16. Particle Stokes Number S_p at different inlet pressures. The designated inlet pressure ($900\ Pa$) is depicted as bold red line and a reduced inlet pressure ($400\ Pa$) is depicted as thin green line. The S_p at the first orifice is indicated by solid diamonds, at the second orifice by open circles and at the nozzle by crosses.

4.7 Characterization of the particle inlet

4.7.1 Equipping a molecular beam inlet with an ADL

For experimental validation of the CFD simulations, an ADL was designed to fit at the existing Particle Mass Spectrometer (PMS) in section 3.8 (see also Figure 4.1). This lens consists of a single focusing orifice with $d_f = 2.10\ mm$ and an accelerating nozzle with $d_f = 2.70\ mm$, only. The inlet pressure was 400 Pa for helium as carrier gas and the pressure downstream from the nozzle was 10 Pa. SiO_2 particles where produced by the MPPS using SiH_4 and O_2 in He with a total flow of 2.5 $10^{-3}\ Pa\ l\ s^{-1}$ at 3000 Pa. The flow limiting orifice was positioned close to the reactor, in order to avoid coagulation of the particles. An aerodynamic skimmer with an opening of $d_f = 1.00\ mm$ is positioned 15 mm downstream from the nozzle in order to differentially pump to 0.01 Pa in the mass spectrometer.

Particles carrying one or two charges of both polarities have been detected by the PMS in comparable fractions. For the subsequent analysis, only single (NP^{1-}) and double (NP^{2-}) negatively charged particles were used (Figure 4.17). The total charge carried by the beam was about 350 pA; the current assigned to NP^{1-} and NP^{2-} is 225 pA and 125 pA, respectively. By means of PMS, the diameter of the particles has been determined to $d_p = (5.7 \pm 0.8)\ nm$. The axial velocity of the particles downstream from the skimmer was measured to $(380 \pm 40)\ ms^{-1}$ by using a chopped beam lock-in technique.

In order to determine the performance of this ADL inlet, the lens was replaced by a classical molecular beam inlet consisting of an flow-limiting orifice in front of an aerodynamic skimmer with an opening of $d_f = 0.50\ mm$. The skimmer was placed 15 mm upstream from the nozzle. SiO_2 particles were produced by means of the MPPS with equal parameters as for the ADL inlet. Figure 4.17 shows the signal intensity of the deflected particle beam for the two inlet systems, the ADL (boxes) and the molecular beam (circles) inlet. Note that the signal recorded using the molecular beam inlet is multiplied by a factor of 100 in order to facilitate a comparison between both experiments. The total charge carried by the beam was about 350 pA and 2.5 pA for the ADL and the molecular beam inlet, respectively.

The particles produced for the experiment with the molecular beam inlet (circles) are about $0.5\,nm$ smaller than the particles used for the ADL inlet experiment (boxes). This is due to a slightly higher pressure within the MPPS in the molecular beam inlet case. As the mass flow of the precursors was carefully controlled, it can be assumed that more particles of smaller size have been produced in the plasma in order to transform all reactants. For this reason the amplification of the transmitted particle beam caused by the ADL might be even higher.

This experiment demonstrates first that the MPPS is a reliable source for intense beams of small nanoparticles in a carrier gas at moderate pressure. Secondly, it shows that a carefully designed ADL enhances the fraction of particles that can be transferred into a vacuum system by about a factor of 100.

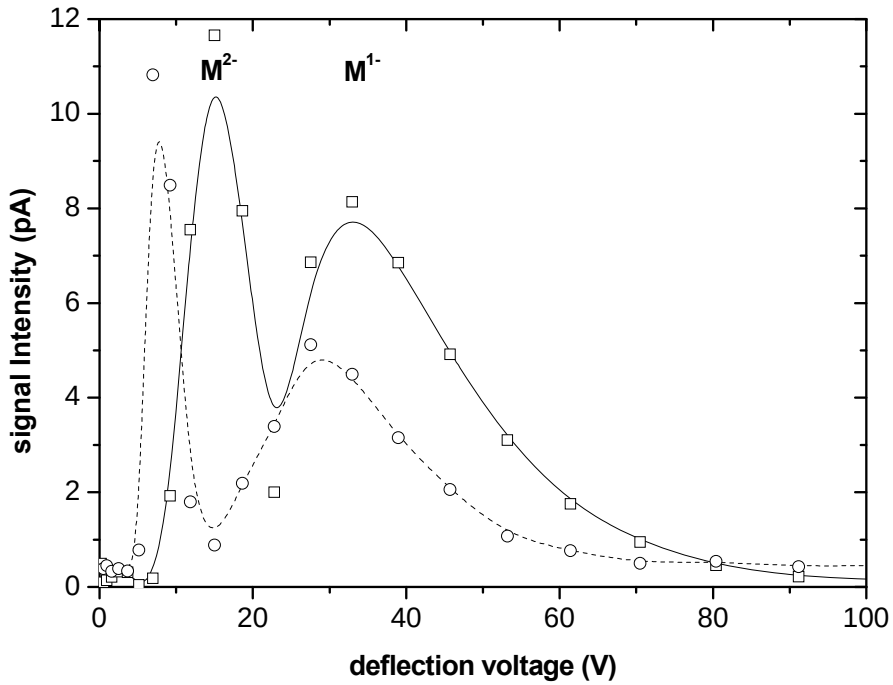

Figure 4.17. Transmission efficiency of a molecular beam inlet with (boxes, drawn line) and without (circles, dashed line) aerodynamic lens. The graph shows the signal intensity over deflection voltage of the ion beam measured by the PMS instrument. Data points are connected by a spline in order to identify the two peaks occurring from the charge states. Data points measured without the ADL are multiplied by a factor of 100.

4.7.2 Performance of the TRAPS ADL

In the following paragraphs the aerodynamic lens used as particle inlet for the TRAPS apparatus is characterized by transmission efficiency and beam diameter experiments. The parameters of this ADL are listed in Table 2. The skimmer with an opening of $d_f = 3.0\,mm$ is positioned $15\,mm$ downstream from the nozzle. The distance between skimmer and inlet lens of the octopole is $23\,mm$. The length of the octopole is $220\,mm$ and the distance between octopole and electrometer is $162\,mm$, whereas the detection area has a diameter of $17\,mm$. SiO_2 particles with $d_p = (6.0 \pm 0.7)\,nm$ were produced by microwave plasma synthesis at $10\,kPa$ and characterized with the TRAPS-TOF device (cf. Section 4.10).

	orifice diameter (mm)		upstream pressure (Pa)		gas velocity (m/s)		distance to next element (mm)		pumping capacity (Pa l/s)	
	ALC	CFX	ALC	CFX	ALC	CFX	ALC	CFX	ALC	CFX
1st orifice	1.22	2.20	1802	900	448	250	45	40		
2nd orifice	1.88	2.40	970	745	355	250	40	40		
nozzle	2.02	2.10	686	605	420	1050	28	30	750	850 (25Pa)
skimmer	-	3.00	-	25	-	200	-	15		
octopole inlet	-	8.00	-	5	-	10	-	23	-	230 (1Pa)

Table 2. Parameters of an ADL for $8\,nm$ SiO_2 particles for the TRAPS apparatus as determined from the aerodynamic lens calculator (ALC) and resulting from fluid dynamics calculations (CFX).

It was shown in section 4.2 that the inlet pressure of the ADL is the key parameter for the focusing performance of the lens since it defines the pressure and velocity of the carrier gas inside the lens. Figure 4.18 shows an experiment demonstrating this relation. The inlet pressure of the ADL is varied by a valve and monitored by a capacitive pressure gauge. Figure 4.18 clearly shows a maximum signal at $860\,Pa$ which is close to the pressure the lens was designed for ($900\,Pa$, see Table 2). An increase of the inlet pressure leads to an increase of the mass flow through the ADL. Therefore, the measurement is corrected for the change of the mass flow (filled spheres in Figure 4.18). The corrected signal can be interpreted as a transmission efficiency of the whole inlet system consisting of ADL, skimmer and octopole.

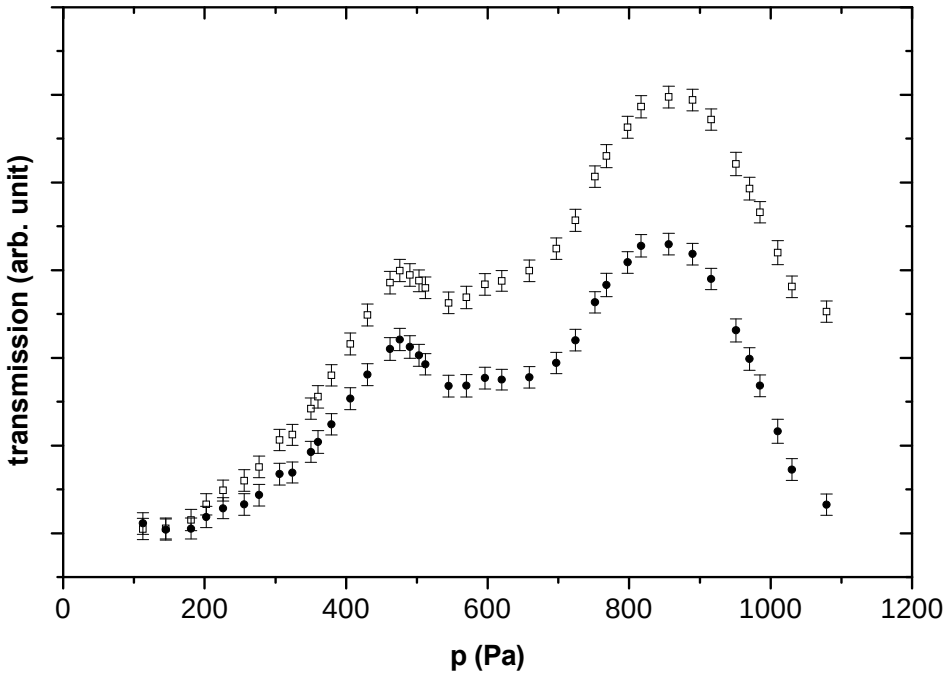

Figure 4.18. Transmission of the aerodynamic lens in dependence of the inlet pressure of the lens probed with 6.0 nm SiO_2 particles. Open squares represent the detector current. In order to have a relative measure for the transmission efficiency of the ADL the data was corrected for the gas flow increasing with inlet pressure (filled bullets).

Surprisingly, there is a second peak at 473 Pa, indicating another optimal working pressure of the aerodynamic lens. This peak was not reproduced by the CFD simulations for $d_p = 6\,nm$ SiO_2 particles. Expanded CFD analysis of the system yielded the explanation of the second maximum: Agglomerates of two SiO_2 particles are focused optimal into the skimmer at 473 Pa when treated as $d_p = 12\,nm$ SiO_2 particles in the simulation. A similar effect was reported by de la Mora et al. [1996] who noticed a stepped collection efficiency of aerodynamic particle impactors for different gas velocities. De la Mora et al. [1996] were able to address this effect to varying classes of particle sizes. Figure 4.19 shows the simulation results yielding particle trajectories passing the skimmer for $d_p = 6\,nm$ and $d_p = 12\,nm$ at 860 Pa and 473 Pa inlet pressure. At 860 Pa $d_p = 12\,nm$ are impinging at the skimmer predominantly (panel d), but they are perfectly focused at an inlet pressure of 473 Pa (panel c).

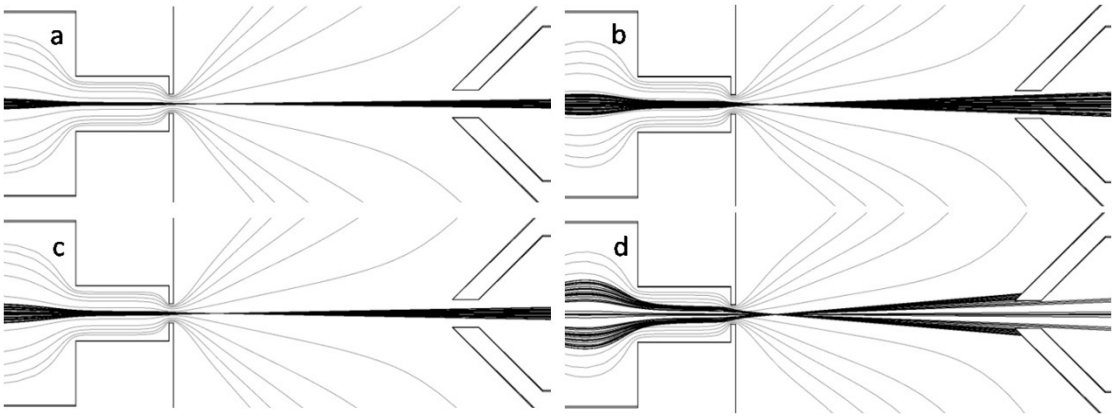

Figure 4.19. Particle trajectories from CFD simulations of SiO_2 particles dispersed in helium, propagating through the accelerating nozzle and the skimmer of the TRAPS apparatus. Particle diameter (a) and (b): $d_p = 6\,nm$; (c) and (d) $d_p = 12\,nm$; ADL inlet pressure (a) and (c) $p = 473\,Pa$; (b) and (d) $p = 860\,Pa$. Particles impinging at the walls are considered to be lost.

4.7.3 Beam profile measurements

The requirements to the beam divergence downstream from the ADL are quite low in our application, since the beam is focused electrodynamically once it is inside the octopole ion-guide. Beam profiles have been measured by sliding a sharp edged copper plate into the beam (see Figure 4.20). The analysis of the detector signal (faraday cup electrometer) with respect to plate position yields the beam profile. Beam diameters are defined following Liu et al. [1995a] as the width of the beam containing 90 % of the particles. It is also known from Eq. 4.35 that the beam has a Gaussian shape. In Cartesian coordinates this relation merges to

Eq. 4.65 $$\mathrm{g(x,y)}dx\,dy = \frac{1}{\pi\,{a_B}^2}\,Exp\left[-\frac{\mathrm{x^2+y^2}}{{a_B}^2}\right]\,dx\,dy$$

For a plate spreading over the whole y-dimension the term is

Eq. 4.66 $$\int_{-\infty}^{+\infty} g(x,y)\;dy = \frac{1}{\sqrt{\pi\,{a_B}^2}}\,Exp\left[-\frac{x^2}{a_B}\right]$$

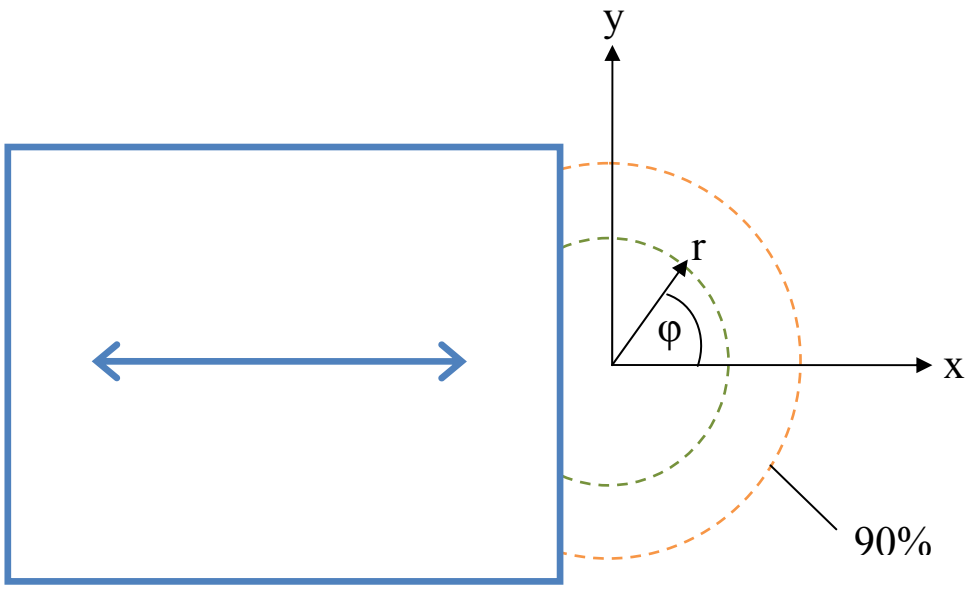

Figure 4.20. Schematic geometry used for beam profile measurements. Large square: sharp edged copper plate. Outer circle: Area in which 90 % of the total particle number flux is enclosed. Inner circle: Area which is described by $f(r, \varphi)$.

Eq. 4.66 is essentially a Gauss function where a_B corresponds to the width of the beam. If the copper plate is moved in x-direction, the number of particles impinging at the plate is a function of x which can be derived by integrating Eq. 4.66.

Eq. 4.67 $$\frac{1}{\sqrt{\pi\, a_B{}^2}} \int Exp\left[-\frac{x^2}{a_B}\right] dx = \frac{1}{2} Erf\left[\frac{x}{a_B}\right]$$

Fitting this function to the data recorded, directly yields a_B and thus the 90 % beam diameter using Eq. 4.39. For real data a constant offset for x position c and signal offset b has to be included in the fit. So the model used for data analysis is

Eq. 4.68 $$f(x) = A\, Erf\left[\frac{x-c}{a_B}\right] + b$$

Figure 4.21 shows raw data from a beam profile measurement of a $d_p = 7.0\, nm$ SiO_2 particle beam (bullets). As the copper plate is gradually moved out of the beam, an increasing number of particles is collected by the detector. The drawn line is the fit to the data applying Eq. 4.68. The coefficients from the fit are $A = 1.03$, $b = 1.00$, $c = 0.39$ and $a_B = 0.88$ which yields a 90 % beam width of $d_B = 2.67\, mm$.

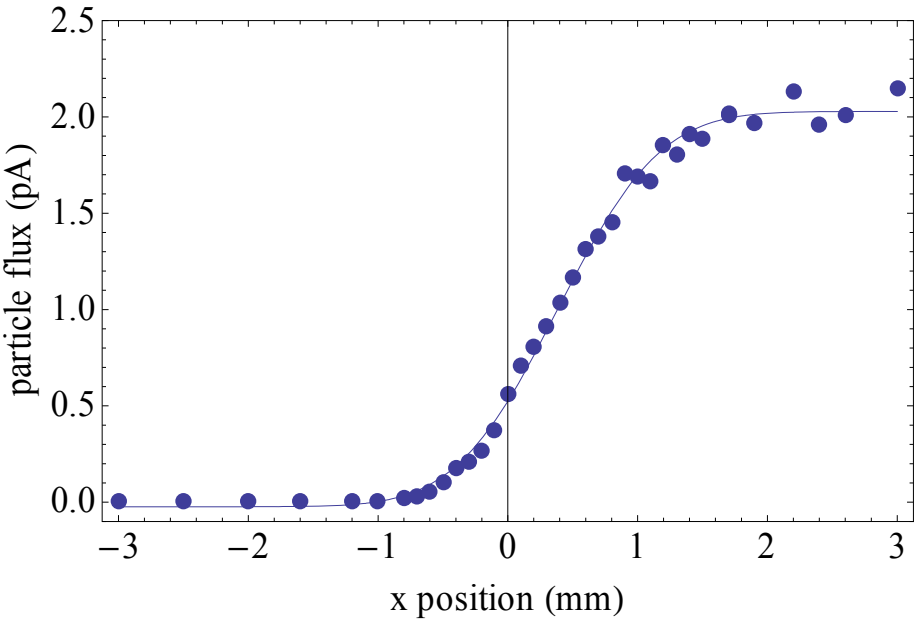

Figure 4.21. Beam profile measurement. Raw data is depicted as bullets. The drawn line is the fit to the data utilizing Eq. 4.68.

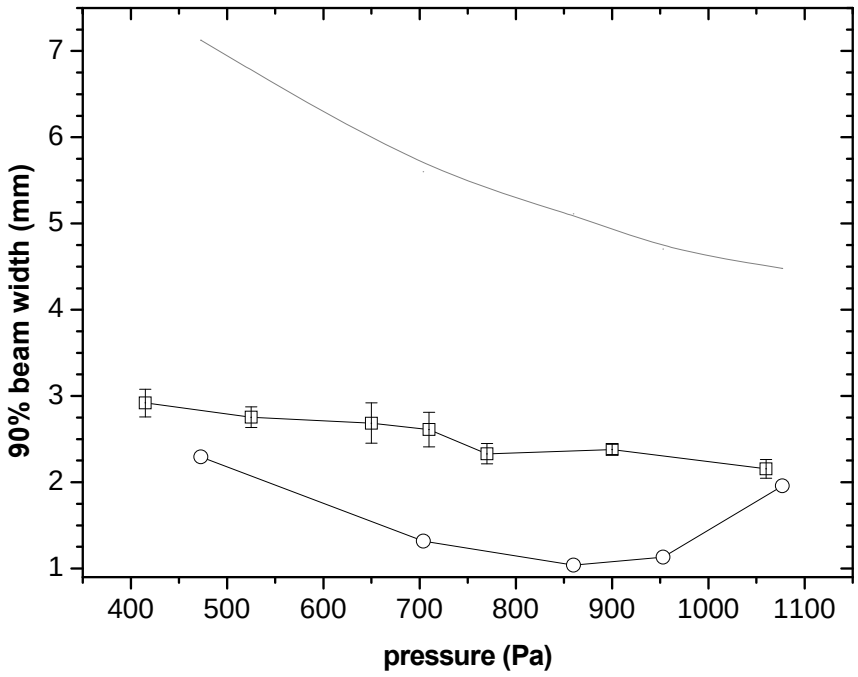

Figure 4.22. Beam diameter $235\,mm$ downstream from the nozzle recorded for $7.0\,nm$ SiO_2 particles with different inlet pressure of the ADL (boxes). The profiles are compared to the results from CFD calculations (circles), which show a minimum at the working pressure of the lens and an overall lower beam diameter. The dashed line shows the Brownian limit of a $7\,nm$ particle beam according to Eq. 4.40.

Figure 4.22 shows the particle beam diameter of $d_p = 7.0\,nm$ SiO_2 particles measured $235\,mm$ downstream from the nozzle (boxes). CFD simulations with appropriate parameters show a minimum at the working pressure of the lens and, as expected, a significant smaller beam size since the CFD code does not account for Brownian broadening (circles). This result shows that the ADL would be able to focus the beam to $1\,mm$ diameter at the working pressure if Brownian motion would be absent. Brownian broadening determines the width of the beam over the full pressure range tested. The beam width measured at working pressure is about $2.4\,mm$. Assuming Eq. 4.40 is valid, this beam diameter corresponds to $12\,nm$ particle diameter while it was determined by Time-Of-Flight (TOF) measurement to be $d_p = (7.0 \pm 0.6)\,nm$ (cf. below). The theoretical Brownian limit for a $7.0\,nm$ SiO_2 particle calculated from Eq. 4.36 and Eq. 4.39 is depicted as dashed line in Figure 4.22. This beam diameter is much wider as the diameter measured. This might be an indication that the assumptions made in the derivation of Eq. 4.40 are not completely valid. The particles are possibly not in perfect thermal equilibrium with the surrounding carrier gas while passing the acceleration nozzle of the ADL. Furthermore, in the discussion of the octopole ion-trap downstream from the skimmer (cf. below) evidence will be presented that the drag force of the low background gas pressure inside the skimmer and the ion-guide is influencing the particle trajectories. CFD simulations show that trajectories of particles with $d_p < 5.0\,nm$ are influenced by the gas flow through the exit lens of the octopole ion-guide (cf. Figure 4.23). This is an indication for an additional focussing effect of the skimmer and the octopole ion-guide geometry.

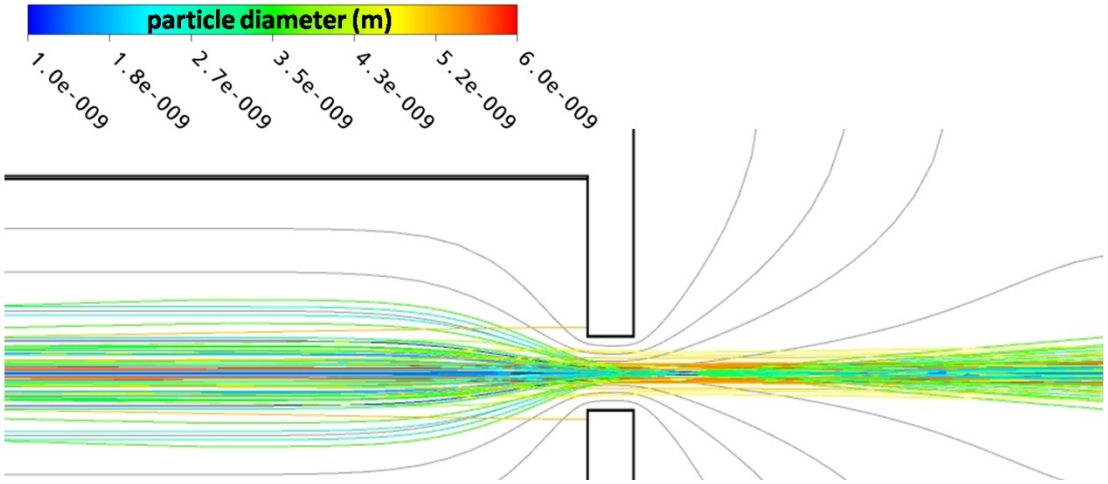

Figure 4.23. CFD simulation result of a particle laden gas flow passing the exit lens of the octopole ion-guide at typical working conditions. Black line: geometry, grey line: streamlines, colored lines: particle trajectories.

4.8 Theory of multipole ion-guides and ion-traps

Linear ion-guides consist of a number of parallel rods of diameter d_r. Two interdigitated sets of rods are evenly distributed about a circle with inner diameter r_0. The voltage applied to one set of rods is $V_0 + k\,V_{rf}\,\cos(\omega\,t)$, and to the other set is $V_0 - k\,V_{rf}\,\cos(\omega\,t)$. The two sets therefore have a 180° phase difference in rf voltage. V_{rf} is the zero-to-peak amplitude of the rf waveform from the power supply and V_0 is the DC offset voltage. A wiring diagram of an octopole ion-guide is given as example in Figure 4.24.

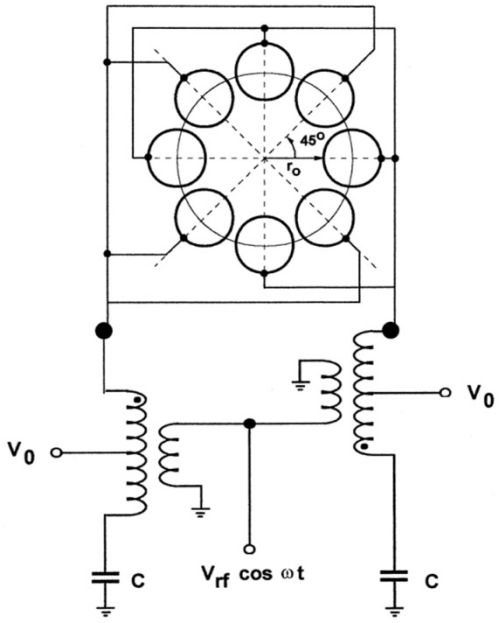

Figure 4.24. Wiring diagram of an octopole ion-guide (adapted from Wang et al. [2000]).

4.8.1 Basic multipole theory

Two dimensional multipole fields are well known. Their use of guiding and trapping ions has been reviewed many times [Gerlich, 1992; Gerlich, 2003; Douglas et al., 2005]. The ions are trapped inside an inhomogeneous electric field which usually has the following time dependence:

Eq. 4.69 $$E_0(r,t) = E_0(r)\,\cos(\omega\,t)$$

The spatial dependence of the field, $E_0(r)$, is given by the boundary conditions imposed by the electrodes. The time dependence of the field is given by the frequency ω. For a given particle with mass m and charge q the equation of motion can be formed to describe the motion of the particle under the influence of a time dependent force. However, the exact motion of charged particles in an arbitrary time dependent electromagnetic field is an unsolved problem. Dissipative forces, e.g. by inelastic collisions, make the problem mathematically complex. One well-known exception for quadrupolar fields is the Mathieu equation which is valid when the field is homogeneous. A simplification of the mathematical problem can be used when the field oscillates with a sufficiently high frequency ω. If the oscillation of the field is faster than the time the particle travels from one electrode to the next in a circular motion, fast and slow components of the particle trajectory can be separated. Within this adiabatic approximation the adiabatic kinetic energy of the particle is conserved and the motion of the particle can be predicted using the effective potential.

Eq. 4.70 $$V^* = q^2 \frac{{E_0}^2}{4\, m\, \omega^2}$$

A quantitative measure for the quality of this approximation is the adiabaticity parameter η.

Eq. 4.71 $$\eta = 2\, |\nabla \boldsymbol{E}| \frac{q}{m} \frac{1}{\omega^2}$$

For $\eta < 0.3$ the adiabatic approximation is valid. So the angular frequency ω must be high enough for a given mass to charge ratio. In practical units Eq. 4.70 and Eq. 4.71 can be written as

Eq. 4.72 $$V^* = \frac{1}{8} \frac{(q\, V_0)^2}{\varepsilon} \left(\frac{r}{r_0}\right)^{2n-2}$$

Eq. 4.73 $$\eta = \frac{n-1}{n} \frac{q\, V_0}{\varepsilon} \left(\frac{r}{r_0}\right)^{2n-2}$$

using

Eq. 4.74 $$\varepsilon = 1.036\, m\, \omega^2 \frac{{r_0}^2}{2\, n^2} \qquad \text{and} \qquad r_0 = \frac{(n-1)\, d_r}{2}$$

where n is the order of the multipole (quadrupole: $n = 2$, octopole: $n = 4$). Thus the motion of a single ion in a quadrupole has an effective potential proportional to r^2, in an octopole proportional to r^6 and so on. Higher multipoles have a relative flat effective potential near the central axis and their effective potential increases more rapidly near the rods. The shapes of the effective potentials for quadrupole and octopole fields are compared in Figure 4.25. The angle of acceptance for ions entering the ion-guide increases with the order of the multipole. A second difference to quadrupoles is that the stability parameter η depends on r and it goes to zero at the limit $r \to 0$. For higher order multipoles the adiabatic approximation is better the closer the trajectory gets to the center line. Therefore, collisional relaxation becomes very efficient in higher order multipoles. For these two reasons an octopole ion-guide is used at the particle inlet of the TRAPS device.

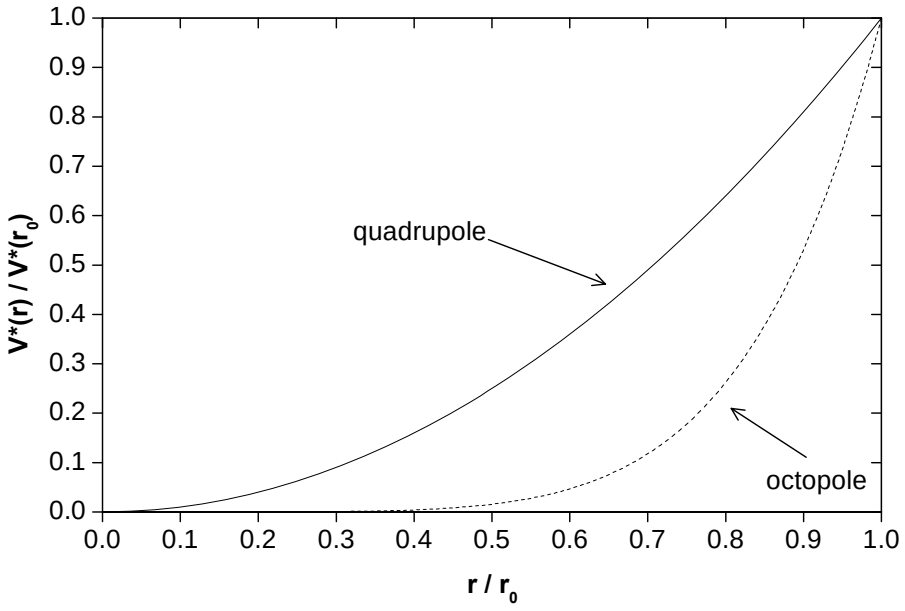

Figure 4.25. Comparison of effective potentials for quadrupole and octopole fields.

4.8.2 Working modes of a linear multipole ion-cage

After passing ADL and skimmer, the particles enter the octopole ion-guide with about $450\ m\ s^{-1}$ axial velocity. The particles are decelerated by collisional relaxation (cooling) with the helium gas. Typically, the background pressure level inside this ion-guide is $1 - 5\ Pa$. In the case of a light background gas moderating much heavier nanoparticles, the action of the background gas can be regarded purely as friction

applying the Cunningham correction to the Stokes law. Filling of the trap and extraction of the nanoparticles are controlled by the electrostatic entrance and exit lens of the trap.

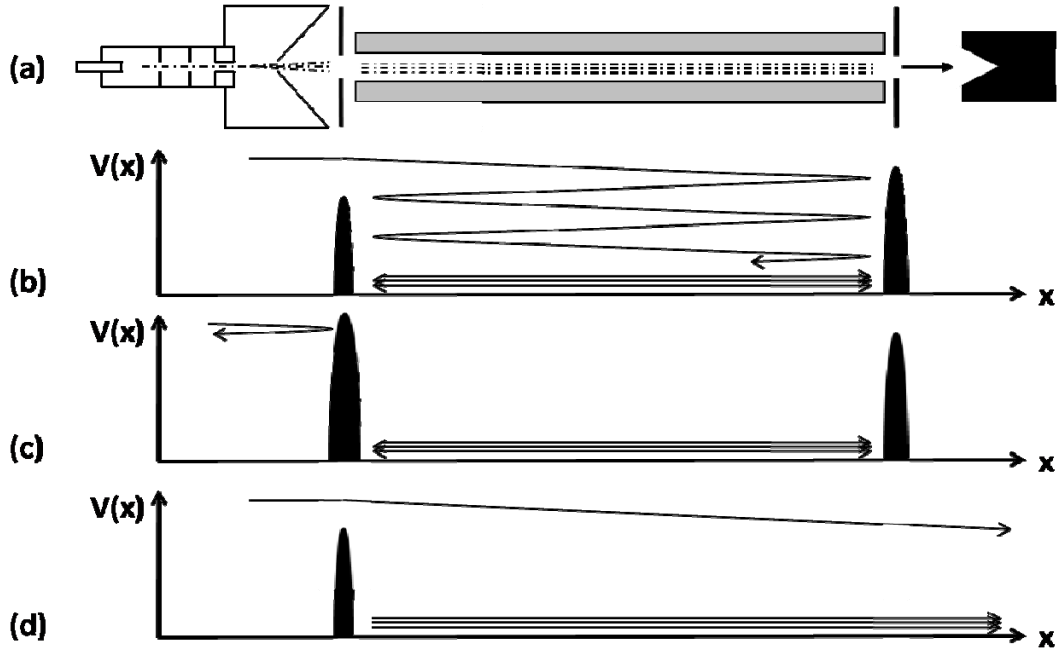

Figure 4.26. Schematic view and operating modes of the trap: (a) trap geometry, (b) filling/storage mode; (c) storage mode; (c) extraction mode.

Figure 4.26 shows the operation modes of the trap. In the filling/storage mode (b), the entrance lens is kept at intermediate repelling potential which is below the kinetic energy of the incoming particles, while the exit lens is at a potential high enough to reflect all particles. By traversing the ion-guide back and forth, the ions loose kinetic energy by collisions with the background gas. The decelerated returning ions are reflected by the entrance lens and are bound to travel between the entrance and exit electrode until their longitudinal kinetic energy is completely thermalized. In storage mode (c) both, entrance and exit lens are kept at such high repelling potentials that particles can neither enter nor leave through the lenses. This mode is useful for leak rate measurements, spectroscopic measurements, or chemical reactions. In order to extract the ions, the exit potential is switched to ground so that the particle can exit the trap (d). The ejected particle cloud is detected on a Faraday cup either directly or after being deflected by 90° in an electrostatic quadrupole bender.

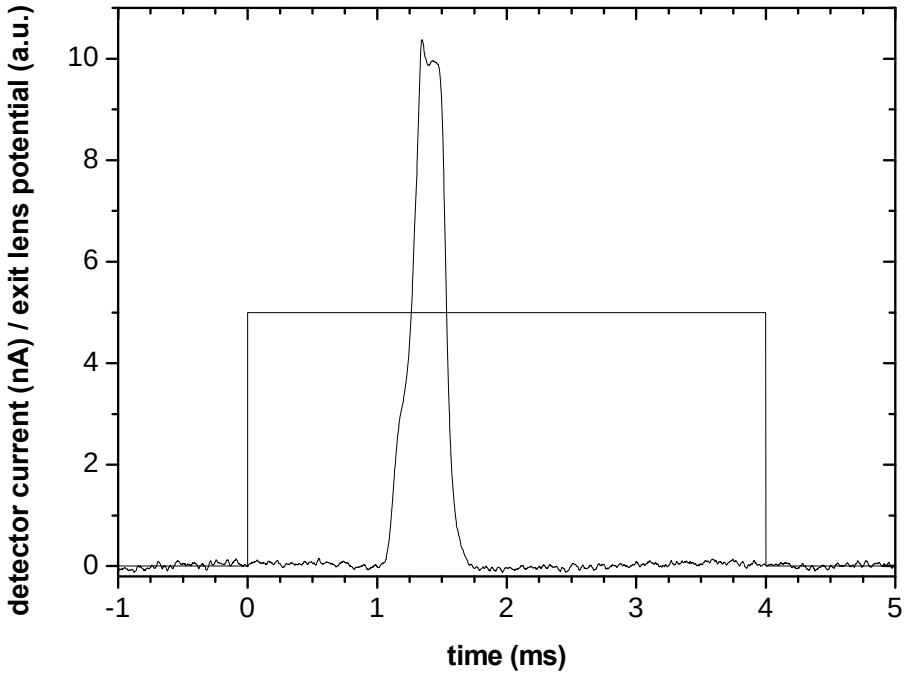

Figure 4.27. Extraction potential and extraction particle pulse from octopole ion-trap (exit lens potential = 0: ion-trap closed; exit lens potential = 5: ion-trap open).

A result from a typical trapping experiment is depicted in Figure 4.27. The trap was kept in filling/storage mode for $0.5\,s$ and then the exit lens was switched to ground at time $t = 0$ to extract the particles. The exit lens potential and the detector current are displayed in Figure 4.27 as a function of time. After a certain flight time, a large particle peak is measured, which reaches its maximum after $1.4\,ms$. After $1.8\,ms$ the trap is emptied and the particle current reaches its continuous value which can hardly be seen in Figure 4.27 (the octopole trap works as an ion-guide) until the exit lens is closed again after $4\,ms$. Integrating the particle peak yields the total charge stored in the trap, which reaches $2\ 10^7$ elementary charges in this case. From the continuous value load current of the trap can be obtained. Here, it is $70\,pA$ corresponding to $4\ 10^7$ particles per second. Thus, for this configuration the particle density in the trap was enhanced by a factor of (66 ± 3). From the time interval between the opening of the ion-trap and the signal on the Faraday cup, the diameter of the particles and their spatial distribution in the trap (cf. section 4.10) can be inferred.

4.8.3 Spatial charge distribution in ion-guides

Multipole ion-traps have recently been used to measure the extreme weak extinction of Ag_9^+ cluster ions by cavity ring-down spectroscopy [Terasaki et al., 2009]. About $9\ 10^8$ ions were stored in a octopole ion-trap, which corresponds to an average ion-density of $2.4\ 10^7\ cm^{-3}$. In the course of these studies, it was found that the radial ion distribution within the trap was not homogeneous. Therefore, it is an important issue to investigate the spatial distribution of the stored ions in the high density regime, where space charge plays a significant role. Figure 4.28 shows the spatial distribution of Ag_9^+ ions in an octopole ion-guide. The distribution clearly exhibits a ring profile. A major part of the ions are found in the outer region rather than in the center of the ion-trap. A pendulum motion of ions along the effective potential would cause a prolonged residence time at the turning point of the ion motion and thus a high ion-density at the outer region. But for lower number of ion loading, the stored ions are confined in the center region of the ion-trap (Terasaki, personal communication). This suggests that the ions are well thermalized after their kinetic energies are transferred to that of the buffer helium gas. Therefore, the ring profile of the ion distribution at higher ion number is only ascribable to the space-charge effect among the thermalized ions.

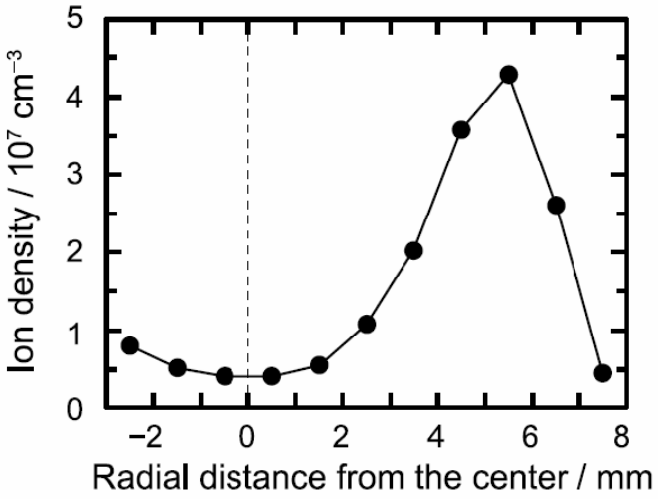

Figure 4.28. A radial profile of distribution of Ag_9^+ in a linear octopole ion-trap; $9\ 10^8$ ions (an average ion-density: $2.4\ 10^7\ cm^{-3}$) are loaded (reproduced from [Terasaki et al., 2009])

The charge distribution of ions in a linear ion-trap can be solved under the assumption that the problem is translational invariant along the z-axis, where it extends from negative to positive infinity $\Phi(r, \varphi, z) = \Phi(r)$. When a certain amount of charge unit per length Q_0 is allowed to distribute freely in such an electrostatic potential $\phi(r)$, the charge will distribute radially with density $\rho(r)$ as to minimize the total electrostatic energy E of the charge unit per length Q_0 in the electrostatic potential ϕ. The total electrostatic energy per unit length E of the charge distribution $\rho(r)$ is composed of the internal energy of $\rho(r)$, i.e. the electrostatic energy resulting from the repulsion between the volume elements of $\rho(r)$ and the external energy of the charge distribution $\rho(r)$ in the external potential $\phi(r)$.

The external electrostatic energy is known as:

Eq. 4.75 $$E_{ext}(V) = \int \Phi \, \rho \, dV$$

With $\Phi(\varphi) = \rho(\varphi) =$ constant, a coordinate transformation can be done.

Eq. 4.76 $$E_{ext}(r, z) = \int E(V) \, d\varphi = 2\pi \iint \phi(R, z) \, \rho(R, z) \, R \, dR \, dz$$

$$= 2\pi \, z \int \phi(R) \, \rho(R) \, R \, dR$$

Using the translational invariance Eq. 4.76 can be normalized to z which yields the external electrostatic energy per unit length $E_{z,ext}$.

Eq. 4.77 $$E_{z,ext}(r) = \frac{E_{ext}(r,z)}{z} = 2\pi \int \phi(R) \, \rho(R) \, R \, dR \; = E_{ext}(r)$$

Eq. 4.77 is valid for the whole space, but only has physical meaning within the circumference of the ion-cloud. The finite circumference of the ion-cloud will be given by minimization of the total electrostatic energy of the problem.

The charge per unit length Q_z, which is spread over the circumference of the ion-cloud with radius r, can be written as:

Eq. 4.78 $$Q(r, z) = \int_V \; \rho(r) \, dV = \iiint \rho(R) \, R \, dR \, d\varphi \, dz = 2\pi \, z \int_0^r \rho(R) \, R \, dR$$

$$Q_z(r) = \frac{Q(r)}{z} = 2\pi \int_0^r \rho(R) \, R \, dR = Q(r)$$

Eq. 4.79 $$\rho(r) = \frac{1}{2\pi\, r} Q'(r)$$

Where the prime symbol on a function denotes the partial derivative with respect to r. $Q(r)$ is defined for $0 \leq r \leq \infty$, its boundary values are $Q(0) = 0, Q(\infty) = Q_0$. Substituting Eq. 4.79 in Eq. 4.77 the external electrostatic potential becomes:

Eq. 4.80 $$E_{ext}(r) = 2\pi \int \phi(R)\, \frac{1}{2\pi\, R} Q'(R)\, dR = \int \phi(R)\, Q'(R)\, dR$$

The first Maxwell Equation describes the electric field $\vec{E}$ of a charge cloud. To access the internal electrostatic energy of the charge cloud E_{int}, the Maxwell Equation is applied over the surface A of an infinite cylinder of radius r along the z-axis.

Eq. 4.81 $$\int_A \vec{E}\, dA = \frac{1}{\varepsilon_0} \int_V \rho(r)\, dV = \frac{Q(r)}{\varepsilon_0}$$

Since the electric field is normal to the cylindrical surface A with radius r, the surface integral yields $2\pi\, r$ and the electric field $\vec{E}(r)$ becomes:

Eq. 4.82 $$\int_A \vec{E}\, dA = 2\pi\, r\, \vec{E} = \frac{Q(r)}{\varepsilon_0} \quad \rightarrow \quad \vec{E}(r) = \frac{Q(r)}{2\pi\, r\, \varepsilon_0}$$

According to classical electrostatics the internal electrostatic energy is given by:

Eq. 4.83 $$E_{int} = \frac{\varepsilon_0}{2} \int_V \vec{E}(r)\, \vec{E}(r)\, dV = 2\pi \frac{\varepsilon_0}{2} \int \vec{E}(R)\, \vec{E}(R)\, R\, dR = \frac{1}{4\pi\, \varepsilon_0} \int \frac{Q(R)^2}{R} dR$$

The total electrostatic energy E_{tot} can be written as a single integral over r combining Eq. 4.80 and Eq. 4.83:

Eq. 4.84 $$E_{tot} = E_{ext} + E_{int} = \int_0^\infty \left\{ \phi(r)\, Q'(r) + \frac{Q^2(r)}{4\, \pi\, \varepsilon_0\, r} \right\} dr$$

This equation is already in the canonical form for variational calculus. The distribution that minimizes E_{tot} under given boundary conditions can be found by solving the Euler-Lagrange Equation:

Eq. 4.85 $$\frac{\partial}{\partial r} \frac{\partial L}{\partial Q'} - \frac{\partial L}{\partial Q} = 0$$

where $L = \left\{\phi(r)\, Q'(r) + \frac{Q^2(r)}{4\,\pi\,\varepsilon_0\, r}\right\}$, the integrand of Eq. 4.84, is the Lagrange Function associated with the variational problem. Eq. 4.85 leads to:

Eq. 4.86 $$Q(r) = 2\pi\epsilon_0\, r\, \phi'(r)$$

$$Q'(r) = 2\pi\epsilon_0 \left(\phi'(r) + r\, \phi''(r)\right)$$

If the cumulative charge $Q(r)$ is the amount of charge within a cylinder of radius r around the z-axis, Eq. 4.86 can be used to finally derive $\rho(r)$ with the help of Eq. 4.79.

Eq. 4.87 $$\rho(r) = \frac{1}{2\pi\, r} Q'(r) = \epsilon_0 \left(\frac{\phi\prime(r)}{r} + \phi''(r)\right)$$

This equation is applicable to calculate $\rho(r)$ for any given cylindrical symmetric potential. The effective electric potential $\phi_{eff}(r)$ of a linear ion-guide scales with the nth power of r [Gerlich, 1992]:

Eq. 4.88 $$\phi_{eff}(r) = \phi_0 \left(\frac{\mathrm{r}}{r_0}\right)^{2n-2} \quad \text{with} \quad \phi_0 = \frac{n^2}{4} \frac{\left(q\, V_{rf}\right)^2}{m\, \Omega^2\, {r_0}^2}$$

Eq. 4.86 shows that $Q(r) = 2\pi\epsilon_0\,(2n-2)\,\phi_{eff}(r)$ is a monotonically rising function with r. The maximum radius r_m to which the charge distribution extends, can be determined by the requirement $Q(r_m) = Q_0$. This yields:

Eq. 4.89 $$r_m = {r_0}^{\sqrt[2n-2]{\frac{Q_0}{2\pi\epsilon_0\,(2n-2)\,\phi_0}}}$$

The charge density within $r < r_m$ is given by Eq. 4.87:

Eq. 4.90 $$\rho(r) = \frac{\epsilon_0}{\mathrm{r}^2}\, \phi_{\mathrm{eff}}(\mathrm{r})\,(2n-2)^2 = (2\mathrm{n}-2)\epsilon_0 \mathrm{Q}_0 \frac{r^{2n-4}}{{r_m}^{2n-2}}$$

Note that for $n = 2$ (parabolic external potential of a quadrupole ion-guide) $\rho(r)$ is independent of r. For potentials with $n > 2$, the charge desity peaks at $r = r_m$. In all cases r_m itself rises with rising charge Q_0, while $\rho(r)$ stays constant for all $r < r_m$. From Eq. 4.89 it follows that this point is reached when $Q_m = 2\pi\epsilon_0\,(2n-2)\,\phi_0$.

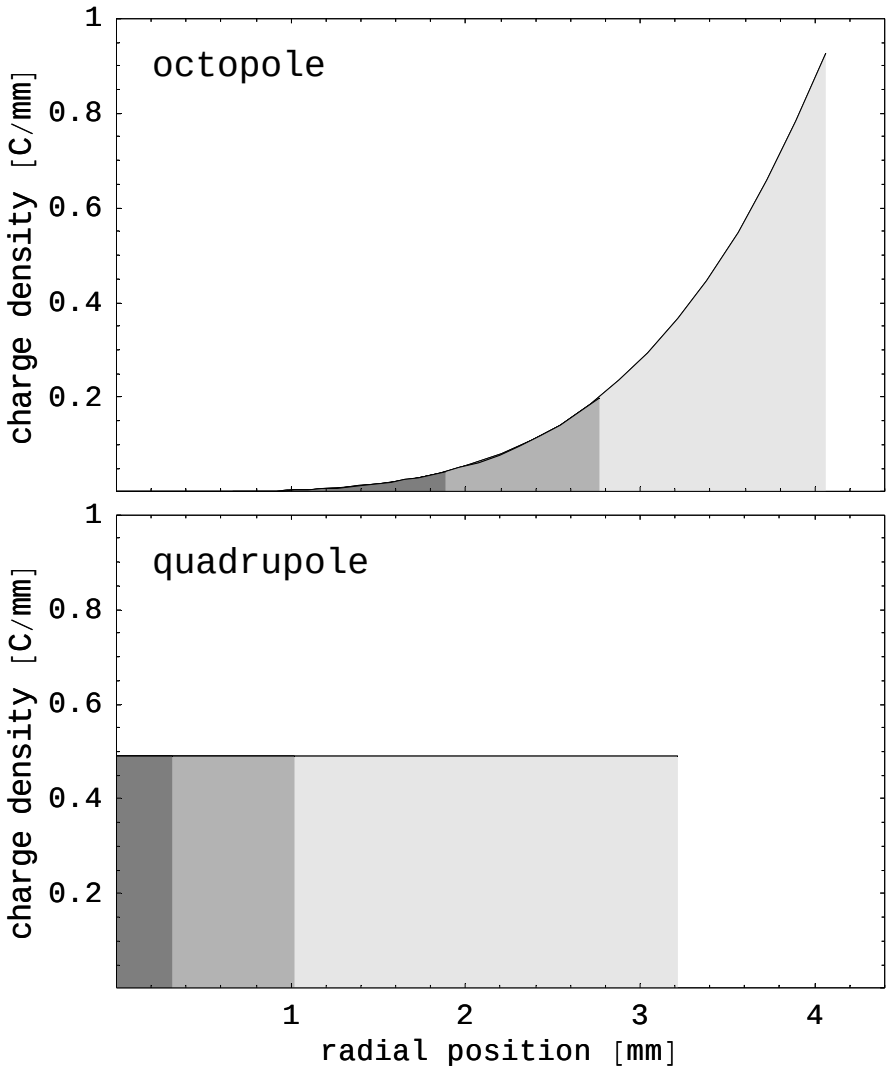

Figure 4.29. Simulated charge distribution of an ion-cloud in an octopolar potential (upper panel) and a quadrupolar potential (lower panel) using Eq. 4.89 and Eq. 4.90 with $\Phi_0 = 500\,\mathrm{V}$ and $r_0 = 6\,mm$. The total number of charge Q_z trapped is $10^9\ cm^{-1}$ (light grey), $10^8\ cm^{-1}$ (middle grey), $10^7\ cm^{-1}$ (dark grey).

For the case of an octopole ion-guide ($n = 4$) Eq. 4.89 and Eq. 4.90 transform to:

Eq. 4.91 $$r_m(n=4) = r_0 \sqrt[6]{\frac{Q_0}{12\pi\epsilon_0\,\phi_0}}$$

Eq. 4.92 $$\rho(r, n=4) = 36\frac{\epsilon_0}{\mathrm{r}^2}\,\phi_{\mathrm{eff}}(\mathrm{r}) \;= 6\,\mathrm{Q}_0\,\epsilon_0\,\frac{r^4}{{r_m}^6}$$

Eq. 4.92 shows that ions in an octopole ion-cage tend to accumulate off center. The size of the ring of maximum ion-density increases with the number of trapped particles (see Figure 4.29). Note, that this model assumes a zero temperature ($T = 0$)

of the particles and no collisions with a quenching gas. However, for ion numbers close to maximum capacity of an ion-cage, the electrostatic forces will be dominating. According to Chamenois [2009] the thermal equilibrium state of a non-neutral plasma in a electrostatic potential and at a temperature T can be described as $\rho \propto \mathrm{Exp}\left(-\mathcal{E}(\boldsymbol{r})/(k_B\,T)\right)$, where $\mathcal{E}(\boldsymbol{r})$ is the energy of a particle at position $\boldsymbol{r}$. It results from the external electrostatic potential and the mean-field Coulomb repulsion potential (internal potential). Since the internal potential is related to the space charge distribution by Poisson's equation, this expression can only be analytical solved in the extreme cases $T \to \infty$ and $T \to 0$. The $T \to 0$ limit of the above expression yields Eq. 4.90.

Ion densities from an experiment with Ar_2^+ ions are depicted as radial distribution in Figure 4.30 along with the model calculation discussed before. At the maximum trapping conditions of $Q = 1.2\,10^9$, ions were located around $r = 4\,mm$ predominantly. This is reproduced well by the model calculation. For a better overlap the simulation result has to be convoluted with the laser-beam profile which has a FWHM of about 2 mm. Detailed analysis will be given in a forthcoming publication[1].

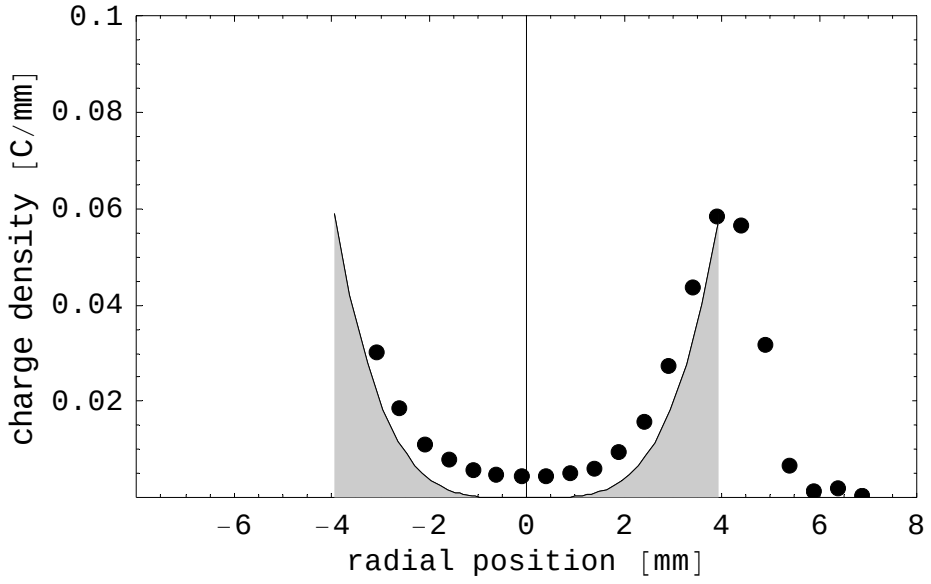

Figure 4.30. Radial distribution of the ion-density in a octopole ion-trap with 200 V rf amplitude. Dots are measured data of Ar_2^+ ions from A. Terasaki (personal communications). The line shows the calculated distribution based on Eq. 4.92.

[1] Terasaki, Kondow, Majima, Santambrogio, Bartels, Meinen and Leisner: Spatial distribution of ions in a linear octopole radio-frequency ion-trap in the space-charge limit Phys. Rev. A, in preparation.

4.9 Characterization of the inlet octopole

The trapping capacity of the octopole ion-trap is the key parameter for being able to do optical or X-ray spectroscopy on small nanoparticles. Up to 10^7 particles per cubic centimeter are required to achieve a measurable optical absorption signal in the visible for strongly absorbing materials like iron oxide particles. As shown in the foregoing section, the spatial distribution of the trapped particles will extend to larger radii with increasing particle number since space charge effects add to the pseudo potential of the electrodynamic trap. This limits the storage capacity of an electrodynamic ion-cage.

4.9.1 Storage capacity

The storage characteristics of the trap were assessed by accumulating particles for various time periods by analyzing the ion pulses leaving the trap. SiO_2 particles from a microwave plasma source were used. The diameter of the particles was determined by the TRAPS-TOF device (see section 4.10) to be $d_p = (6.4 \pm 0.5)\, nm$. The particles were transferred by the ADL into the vacuum as shown in Figure 4.1. After passing the skimmer, the particles enter the octopole ion-guide. The background pressure of the gas inside the octopole is $1.8\, Pa$. The pressure downstream from the octopole was $0.03\, Pa$ with a helium gas flow of $31\, Pa\, L\, s^{-1}$ during the experiment. The octopole was driven with a sinusoidal waveform at a frequency of $50\, kHz$, an amplitude of $255\, V$ and an DC offset voltage of $-186\, V$. This provides a beam current of $100\, pA$ as measured by the electrometer at FC_1. A voltage of $-350\, V$ was applied at the exit lens of the ion-guide for trapping the particles in the octopole ion-trap. This potential could be switched to ground by a fast MOSFET-Push-Pull switch (HTS 61-03-GSM, BEHLKE Electronic GmbH, Germany) within $500\, ns$ for a period of $40\, ms$ (for ion-trap operating modes see Figure 4.26).

Figure 4.31 shows exit pulses for increasing filling time. It is interesting to notice that the pulses first grow in height and then, for prolonged filling time, they grow preferentially in width. This indicates that the trap seems to be gradually filled, beginning from the exit lens towards the inlet. Obviously, the particles are concentrated at the exit of the octopole by the drag force of the gas flow through the

octopole. The average distance between two particles in a maximum loaded trap is about $30\,\mu m$. Thus a Coulomb repulsion of $3\,10^{-19}\,N$ is acting between the two particles. A drag force of the same order of magnitude caused by the gas flowing through the ion-guide is acting on the particles and pushes them towards the exit of the ion-guide. This interpretation is supported by the observation that, under normal operating conditions, no potential at the entrance lens of the octopole is needed in order to trap particles. Figure 4.32 shows the total number of particles trapped as a function of filling time. A maximum trap capacity of $5\,10^{8}$ particles is reached at a filling time of about $10\,s$ with a beam of $6.2\,10^{8}$ particles per second entering the trap. If one assumes that the particle cloud extends to the octopole rods, the particle density is $4\,10^{7}$ particles per cubic centimeter. This is in perfect agreement with the theoretically predicted maximum trap capacity of $3.7\,10^{7}$ particles per cubic centimeter [Douglas et al., 2005].

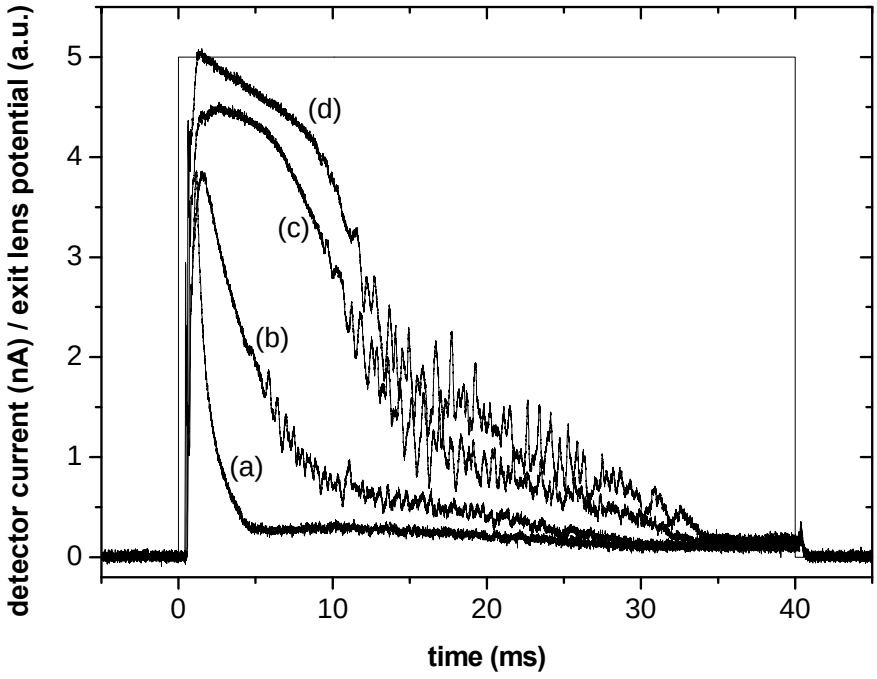

Figure 4.31. Particle pulses obtained from the octopole ion-trap for various filling times dt. (a) $dt = 0.2\,s$, (b) $dt = 0.5\,s$, (c) $dt = 1.5\,s$, (d) $dt = 10\,s$. The intensity of the filling beam was $0.1\,nA$.

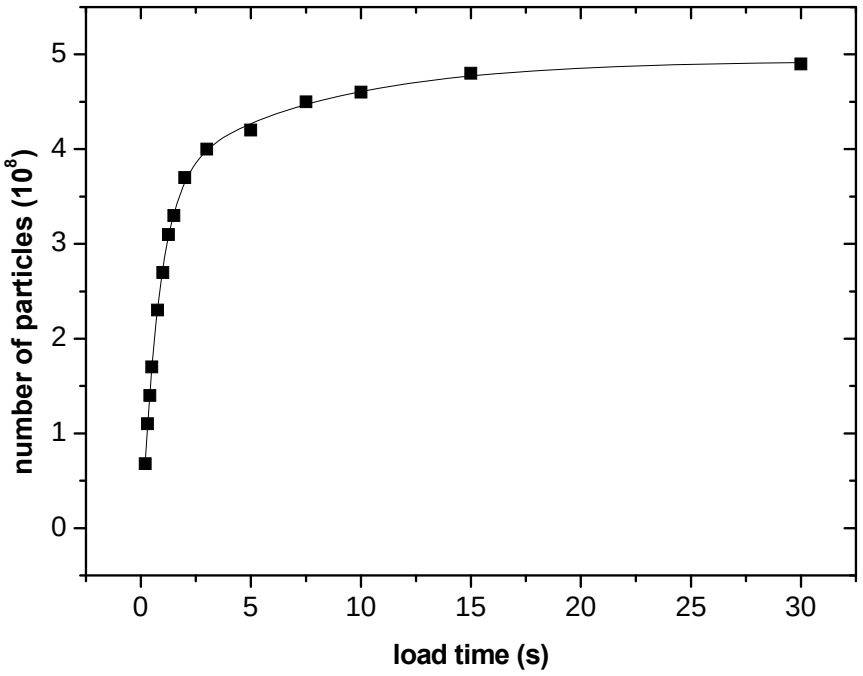

Figure 4.32. Storage capacity of the octopole ion-trap. $(6.4 \pm 0.6)\ nm$ SiO_2 particles have been filled into the octopole ion-trap with a current of $0.1\ pA$ singly charged ions.

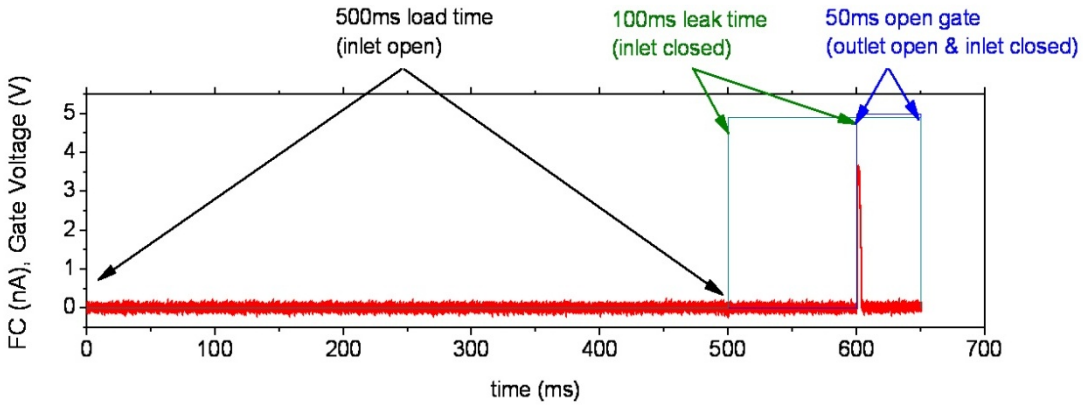

Figure 4.33. Operation chart of the leakage experiment. The signal induced by the particle beam on the Faraday cup electrometer is shown in red. The green line indicates the “closed” status of the inlet lens and the blue line indicates the “open” status of the outlet.

4.9.2 Storage stability

The maximum trap capacity is limited by the number of particles leaking out of the trap. The leakage is due to particle-particle Coulomb interactions, which diphase the particle motion from the RF field. It can be measured by varying the storage time. The operation chart of the leakage experiment is depicted in Figure 4.33. After operating the trap in "filling mode" (see Figure 4.26), the entrance and exit lens are kept at such high repelling potentials that particles can neither enter nor leave through the lens ("storage mode"). The exit potential is switched to ground after a varying storage time ("extraction mode") and the signal induced on the Faraday cup electrometer by the particle beam is recorded. This gives a measure of the particle concentration decay $N(t)$, which can be expressed with the assumption of a constant leakage factor C_l as:

Eq. 4.93 $$\frac{\partial N}{\partial t} = -N\,C_l \quad \rightarrow \quad \ln\left[\frac{N(t)}{N_0}\right] = -C_l\,t$$

Figure 4.34 shows the decrease of the stored particles in the trap as a function of storage time. A linear fit to $\ln[N(t)/N_0]$ over t yields a leakage factor of $C_l = 8.5\,10^{-2}\,s^{-1}$. Thus the mean residence time of the particles in the almost full octopole ion-trap is $12\,s$. This experiment demonstrates the stability of rigid, non-volatile particles inside the trap. But it is known from experiments with flexible bio-molecules that even very labile particles can be trapped in an electrodynamic potential for hours [Iavarone et al., 2006]. If the trapped particles have semi-volatile components, the storage time of the particles might become limited by the evaporation rate. However, it will be shown in section 5.2.2 that residence times up to one hour can be realized in the linear ion-trap EDC 2, if conditions are favorable. The relatively short mean residence time of $12\,s$ in EDC 1 can be explained by losses due to the extreme high inlet velocity of the particles and the carrier gas. Particles entering EDC 2 are decelerated inside EDC 1 already by at least one order of magnitude.

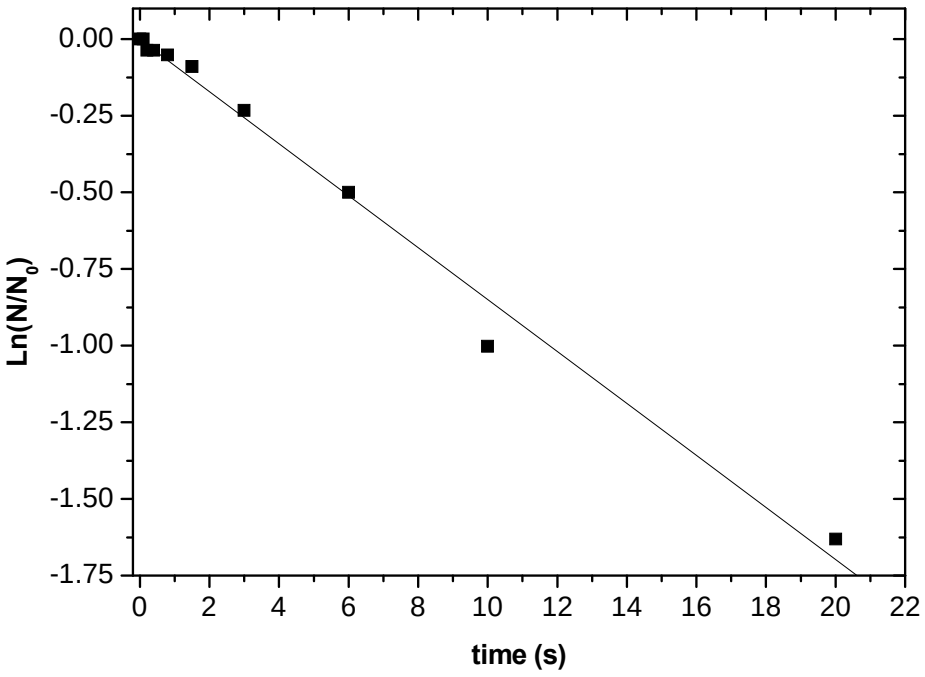

Figure 4.34. Particle retention rates of the octopole trap in storage mode as a function of storage time. The experiment was performed with a beam of $0.1\,pA$ ($1.2\ 10^9$ particles s^{-1}) singly charged $(6.4 \pm 0.6)\ nm$ diameter SiO_2 particles.

4.10 The ion-trap TOF spectrometer

From the time interval between the opening of the ion-trap and the signal on the Faraday cup, the diameter of the particles and their spatial distribution in the trap can be inferred. For these measurements the trap is filled with a comparatively small number of particles in order to minimize space charge effects and to obtain exit pulses sharp in time. By varying the offset potential of the octopole trap, the kinetic energy of the exited particles can be varied. In Figure 4.35 extraction pulses are shown that were obtained by filling a total number of 10^5 particles into the trap before opening the exit lens for $4\,ms$. The DC offset potential U_{DC} of the octopole rods relative to ground was $-179\,V$ and $-155\,V$ for the first and second pulse, respectively. A shift in time occurring from the different acceleration of the ions with the mass m and the charge q is evident.

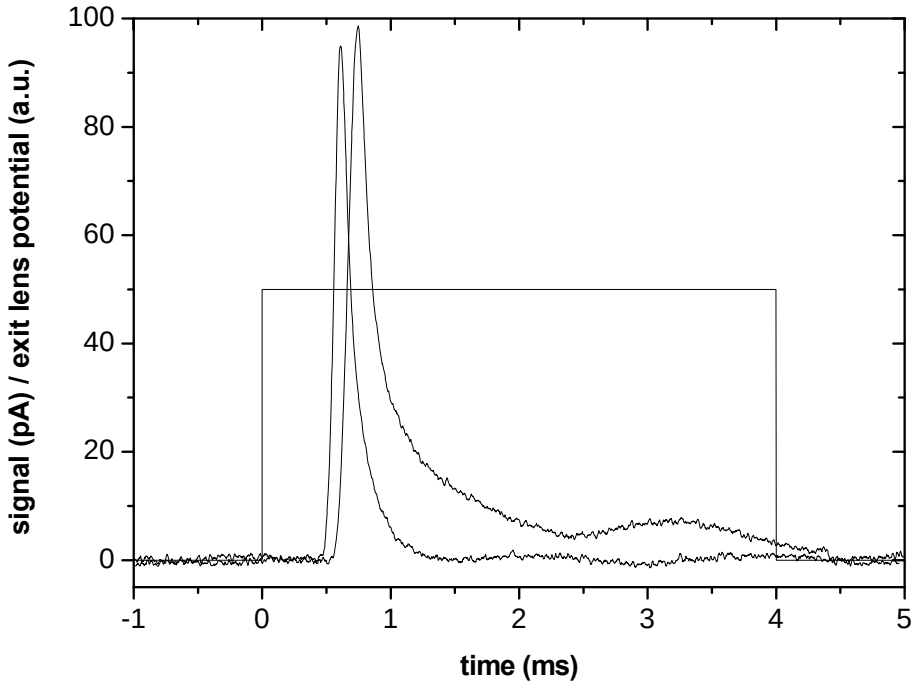

Figure 4.35. Exit lens potential and time-of-flight signals for SiO_2 particles starting from different potentials. The left peak is achieved by $U_{DC} = -179\,V$ and yields a flight time of $0.61\,ms$. The right peak is achieved by $U_{DC} = -155\,V$ and yields a flight time of $0.74\,ms$.

Since the initial velocity v_0 of the particles is a priory unknown, a series of flight times t_i at different accelerating offset potentials was measured in order to eliminate the initial velocity from the mass analysis. The kinetic energy is assumed to be the sum of the initial kinetic energy and the acceleration at U_{DC}.

Eq. 4.94 $$E_{kin,i} = \frac{m}{2} {v_0}^2 + q\, U_{DC,i}$$

If U_{DC} is plotted as a function of ${t_i}^{-2}$, a linear relation is expected which allows m and v_0 to be determined.

Eq. 4.95 $$U_{DC,i} = \frac{{L_{eff}}^2}{2} \frac{m}{q} \left[\frac{1}{t^2}\right]_i - \frac{m}{q} \frac{{v_0}^2}{2}$$

L_{eff} is the effective length of the flight distance which can be deduced from the geometry of the setup. If the particles are assumed as homogeneous spheres carrying a single charge, the particle diameter can be calculated. The analysis of the full dataset, Figure 4.35 was extracted from, yieldes values of $d_p = (6.8 \pm 0.5)\, nm$ and $v_0 = (312 \pm 34)\, ms^{-1}$. The particle diameter and standard deviation corresponds to values achieved by PMS measurements (compare Figure 4.17). The initial velocity seems to be a reasonable value when compared to the calculated particle velocity shown in Figure 4.15.

TOF measurements of $NaHCO_3$ particles have been compared to particle diameters determined by SMPS (DMA Classifier: TSI model 3085, CPC: TSI model 3025) in order to verify this new method. Figure 4.36 shows a particle diameter distribution of $NaHCO_3$ particles in a helium atmosphere produced by an atomizer at atmospheric pressure. The diameter distribution measured by the SMPS peaks at 9.8 nm and has a FWHM of about 3 nm. The mean diameter measured by the TOF is $d_p = (11.7 \pm 2.2)\, nm$. This indicates that both approaches yield virtually the same results, indicating the reliability of the present work.

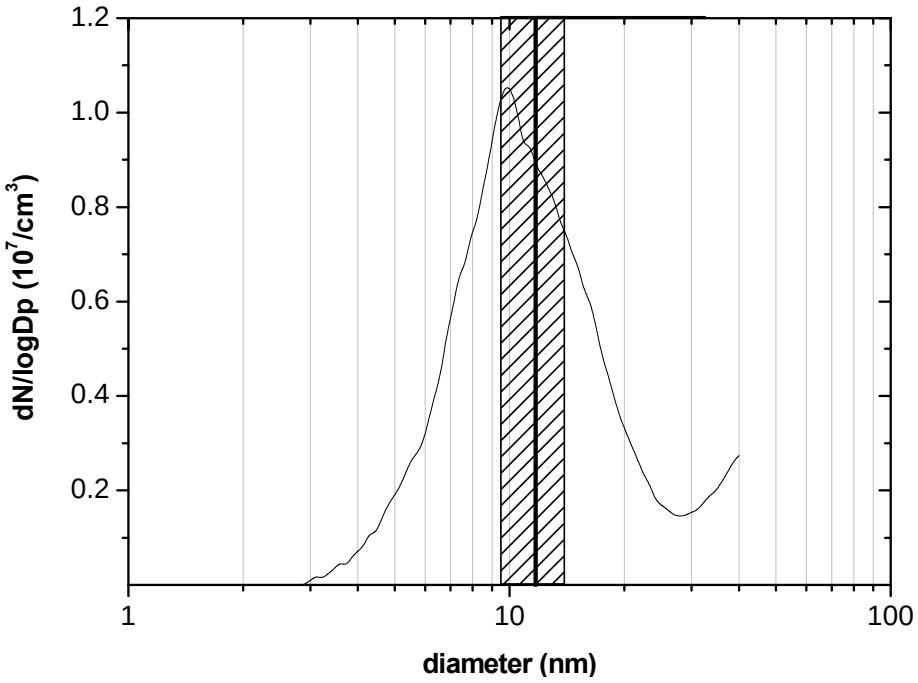

Figure 4.36. $NaHCO_3$ particles in helium produced by the atomizer. Solid line: SMPS measurement. Vertical bold line: TOF result with measurement error (shaded area).

TOF measurements of Si nanoparticles of been compared to TEM measurements. Nanoparticles were produced with the MPPS at $100\,mbar$ pressure and $300\,Watt$ microwave power. Metallic Si nanoparticles were produced by mixing $30\,sccm$ 1 % SiH_4 in He 5. with $3000\,sccm$ He 5.0 upstream from the MPPS. TEM grids (Cu-mesh with carbon coating, No. S160, PLANO GmbH, Wetzlar, Germany) were placed downstream from the quadrupolar ion-trap (EDC 2). Particles were accumulated inside EDC 2 and extracted from the trap on the TEM grid. 300 particle pulses were deposited at the TEM grid which corresponds to a theoretical surface coverage of $1100\ 10^6\ mm^{-2}$.

Nanoparticles coated TEM grids were exposed to the ambient for four weeks prior investigation with a PHILIPS CM 30 T/STEM[2] (300 kV acceleration; point resolution $0.23\,nm$). Figure 4.37 shows the resulting TEM/STEM image. The particles are arranged as agglomerates at the grid's surface. It is quite likely that the agglomeration occurred post deposition at the grids. Agglomeration can occur, when particle with

[2] The Phillips CM 30 was operated by Vigna Szabo, Institute for Material Research (IMF), Karlsruhe Institute of Technology, Germany

charge of different polarity or charged and neutral particles get in contact. Equally charged particles will repel each other. Thus, agglomerates will have different mass/charge ratio (m/z) than the individual particles had before. The quadrupole bender guiding the ion-beam from EDC 1 into EDC 2 is a m/z filter, guiding only a single m/z to EDC 2. Since the agglomerate size in a wide range (and thus in a wide m/z ratio), agglomeration must have occurred past deposition at the grid.

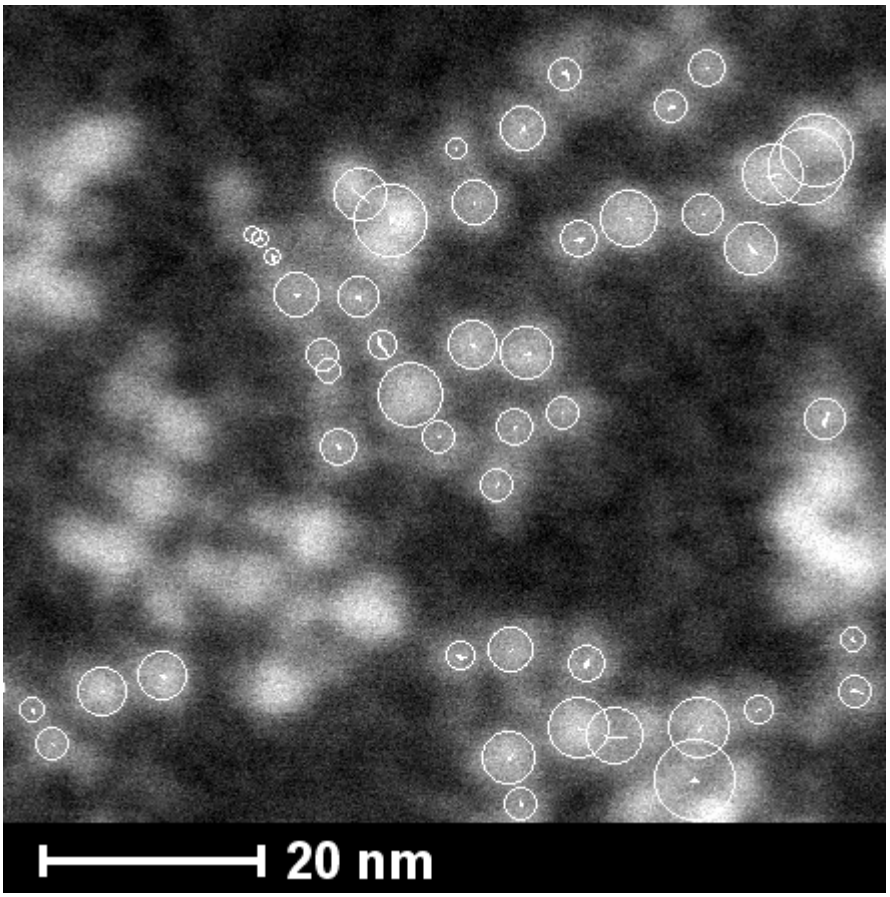

Figure 4.37. Dark-field STEM image of Si nanoparticles on carbon substrate. The circles are the particles sizes fitted to the image for particle size distribution analysis. The resulting gauss distribution peaks at and has a FWHM of .

Size determination of the particles was performed by fitting circles to the particle areas after appropriate image processing (all routines written in LabView 8.6, National Instruments, USA). Analysis of the Si nanoparticles yields a nearly gauss shaped size distribution with a peak at 3.9 nm and a FWHM of 1.11 nm. The mean diameter measured by the TOF is $d_p = (4.9 \pm 0.6)\, nm$. This indicates that both approaches yield virtually the same results, but again, the size measured by TOF is larger than determined by the alternative size determination. If particle sizes of both intercomparison experiments are converted into particle masses, the result obtained by TOF is larger by a factor of 1.75 than the particle mass obtained from the alternative method. In both cases the correlation of the mass determination results is 1 within the measurement precisions.

CHAPTER 5

Optical extinction spectroscopy

Atmospheric aerosols affect Earth's energy budget by scattering and absorbing radiation (the "direct effect") and by modifying amounts and microphysical and radiative properties of clouds (the "indirect effect"). On a global average basis, the sum of direct and indirect forcing by anthropogenic aerosols at high altitudes is almost certainly negative, though the physical details of the underlying processes are on a low level of scientific understanding [IPCC, 2007]. The addition of aerosols to the atmosphere alters the intensity of sunlight scattered back to space, absorbed in the atmosphere, and arriving at the surface. The interaction between aerosols and radiation depends on their complex index of refraction, which is related to the particles' chemical composition. Looking at primary particles in the nanometer range, optical properties become strongly dependent on size and chemical composition [Bruchez et al., 1998; Sun et al., 2003]. For metal or semiconductor materials the optical properties of nano-sized material have their origin in the surface Plasmon, which strongly depends on size, shape and surrounding of the particle [Kreibig et al., 1985; Underwood et al., 1994; Haynes et al., 2001]. Experimental studies of optical properties of nanoparticles are not trivial, since particles in this size range have extreme low absorption cross sections and if deposited on substrates, their surface properties would be altered. This hampers the use of regular spectroscopic methods.

Cavity assisted spectroscopies are an increasingly common techniques for making very sensitive optical extinction measurements [O'Keefe and Deacon, 1988; Romanini et al., 1997; Engeln et al., 1998]. Most of the research with cavity assisted systems has concentrated on gas-phase samples [Berden et al., 2000], but recently there have been several studies of optical extinction by aerosol particles [Sappey et al., 1998; Moosmüller et al., 2005], ions [Terasaki et al., 2007] and clusters [Terasaki et al., 2009].

5.1 Cavity assisted extinction spectroscopy

Cavity assisted extinction spectrometers facilitate an optical cavity, built of two highly reflective mirrors in which photons propagate for a prolonged time. A virtually elongated optical light path for the extinction measurement is provided by such a cavity. The intrinsic loss of the resonator can be measured by the lifetime of the photons within the cavity. In the case of a cavity pumped by light pulses, the decay time of the light leaking out of the cavity yields the mean photon lifetime. This technique is named cavity ring-down spectroscopy (CRDS). Since this technique relates the extinction inside the cavity to decay times, it is insensitive to intensity fluctuations of the light source. If the cavity is pumped by a continuous light source, the light leaking out of the continuously pumped cavity yields the mean photon lifetime. As this technique is more equal to classic absorption spectroscopy, enhanced by a long optical light path, it is named cavity enhanced absorption spectroscopy (CEAS). Bearing the disadvantage of being sensitive to fluctuations of the light source, CEAS is much simpler to realize technically, since no pulsed light source is needed.

Mechanical vibrations of the optical setup in the wavelength range of the light source would cause alternating constructive and destructive interferences of the light beam known as “mode beating”. For this reason, high finesse cavities have to be optically coupled to the light source if the coherence length of the light is not shorter than the source-cavity and mirror-mirror distance. As this is a severe experimental difficulty for setups in vibrating environments, it is advantageous to use incoherent light sources like light emitting diodes (LEDs) [Ball et al., 2004; Meinen et al., 2010b]. Both techniques, CRDS and CEAS, are feasible as monochromatic or “broad-band” spectrometers. The width of the useable wavelength region is determined by the reflectivity of the high reflective mirrors. Usually a bandwidth of 10 to 30 nm can be realized. (Bandwidth of the mirror is defined as the region over which $(1 - R)$ is within a factor of two of the center wavelength peak reflectivity.) The measured extinction of particulate matter depends on the number of particles within the volume of the intracavity light path. As the beam of a laser light source inside a cavity is very narrow, fluctuations in the number of particles inside the beam result in rapid change

in the measured extinction following Poisson statistic [Butler et al., 2009]. This becomes more pronounced at low particle number densities when there might only be $100 - 1000$ particles in the interaction region. Those fluctuations are negligible for studies of gaseous samples where $> 10^6$ molecules will be within the intracavity laser volume. Incoherent light sources usually emit highly diverging light beams which are imaged at the full aperture of the entrance cavity mirror. The resulting light beam inside the cavity also spans over the full aperture of the cavity mirror with a slight tail centered between the mirrors [Spuler and Linne, 2002]. Since particle number densities $> 10^6\ cm^{-3}$ can usually be provided under experimental conditions, particle numbers $> 10^6$ can easily be brought into the large interaction volume and particle number fluctuations are negligible.

Cavity assisted spectrometers measure the total extinction by the sample contained within the optical cavity. The extinction is the sum of scattering and absorption losses. Various strategies have been developed to separate the contributions from the real and complex parts of the refractive indices of the particles. One approach is to measure the extinction efficiency Q_{ext} for various known particle sizes and comparison with Mie scattering calculations [Spindler et al., 2007; Dinar et al., 2008]. Here, Mie calculations are used to verify the extinction cross section determined by CEA spectroscopy (section 5.2.1).

5.1.1 Theory of cavity assisted measurement techniques

Cavity assisted spectrometers make use of a set of high reflective mirrors with reflectivity R to provide long light paths for extinction spectroscopy (see Figure 5.1). A small fraction of light shining on the entrance mirror is transmitted into the resonator. The transmitted intensity is given by the product of the light intensity I_{source} and the transmittance of the mirror $T = 1 - R$. Once inside the cavity, the light with intensity I_{in} propagates the distance L_0 to the second (exit) mirror, were the fraction $I_{in} \cdot R$ is reflected and the tiny fraction $I_{in} \cdot T$ is transmitted by the high reflective mirror surface. The remaining fraction of light inside the cavity propagates back to the entrance mirror, where the process recurs until no light is left inside the cavity. If an absorber with the absorption coefficient α is inside the resonator, the light intensity inside the cavity is reduced by $\alpha \cdot L$ with each traverse. Depending

whether the input intensity I_{source} is pulsed or continuous, the observer looking at the exit mirror senses intensity decay or continuous absolute intensity related to the losses inside the cavity, respectively[1]:

Eq. 5.1 $$I(t,\alpha) = I_{source}\, exp\left[-\frac{c}{L_0}(\alpha\, L + |Ln[R]|)\, t\right] = I_{source}\, exp\left[-\frac{t}{\tau}\right]$$

Eq. 5.2 $$I(\alpha) = I_{source}\, \frac{exp[\alpha\, L](R-1)^2}{exp[2\alpha\, L]-R^2}$$

Eq. 5.1 describes a decay of light inside a cavity (CRDS). As described in Eq. 5.2, the second technique (CEAS), using a continuous light source, measures an extinction loss by reduction of the total transmitted intensity. In the direct application of either technique, the extinction loss is yielded by comparison of a signal from the resonator with and without an absorbing or scattering species inside. In CRDS the decay of the empty (τ_0) and filled (τ) resonator is compared. In CEAS it is I_0 and I, respectively. The absorption coefficient (which is an extinction coefficient, exactly spoken) is determined by:

Eq. 5.3 $$\alpha_{CRDS} = \frac{1}{c}\frac{L_0}{L}\left(\frac{1}{\tau} - \frac{1}{\tau_0}\right)$$

Eq. 5.4 $$\alpha_{CEAS} = \frac{1}{L}\left(\frac{I_0}{I} - 1\right)(1 - R)$$

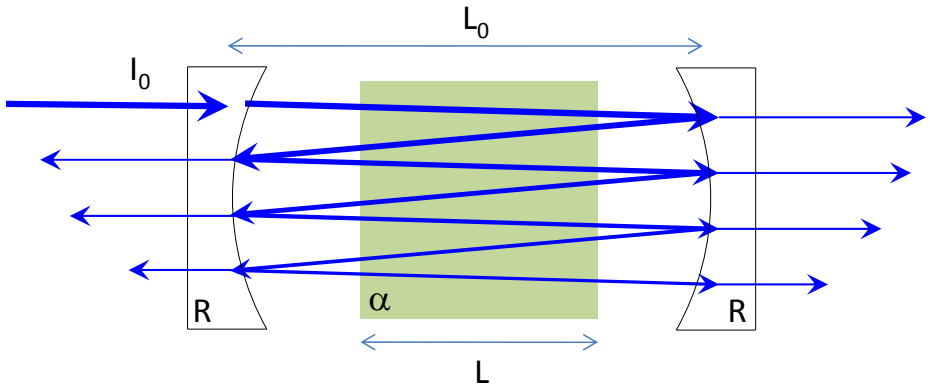

Figure 5.1. Scheme of a cavity assisted extinction spectrometer. I_0: Incident light intensity. R: Mirrors with high reflectivity. L_0: mirror distance. L: Length of the absorption path. α: Absorbing and/or scattering species.

1 Alternatively to this simplified explanation, the process can be described as probability of the existents of a photon inside the cavity. This leads to a mean photon lifetime inside the cavity [Platt et al., 2009].

5.1.2 Calibration of cavity assisted spectrometers

Though cavity assisted spectrometers are often labeled “calibration free” they are not in every case. Either approach demands determination of the resonator quality which is embodied as the mirror reflectivity R. For some evaluation approaches it may also be expressed as mean photon lifetime τ_0 or as a mean optical light path length $\overline{L_0}$ in the cavity [Platt et al., 2009]. These quantities are directly linked to each other by the constants resonator length L_0, and speed of light c: $R = Exp[-L_0/c\,\tau_0]$ and $\overline{L_0} = c/\tau_0$. The resonator quality is needed in Eq. 5.3 and Eq. 5.4 to transform measured optical density into the absorption coefficient α.

The determination of the mirror reflectivity R is usually straight forward for CRDS instruments. The decay of the empty cavity is measured by evacuating the resonator cell or filling it with extinction free “zero-gas”. Since this method does not relate to a known amount of absorber, it is calibration free, indeed. For a CEAS instrument which cannot be switched into CRDS-mode, the determination of R is only possible by introducing a well defined absorber into the cavity and comparing the transmitted intensity of the damped resonator (I) to the empty one (I_0). This can be done by a well characterized concentration of an absorbing gas or a highly polished glass plate with exactly known extinction. The calibration of this method is as good as the known absorption strength inside the resonator. CEAS can become calibration free as well, when the light source can be switched into pulsed operation such that R can be determined by means of CRDS.

For some applications it is beneficial to employ a broadband light source. This may either be the case if a broadband extinction feature is the scope of investigation or an incoherent light source (e.g. LED, Xe-Arc lamp) is used. In this case Eq. 5.3 and Eq. 5.4 become dependent of the wavelength λ, since they are relations of the wavelength dependent parameters $\tau_0(\lambda), \tau(\lambda), I_0(\lambda), I(\lambda)$ and $R(\lambda)$. Since $R(\lambda)$ varies with wavelength, the wavelength integrated decay measured at the exit mirror of the cavity is the summation of decays at different wavelengths covered by the light source (see Eq. 5.1). This effect becomes even more pronounced, when an absorber with an absorption line narrower than the light source spectrum is inside the resonator. The decay of a cavity pumped by a broadband light source can usually not be fitted by

a simple exponential function. Eq. 5.1 can be written as the time dependent signal $S(t)$ that has to be modeled by an integral over the wavelength:

Eq. 5.5 $$S(t) = I_0 \int I(\lambda)\, Exp\left[-\frac{c}{L_0}\left(\alpha(\lambda)\, L + |Ln[\, R(\lambda)\,]|\right) t\right] d\lambda + b$$

Where I_0 is the transmitted intensity at $S(t = 0)$, $I(\lambda)$ is the normalized emission spectrum of the light source, $\alpha(\lambda)$ is the wavelength dependent extinction coefficient and b is a baseline. For an empty resonator or a resonator filled with a species with slowly varying extinction with wavelength, it was shown by Meinen et al. [2010] that Eq. 5.5 can be modeled by a double exponential decay with minor overall error. The nonlinearity of the logarithm of the wavelength integrated decay usually increases with finesse of the resonator. Since mirror coatings are composed of multiple dielectric layers, higher peak reflectivity causes smaller FWHM of the reflectivity.

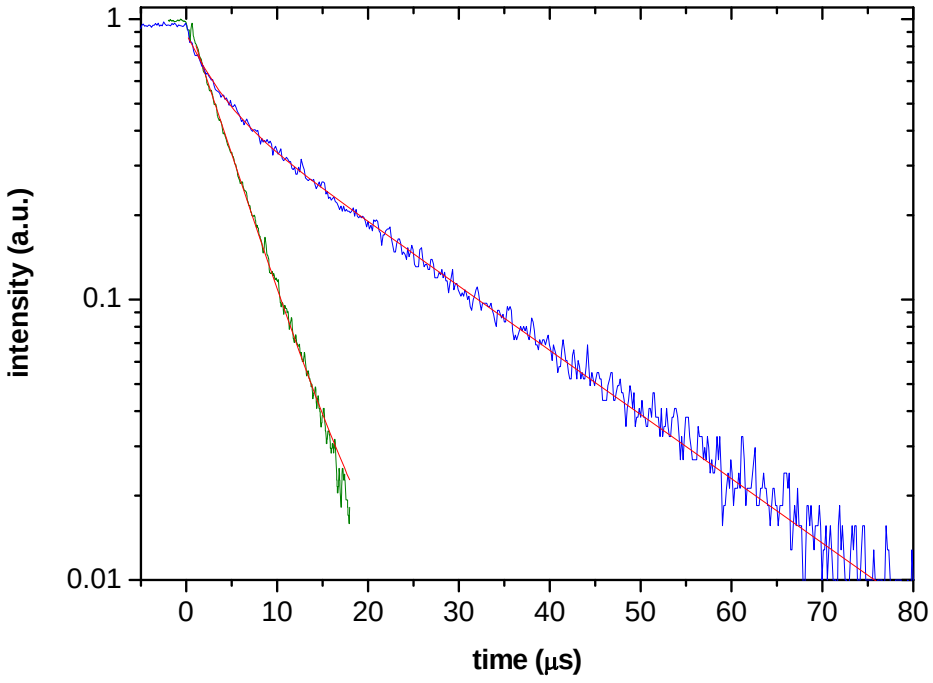

Figure 5.2. Decay of two cavities of different finesse pumped by the same incoherent broadband light source. Green: $R = 0.99980$ mirror. Blue: $R = 0.99995$ mirror. Red: Double-exponential fit to the data (Eq. 5.6).

This effect is demonstrated in Figure 5.2. The resonator of the TRAPS apparatus is equipped with two different pairs of mirrors with peak reflectivity at $405\, nm$ ($R = 0.99980$) and $415\, nm$ ($R = 0.99995$). These mirrors facilitate effective path

length of $4050\,m$ and $16200\,m$ at maximum reflectivity, respectively. An LED with peak emission at $405\,nm$ is used as light source. It can be seen from Figure 5.2, that the cavity with higher finesse has strong nonlinear decay in the log-plot, whereas the decay of the cavity with lower finesse can be modeled by a single exponential function with $\tau_0 = 4.4\,\mu s$ quite well.

The decay of the high reflectivity cavity can be separated in a fast ($\tau_a = 3.1\,\mu s$) and a slow ($\tau_b = 19.0\,\mu s$) component.

Eq. 5.6 $$I(t) = I_a\, exp\left[-\frac{t}{\tau_a}\right] + I_b\, exp\left[-\frac{t}{\tau_b}\right] + \text{b.}$$

The slow component τ_b is assigned to the peak reflectivity of the mirrors. The factor of the slower decay I_b is about twice the factor of the faster decay I_a. The proportion of I_a to I_b changes little, when particles inside the resonator cause a decrease of the time constants. For this reason it is assumed here that the integrated output of the CEAS signal is dominated by the maximum extinction path length. Note, that these assumptions are suitable for proof of principle measurements using the mirrors with higher reflectivity, but for exact extinction measurements the multiexponentiality problem discussed above has to be investigated by exact modeling of Eq. 5.5.

CEAS integrated intensity data is gained by fitting a horizontal line to all data with $t < 0$ by a simplex routine (see Figure 5.2). CRDS evaluation of an experiment requires a fit of two exponentials with five free parameters to the signal for all $t > 0$. Since the double exponential fit does not describe the decay exactly, the resulting parameters are not as stable as fitting a single free parameter to the CEAS data. Fluctuations of the absorption coefficient calculated by CRDS method are almost ten times higher than from the CEAS method. For the proof of principle measurements described below, it is advantageous to employ the CEAS method for obvious reasons.

5.2 Experiments with Fe_2O_3 nanoparticles

5.2.1 Extinction cross section determined by CEAS

For measurement of the extinction cross section of Fe_2O_3 nanoparticles, the quality of the resonator confining the quadrupolar ion-trap of the TRAPS apparatus is determined by its light intensity decay while the ion-trap is empty (helium background pressure $\sim 10^{-2}\, mbar$). 1000 ring-down events are averaged prior fitting a double exponential function with baseline (Eq. 5.6) to the data. The decay of the empty resonator ($\tau_0 = 13.6\, \mu s$) corresponds to a mirror reflectivity of $R = 0.99980$ and a total optical path length inside the cavity of $4080\, m$. Since the ion-trap doesn't extent over the full length of the resonator, the effective optical path length inside the ion-trap is $2266\, m$. Figure 5.3 depicts the transmitted intensity of the cavity. At time steps $0 - 100\, s$ and $700 - 800\, s$ no particles are inside the ion-trap and thus I_0 is recorded. Starting at time steps 100, 210, 360 and $520\, s$ the ion-trap is filled up with Fe_2O_3 particles. It takes about $30\, s$ to reach a constant particle number inside the ion-trap (total particle number (10^8): 2.12, 2.08, 2.05, 2.14). The intensity I for the CEAS evaluation is measured for the following $20\, s$ after the constant particle number is reached. After that, the number of ions is counted by switching the exit potential of the ion-trap to ground and detecting the current carried by the particle pulse by FC_2 (see Figure 5.10 in section 3.5.1). Eq. 5.4 is used to calculate the extinction coefficient of the ion-cloud inside the ion-trap for each particle pulse. The total particle number inside the ion-trap can be converted into a particle number density N_p, if assumed that the ion-trap is homogeneously filled over 95 % of its diameter (ion-cloud volume: $51\, cm^3$). Finally, extinction cross sections $\sigma = \alpha / N_p$ can be calculated from the extinction coefficients α and the corresponding particle number densities N_p. For the data shown in Figure 5.3, this procedure results in four values for the extinction coefficients. The root mean square and it's deviation is $\sigma_{ext} = (0.475 \pm 0.055)\, nm^2$. Mean particle diameter is determined by the TRAPS-TOF spectrometer $d_p = (4.7 \pm 0.4)\, nm$ (see section 4.10).

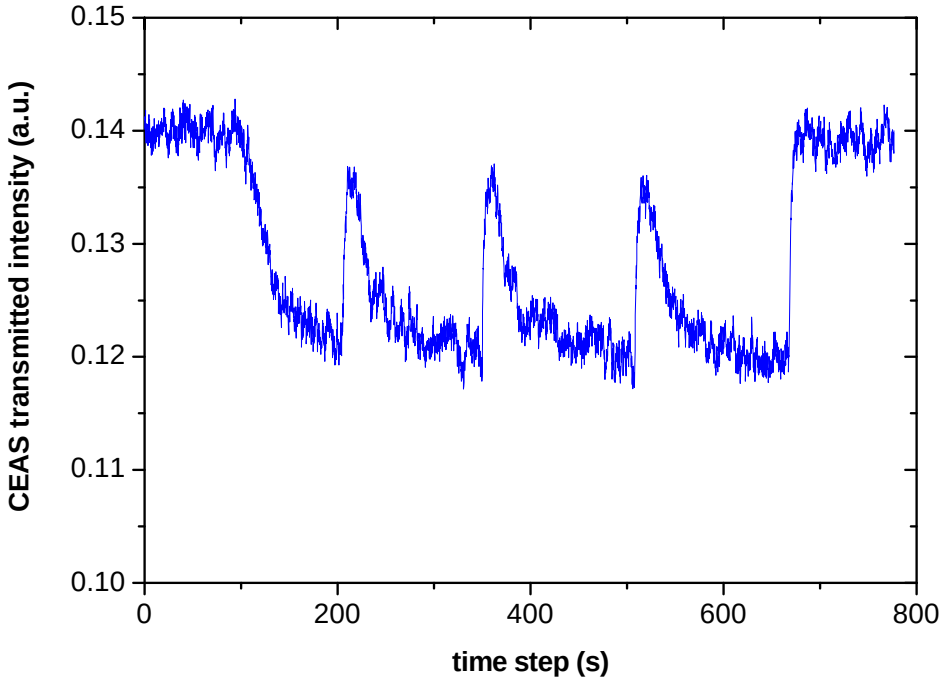

Figure 5.3. Transmitted intensity of a CEAS measurement of Fe_2O_3 with 4.7 nm diameter. First, the ion-trap confined by the cavity mirrors is empty. Minimum in the transmitted intensity correspond to a trap filled with about 10^8 particles.

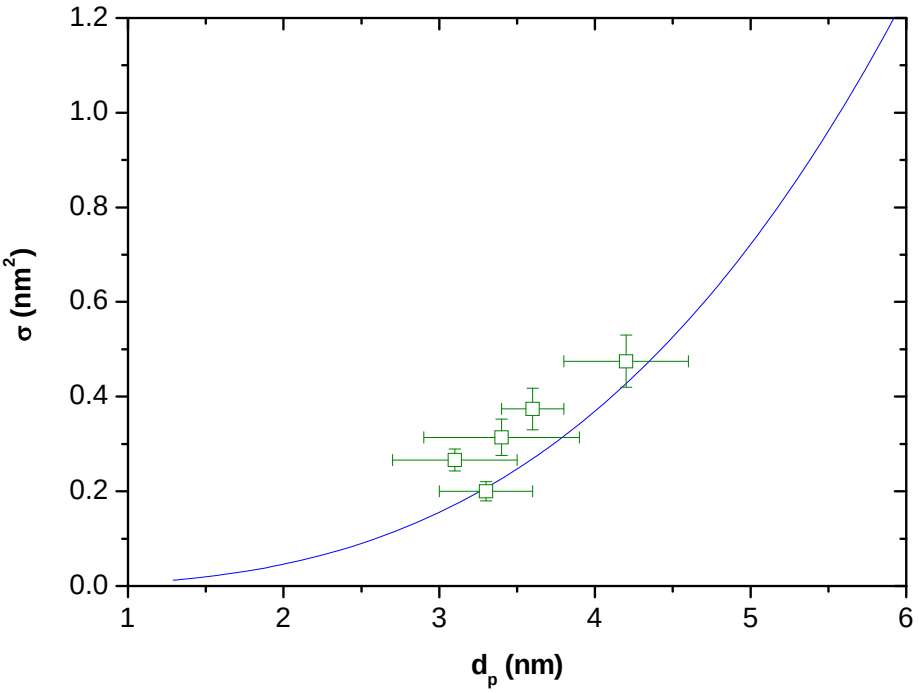

Figure 5.4. Extinction cross sections from CEAS measurements of Fe_2O_3 particles with different sizes (squares); in comparison to theoretical values from Mie-calculations (line).

Light interacting with a particle can be scattered and absorbed by the particle. The sum of these two processes is named extinction. It depends on chemical composition, size, shape, and orientation of the particles, the surrounding medium, and polarization and frequency of the incident light beam. Mie theory is well known to be based on the analytical solution of the Maxwell equations. By this theory, extinction of light by particles can be described. A comprehensive discussion of Mie theory is given in the textbook Boren and Huffmann [1983]. Code, based on this theory, is used to calculate extinction cross sections for Fe_2O_3 particles illuminated with $405\,nm$ wavelength. Optical constants of bulk Fe_2O_3 are $n = 2.43408$ and $k = 1.25912$ (www.astro.uni-jena.de). The calculated extinction cross section for particle in the diameter range $1 - 6\,nm$ is shown in Figure 5.4. Extinction cross sections determined by CEAS for different particle sizes are depicted in Figure 5.4 as well. Measured absorption cross sections are about $30\,\%$ higher than predicted by Mie-calculations. It is assumed in the calculation, that the particles are perfect spheres and the bulk optical constants are applicable for nanoparticles in the size range under investigation. Under these prerequisites there are three major uncertainties left: (1) Particle number density is underestimated because the ion-trap is not homogeneously filled up to 95 % of its diameter. (2) The mean (or dominant) mirror reflectivity is underestimated by fitting a double-exponential function to the decay of the empty resonator. (3) The TRAPS-TOF spectrometer has a systematic error overestimating the particle diameter. The first uncertainty can be investigated by analysis of the spatial distribution of the particles inside the ion-trap. An experimental setup as discussed in section 4.8.3 is suitable for this task. The contribution of the second uncertainty can be estimated by model calculations using Eq. 5.5 and Eq. 5.6. Similar model calculations have been reported for spectroscopy of the NO_3 radical with CRDS and CEAS-like spectroscopy [Meinen et al., 2010]. The third uncertainty can be minimized by facilitating a TOF spectrometer of higher performance and quality.

5.2.2 Ice nucleation on nanoparticles

Ice nucleation and reaction kinetics on small particles is the field of numerous studies in atmospheric science [Barthazy et al., 2006; Kulmala et al., 2007; Mason et al., 2007]. It was recently reported, that the hygroscopic growth rate of particles in the atmosphere can be affected significantly by coatings of organic material [Saathoff et al., 2003]. Möhler et al. [2005] reported that the formation rate of ice crystals on soot with 40 % organic compounds is two orders of magnitude less than for soot particles of the same size but with 16 % organic compounds, only. The authors argue that the ice nucleation of soot particles with low organic compound content is due to the deposition nucleation mode on soot particles that are only partly covered with organic carbon. There was no experimental technique available up to now, which is suitable to address this phenomenon. The TRAPS apparatus enables (1) to levitate free size-selected nanoparticles of different material and coating, (2) to collisionally cool them to very low temperatures ($< 100K$), (3) to expose the nanoparticles to an atmosphere with variable water vapor concentration, (4) to observe the growth of the nanoparticles by optical extinction spectroscopy, (5) and to investigate whether the ice nucleation starts on the clean soot surface or the organic coating at the soot surface by core level spectroscopy. In this section it will be demonstrated by a proof of principle experiment, that ice nucleation occurs on nanoparticles in a cooled quadrupolar ion-trap. The growth of the particles due to ice nucleation is monitored by CEA spectroscopy and particle loss rates of the electrodynamic cage.

Extinction coefficients and particle number density of nanoparticle clouds in the quadrupolar ion-trap are determined as described in section 5.2.1. The central quadrupolar ion-trap can be used for conditioning of the nanoparticles as described in section 3.5.3. Figure 5.5 shows data of two different experiment days. Nanoparticles where stored in the ion-trap which was cooled to $66\,K$ and $120\,K$. The helium gas pressure inside the ion-trap was leveled to $3.90\ 10^{-2}\ mbar$ by a leak valve. The gas passes the cold quadrupole rods prior to entering the center region of the ion-trap and thus adapted to the temperature of the cooled housing. Helium 5.0 with water content of $2\ ppm$ was either directly feed into the ion-trap, or the helium was humidified by a gas bubbler as described in section 3.5.3.

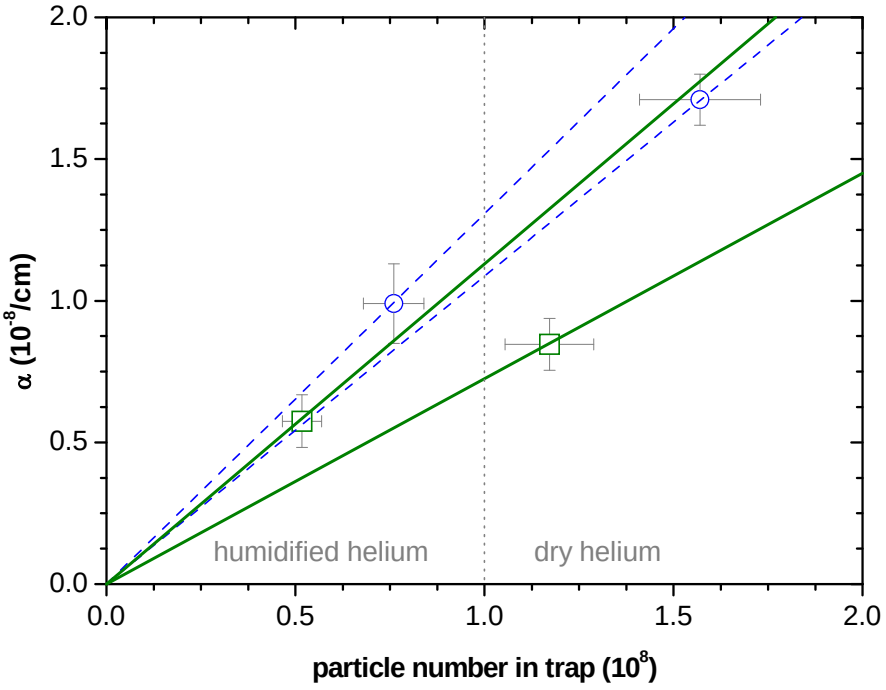

Figure 5.5. Ice nucleation experiment. Change in absorption cross section of cooled nanoparticles in a humidified atmosphere is monitored by CEAS. Experiment temperature 120 K (circles) and 66 K (squares).

Figure 5.5 shows absorption coefficients of Fe_2O_3 (size not determined) nanoparticle clouds in the ion-trap with the corresponding number of particles inside the trap from the two different experiment days. Extinction cross sections could be derived by $\sigma = \alpha / N_p$, but the embodiment of Figure 5.5 enables us to note two important features: (1) When humidified helium is introduced into the ion-guide, the total particle number inside the trap decreases. (2) The ratio of absorption coefficient and particle number, which is the extinction cross section, increases when humidified helium is present. Evidence for ice nucleation at the Fe_2O_3-particles is given by these observations. Apparently, particles get larger with higher water vapor content which is directly measured by the increasing extinction cross section. Furthermore, the lower number of particles inside the trap at constant filling rate indicates a shorter mean residence time of the particles in the trap. This can be explained by the increasing mass of particles where ice is nucleating on. The electrodynamic potential of the ion-trap is able to trap a certain particle mass to charge ratio. If the particle mass is increasing, the grown particles will literally fall out of the trap or hit the electrode rods.

The latter interpretation can be verified by a storage stability analysis of the ion-trap under several ice nucleation conditions. The leak rate of the ion-trap can be determined as described in section 4.9.2. The ion-trap is filled for $1000\,ms$ with a constant filling rate ("filling mode"). Than the entrance and exit potential of the ion-trap are kept at such high repelling potential that the particle can neither enter nor leave through the lenses ("storage mode"). In this time the particles grow due to ice nucleation and fall out of the trap when exceeding a certain mass to charge ratio. Finally the exit potential is switched to ground after a varying storage time ("extraction mode"), and the number of particles exiting the trap is determined by the current carried to FC_2. It can be seen from Figure 5.6 that the mean residence time of Fe_2O_3 particles with $d_p = (4.7 \pm 0.4)\,nm$ is longer when the ion-trap is at room temperature and helium gas sampled directly from a compressed gas cylinder (mean residence time $\sim 3200\,s$). If cooled to $120\,K$, the particle loss rate increases, such that the mean residence time is about $26\,s$. When helium is humidified prior entering the ion-trap, the mean residence time of the particle is about $9\,s$, only. This again, is indication for ice nucleation on the particles' surface. Even the small water vapor amount in the helium compressed gas cylinder is sufficient to let the particles grow to a mass which cannot be trapped by the ion-trap within $26\,s$. The nucleation rate increases with increasing water vapor concentration.

The particle growth rate can be estimated with some basic assumptions from the leak-rate experiment. For a quadrupolar ion-trap filled with the maximum number of ions, Eq. 5.91 from section 4.8.3 transforms to

Eq. 5.7 $$\rho(r) = 4\frac{\epsilon_0}{r^2}\,\phi_{\mathrm{eff}}(r) = \frac{2\,\epsilon_0}{{r_0}^3}\frac{q^2\ {V_{rf}}^2}{m\,\Omega^2}$$

The number of ions trapped per unit length is

Eq. 5.8 $$N = \int_0^{r_0}\rho(r)\,dr = \frac{2\,\epsilon_0}{{r_0}^2}\,\frac{q^2\ {V_{rf}}^2}{m\,\Omega^2}$$

From Eq. 5.8 it follows that the product of particle number per unit length N and particle mass m is constant, if no trap parameters are changed.

Eq. 5.9 $$N\,m = \frac{2\,\epsilon_0}{{r_0}^2}\,\frac{q^2\ {V_{rf}}^2}{\Omega^2} = \mathrm{constant}$$

If the mean particle mass increases due to ice nucleation at the particle's surface, the particle number per unit length decreases by particle loss with the same factor. For an experiment starting with the particle number per unit length N_0 and the mean particle diameter d_{p0} the mean particle number per unit length decreases with

Eq. 5.10 $$N(t > 0) = N_0 \left(\frac{d_{p0}}{d_p}\right)^3$$

The scale of Figure 5.6 can be transformed by

Eq. 5.11 $$\mathrm{Ln}\left[\frac{d_p}{d_{p0}}\right] = -\frac{1}{3}\,\mathrm{Ln}\left[\frac{N}{N_0}\right]$$

The transformed scale of Figure 5.6 gives an estimate of the particle growth factor for the experiments. The particle diameter is grown by ~20 % and by ~50 % within 10 s for the experiment where helium from compressed gas cylinder and from the bubbler is filled into the cooled ion-trap, respectively.

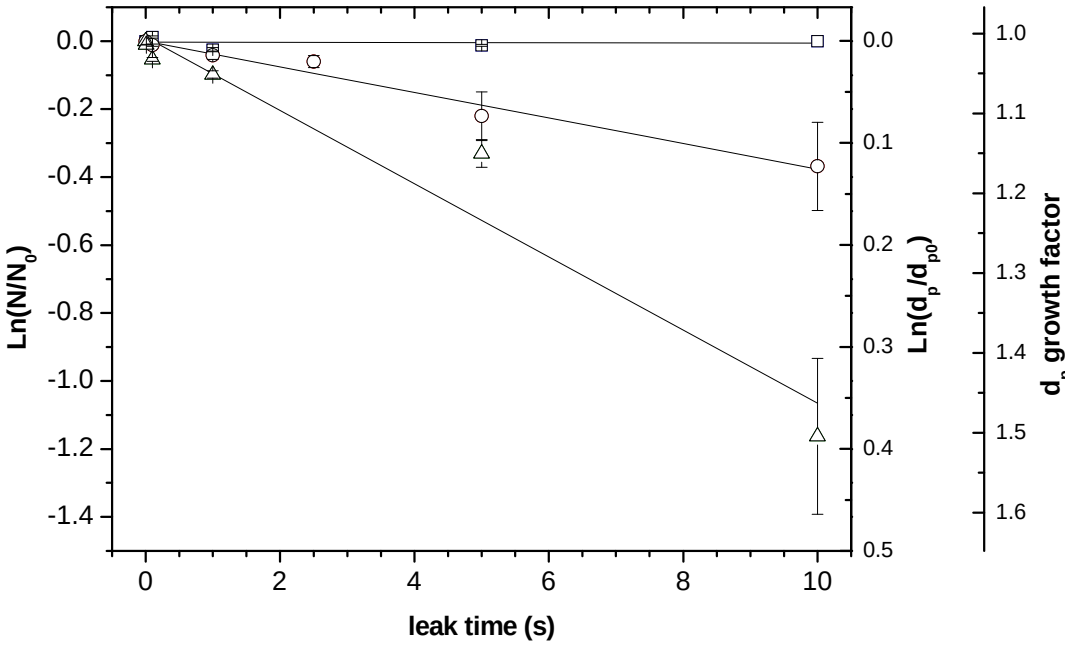

Figure 5.6. Particle retention rates of the quadrupolar ion-trap in storage mode as a function of storage time. Squares: Trap at 296 K, helium from bottle. Circles: Trap at 120 K, helium from bottle. Triangles: Trap at 120 K, humidified helium.

Having determined the growth factors occurring in the experiment, classical liquid drop theory can principally be used for further analysis of the data. Again, it should be noted that the application of classical nucleation theory as used below must be questioned at the saturation ratios, nuclei dimensions, and nuclei-types under consideration [Gumbel and Megner, 2009; Rapp and Thomas, 2006; Plane, 2003]. Furthermore, the quality of the data available from the proof-of-principle measurement is not sufficient to make an accurate statement wheatear classical nucleation theory is applicable or not. However, with some basic assumptions the potential of this methodology, for the investigation of nucleation processes under mesopause conditions, can be demonstrated.

It is assumed that the particles are perfectly wettable, so that the water molecules condensing onto the nucleus do not experience any difference between the nucleus surface and a pre-existing pure ice surface. In that case, nucleation occurs immediately if the diameter of the nucleus exceeds the critical nucleus diameter d^* given by Gumbel and Megner [2009], which is needed to overcome the Gibbs free energy barrier of heterogeneous ice particle formation on Fe_2O_3 particles (see Fig. 2.4).

Eq. 5.12 $$d^* = \frac{4\, m_{H2O}\, \sigma_{ice}}{k\, T\, \rho_{ice}\, \ln S}$$

m_{H2O} is the mass of the vapor molecule, σ_{ice} is the surface tension ($\sigma_{ice} = 0.122\ J\ K^{-1}$, Rapp and Thomas [2006]), ρ_{ice} is the density ($\rho_{ice} = 930\ kg\ m^{-3}$), and S is the supersaturation ratio. With the conditions of the experiment the critical diameter was about $d^* = 2\ nm$. The particle diameter was $4.7\ nm$ so that that heterogeneous nucleation can occur without any energetic barrier in this experiment. Note that Eq. 5.12 does not account for the effect of an electrical charge on the particle, which would even lower the critical diameter by the interaction between the central charge of the particle and the dipole of the water molecule.

In the following, the effect of ice embryo growth on a particle's surface [Gumbel and Megner, 2009] is neglected. For the high supersaturation conditions prevailing at the cold summer mesopause, sublimation rates are so low that essentially every molecule deposited from vapor phase stays on the nucleus. An ice particle tends to

adapt to a diameter where the chemical potential of the particle is in balance to the chemical potential of the surrounding atmosphere. The chemical potential of a neutral particle is given by the potential of the ice phase and the potential of the particle surface (Kelvin effect). The chemical potential of the surrounding atmosphere is given by the potential of the vapor face of the water molecules. The growth rate of the particle is determined by the chemical potentials and the diffusion of water molecules to the particle's surface. The diffusion is described by Fick's first law. It is shown in Pruppacher and Klett [1997] and more recently in Maus [2010] that for the radius of a neutral ice particle the relation is

Eq. 5.13 $$r' \frac{\partial r'}{\partial t'} = \frac{D_w M_w}{R T \rho_{ice}} p_{sat} (RH_w - 1)$$

Where D_w is the diffusion coefficient of water molecules in air, M_w is the water vapor molecular weight, ρ_{ice} is the density of ice, p_{sat} is the saturation vapor pressure of water in air, and T and RH_w are the temperature and relative humidity of the atmosphere surrounding the particle. Thought this differential equation can be solved analytically, the more complex equation including charge effects have to be solved numerically [Maus, 2010]. The expected growth factor for this experiment is about 12 % larger if the charge effect is included in the calculation. This deviation is less than the accuracy of these proof-of-principle results, and thus the charge effect is neglected in the following discussion. From Eq. 5.13 a growth factor F can be derived:

Eq. 5.14 $$F = \frac{d}{d_0} = \sqrt{1 + \frac{8 D_w p_{sat} M_w (RH_w - 1)}{R T \rho_{ice} d_0^2} t}$$

The saturation vapor pressure of water in air p_{sat} at low temperatures can be found in Rapp and Thomas [2006].

Eq. 5.15 $$p_{sat} = Exp[A - B/T + C \ln T - D T]$$

$$A = 9.550426, B = 5723.265, C = 3.53068, D = 0.00728332$$

An expression for the diffusion coefficient of water molecules in air D_w can be found in Pruppacher and Klett [1997].

Eq. 5.16 $$D_w = K \left(\frac{T}{T_0}\right)^{1.94} \left(\frac{p_0}{p}\right)$$

$$K = 0.211\ 10^{-4}\ m^2\ s^{-1}$$

Thus Eq. 5.14 becomes

Eq. 5.17 $$F = \sqrt{1 + \frac{8\ Exp\left[a - \frac{b}{T} - d\ T\right] K\ M_w\ T^{c-1}\ p_0 \left(\frac{T}{T_0}\right)^{1.94} (RH_w - 1)}{p\ R\ \rho_{ice}\ d_0^2}\ t}$$

For the parameters of this experiment, Eq. 5.17 is nearly a linear expression for $0 \leq t \leq 10\ s$. Therefore, the Taylor series second order of Eq. 5.17 is used in the following:

Eq. 5.18 $$F(t) = 1 + \frac{4\ Exp\left[a - \frac{b}{T} - d\ T\right] K\ M_w\ T^{c-1}\ p_0 \left(\frac{T}{T_0}\right)^{1.94} (RH_w - 1)}{p\ R\ \rho_{ice}\ d_0^2}\ t + O[t]^2$$

Eq. 5.19 $$F(t) = 1 + \chi\ t$$

In Figure 5.7, this relatiob is used for a fit to the growth factor data of Figure 5.6.

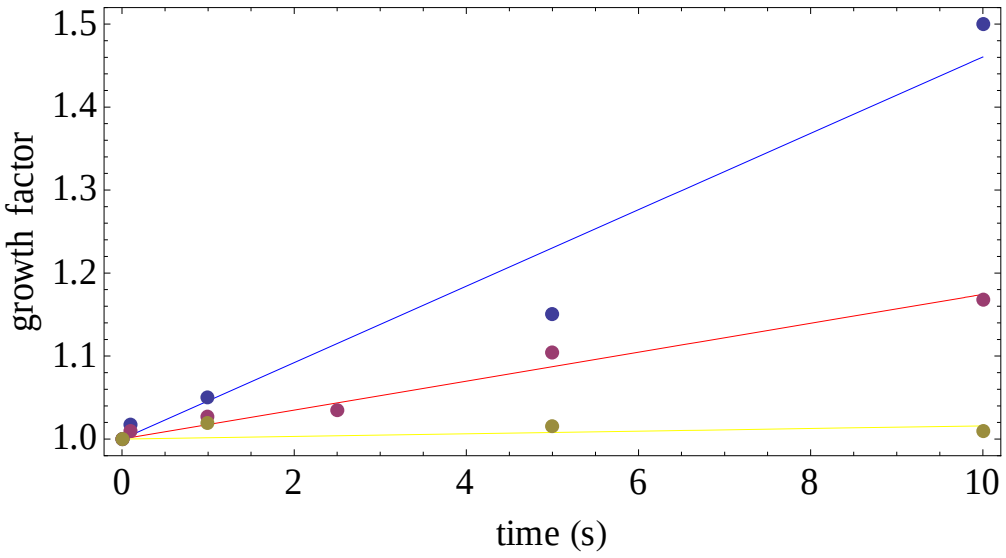

Figure 5.7. Growth factor data treatment of the experimental results shown in Figure 5.6. Yellow: Trap at $296\ K$, helium from bottle. Red: Trap at $120\ K$, helium from bottle. Blue: Trap at $120\ K$, humidified helium.

experiment	**trap temperature**	**water mole fraction**	**growth rate**
1 – yellow	$T_1 = 296\ K$	$2\ ppm$	$\chi_1 = 0.0015873$
2 – red	$T_2 = ?$	$2\ ppm$	$\chi_2 = 0.0174316$
3 – blue	$T_3 = T_2$	?	$\chi_3 = 0.0460416$

Table 5.1. Result from the fit of Eq. 5.19 to the data of Figure 5.7.

The fit of Eq. 5.19 to the data of Figure 5.7 yields the data shown in Table 5.1. Here, it is assumed that the water mole fraction inside the ion-trap is equal to the water mole fraction inside the helium gas bottle from which a constant gas flow is leaking into the ion-trap. This is a reasonable assumption, since the relationship of the mean diffusion time of a water molecule initially located in the center of the trap to the cooled housing is about 50 times larger than the residence time of the gas which passes the ion-trap with high velocity. Thus high supersaturation is possible, since the water partial pressure inside the ion-trap can be considered as decoupled from the saturation vapor pressure at the cooled ion-trap housing.

With this assumptions and the growth rate χ_2, Eq. 5.18 can be solved numerically for T_2. According to this analysis the temperature of the gas and the particles inside the ion-trap was $151\ K$. Note, that the measured temperature of the ion-trap housing was $(120 \pm 5)\ K$. This is a reasonable result within the measurement accuracy. It can be assumed, that the gas and the particle have the same temperature [Wolf, 1997] which was constant during all experiments. With this assumption Eq. 5.18 can be solved for the unknown water mole fraction in experiment 3. According to this analysis the water mole fraction was $5.3\ ppm$ which corresponds to the saturation vapor pressure of water at $155\ K$.

Note that the analysis of the exact gas temperature inside the ion-trap is of great importance for quantitative analysis of nucleation rates and growth factor. The relative humidity is highly temperature dependent at typical experimental conditions (see Figure 5.8).

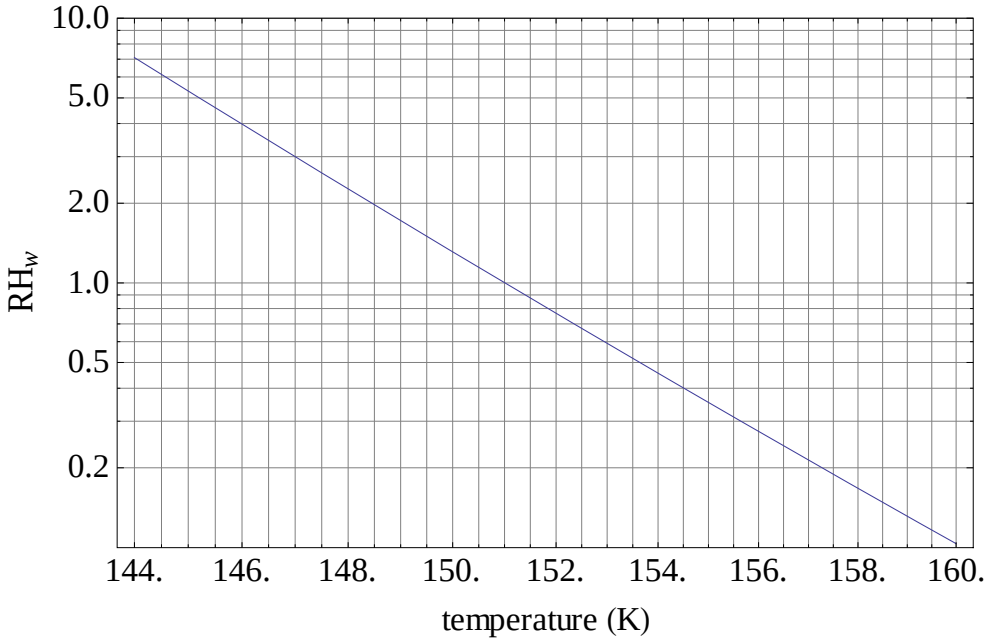

Figure 5.8. Relative humidity of water at low total gas pressure. The values are calculated from Eq. 5.15 with typical experimental parameters: 2 ppm water vapor in Helium at a total pressure of 4 Pa.

If the water mole fraction inside the ion-trap is accurately determined by a quadrupole mass spectrometer (QMS) and pressure and temperature of the water vapor is deduced from IR-spectra achieved by optical feedback CRDS [Habig, 2009], the applicability of classical nucleation theory and the influence of charges at the particles on the nucleation rates can be investigated at mesopause conditions.

CHAPTER 6

Core level photoionization spectroscopy

Properties of aerosols have been investigated with a number of different techniques in the past, including aerosol mass spectrometry [Jayne et al., 2000], scanning transmission x-ray microscopy [Maria et al., 2004], electron microscopy [Laskin et al., 2003], and others. Most of these techniques probe the entire particle volume and do not directly measure the surface composition of the aerosol. Thus, little is known of the composition of free nanoscopic aerosol particles. Furthermore all of the these techniques are limited to particles with diameter $\geq 100\,nm$. Surface properties are altered if particles are collected at a surface prior to investigation. Also charging of particles, exposed to x-ray radiation for a prolonged time, induces radiation damage and affects absorption characteristic of the particles [Grimm et al., 2006]. For these reasons, free beams of nanoparticles in narrow size distributions in a controlled charge state and in the gas atmosphere of interest represent the ideal way to perform process studies in the laboratory on charged nanoscopic objects of relevance to atmospheric research.

Core level photoionization x-ray spectroscopy (XPS) is a method for the investigation of chemical composition and speciation of the chemical composition and constituents at the particle surface. It has been applied to free clusters [Hatusi et al., 2005] and nanoparticles prepared in a beam [Mysak et al., 2010; Bresch et al., 2008]. However, the reported techniques are limited on the one hand to clusters prepared in

wide size distribution and on the other hand to free nanoparticles of large diameters $> 40\,nm$ [Bresch et al., 2008; Wilson et al., 2007], if synchrotron radiation is used as a radiation source. Low target dentisty can be compensated by ultraintense soft X-ray sources, such as free electron lasers, permitting XPS studies on size selected clusters. However, low target density in a high pressure background atmosphere is another challenging difficulty in spectroscopy of free nanoparticle beams.

Mysak et al. [2010] recently reported Si 2p and O 1s XPS spectra from a particle beam of SiO_2 particles with $270\,nm$ diameter. The particle diameter range of their experiment is physically limited by the aerodynamic lens to $50 - 1000\,nm$. The signal to noise ratio achieved during 33 minutes integration for the O 1s spectrum limits their approach to particle diameters $> 150\,nm$. Low target density in a high pressure background atmosphere is the challenging difficulty in spectroscopy of free particle beams. While the particle source / aerodynamic lens inlet combination of Mysak et al. [2010] provides a particle beam a with number density of about $2.5\ 10^4\ cm^{-3}$ at $6\ 10^{-3}\ mbar$. The high density nano-particle beam inlet system of the TRAPS apparatus provides a particle beam with number density of $> 10^7\ cm^{-3}$ at $< 10^{-5}\ mbar$. This significantly enhanced target density permits to measure XPS spectra from sub $10\,nm$ particles using synchrotron radiation as a relatively weak tuneable soft X-ray source (instead of free electron lasers). The helium atom number density in the TRAPS particle beam is about $2.6\ 10^{11}\ cm^{-3}$. If the particle diameter is about $10\,nm$ and SiO_2 particles are sampled, the silicon atom number dfensity is approximately $1.2\ 10^{11}\ cm^{-3}$. The ionization probability of helium and silicon atoms excited by an x-ray photon is assumed to be similar, but the absorption efficiency of a $d_p = 10\,nm$ SiO_2 particle must be considered. The absorption probability can be calculated from Mie theory to be $Q_{abs} = 0.066$. Thus the efficient silicon atom number density is $8.5\ 10^8\ cm^{-3}$, if it is assumed that all photoelectrons get emitted into the vacuum. From this estimation it can be seen, that proportion of photoelectrons from the nano-particle to the photoelectrons from the helium background gas is about $1 : 1000$, respectively. For the measurement of XPS spectra from small nano-particles it is essential to separate the photoelectrons of different origin prior to detection.

6.1 Basic characteristics of synchrotron radiation sources and its beamlines.

6.1.1 Synchrotron radiation

Synchrotron Radiation is a valuable tool for probing the nano-world. It's outstanding quality in properties as brilliance, beam quality, tuneability and time structure makes it suitable especially for the investigation of nano-sized and nano-structured material.

Electrons submitted to an acceleration field emit electromagnetic waves. This is well known from applications like antennas, klystrons and magnetrons. In a synchrotron, electrons are accelerated to relativistic energies (GeV) by a microwave cavity. After acceleration the electrons are kept in a circular path by strong magnetic fields while being repeatedly accelerated. The magnetic field in the bending magnets induces a very strong centripetal acceleration in the highly relativistic electrons, with an energy $E \gg m \cdot c^2$ where m is the rest mass of the electron. The acceleration induces an electromagnetic wave emission up to several hundred keV in the most powerful machines. This radiation is named Synchrotron Radiation (SR).

Synchrotron storage rings consist of arrays of magnets for focusing and bending the electron beam, and straight linear sections for accelerating the particles. In the linear sections insertion device magnets are used to produce dedicated SR for experimental usage. Rays with spectral range from infrared to visible and ultraviolet to hard X-Rays can be produced. SR has a number of outstanding properties: A continuous spectrum from the infrared to the X-Ray region; high intensity, owing to the high electron current accumulated in the storage ring; collimation of the emitted radiation in the instantaneous direction of the emitting particles; linear polarization with the electric vector parallel to the plane of the orbit; circular polarisation above and below the plane of the orbit; high brilliance of the source; a time structure with pulse length down to the ps regime.

Besides the tuneability the high brilliance is the key parameter for probing nanoparticles. It is essential to focus all the photons to a very small sample spot without losing photons on small apertures. SR, inherently to its generation process, is

emitted into a narrow angle. The brilliance achieved with modern SR sources is usually associated with lasers in the visible, IR and UV regime, only. This brilliance cannot be reached by other X-Ray and far UV sources.

6.1.2 Generation of Synchrotron Radiation

The properties of SR can be derived by applying the methods of classical electrodynamics to the motion of relativistic electrons of positrons in circular orbits. Comprehensive overviews and derivations of the key formulas can be found in various publications [Gohshi, 1996; Attwood, 1999; Jackson, 1962]. Here, a very brief review of the most important features of SR is given and examples from the synchrotron BESSY II in Berlin are given.

An electron, which is kept on a circular trajectory by a magnetic field B, is affected the Lorentz force $\boldsymbol{F} = e \cdot \boldsymbol{v} \times \boldsymbol{B}$. In the classic electrodynamic view, electromagnetic radiation is emitted in all directions except the direction of acceleration. The energy of the emitted photons is low ($\sim eV$), even if the frequency is in the microwave region. But in a synchrotron the velocity v of the electrons is close to the speed of light c. These electrons are named relativistic electrons and the Lorentz transformation has to be applied to describe their properties in the frame of the observer. From the relativistic equation of motion it can be shown, that the observed SR is folded into a narrow cone around the motion direction (see Figure 6.1).

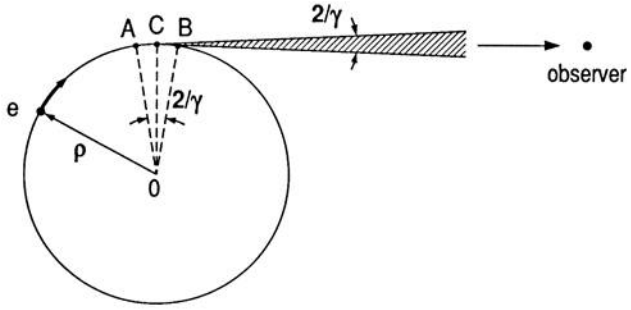

Figure 6.1: Electrons in circular motion and synchrotron radiation emitted by the electrons in a tangential direction (reproduced from [Gohshi, 1996]).

In the synchrotron light source BESSY II the velocity of the electrons in the storage ring with radius ρ is only $14\,ms^{-1}$ slower than the vacuum light speed c.

With this speed the vertical emission angle is $0.15\,mrad$ (0.01°). Horizontally, the radiation from the bending magnet is spread out in a much larger angle since the electron trajectory is curved and the z direction varies for each source point. This disadvantage can be overcome by the use of undulators as described below.

The storage ring is filled with electron bunches in order to accelerate them after each turn by means of a microwave cavity. The electron bunches are injected into the ring with a timing such that they arrive in the microwave cavity at the moment they are synchronous with the wave. If a storage ring is driven by a $500\,MHz$ microwave, every $2\,ns$ a bunch of electrons with a length of about $35\,ps$ can be filled in the storage ring. A single bunch contains about 10^{10} electrons. The storage ring is optimized in a way, that bunches are small in space and hence each individual bunch gives a short, timed synchrotron light flash when it passes a magnet or undulator.

Electrons propagating in a circular orbit with non-relativistic velocity emit with an angular frequency equal to the electron revolution frequency $\omega_0 = v/\rho$. A relativistic electron has the same base frequency but a continuum of higher harmonics is also generated. An observer will be subjected to the radiation which is tangential emitted by the electrons moving between A and B of Figure 6.1 on the circular arc. The length of this arc is $2\,\rho/\gamma$. The time interval of the radiation to which the observer is exposed will be the time that the radiation travels from A to B, subtracted from the time that the electron moves along the arc $\overline{AB}$. This time interval is Lorentz-contracted for the observer; hence the radiation is confined to an extremely short pulse, much shorter than the duration of one electron circle. The frequency distribution $E(\omega)$ of such a pulse-train from a synchrotron can be derived from the Fourier transformation of the time structure $E(t)$ of the pulse. In the BESSY II case, $E(t)$ is a periodic pulse with the pulse width of $\rho/(c \cdot \gamma^3)$, and the pulse interval $2\pi \cdot \rho/c$. The frequency spectrum from the Fourier transformation has the base frequency ω_0 and an upper limit $\omega_c = \frac{2}{3}\gamma^3 \cdot \omega_0$ above which the frequency power-spectrum decays rapidly. In the storage ring BESSY II with electron energy of $1.7\,GeV$ the critical energy from the 1.3 Tesla bending magnets is $2.5\,keV$ which corresponds to a wavelength of $0.5\,nm$. The resulting photon flux spectral

distribution is shown in Figure 6.2 for the example of BESSY II and the MLS (Metrology Light Source, Berlin).

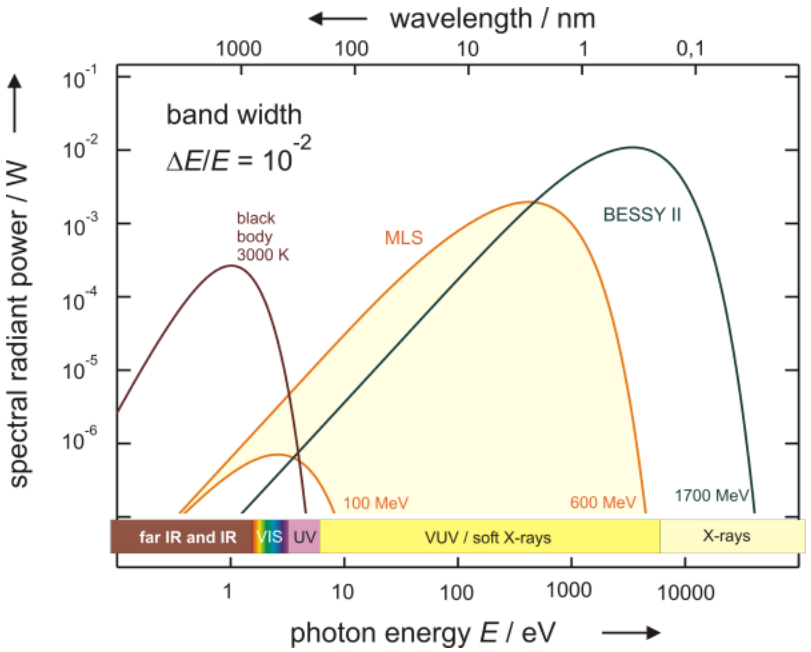

Figure 6.2: Calculated radiant power for a $3000\ K$ blackbody radiator, BESSY II and MLS. (The parameters used for the calculation are: BESSY II: $W = 1700\ MeV$, $B = 1.3\ T$; $I = 200\ mA$, $\rho = 20\ m$; MLS: $W = 600\ MeV$ $(100\ MeV)$, $B = 1.3\ T$ $(0.22\ T)$, $I = 200\ mA$, $\rho = 5\ m$; Black Body: $T = 3000\ K$, $A_{em} = 78.5\ mm^2$, $\rho = 1\ m$;) (from: www.ptb.de/mls/)

Using the radiation from a bending magnet has the disadvantage that the radiation is spread out horizontally throughout the total arc in that magnet. In order to get most of the radiation into a well collimated beam with low divergence, magnetic structures are built into the straight sections of the storage ring. These magnetic structures are named insertion devices. Usually the magnetic field of these structures is variable and can reach much higher values than the bending magnets without kicking the electrons out of the circular orbit. Therewith a larger spectral range of SR and higher photon energy can be achieved.

Depending on whether the radiation from different magnets superposes coherently or just adding up their intensity, the insertion devices are called undulators or wigglers. Wigglers are periodical arrays of magnet pairs with altering fields in which the electrons undergo a sinusoidal movement. The radiation from each deflection at a magnet pair is superimposed so that with N magnet pairs the spectral continuum

distribution is N times the intensity of a bending magnet. The horizontal beam divergence is determined by curvature of the sinusoidal electron trajectory in the magnetic structure. In case of small deflection of the electron beam the radiation emits in different wiggles show interference effects (see Figure 6.3). Positive interference occurs for a time difference $n \cdot \lambda$ between the light travels from wiggle to wiggle compared to the time the relativistic electron needs for the same distance. This non-continuum source is called an undulator. With a large number of periods all photons interfere destructive and the angular distribution limits the emission of the n^{th} harmonic λ_n to a narrow angle.

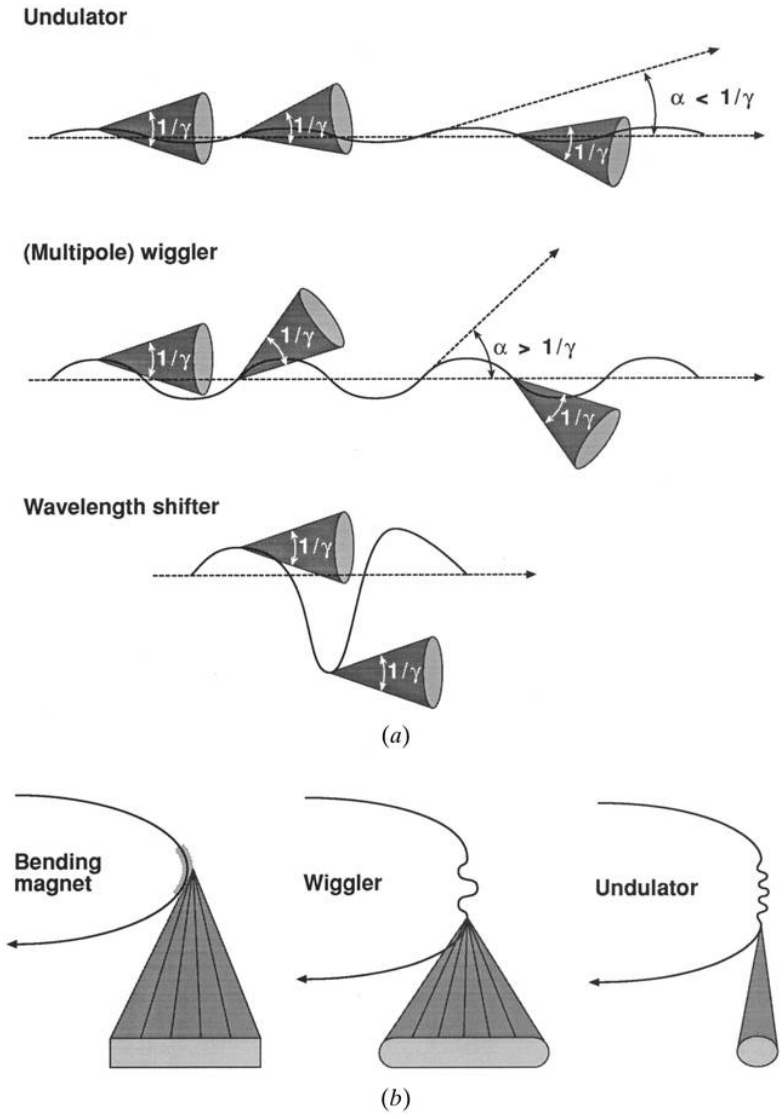

Figure 6.3: Insertion devices. (a) The various types of insertion device called multipole wigglers, undulators or wavelength shifters. (b) Beam shapes generated by insertion devices. (reproduced from [Lindley, 1999])

6.1.3 The UE56/2-PGM-2 Beamline at BESSY II

The function of a beamline is to guide photons from the insertion device to the experiment, preserving or improving its properties. In most cases a small spot of monochromatic light is needed. Extreme-ultraviolet and soft X-Ray light would completely be absorbed by glass windows or high gas pressure. Beamlines for this energy have to be under high vacuum without windows towards the synchrotron. By the same reason no glass optical elements can be used. Coated mirrors and gratings are used under grazing angles in order to achieve high reflectivity for high energy photons.

Figure 6.4 shows a schematic overview of the UE56/2-PMG-2 beamline at BESSY II. This beamline provides circular polarized light by means from an elliptical double undulator of Sasaki type [Sawhney et al., 1997]. The undulator provides, through emission in first, third and fifth harmonics, circular polarized radiation in the energy range $89 - 1328\,eV$. The beamline consists of a pre (M1) and two post monochromator mirrors (M3, M4) for horizontal and vertical focussing, respectively.

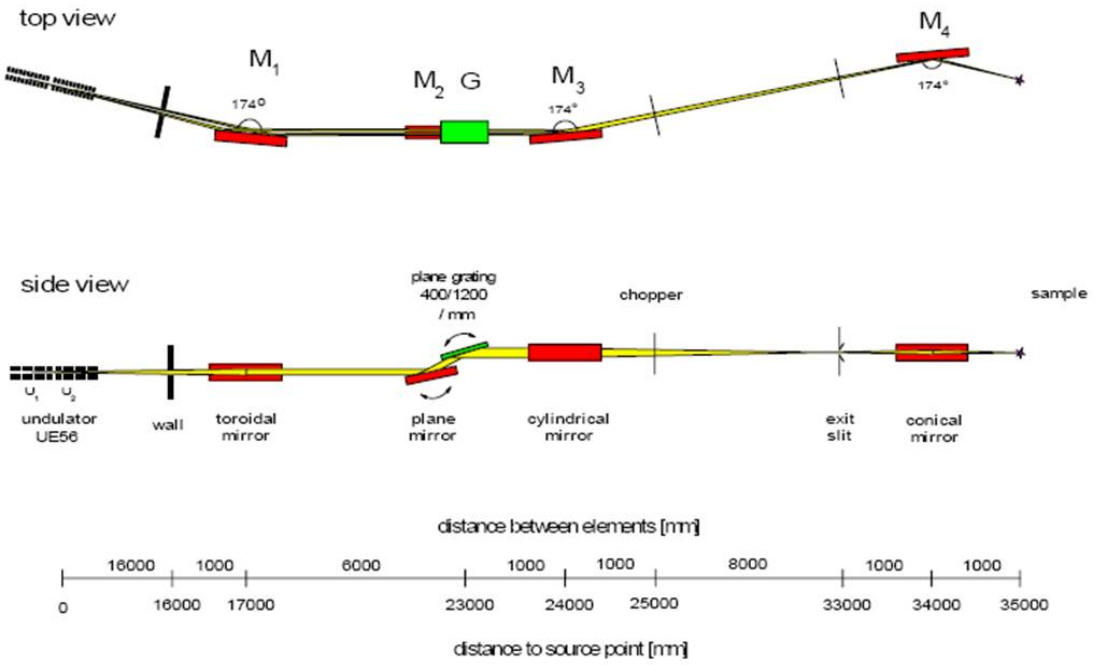

Figure 6.4: Schematic of the UE56/2-PGM-2 beamline at BESSY II (reproduced from [Sawhney et al., 1997]).

A plane grating monochromator (PGM) employing only one set of optical elements (M2, G) for steering and monochromatizing the beam is mounted between M1 and M3. An energy resolution from 6000 to 90000 can be achieved at a photon flux between 10^{12} and 10^{14} photon/s. The main parameters of the insertion device and the beamline are given in Table 1. In order to achieve maximum photon flux the first harmonic of the 400 $lines/mm$ grating was used, only.

Nominal electron energy	1.7 GeV
Stored current	100 mA
Horizontal source size	0.310 mm
Vertical source size	0.022 mm
Undulator period	56 mm
Number of periods	2 x 30 n
K-parameter	0.5 to 3.0
Horizontal peak magnetic field	0.38 T
Vertical peak magnetic field	0.63 T
Photon Energy	
First harmonic ($K = 3 - 0.5$)	$89 - 436$ eV
Third harmonic ($K = 2.5 - 1.0$)	$357 - 981$ eV
Fifth harmonic ($K = 2.5 - 1.3$)	$594 - 1328$ eV
Maximum total emitted power	104 W
Photon flux	4.00 10^{15}
Energy resolution	90000 at 64 eV
Divergence horizontal	1 $mrad$
Divergence vertical	1 $mrad$

Table 1: Parameters of BESSY II at the beamline UE56/2-PGM-2.

6.2 Core-level photoionization spectroscopies

Core level spectroscopy is a valuable tool for investigation of electronic and geometric structure of atoms, molecules, clusters, small particles and solids. The techniques include photoelectron spectroscopy (PES), Auger electron spectroscopy (AES), Resonant Auger electron spectroscopy (RES) and X-ray absorption spectroscopy (XAS, NEXAFS). Due to the atomic character of the core orbitals, core-level spectroscopy probes the local surrounding of the core site. Surface and bulk spectral features and even different types of surface sites can be separated in the spectra. Since many of the interesting features of nano-particles are assigned to active surface sites and the accompanying changes in electronic structure of the site, it is highly desirable to apply these spectroscopies to nano-particles.

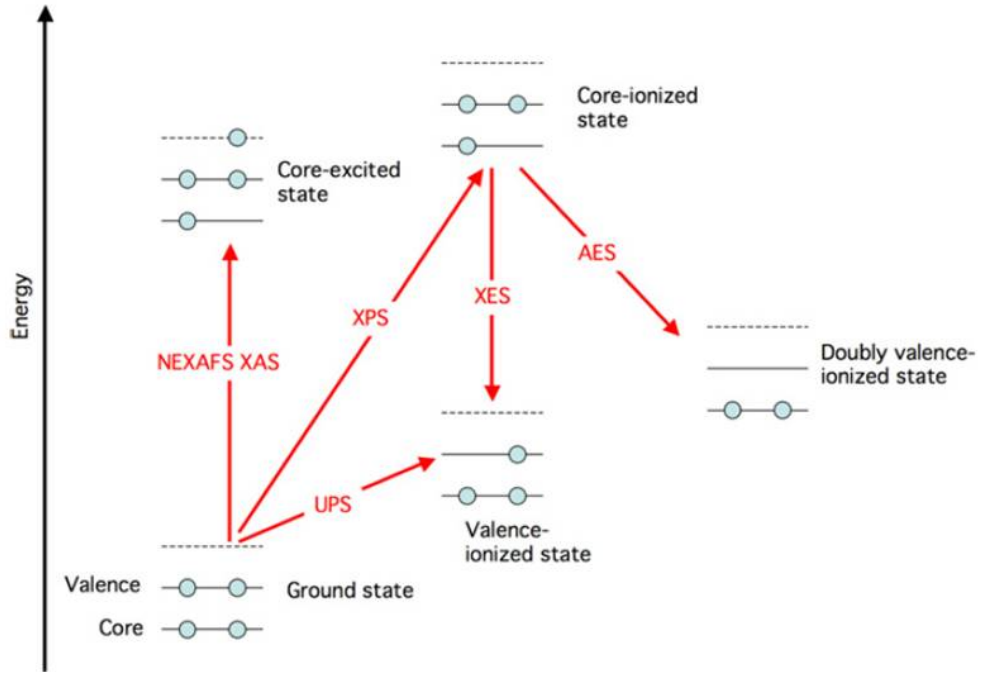

Figure 6.5. Schematic overview of the relations between some core-level spectroscopies (reproduced from [Björneholm et al., 2009]).

Figure 6.5 shows the relation between XPS, AES, RAS and NEXAFS. The electronic structure of any systems build up by atoms consists of core levels and valence levels. The valence level electronic structure is responsible for the macroscopic properties of the system. It is responsible for the interatomic bonding and forms delocalized molecular orbits and bands. The atomic like core levels are strongly localized since they are not affected by the interatomic bonding. Core-level

spectra will thus contain information about the elements in the sample and of the number of chemically inequivalent bonding situations within the sample.

In NEXAFS spectroscopy resonances from the excitation of core level electrons into the unoccupied π^* and σ^* orbitals are probed. π^* orbitals are below and σ^* orbitals above the ionization energy (see Figure 6.6). In molecules with low atomic number, π^* orbitals cause a peak in the NEXAFS spectrum below the ionization energy, since the missing core electron causes an increased Coulomb attraction. The same is true for the σ^* orbitals if the sum of the atomic numbers in a molecule is < 15. In the textbook from Stöhr [2003] a detailed discussion of NEXAFS spectroscopy can be found.

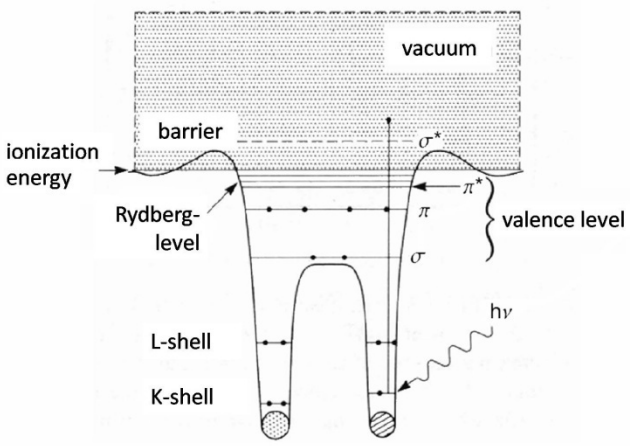

Figure 6.6. Core-level excitation of electrons into unoccupied orbitals (adapted from [Stöhr, 2003]).

6.3 Experimental setup at the SR source BESSY II

Figure 6.7 shows a schematic of the setup used at the UE56/2 PGM-2 beamline at BESSY II synchrotron radiation facility in Berlin (Germany). An overview of all relevant experiment parameters is given in Table 2. The monochromator was operated at the 1st harmonic, 1st order of the $400\ l/mm$ grating. Elliptic polarized lighted was passed through a $1700\ \mu m$ monochromator slit, which results in a bandwidth of $380\ meV$ to $700\ meV$ at $100\ eV$ and $150\ eV$ central wavelength, respectively. A differential pumping stage separates the beamline under ultra high vacuum ($< 3\ 10^{-9}\ mbar$) from the experiment chamber ($< 5\ 10^{-5}\ mbar$). SiO_2 particles where synthesized in-situ by the microwave plasma particle source (MPPS) described above. $3000\ sccm$ He grade 4.6, $500\ sccm$ O_2 in He ($(20.10 \pm 0.40)\ Vol-\%$) and $50\ sccm$ SiH_4 in He ($(0.970 \pm 0.019)\ Vol-\%$) were mixed upstream from the plasma (all gases provided by AirLiquide, Germany). The plasma was ignited by $200\ Watt$ microwave power at a pressure of $80\ mbar$. The resulting particle diameter was $dp = (8.2 \pm 1.3)\ nm$. The gas/particle stream propagates to the ADL through an ISO-KF16 flexible metal hose and enters the ADL through a flow limiting orifice with $1.0\ mm$ diameter. A roughing pump keeps the pressure at the outlet of the ADL at $1.2\ mbar$. The particles pass through a skimmer with $3\ mm$ diameter into the octopole ion-guide.

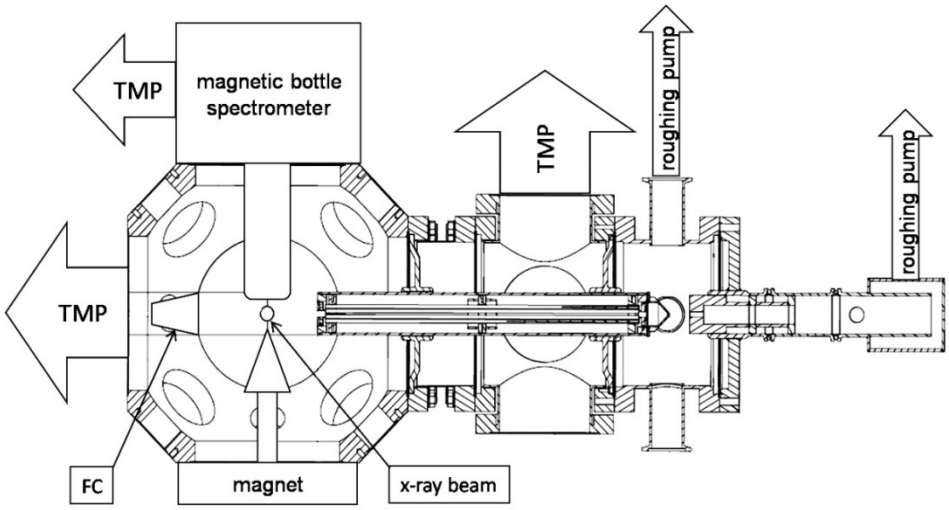

Figure 6.7. Schematic diagram of the experimental setup used for XPS studies from a free nanoparticle beam using synchrotron radiation at the BESSY II facility (TMP: turbomolecular pump).

ring current	15.8	mA	lifetime	4.2	h
harmonic	1^{st}		slit width	1700	μm
grating	400	l/mm	cff	2.25	
bandwidth	380 – 699	meV			
(at energy)	(100 – 150)	(eV)			
p ADL in	10.0	$mbar$	p ADL out	1.2	$mbar$
p okt.	0.16	$mbar$	p Experiment	$2.4\ 10^{5}$	$mbar$
U lens in (okt.)	-110	V	U lens out (okt.)	-320	V
U DC (okt.)	-120	V	U RF (okt.)	432	V
f RF (okt.)	46	kHz	nb. of particles	$1.95\ 10^{8}$	$pulse^{-1}$

Table 2. Experiment parameters of scan0097.

In the octopole ion-guide the ions are decelerated by collision with the background gas ($0.16\ mbar$). Entrance and exit potentials are applied in order to accumulate particles in the electrodynamic cage. Particle pulses were extracted from the trap with $10\ Hz$ repetition rate. The concentrated particle pulse passes the front of the entrance aperture of the magnetic bottle spectrometer, and a Faraday cup electrometer (FC) records the charge carried by the pulse. A area of approximately $1 \times 3\ mm$ of the particle beam is irradiated by the incident monochromatic x-rays.

A “magnetic-bottle”-type TOF electron spectrometer combines the advantage of high detection efficiency for the detached electrons and a high energy resolution [Kruit and Read, 1983; Cheshnovsky et al., 1987]. For the XPS experiment, such a spectrometer following the design of Cheshnovsky et al. was provided by Burkhart Langer[1].

The TOF spectrometer consists of a drift tube of $1.4\ m$ length, which comprises a guiding magnetic field from a solenoid for directing the electrons down the drift tube to a MCP detector (see Figure 6.8). The kinetic energy of the electrons is calculated from the TOF of the electrons between the interaction region of the x-rays and the particle beam to the detector. A diverging magnetic field is used to collect the photoelectrons with $2\pi\ sr$ collection efficiency since they are forced to travel along

[1] Dr. Burkhard Langer, Institut für Chemie und Biochemie - Physikalische und Theoretische Chemie, Freie Universität Berlin, Takustr. 3, 14195 Berlin.

field lines. Compared with a conventional TOF spectrometer, a spectrum can be recorded from about four orders of magnitude smaller number of photoelectrons. Thus the total number of atoms of interest in a particle beam suffices even for small nanoparticles.

Photoelectrons impinging at the MCP effect an electron avalanche and the resulting current pulses are transformed into a voltage signal by a fast current-to-voltage amplifier. Pulses exceeding a discriminator level above electronic background noise are transformed into TTL pulses. Note that the magnetic-bottle TOF-electron spectrometer can be operated with a pulsed light source, such as the single bunch mode of the BESSY II light source. It provides soft X-ray pulses of typically $35\,ps$ length. The electronic bunch marker of the electron storage ring triggers a time-to-digital converter (TDC) with $60\,ps$ resolution, which adds a time-stamp to each electron signal, which was converted into a TTL pulse before. The number of pulses is displayed and saved as a time based histogram. The total length of each electron TOF-spectrum is $800\,ns$.

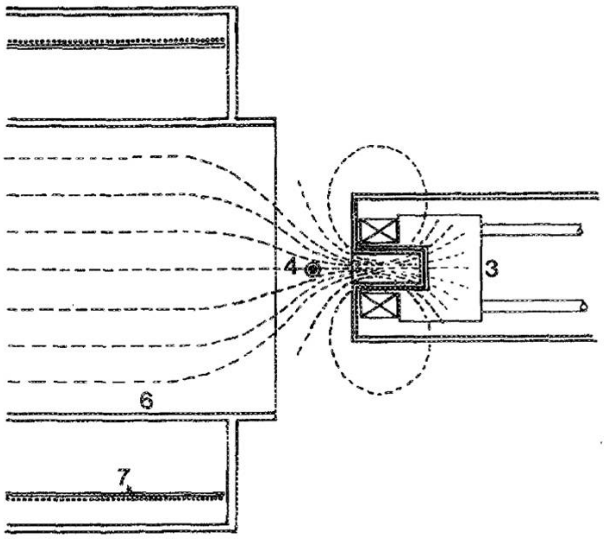

Figure 6.8. An expanded view of the main parts of the photoelectron spectrometer (reproduced from [Cheshnovsky et al., 1987]: 3. Permanent magnet. 4. Interaction zone. 6. Photoelectron flight tube. 7. Low field guiding solenoid. Dashed lines: Magnetic field lines.

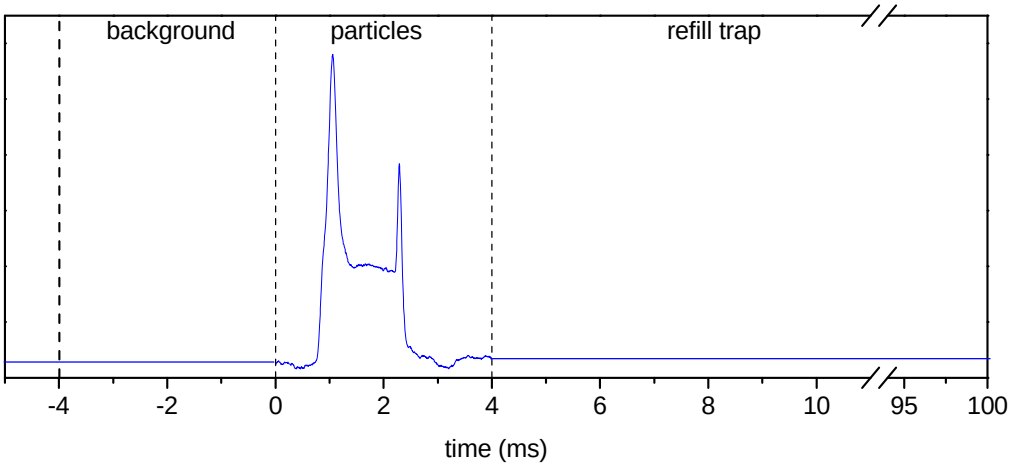

Figure 6.9. Timing diagram of the experiment. A particle pulse exits the ion-trap when the exit electrostatic potential is switched to zero at $t = 0\,ms$. After a distinct time period, the particles are measured as a current at the Faraday cup. A detailed description of this approach and the particle pulse shape given by Meinen et al. [2010a] and section 4.8.2.

For the nanoparticles pulse passing the interaction zone, the SR source is quasi continuous, although it is used in single bunch mode of the storage ring. Every $800\,ns$ an electron bunch passes the undulator of the beamline, so the particle pulse, which typically spreads over $2\,ms$ (see Figure 6.9), is irradiated by 2500 X-ray pulses. A logic unit is used to measure counts from the magnetic-bottle spectrometer only when a particle pulse traverses the ionization zone. A background spectrum is recorded for the same time interval before the particle pulse exits the trap (see Figure 6.9). While the trap is refilled with new charged particles, no spectra are taken. This procedure maximizes the photoelectrons from the nano-particles relative to those from the background gas. Furthermore, background spectra are recorded during the time which is required for refilling the trap.

6.4 X-Ray photoionization spectroscopy at the Si $L_{3,2}$-edge of sub 10 nm SiO_2 particles

The experimental method described above provides a set of time-of-flight spectra for each step of a photon energy scan. Figure 6.10 shows such a set of spectra depicted as a colored contour plot. The channel number corresponds to the time bin photoelectrons are allocated to. Fast photoelectrons impinge at the detector prior to slow photoelectrons, so they are allocated to low channel numbers. The bold line with highest count rates originates from He K-shell ($n = 1$) electrons with an ionization potential of $25\,eV$. At $100\,eV$ photon energy, these electrons are slower as those excited with $150\,eV$ photons. Thus the line must have a negative slope. The second line starting at channel number $4.5\ 10^3$ $(100eV)$ propagating to $3.2\ 10^3$ $(150eV)$ is a He^+ ($n = 2$) satellite [Langer and Becker, 2009]. A third sparely shaded line can be found starting at $9.0\ 10^3$ $(115eV)$ propagating to $5.8\ 10^3$ $(135eV)$. This line can be assigned to photoelectrons of Si L-shell ionization, since it has the appropriate ionization energy and the line disappears if the particle flow is stopped at constant flux of the carrier gas. The edge starting at $6.2\ 10^3$ $(100eV)$ can be assigned to a bunch structure where a very small electron bunch follows $3\,ns$ past the main bunch in the synchrotron storage ring.

The recorded spectrum in the time domain can be converted into a photoelectron kinetic energy diagram in three steps: (i) flight-time to energy conversion using a well characterized system, (ii) scaling of the dataset to be equidistant in kinetic energy, (iii) fine tuning of the binding energy scale using the well-known binding energy of the He K-shell photoelectrons.

The flight-time to energy conversion is accomplished by using:

Eq. 6.1 $$E_{kin}(t) = U_0 + \frac{1}{2}\frac{m_e}{q}\left(\frac{d}{t-t_0}\right)^2$$

Here, t is the flight time with an instrumental offset t_0, d is the flight distance, m_e and q are mass and charge of the electron, and U_0 is an accelerating potential. Photoelectron spectra from argon and neon are recorded at the $L_{3,2}$ edges for determining d and t_0. It is found, that there is some additional potential U_0

accelerating the electrons in arbitrary direction. This potential might arise from the charge of the particle beam, ionized gas molecules or the exit potential of the ion-trap. U_0 is not determined from the rare gas calibration data, since it is highly variable, depending on the particle beam density, background pressure, and the magnitude of exit potential. This quantity has been determined line by line for each photon energy by adjusting the energy scale to the He K-shell photoelectron peak, corresponding to the above mentioned step (iii).

Electrons impinging at the detector are assigned to time bins of equal length. As the energy conversion (Eq. 6.1) has quadratic dependence of t^{-1}, high (or late) time bins are compressed to small energy bins at low kinetic energy and low (or early) time bins are stretched to long energy bins at high kinetic energy. For this reason the count rates of the energy bins have to be scaled by ${E_{kin}}^{-2}$ prior to interpolation of the data to equidistant kinetic energy bins. The described procedure results in Figure 6.11.

In Figure 6.11 the kinetic energy of the He photoelectrons is $90\,eV$ at $100\,eV$ photon energy. Since the ionization energy of the He K-shell is $25\,eV$ a kinetic energy of $75\,eV$ is expected at this photon energy. Thus there is an accelerating electric potential of $U_0 = 15\,V$. The spectrum at $100\,eV$ photon energy has to be adjusted to lower kinetic energies by $15\,eV$. This fine tuning of the energy scale has to be executed for each photon energy and results in the fully corrected kinetic energy spectrum after subtraction of an equally treated background (Figure 6.12). A linear fit to the Si $L_{3,2}$-line yields a binding energy of $108\,eV$. The binding energy of the Si $L_{3,2}$-edge has been reported to be $(108.0 \pm 0.3)\,eV$ relative to the vacuum level [Bianconi, 1979], which is in full agreement with the binding energy deduced from Figure 6.12. No spin-orbit split Si $L_{3,2}$-signal can be resolved. This is on the one hand due to the bandwidth of the X-rays ($3.8 - 7.0\,meV$) and on the other hand it is known that of the disorder of materials may also contribute that no fine structure splitting can be resolved [Anandan and Williams, 1990].

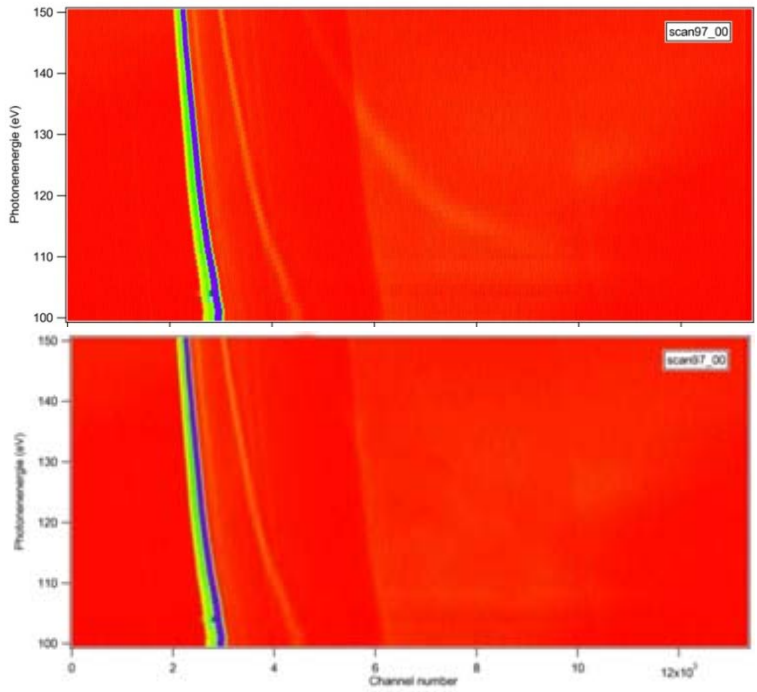

Figure 6.10. Photoelectron time-of-flight data of photon energy scan (scan0097). Increasing count rates are color coded from red to yellow, green, and blue to violet. Upper panel: Spectrum of SiO_2 particle beam. Lower panel: Background spectrum without particles. (Egill Antonsson[2], private communications).

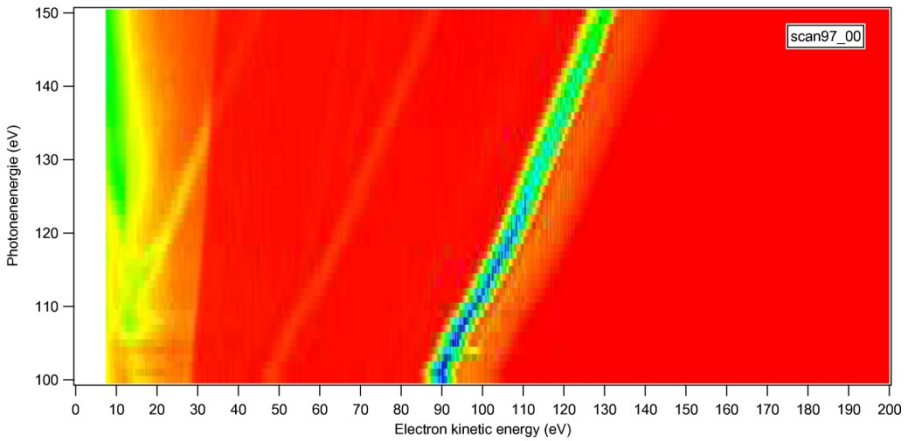

Figure 6.11. Photoelectron time-of-flight data of scan0097 after time-to-energy conversion and interpolation of the data.

[2] Egill Antonsson, Institut für Chemie und Biochemie - Physikalische und Theoretische Chemie, Freie Universität Berlin, Takustr. 3, 14195 Berlin

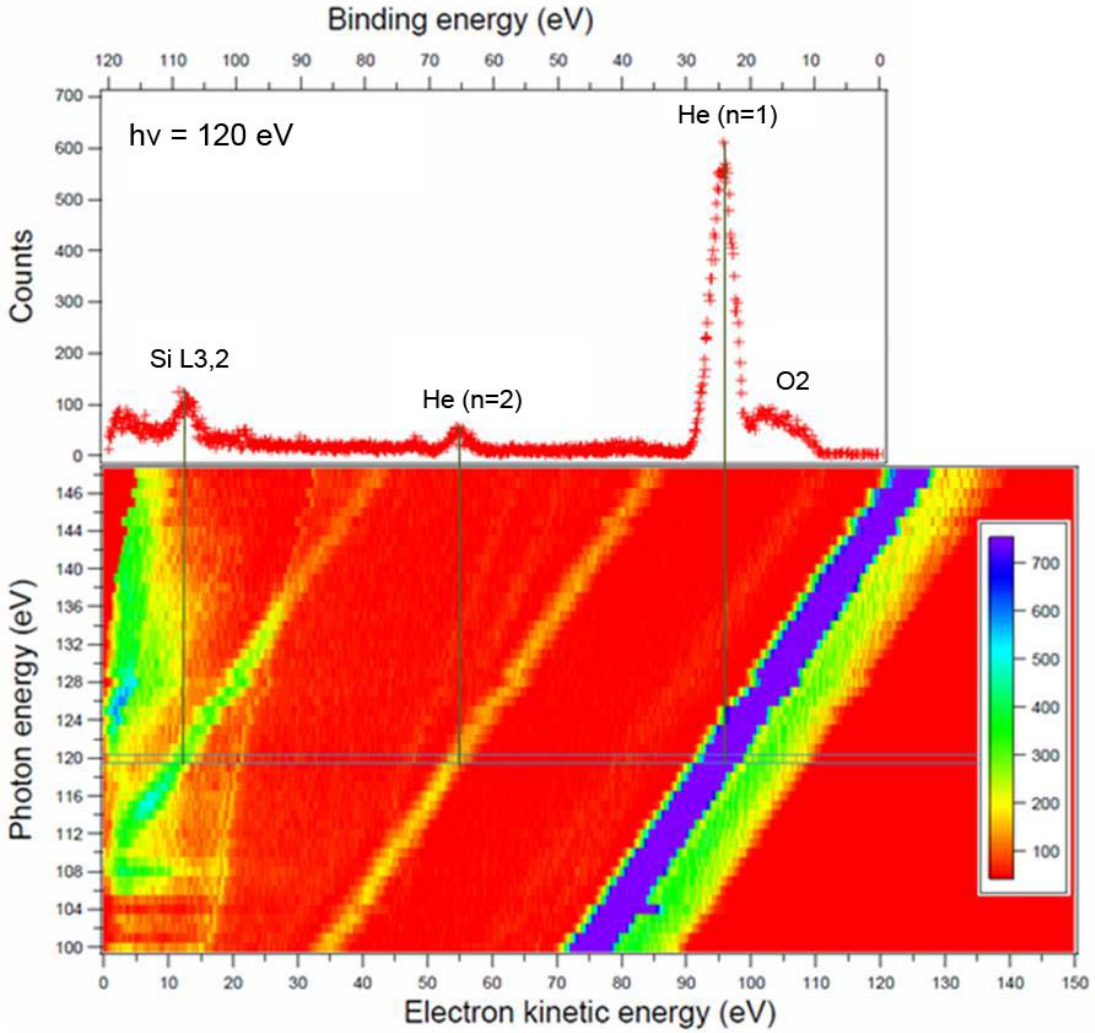

Figure 6.12. Lower panel: Si $L_{3,2}$-edge photoelectron kinetic energy spectrum of a free particle beam of SiO_2 particles with $(8.2 \pm 1.3)\,nm$ diameter after time-to-energy conversion and interpolation of the data. Upper panel: Single photon energy XPS-scan from the lower panel at $120\,eV$ photon energy on a binding energy scale. (reproduced from Meinen et al. [2010c])

Several features observed in Figure 6.12 correspond to artifacts, as clarified in the following. Specifically, the weak line starting at $15\,eV$ kinetic energy for a photon energy of $100\,eV$ with a slope > 1 is assigned to correspond to a sub-bunch, following the main bunch with a delay of $3\,ns$ in the electron storage ring. Such a distorted bunch structure occurs only occasionally depending on the operation of the storage ring. The broad and unstructured features appearing at low kinetic energies are most likely due to noise pile up after background subtraction and flight time to kinetic energy conversion.

In the upper panel of Figure 6.12, a single scan recorded at $120\ eV$ photon energy is shown on a binding energy scale. It is derived from the difference between the photon energy and the electron kinetic energy. The width of the Si $L_{3,2}$-peak is a consequence of the broad spectral bandwidth of the X-rays, which was required to have sufficient flux to take the XPS data.

Total electron yield spectra can be extracted from the raw data (Figure 6.10) by separation of fast and slow photoelectrons emitted from the background gas and the SiO_2 nanoparticles, respectively. First the background data is subtracted from the data recorded with particle beam. Than data from channel number $5.8\ 10^3$ to $9.0\ 10^3$ is summed up for each photon energy. This procedure results in the total electron yield spectrum shown in Figure 6.13. Comparison to spectra recorded from larger particles [Bresch, 2007] helps to identify the characteristic resonances of the Si $L_{2,3}$-edge. The Si $2p \rightarrow t_2^*$ (b) and the Si $2p \rightarrow e$ (d) resonances can clearly be identified. Even the Si $2p_{1/2} \rightarrow a_1^*$ (a´) feature is indicated in the spectrum as a red-shifted shoulder of the Si $2p \rightarrow t_2^*$ peak.

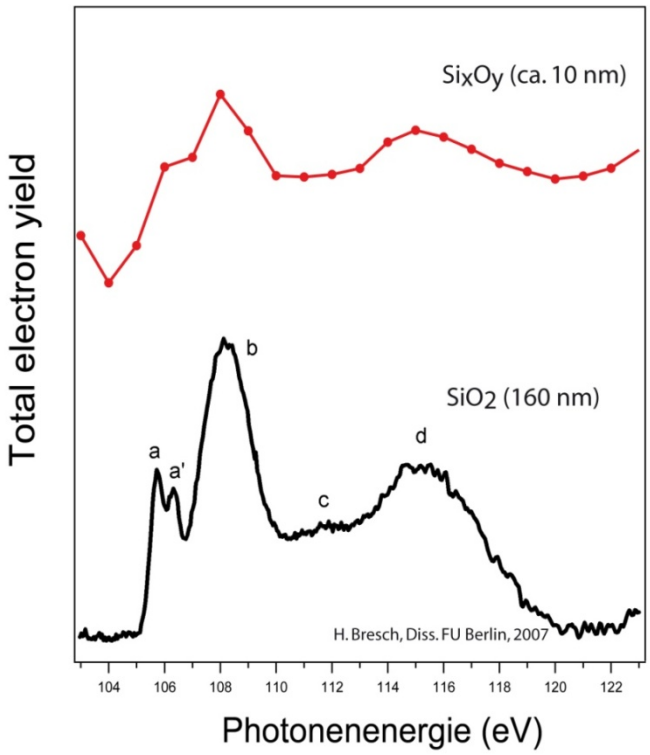

Figure 6.13. Si $L_{2,3}$-edge total electron yield spectrum of a free particle beam of SiO_2 particles with $d_p = (8.2 \pm 1.3)\ nm$ compared with a NEXAFS spectrum of particles with $d_p = 160\ nm$. (Egill Antonsson, private communications)

6.5 Conclusion

In conclusion, it was shown by this experiment that gas phase SiO_2 nanoparticles in the sub $10\,nm$ range can be prepared in sufficient concentration to perform photoelectron spectroscopy in the core level regime with X-rays from a third generation synchrotron radiation source operating in single bunch mode. This is accomplished by using an intense nanoparticle source in combination with efficient aerodynamic focusing of the particle beam into a linear ion-trap, where the particles are accumulated. Furthermore, pulsed ejection of the nanoparticles from the trap into the interaction region and efficient collection of the photoelectrons using a magnetic-bottle-type electron spectrometer are key parameters to have sufficient photoelectron signal. This approach appears to be promising for a broad range of studies of fundamental and applied research including environmental studies, since it does not require the use of free electron lasers, where access is presently limited to prototype experiments.

CHAPTER 7

Summary and Conclusion

TRAPS is a novel apparatus that allows gas-born nanoparticles in a diameter range from 3 to 15 nm to be efficiently transferred into vacuum for further investigation. With this system, nanoparticles with a size in the transition region from clusters to particles become accessible for analysis by a variety of techniques for the first time. The groundbreaking advantage over conventional techniques is that the nanoparticles are not collected on a substrate or filter prior investigation and thus it is ensured that their particular surface properties are unaffected upon examination. Furthermore the TRAPS enables to investigate nanoparticles with atmospheric relevance in the presence of the gas atmosphere conditions of interest. The obtained results are a good basis for applications in different fields. It was shown that gas phase SiO_2 nanoparticles in the sub$-10\,nm$ diameter range can be prepared in sufficient concentration to perform photoelectron spectroscopy in the core level regime with X-rays from a third generation synchrotron radiation source. This approach appears to be very promising for a broad range of studies of fundamental and applied research including environmental studies, since it does not require the use of free electron lasers, where access is presently limited to prototype experiments. Furthermore, it was shown that heterogeneous nucleation rates of ice on nanoparticles and ice particle growth rates can be determined by cavity assisted extinction spectroscopy. By this experiment, fundamental questions of mesopause ice cloud research can be investigated by laboratory experiments instead of rocket missions.

7.1 Technical advances

The inlet section of the modular TRAPS apparatus comprises nanoparticle sources, an aerodynamic lens particle inlet with subsequent differential pumping, and an octopole ion-guide. With this setup nanoparticles in a diameter range from 3 to $15\,nm$ which are produced in situ can efficiently be transferred into an ion-guide where either a tight nanoparticle beam is formed or the particles are accumulated and stored for a prolonged time for further analysis.

Electrospray and atomizer **particle sources** are used to produce salt nanoparticles of NaCl, $NaHCO_3$, and $Mg(NO_3)_2$ in helium carrier gas with particle number concentration of about $10^6\ cm^{-3}$. The typical mean diameter of these salt particles is $10-50\,nm$. A microwave plasma particle source is used for the in situ production of nanoparticles of different silicon oxides and iron oxides in helium carrier gas with high concentration up to $10^9-10^{12}\ cm^{-3}$. The oxidation state is selectable by the amount of oxygen given to the plasma. The particle size is variable from $3-15\,nm$ and the particle size FWHM is usually $<1\,nm$.

Nanoparticles are transferred into the vacuum device by a tunable **aerodynamic lens particle inlet**. The aerodynamic lens was refined from ordinary designs by computational fluid dynamic simulations to fulfill the demand of focusing particles in a size regime dominated by Brownian diffusion. A further novelty of the lens is its tuneability by which is become suitable for a wide range of particle size, martial density and carrier gas composition. The lens was proven to enhance the number of particles transferred into the subsequent experiment by a factor of 100 compared with traditional molecular beam inlets.

The octopole **ion-guide** is used to transfer charged particles entering the apparatus through a differential pumping section into high vacuum $\sim 10^{-5}\ mbar$. A special rf-power supply was developed and applied for a patent enabling storage of up to $5\ 10^8$ nanoparticle ions in the $20\ cm$ long ion-guide. A particle pulse exiting the ion-guide has a particle number density of up to some $10^7\ cm^{-3}$.

The experiment section of the modular TRAPS apparatus comprises a linear quadrupole ion-trap, nanoparticle detectors, a time-of-flight spectrometer, and an optical extinction cell. With this setup nanoparticles can be detected as pulse of many particles or as single particle. In the ion-trap nanoparticles can be investigated under atmospheric conditions of choice.

The **linear quadrupole ion-trap** provides a high density ion-cloud of homogeneous ion-density up to some $10^7\ cm^{-3}$. An arbitrary background gas can be filled into the ion-trap until a pressure range from 10^{-3} to $10^{-1}\ mbar$ is reached. The background gas can be humidified and the ion-trap can be cooled to sub $100\ K$ in order to simulate atmospheric conditions to be found in the mesopause region. The ion-cloud inside the ion-trap is accessible for photon beams.

The **nanoparticle detectors** are capable to detect a beam of singly charged particles as low as $2\ 10^6$ particles s^{-1} with up to $50\ kHz$ bandwidth by a faraday cup electrometer. A concept study of a "single particle" detector based on a channel-electron-multiplier has shown the ability to separate particle hitting rates $< 10^3\ s^{-1}$ from noise.

The **time-of-flight particle mass spectrometer** enables to in-situ monitor the mean particle mass of nanoparticles accumulated in an ion-trap.

The **optical extinction experiment** based on cavity enhanced technology provides an extinction light path through an ion-cloud inside the quadrupole ion-trap of $> 2000\ m$ at $405\ nm$ wavelength. Extinction coefficients as low as $2\ 10^{-10}\ cm^{-1}$ can principally be detected.

The whole TRAPS apparatus is modular and can be attached any or all of which to other vacuum equipment. It has been shown, that the high density particle inlet can be used for experiments at a synchrotron radiation beamline in combination with an electron time-of-flight spectrometer.

7.2 Methodical advances

High number densities of differently sized nanoparticles and variable stoichiometric composition can be produced in a very controlled environment by a microwave plasma particle source. This means that all experiments with the TRAPS apparatus can be performed dependent on particle size and stoichiometric composition.

Up to $5\ 10^8$ particles can be stored in the inlet octopole ion-guide and in the linear quadrupolar ion-guide. This target density principally suffices for direct absorption measurement in the visible, UV and X-ray regime. Particles can be extracted from the two ion-traps in sharp pulses of high particle density ($> 10^7\ cm^{-3}$). Flight time of the particles can be used to measure their mass-to-charge ratio yielding the mean particle size.

It was shown that the high density particle pulse enables to record x-ray photoionization spectra at the Si $L_{3,2}$ edge of sub $10\,nm$ SiO_2 particles at a synchrotron light source. Note, that such measurements have to our knowledge never been reported before for free nanoparticles of sub $150\,nm$ size.

It was shown that extinction cross sections of nanoparticles trapped inside the linear quadrupole ion-trap can be determined by cavity assisted spectroscopy. Furthermore ice nucleation on sub $10\,nm$ nanoparticles was monitored by cavity assisted spectroscopy and ion leak-rates of the quadrupolar ion-trap. Note, that ice nucleation experiments on free particles of that size have to our knowledge never been reported before.

7.3 Outlook on experiments relevant for NLC and PMSE research

For the case of meteoric smoke particles and ice particles forming NLCs and PMSEs, open questions have been discussed in the chapter 2. Some statements of leading researchers in this field were cited that underline the need for the investigation of the physical and chemical properties of meteoric smoke and ice particle found in the mesopause region. The most recent comment on the lack of experimental techniques was given by Rapp [2009] who noted that *'quantitative information from laboratory measurements of the photoemission properties of meteoric smoke particles is not available'* and thus *'laboratory measurements of processes like electron capture and photoemission in the transition size region from molecular clusters to nanoparticles are badly needed'*. An outlook to experiments directly feasible with the TRAPS apparatus is proposed below:

Experiments without supplementary instrumentation

1. It is questionable whether **optical parameters of nanoparticles** in the transition region from cluster to particle exhibit characteristics of the bulk material. For the determination of extinction coefficients with high accuracy three parameters have to be measured properly:
    a. The absorption coefficient of the nanoparticle cloud inside the ion-trap must be well known. Therefore the cavity assisted extinction signal evaluation approach, described in section 5.1, must be reexamined. The approach must be carefully checked by simulations of Eq. 5.5 and Eq. 5.6. A new LED light source with center wavelength at $415\,nm$ would reduce the problems with the multiexponential decay of the optical cavity employing the mirrors of higher reflectivity (Los Gatos Research).
    b. The particle number density inside the ion-trap must be exactly determined. It has to be double-checked, whether all trapped particles are counted by the faraday cup electrometer. Furthermore

the size of the ion-cloud has to be exactly known. This can either be done by simulations or by measurement of the spatial charge distribution as described in section 4.8.3.

c. The exact particle size and particle size distribution of the nanoparticles under investigation must be known. This will be feasible shortly, by a new designed time-of-flight particle mass spectrometer currently under construction.

2. The **complex refractive index** of nanoparticles with varying composition can be determined by evaluating extinction cross sections determined by experiment proposal 1. with Mie theory. Extinction cross sections for various nanoparticle sizes are required for this approach as described in section 5.2. This experiment can be performed at several wavelengths if appropriate sets of mirror and light sources are provided.
3. **Ice nucleation rates** dependent on particle size and stoichiometric composition can be determined by time resolved particle size determination at various ice saturation ratios. The efficiencies of the various aerosols to act as ice nuclei in the deposition mode of heterogeneous ice nucleation can be obtained by treating the measured data with process models well known from experiments in the AIDA cloud simulation chamber [Saunders, 2010]. It is assumed that heterogeneous nucleation critically depends on the number of ice nucleation active sites. The probability of a particle containing such an active site on the surface increases with surface area of the particle. Heterogeneous freezing rate can thus be determined by the fraction of particles which is frozen after a certain time in dependency of particle size [Archuleta, 2005].

   a. Particle sizes can either be determined by measurement of the optical extinction cross sections or by the ion-trap particle loss rate.
   b. For the determination of nucleation rates, gas temperature, and humidity inside the ion-trap must be well known. Temperature profiles inside the trap should be recorded since the temperature of the ion-trap housing can be monitored, only. The exact partial pressure of water inside the ion-trap will be monitored by a quadrupole mass spectrometer which is currently under setup.

Experiments with supplementary instrumentation

1. Quantitative information of the **photoemission properties** of meteoric smoke particles can easily be measured with the TRAPS apparatus and an appropriate light source. Laser systems and synchrotron radiation can be used as tunable light sources from the EUV to IR. Photodetachment and photoemission rates can be determined by irradiating an ion-cloud inside the quadrupolar ion-trap and monitoring the particle loss rate.
2. **Photoionization potentials** of the constituents in meteoric smoke particles can be measured in the EUV and soft x-ray regime with synchrotron radiation. A free nanoparticle beam setup as discussed in chapter 6 is suitable for this experiment. Shifts in core-to-valence transitions are unique to relate changes in electronic structure to the local geometric structure.
3. **Crystalline structure** and **stoichiometric composition** of nanoparticles can be determined by recording NEXAFS spectra with synchrotron radiation. In order to improve the quality of a photoelectron kinetic energy spectrum as shown in chapter 6, an additional differential pumping stage should be used to lower the background gas pressure by two orders of magnitude.
4. NEXAFS spectroscopy of the O K-edge of water assembled as a thin layer at the particle's surface will give insides of **water nucleation physics** on nanoparticles of different size and composition (recorded spectra must be compared to theoretical model calculations). Model calculations have predicted that two fold coordinated silicon atoms in SiO_2 are possible active sites on SiO_2 surfaces [Gritsenko, 2002]. This experiment bears technical difficulties:
    a. In the free nanoparticle beam setup described in chapter 6 the inlet octopole can be connected to a cryostat and humidified air can be mixed to the helium background gas inside the octopole in order to apply some layers of water at the particle surfaces. But the density of the free particle beam may not be sufficient to achieve a usable signal from a monolayer of water at the particle's surface.

   b. The sensitivity of the experiment can be increased by facilitating the charge reversal spectroscopy approach by trapping nanoparticles inside the linear quadrupolar ion-trap as described in section 3.7. But water layers may grow to fast at the trapped particles such that the technique is not sensitive for the bond of the first monolayer of water.

4. The latter technique (4.b) can be used for the determination of the **crystalline structure of ice** nucleated on nanoparticles. NEXAFS spectra will yield the information whether the structure is amorphous, cubic or hexagonal. When the ice core is nucleated on the particle prior trapping in the linear quadrupolar ion-trap, phase transitions of the crystalline structure of ice may be monitored by variation of the ion-trap temperature.
5. **Heterogenous chemistry** at the nanoparticle's surface can be investigated by XPS techniques. Experiments with atmospheric relevance would be the reaction of organic coatings by OH radicals, and the uptake and oxidation of sulfur dioxide to sulfate in sea-salt particles.

7.4 Acknowledgement

Herrn Prof. Dr. Thomas Leisner habe ich den wesentlichen Teil meiner wissenschaftlichen und beruflichen Erfahrung zu verdanken. Ohne das große Vertrauen, dass er mir entgegenbrachte als er mir dieses umfangreiche und verantwortungsvolle Projekt übertrug und mir dabei weitestgehend freie Hand bei der Umsetzung ließ, hätte ich mich sicherlich weniger weit entwickeln können. Die Arbeitsumgebung in seinem Institut und die Förderung meiner fachlichen und fachübergreifenden Fähigkeiten hätten nicht besser sein können. Für die gute Zeit unter seinen Fittichen möchte ich mich herzlich bedanken.

Herrn Prof. Dr. Ulrich Platt möchte ich für die zahlreichen Stunden danken, die er mit mir über resonatorverstärkte Extinktionsspektroskopie diskutiert hat. Er hatte eine schier unendliche Geduld mir beizubringen ein schwieriges Reviewverfahren zu überstehen.

Herrn Prof. Dr. Eckart Rühl sei für die Koordinierung des BMBF-Projektes gedankt, in das meine Arbeit eingebettet war. Vor allem die unkomplizierte und freundschaftliche Kommunikation haben die gemeinsamen Projekttreffen und die Arbeit an den Publikationen sehr beflügelt.

Dr. Markus Eritt und **Svetlana Khasminskaya** danke ich für die gute Kollegialität und Zusammenarbeit in der Atmospheric Nanoscience Gruppe. Vor allem war es bemerkenswert, wie sie meine Launen bei unserer BESSY Strahlzeit im Oktober 2009 kommentarlos ertragen haben.

Jan Christoph Habig sei dafür gedankt, dass er immer ein geeigneter Kandidat war, um über die verschiedensten Techniken der resonatorverstärkten Extinktionspektroskopie zu reden oder einfach nur so Quatsch im Labor zu machen. Ich hoffe, dass es ihm nicht all zu sehr auf die Nerven gefallen ist mein Versuchskaninchen gewesen zu sein, nachdem ich ein Seminar zur Personalführung besucht hatte.

Jim Thieser danke ich dafür als mein erster Diplomand das in meiner Diplomarbeit begonnene Projekt fortzuführen und so Daten zu meiner ersten Publikation beizusteuern.

Dr. Harald Saathoff danke ich für die vielen kleinen Tipps und Hilfestellungen in Sachen Aerosolphysik und –messtechnik, die er mir auf dem Weg zur Kantine mitgegeben hat.

Steffen Vogt, Meinhard Koyro, Thomaz Chudy, Rainer Buschbacher und **Georg Scheurig** haben mir als technische Crew im Institut die Arbeit unglaublich erleichtert. Ein so ambitioniertes Neubauprojekt hätte ohne ihre professionelle Hilfe niemals in der Kürze der Zeit umgesetzt werden können. Vielen Dank!

Egil Antonsson und **Dr. Burkhard Langer** sei für die Expertise in Sachen Synchrotronspektroskopie und ihren Einsatz bei unserer BESSY Strahlzeit im Oktober 2009 gedankt.

Werner Baumann war der Mann, der mich vor allem zu Beginn meiner Arbeit immer wieder motiviert hat meine Aerodynamischen Linsen zu verbessern, indem ich an seiner MPPS Partikelquelle und seinem PMS arbeiten durfte und indem er mich in die Aerosol-Massenspektrometrie Community einführte. Hierfür herzlichen Dank.

Dr. Vigna Szabo danke ich für die große Hilfe beim Aufbau der MPPS Quelle und für die Charakterisierung der Partikel mit Hilfe ihres TEMs.

Bob Martin hat sich die Bürde auferlegt das Englisch meiner Arbeit zu korrigieren. Obwohl für ihr als Fachfremder der Inhalt sicher langweilig gewesen ist, hat er sich eisern Satz für Satz durch die vielen Seiten gekämpft und Grammatik, Interpunktion und Ausdruck verenglischt. Dafür gilt ihm mein besonderer Dank.

Susanne Schulze hat sich nicht nur beim Korrekturlesen verdient gemacht, sondern hat mir die gesamten drei Jahre unnachgiebig im Nacken gesessen zielstrebig mein Projekt voranzutreiben und zum Erfolg zu führen. Vor allem sei ihr auch dafür gedankt, mir in den schwierigen Phasen meiner Arbeit den nötigen moralischen Rückhalt gegeben zu haben.

Appendix A

A – User Particle drag model for ANSYS CFX

ANSYS CFX requires user subroutines to be written in FORTRAN 77. This routine replaces the internal particle drag model by the model derived above. It calculated the Stokes particle drag force considering the Reynolds number correction (Eq. 4.16) and Cunningham slip correction (Eq. 4.18**Fehler! Verweisquelle konnte nicht gefunden werden.**).

```
#include "cfx5ext.h"
dllexport(pt_mom_source)
      SUBROUTINE PT_MOM_SOURCE(NLOC,NRET,NARG,RET,ARG,CRESLT,
     &                         CZ,DZ,IZ,LZ,RZ)
CC
CC User routine: Schiller-Naumann Drag Force corrected with Cunningham
CC
CC --------------------
CC        Input
CC --------------------
CC
CC  NRET   - number of components in result
CC  NARG   - number of arguments in call
CC  ARG() - (NARG) argument values
CC
CC --------------------
CC      Modified
CC --------------------
CC
CC  Stacks possibly.
CC
CC --------------------
CC        Output
CC --------------------
CC
CC  RET()  - (NRET) return values
CC
CC --------------------
CC       Details
CC --------------------
CC
CC=========================================================================
C
C ----------------------------
C     Preprocessor includes
C ----------------------------
C
C
C ----------------------------
C        Global Parameters
C ----------------------------
C
C
C ----------------------------
C        Argument list
C ----------------------------
C
      INTEGER NLOC,NARG,NRET
C
      REAL ARG(NLOC,NARG), RET(NLOC,NRET)
C
      CHARACTER CRESLT*(*)
C
      INTEGER IZ(*)
      CHARACTER CZ(*)*(1)
```

```
      DOUBLE PRECISION DZ(*)
      LOGICAL LZ(*)
      REAL RZ(*)
C
C ------------------------------
C        External routines
C ------------------------------
C
C
C ------------------------------
C        Local Parameters
C ------------------------------
C
C
C ------------------------------
C        Local Variables
C ------------------------------
C
C ------------------------------
C        Stack pointers
C ------------------------------
C
C=======================================================================
C
C --------------------------
C    Executable Statements
C --------------------------
C
C=======================================================================
C
C     Argument variables stack:
C     -------------------------
C
C     Particle diameter   :     DIAM_PT    = ARG(1,1)
C     Particle velocity   :     VEL_PT     = ARG(1,2:4)
C     Reynolds number     :     RE_PT      = ARG(1,5)
C     Slip velocity       :     SLPVEL_PT  = ARG(1,6)
C     Fluid density       :     DENSITY_FL = ARG(1,7)
C     Fluid velocity      :     VEL_FL     = ARG(1,8:10)
C     Fluid pressure      :     PRES_FL    = ARG(1,11)
C     Fluid Molar Weight  :     MW_FL      = ARG(1,12)
C     Fluid Temperature   :     TEMP_FL    = ARG(1,13)
C     Fluid dyn viscosity :     VISC_FL    = ARG(1,14)
C
C     Return variables stack:
C     -----------------------
C
C     Source term         :     SOURCE     = RET(1,1:3)
C     Source coefficient  :     COEF_PT    = RET(1,4)
C     Source coefficient  :     COEF_FL    = RET(1,5)
C
C=======================================================================
C
C-----------------------------------------------------------------------
C     Calculate the momentum source and source term coefficient
C-----------------------------------------------------------------------
C
      CALL USER_MOMENTUM_SOURCE (RET(1,1),RET(1,4),RET(1,5),
     &                           ARG(1,1),ARG(1,2),ARG(1,5),ARG(1,6),
     &                           ARG(1,7),ARG(1,8),ARG(1,11),ARG(1,12),
     &                           ARG(1,13),ARG(1,14))
C
      END

      SUBROUTINE USER_MOMENTUM_SOURCE (SOURCE,COEF_PT,COEF_FL,
     &                                 DIAM_PT,VEL_PT,RE_PT,SLPVEL_PT,
     &                                 DENSITY_FL,VEL_FL,PRES_FL,MW_FL,
     &                                 TEMP_FL,VISC_FL)
C
C=======================================================================
C     Calculate the momentum source and source term coefficient
C=======================================================================
C
C ------------------------------
C     Preprocessor includes
```

```
C ------------------------------
C
#include "cfd_sysdep.h"
#include "cfd_constants.h"
C
C ------------------------------
C        Argument list
C ------------------------------
C
      REAL               SOURCE(3), COEF_PT, COEF_FL,
     &                   DIAM_PT, VEL_PT(3), RE_PT, SLPVEL_PT,
     &                   DENSITY_FL, VEL_FL(3), PRES_FL, MW_FL,
     &                   TEMP_FL, VISC_FL
C
C ------------------------------
C        Local variables
C ------------------------------
C
      REAL               AREA, CD, FACT, CU, LAMBDA, MVELO
C
C ------------------------------
C    Executable statements
C ------------------------------
C
C---- Calculate the particle reference area
C
      AREA = PI*DIAM_PT**2*QUARTER
C
C---- Calculate the Schiller-Naumann drag coefficient
C
      IF (RE_PT.LT.1000.) THEN
        CD = 24./RE_PT*(1+0.15*RE_PT**0.687)
      ELSE
        CD = 0.44
      ENDIF
C
C---- Calculate the mean velocity of the gas molecules
C
      MVELO = SQRT(66.516*TEMP_FL/(3.1415*MW_FL))
C
C---- Calculate the mean free pathlength of the gas
C
      LAMBDA = 3.*VISC_FL/(DENSITY_FL*MVELO)
C
C---- Calculate the Cunningham correction for air
C
      CU = 1.+LAMBDA/DIAM_PT*(2.514+0.80*EXP(-0.55*DIAM_PT/LAMBDA))
C
C---- Calculate the momentum soure term and linear coefficients
C
      FACT = HALF*DENSITY_FL*AREA*CD*SLPVEL_PT/CU
C
      SOURCE(1) = FACT*(VEL_FL(1)-VEL_PT(1))
      SOURCE(2) = FACT*(VEL_FL(2)-VEL_PT(2))
      SOURCE(3) = FACT*(VEL_FL(3)-VEL_PT(3))
C
      COEF_PT = -FACT
      COEF_FL =  FACT
C
      END
```

References

Abu-samha, M., Borve, K.J., Harnes, J. and Bergersen, H. (2007) What can C1s photoelectron spectroscopy tell about structure and bonding in clusters of methanol and methyl chloride. J. Phys. Chem. A 111:8903-8909.

Allen, M.D. and Raabe, O.G. (1985). Slip Correction Measurements of Spherical Solid Aerosol Particles in an improved Millikan Apparatus. *Aerosol Sci. Technol.* 4:269-286.

Anandan, C. and Williams, R.H. (1990) Investigation of HF etched hydrogenated amorphous silicon surfaces by X-ray photoelectron spectroscopy. Semiconductor Science and Technology 5:265.

ANSYS CFX-Solver Modeling Guide. ANSYS CFX Release 11.0. © 1996-2006 ANSYS Europe, Ltd. (2005) 566 pages.

ANSYS CFX-Solver Theory Guide. ANSYS CFX Release 11.0. © 1996-2006 ANSYS Europe, Ltd. (2006) 312 pages.

Archuleta, C.M., DeMott, P.J. and Kreidenweis, S.M. (2005) Ice nucleation by surrogates for atmospheric mineral dust and mineral durst/sulfate particle at cirrus temperatures. Atmos. Chem. Phys. 5:2617-2634.

Attwood, D. (1999). Soft X-Rays and Extreme Ultraviolet Radiation. Cambridge University Press.

Backhouse, T.W. (1886) The bright clouds, Nature, 34:312.

Baker, R.C. (2000). Flow measurement handbook: industrial designs, operating principles, performance, and applications. Cambridge University Press, p. 524.

Ball, S.M., Langridge, J.M., and Jones, R.L. (2004) Broadband cavity enhanced absorption spectroscopy using light emitting diodes. Chem. Phys. Lett. 398:68-74.

Baumann, W, Thekedar, B.S., Paur, H.R. and Seifert, H. (2005). Characterisation of Nanoparticles Synthesized in the Microwave Plasma Discharge Process by Particle Mass Spectrometry and Transmission Electron Microscopy. News – Forschungszentrum Karlsruhe, 37:89-95

Berden, G., Peeters, R. and Meijer, G. (2000) Cavity ring-down spectroscopy: Experimental schemes and applications.

Bianconi, A. (1979) Core excitons and inner well resonances in surface soft x-ray absorption (SSXA) spectra. Surface Science 89:41.

Björneholm, O., Öhrwall, G. and Tchaplyguine, M. (2009) Free clusters studied by core-level spectroscopies. Phys. Res. A 601:161-181.

Boulos M.I. (1984) Modelling of plasma processes. In: SzekelyJ, Apelian D. (eds) Plasma processing and synthesis ofmaterials symposium. North-Holland, New York, NY,USA, pp 53–60

Boren, C.F. and Huffmann, D.R. (1983) Absorption and scattering of light by small particles. New York, Wiley-Interscience.

Boren, C.F. and Olivero, J.J. (1984) Evidence for haematite particles at 60 km altitude. Nature 310:216-218.

Brattli, A., Lie-Svendsen, O., Svenes, K., Hoppe U.-P., Strelnikova, I., Rapp, M., Latteck, R. and Friedrich, M. (2009) The ECOMA 2007 campaign: rocket observations and numercical modeling of aerosol particle charging and plasma depletion in a PMSE/NLC layer. Ann. Geophys. 27:781-796.

Bresch, H. (2007) Photoionisation von freien Aerosolpartikeln mit Synchrotronstrahlung. PhD-Thesis, Freie Universität Berlin, Germany, pp210.

Bresch, H. Wassermann, B., Langer, B., Graf, C., Flesch, R., Becker, U., Österreicher, B., Leisner, T., and Rühl, E. (2008) Elastic light scattering from free sub-micron particles in the soft X-ray regime. Faraday Discuss. 137:2008.

Bruchez, M., Moronne, M., Gin, P., Weiss, S. and Alivisatos, A.P. (1998) Semiconductor Nanocrystals as Flourescent Biological Labels. Science 281:2013-2016.

Butler, T.J.A., Mellon, D., Kim, J., Litman, J. and Orr-Erwig A.J. (2009) Optical-Feedback Cavity Ring-Down Spectroscopy Measurements of Extinction by Aerosol Particles. J. Phys. Chem. A 113:3963-3972.

Castleman Jr., A.W., Holland, P.M. and Keese, R.G. (1978) The properties fo ion clusters and their relationship to heteromolecular nucleation. J.Chem. Phys. 68:1760-1767.

Champenois, C. (2009) About the dynamics and thermodynamics of trapped ions. *J. Phys. B.* 42:154002.

Chen, D.R., Pui, D.Y. and Kaufman, S.L. (1995). Electrospraying of Conducting Liquids for Monodisperse Aerosol Generation in the 4 nm to 1.8 μm Diameter Range. *J. Aerosol Sci.* 26:963-977.

Chen, D.R.; Pui, D.Y.H, Hummes, D., Fissan, H., Quant, F.R. and Sem, G.J. (1998). Design and evalution of a nanometre aerosol differential mobility analyzer. *J. Aerosol Science*, 29:497-509.

Cheshnovsky, O., Yang, S.H., Pettiette, C.L., Craycraft, M.J. and Smalley, R.E. (1987) Magnetic time-of-flight photoelectron spectrometer for mass-selected negative cluster ions. Rev. Sci. Instrum. 58:2131-2137.

Cho, J.Y.N. and Röttger, J. (1997) An updated review of polar mesosphere summer echoes: Observation, theory and their relationship to noctilucend coulds and subvisible aerosol. J. Geophys. Res. 102:2001-2020.

Cole, R.B. (1997). Electrospray ionization mass spectrometry: fundamentals, instrumentation and applications. New York u.a. : Wiley, p. 600.

Daly, N.R. (1960) Scintillation Type Mass Spectrometer Ion Detector. Rev. Sci. Instr. 3:264-267.

Ding, L., Sudakov, M. and Kumashiro, S. (2001) A simulation study of the digital ion trap mass spectrometer. Int. J. Mass. Spectrom. 221:117-138.

Ding, L.; Sudakov, M., Brancia, F.L., Giles, R. and Kumashiro, S. (2004). A digital ion trap mass spectrometer coupled with atmospheric pressure ion sources. *Journal of Mass Spectrometry*, 39: 471-484

Dinar, E., Abo Riziq, A., Spindler, C., Erlick, C., Kiss, G. and Rudlich, Y. (2008) The complex refractive index of atmospheric and model humic-like substances (HULIS) retrieved by a cavity ring down aerosol spectrometer (CRD-AS). Faraday Discuss. 137:279-295.

Douglas, D.J., Frank, A.J. and Dunmin, M. (2005). Linear Ion Traps in Mass Spectrometry. *Mass Spectrometry Reviews*, 24:1-29.

Ecklund, W.L. and Balsley, B.B. (1981) Long-Term Observations of the Arctic Mesosphere with the MST Radar at Poker Flat, Alaka, J. Geophys. Res., 86:7775-7780.

Engeln, R., Berden, G., Peeters, R. and Meijer, G. (1998) Cavity enhanced absorption and cavity enhanced magnetic rotation spectroscopy, Rev. Sci. Instrum. 69:3763-3769.

Epstein, P.S. (1924). On the Resistance Experienced by Spheres in their Motion through Gases. *Phys. Rev*. 23:710-733

Fuchs N.A. (1963). On the Stationary Charge Distribution on Aerosol Particles in a Bipolar. Ionic Atmosphere. Geophys. Pura Appl. 56 :185-193.

Fraser, G.W. (2002) The ion detection efficiency of microchannel plates (MCPs). Int. J. Mass. Spectrom. 215:13-30.

Gadsden , M (1982). Noctilucent clouds. Space Science Review 33:279-334

Gadsden, M., Schröder, W. (1989) Noctilucent Clouds. Springer Verlag, New York, Berlin.

Gard, E., Mayer, J.E., Borrical, B.D., Dienes, T., Fergenson, D.P. and Prather, K.A. (1997) Real-Time Analysis of Individual Atmospheric Aerosol Particles: Design and Performance of a Portable ATOFMS, Anal. Chem. 69:4083-4091.

Gelinas, L. J., Lynch, K. A., Kelley, M. C., Collins, S., Baker, S., Zhou, Q., and Friedman, J. S. (1998) First observation of meteoritic charged dust in the tropical mesosphere. Geophys. Res. Lett. 25:4047-4050.

Gerlich, D. (1992). Advances in chemical physics LXXXII. Inhomogeneous RF fields: A versatile tool for the study of processes with slow ions. New York: John Wiley and Sons. Pp 1-176

Gerlich, D. (2003). Molecular Ions and Nanoparticles in RF and AC Traps. Hyperfine Interactions 146/147 293-306.

Gilmore, I.S. and Seah, M.P. (2000) Ion detection efficiency in SIMS: dependencies on energy, mass and composition for microchannel plates used in mass spectrometry. Int. J. Mass Spectrom. 2002:217-229.

Gohshi, Y. (1996). Applications of Synchrotron Radiation to Material Analysis. Elsevier, Amsterdam

Goodrich, G.W. and Wiley, W.C. (1962) Continuous Channel Electron Multiplier. Rev. Sci. Instr. 33:761.

Grassia, P.S. (2001). Dissipation, Fluctuations, and Conservation Laws, Amer. J. Physics 69(2):113-119.

Grimm, M., Langer, B., Schlemmer, S., Lischke, T., Becker, U., Widdra, W., Gerlich, D., Flesch, R., and Rühl, E. (2006) Charging Mechanisms of Trapped Element-Selectively Excited Nanoparticles Exposed to Soft X-Rays. Phys. Rev. Lett. 96:066801-1-4.

Gritsenko, V.A., Shaposhnikov, A.V., Zhidomirov, G.M. and Roger, M. (2002) Two fold coordinated silicon atom: a hole trap in SiO2. Solid State Comm. 121:301-304.

Gumbel, J., Siskind, D. E., Witt, G., Torkar, K. M., and Friedrich, M. (2003) Influence of ice particles on the ion chemistry of the polar summer mesosphere. J. Geophys. Res. 108:3.1-3.16

Gumbel, J. and Megner, L. (2009) Charged meteoric smoke as ice nuclei in the mesosphere: Part 1 – A review of basic concepts. J. Atmos. Solar-Terrestrial Phys. 71:1225-1235.

Hatusi, T., Setoyama, H., Kosugi, N., Wassermann, B., Bradeanu, I.L., and Rühl, E. (2005) Photoionization of small krypton clusters in the Kr 3d regime: Evidence for site-specific photoemission. J. Chem. Phys. 123:154304.

Habig, J.C. (2009) Aufbau und Charakterisieung eines resonatorverstärkten Wasserdampf Absorptionsspektrometers. Diplomarbeit, Fakultät für Physik und Astronomie, Ruprecht-Karls-Universtität Heidelberg.

Haynes, C.L. and Van Duyne, R.P. (2001) Nanosphere Lithography: A versatile nanofabrication tool for studies of size-dependent nanoparticles optics. J. Phys. Chem. B 105:5599-5611.

Heberlein J.V.R. (1989) Plasma technology in materials processing. Cryst Prop Prep 22–25:707–726

Hinds, W.C. (1999) Aerosol Technology, 2. New York, Chichester, Weinheim, Brisbane, Singapore, Toronto: John Wiley & Sons Inc

Huffman, J., Jayne, J., Drewnick, F., Aiken, A., Onasch, T. and Worsnop, D. (2005). Design, modeling, optimization, and experimental tests of a particle beam width probe for the aerodyne aerosol mass spectrometer. Aerosol Science and Technology, 39:330-337.

Hunten, D. M., Turco, R. P. and Toon, O. B. (1980) Smoke and Dust Particles of Meteoric Origin in the Mesosphere and Stratosphere. J. Atmos. Sci. 37: 1342–1357.

IPCC (2007): Solomon, S., D. Qin, M. Manning, Z. Chen, M. Marquis, K.B. Averyt, M. Tignor and H.L. Miller (eds.). Contribution of Working Group I to the Fourth Assessment Report of the Intergovernmental Panel on Climate Change, 2007. Cambridge University Press, Cambridge, United Kingdom and New York, NY, USA.

Jackson, J.D. (1962). Classical Electrodynamics. Wiley, New York

Janzen, C. (2002). Untersuchungen zur Synthese von Eisenoxid-Nanopartikeln in der Gasphase. Doctoral thesis.

Jayne, J.T., Leads, D.C., Zhang, X., Davidovits, P., Smith, K.A., Kolb, C.E. and Worsnop, D.R. (2000) Development of an aerosol mass spectrometer for size and composition analysis of submicron particles. Aerosol Sci. and Technology 33:49-70.

Kalashnikova, O., Horanyi, M., Thomas, G. E. and Toon, O. B. (2000) Meteoric smoke production in the atmosphere. Geophys. Res. Lett. 27: 3293–3296.

Kaneko, T., Odaka, Y., Tada, E., Hatakeyama, R. (2002) Generation and control of field-aligned flow velocity shear in a fully ionized collisionless plasma. Rev Sci Instrum 73: 4218–4222

Kuhn, H.R., Koch, J., Hergenröder, R., Niemax, K., Kalberer, M. and Günther, D. (2005). Evaluation of different techniques for particle size distribution measurements on laser-generated aerosols. J. Anal. At. Spectrom, 20:894-900.

Kreibig, U. and Genzel, L. (1985) Optical absorption of small metallic particles. Surface Science 156:678-700.

Kruit, P. and Read, F.H. (1983) Magnetic field paralleliser for 2π electron-spectrometer and electron-image magnifier. J. Phys. E: Sci. Instrum. 16:313-324.

Langer, B. and Becker, U. (2009) Correlation and coherence phenomena studied by photoelectron spectroscopy. Nuclear Inst. and Methods in Physics Research, A 601:78-87.

Laskin, A., Iedema, M.J. and Cowin J.P. (2003) Time-Resolved Aerosol Collector for CCSEM/EDX Single-Particle Analysis. Aerosol Sci. Technol. 37:246-260.

Lee, K.S., Cho, S.W. and Lee, D. (2008). Development and experimental evaluation of aerodynamic lens as an aerosol inlet of single particle mass spectrometry. *J. Aerosol Sci.* 39:287-304.

Lesli, R.J. (1885) Sky glows, Nature, 33:245.

Li, Z. and Wang, H. (2003a) Drag force, diffusion coefficient, and electric mobility of small particles. I. Theory applicable to the free-molecular regime, *Physical Review E* 68(61):61206-1-9

Li, Z. and Wang, H. (2003b) Drag force, diffusion coefficient, and electric mobility of small particles. II.Application, *Physical Review E* 68(61):61207-1-13

Lindley, P.F. (1999). Macromolecular crystallography with a third-generation synchrotron source. Biological Crystallography 55:1654-1662

Liu, B.Y.H. and Lee, K.W. (1975) An Aerosol Generator of High Stability. *Am. Ind. Hyg. Assoc. J.* 36:861–865

Liu, P., Ziemann, P.J., Kittelson, D.B. and McMurry, P.H. (1995a) Generating Particle Beams of Controlled Dimensions and Divergence: I. Theory of Particle Motion in Aerodynamic Lenses and Nozzle Expansions. *Aerosol Sci. Technol.* 22:293-313.

Liu, P., Ziemann, P.J., Kittelson, D.B. and McMurry, P.H. (1995b) Generating Particle Beams of Controlled Dimensions and Divergence: II. Experimental Evaluation of Particle Motion in Aerodynamic Lenses and Nozzle Expansions. *Aerosol Sci. Technol*. 22:314-324.

Liu, P., Rao, N.P., Kittelson, D.B. and McMurry, P.H. (1996) Optimizing the Detection Efficiency of a Low Pressure, In-situ Particle Monitor Using Aerodynamic Focusing Lenses. Proceedings – Institute of Environmental Science: 1-8.

Liu, P.S.K., Deng, R.,; Smith, K.A., Williams, L.R., Jayne, J.T., Canagaratna, M.R., Moore, K., Onasch, T.B., Worsnop, D.R. and Deshler, T. (2007) Transmission Efficiency of an Aerodynamic Focusing Lens System: Comparison of Model Calculations and Laboratory Measurements for the Aerodyne Aerosol Mass Spectrometer. *Aerosol Sci. Technol.* 41:721-733.

Loboda, A., Drutchnsky, A., Loboda, O., McNabb, J., Spicer, V., Ens, W. and Standing, K. (2000) Novel LINAC II Electrode Geometry to Create an Axial Field in a Multipole Ion Guide. Euro. J. Mass Spectrom. 6:531-536.

Loscertales, I.G. (2000). Mass Diameter Versus Aerodynamic Diameter of Nanoparticles. Implications on the Calibration Curve of an Inertial Impactor, *J. Aerosol Sci.* 31(8):923-932

Love, S. G. and Brownlee, D. E. (1991) Heating and thermal transformation of micrometeoroids entering the Earth's atmosphere. Icarus 89:26-43.

Lübken, F.-J. (1999) Thermal structure of the Arctic summer mesosphere. J. Geophys. Res. 104:9135-9149.

Lübken, F.-J., Zecha, M., Höffner, J., and Röttger, J. (2004) Temperatures, polar mesosphere summer echoes, and noctilucent clouds over Spitsbergen (78±N), J. Geophys. Res., 109:11203 1-14.

Lundwall, M., Tchaplyguine, M., Öhrwall, G., Lindblad, A., Peredkov, S., Rander, T., Svensson, S. and Björneholm, O. (2005) Enhanced surface sensivity in AES relative to XPS observed in free argon clusters. Surface Science 594:12-19.

Lynch, K. A., Gelinas, L. J., Kelley, M. C., Collins, R. L., Widholm, M., Rau, D., MacDonald, E., Liu, Y., Ulwick, J., and Mace, P.(2005) Multiple sounding rocket observations of charged dust in the polar winter mesosphere. J. Geophys. Res. 110:A03302.

Mamija, T., Terasaki, A. and Kondow, T. (2008) Optical pumping by a laser pulse traveling in a cavity. Phys. Rev. A 77:033417-4.

Manolache, S. and Denes, F. (2000) Synthesis of nanoparticles under cold-plasma conditions. J Photopolym Sci Technol 13: 51–62

Maria, S.F., Russell, L.M., Gilles, M.K. and Myneni, S.C.B. (2004) Organic Aerosol Growth Mechanisms and Their Climate-Forcing Implications. Science 306:1921-1924

Maus, C. (2010) Laborexperimente zur Mikrophysik geladener Wolkentropfen – Untersuchungen in einem elektrodynamischen Levitator, Bachelorarbeit, Institut für Physik der Technischen Universität Ilmenau.

Mätzing, H., Baumann, W., Hauser, M., van Raaij, A., Paur, H.-R., Seifert, H. and Roth, P. (2003) Mass Spectrometer for Particles in the Nanometer Size Regime. Abstracts of the European Aerosol Conference, J. Aerosol Sci. 34:277-8.

Megner, L., Sisking, D.E., Rapp, M. and Gumbel, J. (2008) Global and temporal distribution of meteoric smoke: A two-dimensional simulation study. J. Geophys. Res. 113:D03202.

Megner, L. and Gumbel, J. (2009) Charged meteoric particles as ice nuclei in the mesosphere: Part 2 – A feasibility study. J. Atmos. Solar-Terrestrical Phys. 71:1236-1244.

Meinen, J., Österreicher, B., and Leisner, T (2009) Patent Pending at German Patent Office. Reference Number 10 2009 023 700.3.

Meinen, J.; Khasminskaya, S.; Baumann, W.; Rühl, E. and Leisner, T. (2010a) The TRAPS apparatus: Enhancing target density of nanoparticle beams in vacuum for X-ray and optical spectroscopy. Aerosol Science and Technology, 44:316-328.

Meinen, J.; Thieser, J.; Platt, U.; Leisner, T. (2010b) Technical Note: Using a high finesse optical resonator to provide a long light path for differential optical absorption spectroscopy: CE-DOAS. Atmos. Chem. Phys., 10:3901-3914.

Meinen, J.; Khasminskaya, S.; Eritt, M.; Leisner, T., Antonsson, E.; Langer, B.; Rühl, E. (2010c) Core level photoionization on free sub-10 nm nanoparticles using synchrotron radiation. Rev. Sci. Instr., in review.

Moosmüller, H., Varma, R. and Arnott, W.P. (2005) Cavity ring-down and cavity-enhanced detection techniques for the measurement of aerosol extinction. Aerosol Sci. and Technol. 39:30-39.

de la Mora, J.F. (1996) Drastic improvement of the resolution of aerosol size spectrometers via aerodynamic focusing: The case of variable-pressure impactors, *Chem. Engineering Comm.* 151:1,101-104.

de la Mora, J.F., de Juan, L., Liedtke, K. and Schimidt-Ott, A. (2003). Mass and Size Determination of Nanometer Particles by Means of Mobility Analysis and Focused Impaction, *J. Aerosol Sci.* 34:79-98

Mühlhopt, S., Baumann, W., Mätzing, H., Roth, P., van Raaij, A. and Paur, H.-R. (2002) Partikelmassenspektrometer für gasgetragene Nanopartikel, Chemie-Ingenieur-Technik 54:548.

Mysak, E.R., Starr, D.E., Wilson, K.R. and Bluhm, H. (2010) Note: A combined aerodynamic lens/ambient pressure x-ray photoelectron spectroscopy experiment for the on-stream investigation of aerosol surfaces. Rev. Sci. Instr. 81:016106

Naumann, K.H. (2003). COSIMA – a computer program simulating the dynamics of fractal aerosols. *J.Aerosol Science.* 34:1371-1397.

O'Keefe, A. and Deacon, D.A.G. (1988) Cavity ring-down optical spectrometer for absorption measurement using pulsed laser sources. Rev. Sci. Instrum. 59:2544.

Passig, J.; Meiwes-Broer, K.-H. and Tiggesbäumker, J. (2006) Collimation of metal Nanoparticles beams using aerodynamic lenses. Rev. Sci. Instr. 77:093304.

Paur, H.-R., Baumann, W., Mätzing, H. and Seifert, H. (2005) Formation of nanoparticles in flames; measurement by particle mass spectrometry and numerical simulation. Nanotechnology 16:354-361.

Plane, J.M.C. (2003) Atmospheric Chemistry of Meteoric Metals. Chem. Rev. 103:4963-4984.

Pruppacher, H.R. and Klett, J.D. (1997) Microphysics of clouds and precipitation, 2. Überarbeitete Auflage, Kluwer Academic Publishers, Dordrecht.

Rapp, M. and Lübken, F.-J. (2004) Polar mesosphere summer echoes (PMSE): review of observations and current understanding. Atmos. Chem. Phys. 4:2601-2633.

Rapp, M., Hedin, J., Strelnikova, I., Friedrich, M., Gumbel, J., and LÄubken, F.-J. (2005) Observations of positively charged nanoparticles in the nighttime polar mesosphere. Geophys. Res. Lett. 32:L23821.

Rapp, M. and Thomas, G.E. (2006) Modeling the microphysics of mesospheric ice particles: Assessment of current capabilities and basic sensivities. J. Atmos. And Solar-Terrestrial Phys. 68:715-744.

Rapp, M. (2009) Charging of mesospheric aerosol particles: the role of photodetachement and photoionization from meteoric smoke and ice particles. Ann. Geophys. 27:2417-2422.

Rietmann, T., Sohn, S., Schröder, M., Lipinsky, D. and Arlinghaus, H.F. (2006) Comparison of detection efficiencies of negatively charged gold-alkanethiolate-, gold-sulfur- and gold-clusters in ToF-SIMS. Appl. Surf. Sci. 252:6640-6643.

Rietmeijer, F. J. M. (2001) Identification of Fe-rich meteoric dust. Planet. Space Sci. 49:71-77.

Romanini, D, Kachanov, A.A., Sadeghi, N. and Stoeckel, F. (1997) CW cavity ring down spectroscopy. Chem. Phys. Lett. 264:316-322.

Sappey, A.D., Hill, E.S., Settersten, T. and Linne, M.A. (1998) Fixed Frequency cavity ringdown diagnostic for atmospheric particulate matter. Opt. Lett. 23:954

Saunders, R.W., Möhler, O., Schaiter, M., Benz, S., Wagner, R., Saathoff, H., Conolly, P.J., Burgess, R., Murray, B.J., Gallagher, M., Wills, R. and Plane, J.M.C. (2010) An aerosol chamber investigation of the heterogeneous ice nucleation potential of refractory nanoparticles. Atmos. Chem. Phys. 10:1227-1247.

Sawhney, K.J.S.; Senf, F.; Scheer, F.; Schäfers, F.; Bahrdt, J.; Gaupp, A. and Gudat, W. (1997). A novel undulator-based PGM beamline for circularly polarised synchrotron radiation at BESSY II. Nucl. Instr. Meth. A, 390:395-402.

Schulte, P. and Arnold, F. (1992) Detection of upper atmospheric negatively charged microclusters by a rocket-borne mass spectrometer. Geophys. Res. Lett. 19:2297-2300.

Seele, C. and Hartogh, P. (1999) Water vapor oft he polar middle atmosphere: Annual variation and summer mesosphere Conditions as observed by ground based microwave spectroscopy. Geophys. Res. Lett., 26:1517-1520.

Sigloch, H. (2008). *Technische Fluidmechanik*. 6. Auflage. Springer-Verlag Berlin Heidelberg, p. 581.

Spindler, C., Abo Riziq, A. and Rudlich, Y. (2007) Retrieval of Aerosol Complex Refractive Index by Combining Cavity Ring Down Aerosol Spectrometer Measurements with Full Size Distribution Information. Aerosol Sci. and Technology 41:1011-1017.

Spuler, S. and Linne M (2002) Numerical Analysis of Beam Propagation in Pulsed Cavity Ring-Down Spectroscopy. Appl. Optics 41:2858-2868.

Stöhr, J. (1996). NEXAFS Spectroscopy. Corr. 2. Printing. Springer-Verlag Berlin Heidelberg.

Sun, Y. and Xia, Y. (2003) Gold and silver nanoparticles: A class of chromophores with colors tunable in the range from 400 to 750 nm. Analyst 128:686-691.

Szabo, D.V., Vollath, D., Taylor, R.D. and Willis, J.O. (1997). Synthesis and magnetic properties of nanostructured maghemite. *Journal of materials research*. 12:2175-2182.

Szabo, D.V. and Vollath, D. (1999). Nanocomposites from coated nanoparticles. *Advanced material*. 11:1313-1316.

Szekely J. (1984) An overview of plasma processing. In: Szekely J, Apelian D (eds) Plasma processing and synthesis of materials symposium. North-Holland, New York, NY, USA, pp 1–11.

Tammet, H. (1995). Size and Mobility of Nanometer Particles, Clusters and Ions, *J. Aerosol Sci.* 26(3):459-475

Taylor, P.R., Vidal, E.E. (1999) Thermal plasma synthesis of ceramic powders. In: Marquis EDS (ed) Powder materials: current research and industrial practices. Proceedings of symposium held during 1999 TMS fall meeting. TMS Miner Metals & Mater Soc, Warrendale, PA, USA, pp 173–185

Terasaki, A., Majima, T. and Kondow, T. (2007) Photon-Trap spectroscopy of mass-selected ions in an ion trap: Optical absorption and magneto-optical effects. J. Chem. Phys. 127:231101-4.

Terasaki, A.; Majima, T.; Kasai, C. and Kondow, T. (2009) Photon-Trap spectroscopy of size-selected free cluster ions: "direct" measurement of optical absorption of Ag_9^+. Eur. Phys. J. D. 52:43-46

Underwood, S. and Mulvaney, P. (1994) Effect of the solution refractive index on the color of gold colloids. Langmuir 10:3427-3430.

Vissokov, G., Grancharov, I., Tsvetanov, T. (2003) On the plasmachemical synthesis of nanopowders. Plasma Sci Technol 5(6):2039–2050

Vollath, D. (2007) Plasma synthesis of nanoparticles. Kona 25:39–55

Vollath D. (2008). Plasma synthesis of nanopowders. *Journal Nanopart. Res*.

Wang, Y., Shi, S. D.-H., Hendrickson, C.L. and Marshall, A.G. (2000) Mass-selective ion accumulation and fragmentation in a linear octupole ion trap external to a Fourier transform ion cyclotron resonance mass spectrometer. *Intl. J. Mass. Spec.* 198:113-120.

Wang, X., Kruis, F.E. and McMurry, P.H. (2005a) Aerodynamic Focusing of Nanoparticles: I. Guideslines for Designing Aerodynamic Lenses for Nanoparticles. *Aerosol Sci. Technol.* 39:611-623.

Wang, X., Gidwani, A., Girshick, S.L. and McMurry, P.H. (2005b). Aerodynamic Focusing of Nanoparticles: II. Numerical Simulation of Particle Motion Through Aerodynamic Lenses. *Aerosol Sci. Technol.* 39:624-636.

Wang, X. and McMurry, P. (2006). A Design Tool for Aerodynamic Lens Systems. *Aerosol Sci. Technol.* 40:320-334.

Ward-Smith, A.J. (1979). Critical Flowmetering: The Characteristics of Cylindrical Nozzles with Sharp Upstream Edges, *Int. J. Heat and Fluid Flow* 1(3):123-132.

Wayne, R.P. (2000) Chemistry of the Atmospheres, Oxford University Press, Oxford.

Wilcox, B.E., Hendrikson, C.L. and Marshall, A.G. (2002) Improved Ion Extraction from a Linear Octopole Ion Trap: SIMION Analysis and Experimental Demonstration, J. ASMS 13:1304-1312.

Wilson, K., Zou, S., Shu, J., Rühl, E., Leone, S.R., Schatz, G.C., and Ahmed, M. (2007) Size-Dependent Angular Distributions of Low-Energy Photoelectrons Emitted from NaCl Nanoparticles. Nano Lett. 7:2014.

Witt, G. (1969) The nature of noctilucent clouds. Space Res. 9:157.

Wizas J.L. (1979) Microchannel Plate Detectors. Nucl. Instr. Methods B 162:587-601.

Wolf, S.; Sommerer, G.; Rutz, S.; Schreiber, E.; Leisner, T. and Woste, L. (1995) Spectroscopy of Size-Selected Neutral Clusters – Femtosecond Evolution of Neutral Silver Trimers. *Phys. Rev. Lett.* 74:4177-4180.

Wolf, S. (1997) Zeitaufgelöste Spektroskopie an Silberclustern. Dissertation, Freie Universität Berlin.

Zasetsky, A.Y., Petelina, S.V. and Svishchev, I.M. (2009) Thermodynamics of homogeneous nucleation of ice particles in the polar summer mesosphere. Atmos. Chem. Phys. 9:965-971.

Zhang, X., Smith, K.A., Worsnop, D.R., Jiménez, J., Jayne and J.T., Kolb (2002). Numerical Characterization of Particle Beam Collimation: Part I. An individual lens or nozzle. *Aerosol Sci. Technol.* 36:617-631.

Zhang, X., Smith, K.A., Worsnop, D.R., Jiménez, J., Jayne, J.T., Kolb, C.E., Morris, J. and Davidovits, P. (2004). Numerical Characterization of Particle Beam Collimation: Part II Integrated Aerodynamic Lens-Nozzle System. *Aerosol Sci. Technol.* 38:619-638.

Ziemann, P.J., Liu, P., Kittelson, D.B. and McMurry, P.H. (1995) Electron Impact Charging Properties of Size-Selected, Submicrometer Organic Particles. J. Phys. Chem. 99:5126-5138.

Zierep, J. (1993). Grundzüge der Strömungslehre, 5. Auflage, Springer, Berlin.